



HAL
open science

Thermal characterization of nanostructures using scanning thermal microscopy

Indrayush De

► **To cite this version:**

Indrayush De. Thermal characterization of nanostructures using scanning thermal microscopy. Mechanics [physics]. Université de Bordeaux, 2017. English. NNT : 2017BORD0563 . tel-01545383

HAL Id: tel-01545383

<https://theses.hal.science/tel-01545383>

Submitted on 22 Jun 2017

HAL is a multi-disciplinary open access archive for the deposit and dissemination of scientific research documents, whether they are published or not. The documents may come from teaching and research institutions in France or abroad, or from public or private research centers.

L'archive ouverte pluridisciplinaire **HAL**, est destinée au dépôt et à la diffusion de documents scientifiques de niveau recherche, publiés ou non, émanant des établissements d'enseignement et de recherche français ou étrangers, des laboratoires publics ou privés.

THÈSE PRÉSENTÉE
POUR OBTENIR LE GRADE DE
DOCTEUR DE
L'UNIVERSITÉ DE BORDEAUX

SCIENCES POUR L'INGÉNIEUR
INGÉNIERIE MÉCANIQUE

par Indrayush DE

**THERMAL CHARACTERIZATION OF NANOSTRUCTURES
USING SCANNING THERMAL MICROSCOPY**

Sous la direction de : Mr. Jean-Luc BATTAGLIA

Soutenue le 31/03/2017

Membres du jury :

Mr. REMY, Benjamin	Professeur	Université de Lorraine	Rapporteur
Mr. BERTRAND, Garnier	CR1 - HDR	LTN, Polytech'Nantes	Rapporteur
Mme. TRANNOY, Nathalie	Professeur	Université de Reims Champagne-Ardenne, GRESPI	Examinateur
M. DAUVERGNE, Jean-Luc	Ingénieur	ÉPSILON	Examinateur
Mme. PRADERE, Marta	Responsable	EPSILON	Invitée

Directeur de thèse : Jean-Luc BATTAGLIA

Titre : Caractérisation thermique des nanostructures avec une microscopie thermique à balayage « SThM »

Résumé : La caractérisation thermique est cruciale pour la conception et le développement d'applications critiques dans divers domaines. Elle trouve son utilisation dans la détection de défauts et de points chauds dans la fabrication de semi-conducteurs, l'imagerie sous-sol ainsi que la recherche de transport thermique et de charge à des longueurs inférieures à 100 nm. La capacité de comprendre et de contrôler les propriétés thermiques des nanostructures à un niveau de sous-micron est essentielle pour obtenir les performances souhaitées. Pour atteindre cet objectif, la microscopie thermique à balayage (SThM) est très bien adaptée pour cartographier la conductivité thermique à la surface des matériaux et des appareils à l'échelle nanométrique. SThM est une technique d'imagerie "champ proche". C'est une méthode de contact, la sonde étant en contact avec la surface à une force contrôlée. STHM utilise une structure cantilever identique à celle des sondes utilisées dans un Microscope à Force Atomique (AFM). La principale différence est le fait qu'un capteur thermique est intégré à la pointe de la sonde. En outre, ce capteur peut également être utilisé comme chauffage dans le cas d'éléments thermorésistants tels que Pt ou Pd. Par conséquent, le SThM est le résultat d'un AFM équipé d'une sonde thermique. Cet instrument fournit une résolution sous-micromètre dans la résolution spatiale, c'est-à-dire plus que la résolution des techniques optiques dans la gamme de longueurs d'onde visible. La résolution classique qui est réalisée de nos jours est de l'ordre de moins de 100 nanomètres alors que celle obtenue avec la première sonde Wollaston était environ 10 fois plus élevée.

Par conséquent, mesurer la température et les propriétés thermiques de la matière à la microscale sont deux objectifs difficiles qui ont monopolisé l'énergie et le temps de nombreux chercheurs partout dans le monde depuis plusieurs décennies. Ces deux objectifs ne sont pas similaires. Tout d'abord, la mesure d'une température dans un domaine dont la dimension caractéristique est inférieure au micromètre semble moins difficile que mesurer la conductivité thermique d'un

matériau à cette échelle. En effet, la loi de Fourier $\vec{q} = -k \vec{\nabla} T$ mais informe que la mesure d'une conductivité thermique k nécessite non seulement la mesure de la température à deux emplacements différents ($\vec{\nabla} T$) mais aussi le flux de chaleur (\vec{q}) par conduction entre ces deux points. D'autre part, il faut rappeler que la température est une quantité statistique reflétant la

variation de l'énergie cinétique moyenne des transporteurs de chaleur (phonons et électrons) dans la matière. Par conséquent, il faut tenir compte de la dimension du domaine où la moyenne est effectuée. La notion de supports de chaleur libre parcours moyen (PMF) est fondamentale lorsque l'on veut accéder à l'enquête thermique de la matière à l'échelle microscopique. Le PMF de l'électron et du phonon est quelque chose de difficile à connaître a priori. Cela dépend, au premier ordre, de la structure du matériau et de la température elle-même. En effet, on a observé que le PMF varie selon l'état cristallin, de la structure amorphe à la structure bien organisée, et aux effets quantiques qui se produisent inévitablement à basse température. Bien que l'analyse de la PMF ne constitue pas un objectif du présent travail, elle doit rester présente aux différentes étapes de nos développements expérimentaux et théoriques.

En supposant que les conditions d'existence de la température et du gradient de température sont vérifiées à l'échelle sur laquelle nous travaillons, c'est-à-dire à la microscale, le problème de la mesure des propriétés thermiques reste essentiellement le même que celui de la macroscale. Il s'agit d'un problème inverse de conduction thermique (PICT). La résolution d'un tel problème est maintenant bien connue. Au moins, nous savons que cela consiste à minimiser l'écart entre les mesures et les résultats simulés d'un modèle qui devrait reproduire l'expérience aussi précisément que possible. Comme d'habitude, les questions qui se posent quand on essaie de résoudre le PICT sont: i/ quels sont les phénomènes physiques qui doivent être pris en compte dans le modèle? ii/ quels sont les paramètres qui sont bien connus? Et iii/ parmi tous les paramètres inconnus, quels sont les identifiables? La réponse au premier point conduit à éviter un biais dans le modèle et donc un biais sur les paramètres identifiés en leur attribuant un certain comportement physique qui n'est pas décrit dans le modèle. Répondre au deuxième point permet de maximiser la parcimonie et la fiabilité du modèle. Enfin, répondre au dernier point est lié à l'analyse de sensibilité de la quantité mesurée par rapport aux paramètres inconnus à l'aide du modèle. Cette

approche est bien établie dans la communauté de transfert de chaleur. Il a été appliqué avec succès dans une très large gamme d'applications. À notre avis, il n'a pas été appliqué dans sa formulation rigoureuse dans le domaine de la microscopie thermique à balayage, et c'est peut-être l'un des aspects les plus originaux de cette thèse.

Le principe de base pour mesurer les propriétés thermiques à la microscale reste essentiellement identique à celui de la macroscale: une perturbation thermique est générée dans le matériel étudié et la variation (absolue ou relative) de la température est mesurée à un ou plusieurs endroits dans le matériel. Il n'est donc pas très surprenant de trouver que les méthodes développées pour les matériaux en vrac ne changent pas lorsqu'elles s'approchent de l'échelle inférieure.

Nous examinons également le travail qui a été publié par plusieurs auteurs sur la microscopie thermique à balayage (S_{Th}M). Nous essayons de voir pourquoi S_{Th}M est plus avantageux par rapport aux autres types de techniques thermiques microscopiques et aux progrès réalisés sur une courte période de temps. Nous examinons les différents types de sondes thermiques (thermorésistantes, Wollstone et micro-fabriquées) et les différents types de modes expérimentaux (modes AC et DC). Grâce à des recherches antérieures, nous voyons également comment les chercheurs ont défini le transfert de chaleur entre la sonde et le matériau (rayonnement, ménisque d'eau, transfert de chaleur dans l'air et conduction thermique solide-solide) qui leur a finalement permis d'obtenir la température et / ou mesures de propriétés thermiques.

Ensuite, nous commençons à examiner de plus près les recherches que nous avons réalisées pour ce doctorat. En essayant d'expliquer la configuration expérimentale que nous avons développée (sondes thermiques, générateur de fonctions, amplificateur à verrouillage, mesure 3ω et poste de travail). Nous examinons les modes de travail qui peuvent être réalisés en utilisant ce type de configuration (mode passif et mode actif) ainsi que l'étalonnage de la sonde et les paramètres sensibles (force de contact, mouvement de la vitesse de la sonde, temps d'intégration et temps d'acquisition) qui affectent les Résultats expérimentaux et nous permettent d'obtenir le rayon de sonde effectif et la résistance au contact thermique. Grâce à nos expériences et à notre analyse, nous verrons que le rayon effectif et la résistance effective au contact thermique entre la sonde et

l'échantillon restent constants pour une large gamme de matériaux, y compris les diélectriques et les semi-conducteurs.

Nous avons développé un modèle de transfert de chaleur utilisant un réseau d'impédances thermiques qui utilise des transformations intégrales. Nous présentons également l'utilisation de l'analyse des éléments finis (FEA) avec des domaines semi-infinis pour la fréquence élevée. L'approche originale principale, en ce qui concerne les travaux antérieurs sur le sujet, est d'utiliser la température de la sonde dépendante de la fréquence comme impédance thermique de la sonde lorsque la sonde est hors contact. Nous justifions cette approche en utilisant la FEA et des solutions approximatives. Nous effectuons également une analyse de sensibilité de la température de la sonde à un paramètre critique pour déterminer quel paramètre peut être ou non déterminé simultanément.

En outre, nous souhaitons valider notre modèle thermique et l'étalonnage de la sonde en connaissant les paramètres sensibles en analysant en profondeur l'effet du mouvement de la sonde sur le rayon de contact effectif et la résistance du contact entre la sonde et l'échantillon. Nous essayons d'identifier le rayon de sonde effectif expérimentalement aussi via l'analyse des éléments finis. Ensuite, nous concluons en effectuant des expériences sur un échantillon avec des propriétés thermiques connues pour prédire la limite de la conductivité thermique mesurable en utilisant des sondes SThM modernes. On voit que le développement des sondes a conduit à la réduction du rayon de la sonde. Cela a permis d'améliorer la résolution spatiale mais en même temps il réduit la sensibilité de la sonde aux matériaux à conductivité thermique plus élevée.

Ayant toutes les informations, nous effectuons différentes applications en utilisant SThM. Ces applications vont de nano-fil à nano-diapositif 3D GST et complexes composites pyrocarbonés. Nous avons utilisé les techniques expérimentales et le modèle thermique que nous avons décrit dans la thèse ainsi que l'analyse des éléments finis pour comprendre et étudier les propriétés thermiques de divers types d'échantillons. Nous obtenons la résistance aux limites thermiques entre les couches verticales du dispositif de mémoire de changement de phase consistant en une tranchée μ -GST, la résistance thermique transversale d'un nanofil et la conductivité thermique effective ainsi que la résistance aux limites thermiques de la fibre et la matrice d'un complexe

CC composite. Les résultats de ces analyses ont également été publiés dans des revues scientifiques.

Mots clés : caractérisation thermique, microscopie thermique à balayage, SThM, résistance thermique, rayon de contact, conductivité thermique, résistance aux limites thermiques

Title : Thermal Characterization of Nanostructures using Scanning Thermal Microscopy

Abstract : The objective of this thesis is to master quantitative aspects when using near-field thermal microscopy by using the scanning thermal microscopy technique (SThM). We start by taking an in-depth look into the work performed previously by other scientist and research organizations. From there, we understand the progress the SThM probes have made through the decades, understand the probe sensitivity to the range of conductivity of the materials under investigation, verify the resistances encountered when the probe comes in contact with the sample and the applications of SThM.

Then we look into the equipment necessary for performing tests to characterize material thermal properties. The SThM we use is based on atomic force microscope (AFM) with a thermal probe attached at the end. The AFM is described in this work along with the probes we have utilized. For the purpose of our work, we are only using thermoresistive probes that play the role of the heater and the thermometer. These probes allow us to obtain sample temperature and thermal conductivity. We use two different types of thermal probes – 2-point probe and 4-point probe with SiO₂ or with Si₃N₄ cantilever. Both the probes are very similar when it comes to functioning with the major difference being that the 4-point probe doesn't have current limiters. Then, we present the use of recent heat-resistive probes allowing to reach a spatial resolution of the order of 100 nm under atmosphere and of 30 nm under vacuum. These probes can be used in passive mode for measuring the temperature at the surface of a material or component and in active mode for the determination of the thermal properties of these systems. Using thermoresistive probes means that no specialized devices are necessary for operation. Using simple commercial solutions like simple AC or DC current and Wheatstone bridge are sufficient to provide basic

thermal images. In our case we have also utilized other industrial devices and a homemade SThM setup to further improve the quality of measurement and accuracy. All the elements of the experimental setup have been connected using GPIB and that have been remotely controlled from a computer using a code developed under Python language. This code allows to make the frequency dependent measurement as well as the probe calibration.

Intensive work has been performed to investigate the heat transfer model within the SThM experiment. Our goal is to show that a pragmatic and efficient way to model the heat transfer in such a complex experiment can be done by making a parsimonious choice of the main parameters. Indeed, it appears that the most efficient way, with respect to the identification of thermal properties of an investigated material is to first identify the frequency dependent transfer function of the probe from measurements of the amplitude and the phase when the probe is out-of-contact from the surface, then merge the entire physical phenomena that occur at the interface between the probe and the surface in a single thermal boundary resistance and finally use either an analytical or discrete solution for the heat transfer within the investigated material according to its geometry and to the location of the probe on the surface. This methodology aims to finally identify the entire unknown within such a complex problem. We propose a model of the experiment that involves only a very limited number of parameters. Our model is very unique where we utilize the thermal impedance formalism allowing us not to consider the properties and the geometry of the probe. This method allows us to obtain the probe out-of-contact resistance experimentally and can be used for all types of thermal probes. Our approach consists in using this thermal model and the measurements carried out to solve the inverse problem of heat conduction in the studied systems.

We also talk about all the technical factors that come into play while performing experiments using the setup. We started with the 2-point probe in static contact (motionless probe) with a SiO₂ substrate. The thermal properties of the substrate are well known and therefore this experiment leads us to identify the contact resistance at the interface between the probe and the surface assuming a value for the radius contact area. Then, we look into is the effect of the speed of the probe while scanning the SiO₂ surface. Since our numerical model is based on the consideration that the probe is in static condition at each acquisition step, it is easy to check this assumption with the experimentation and see if the results are in agreement with our model. The next important thing that we look into is the radius of the contact area between the probe and the

surface assuming it is the shape of a disk. In this case, we are trying to obtain the effective radius considering the presence of water meniscus. To achieve this objective, we used two different approaches. The first one is based on the “step” method that consists in a SiO₂ thin layer deposited as a step on a GaAs substrate. The edge of the step is expected to have an impact on the measured temperature of the probe and this impact is directly proportional to the contact radius. Therefore the contact radius can be determined ‘graphically’ from the temperature evolution along the scan. On the other hand, we proposed to use those measurements as the input of an inverse heat conduction problem (IHCP) to identify the probe radius. The model is solved using the finite element method using the precautions presented in the chapter 4. Finally, we perform DC and AC (3ω) measurement on samples whose thermal conductivity is well known and varies from 0.1 to 40 W.m⁻¹.K⁻¹. Those measurements have been performed first in dynamic mode and in ambient conditions. Then the experiments have been repeated in static mode (motionless probe), under vacuum and using the 4-point probe. This kind of experiments is very useful to predict the limit of the measurable thermal conductivity using this probe and to quantify the role of the experimental conditions on the contact radius and thermal contact resistance at the interface between the probe and the investigated surface. When the probe comes in contact with the sample, there is the obvious contact resistance and the radius of contact between the probe and the sample. We try to obtain the values of the effective thermal contact resistance considering all the effects (water meniscus, radiation, constriction of thermal lines, etc.) as well as the effective probe radius. We find out that these above mentioned quantities remain constant for a wide range of materials including dielectrics and semiconductors. We also investigate the sensitivity of the probe and we deduce that it is difficult for our SThM to provide accurate data when the sample thermal conductivity is more 25 W/m/K. With time, there has been a reduction in the size of the tip of the probe. This has led to the increase in the spatial resolution but has reduced the probe sensitivity. Moreover, we also prove that using SThM we can only calculate the effective thermal conductivity of materials. We also monitor the effect of the speed of the probe on the experiments as well as other sensitive parameters including force of contact, sample roughness, etc.

Knowing the experimental setup, validating the setup to be used and after developing the thermal model, we take a look at the different applications that we have been performed using scanning thermal microscopy. We have utilized the experimental technique and the thermal model we

have described in the previous chapters to understand and investigate the thermal properties of various types of sample. We have used a range of samples with varying thermal properties, dimensions and methods of fabrication. We utilize materials such as nanowires (investigation of thermal resistance in the transverse direction), complex C-C composites (investigation of the thermal boundary resistance between the fiber and matrix as well as the effective thermal conductivity of the matrix) as well as on an electronic component using a phase change material (investigation of the thermal boundary resistance of a μ -trench). Through our research we clearly see that SThM is best suited for providing accurate quantitative thermal measurement at the nanoscale with high spatial resolution for a wide variety of materials with different configurations.

Finally, we finish by concluding with the findings we have discovered during this research and provide our perspective towards the further development and utilization of scanning thermal microscopy.

Keywords : thermal characterization, scanning thermal microscopy, SThM, thermal resistance, radius of contact, thermal conductivity, thermal boundary resistance

Unité de recherche

Institut de Mécanique et d'Ingénierie (I2M, CNRS UMR 5295)
Fluides-Transferts - TREFLE
Esplanade des Arts et Métiers
33405 TALENCE Cedex



Contents

2.1. Introduction	21
2.2. Experimental techniques for temperature measurement and thermal characterization at the microscale	21
2.3. A short overview of progress in SThM, STP and thermocouple probe	28
2.4. The Thermoresistive probes	35
2.4.1. The Wollastone probe	36
2.4.2. The micro-fabricated probes	38
2.4.3. Dynamic Probes	43
2.4.4. Other Modern Probes	45
2.4.5. Summarize.....	46
2.5. The Experimental Modes	47
2.5.1. The DC mode	47
2.5.2. The AC mode	49
2.5.3. Advantages and drawbacks of DC and AC modes.....	52
2.6. Heat Transfer at the probe-material interface.....	52
2.6.1. Physical phenomena description	52
2.6.2. Radiation	54
2.6.3. Water Meniscus.....	54
2.6.4. Heat transfer in air.....	57
2.6.5. Solid-Solid Thermal Conduction.....	59
2.7. Illustrations of the SThM application.....	61

2.7.1.	Temperature measurement	61
2.7.2.	Thermal properties measurements	63
2.8.	Conclusions	65
2.9.	References	65
3.1.	Introduction	71
3.2.	Experimental setup	71
3.2.1.	Global presentation.....	71
3.2.2.	The AFM	72
3.2.3.	Thermal Probes.....	73
3.2.3.1.	Probe Fabrication	73
3.2.3.2.	The 2 point probe	75
3.2.3.3.	The 4 Point Probe	77
3.2.4.	The function generator	78
3.2.5.	The lock-in amplifier	79
3.2.6.	The 3ω measurement.....	83
3.2.7.	The workstation	87
3.3.	Sample surface preparation	89
3.4.	The working modes	91
3.4.1.	The passive mode	91
3.4.2.	The active mode	94
3.4.2.1.	The continuous wave mode (DC).....	94
3.4.2.2.	The 3ω mode (AC).....	95
3.5.	Probe coefficient of resistance measurement	99
3.5.1.	Experimental setup for the calibration	99
3.5.2.	2-point probe	100
3.5.3.	4-point probe	103
3.6.	Sensitive parameters (force contact, probe motion speed, integration time, acquisition time).....	105
3.6.1.	Contact force	105
3.6.2.	Scan velocity, Acquisition Time and Integration Time	106
3.7.	Influence of the laser	109
3.8.	Conclusion.....	111
3.9.	Reference.....	111
4.1.	Introduction	113

4.2.	General formulation of the heat transfer model	115
4.2.1.	The use of thermal impedances network.....	115
4.2.2.	Link with experimental measurements.....	117
4.3.	-Heat transfer in the investigated medium	118
4.3.1.	Analytical expression based on integral transforms.....	118
4.3.2.	The use of the finite element Method.....	119
4.3.2.1.	1D case	120
4.3.2.2.	2D-axi case	124
4.4.	Heat transfer in the probe	126
4.4.1.	Complete model	126
4.4.2.	Approximate model.....	128
4.4.3.	Identified model	132
4.5.	Sensitivity analysis	135
4.6.	Conclusion.....	137
4.7.	Appendix	138
4.7.1.	Appendix A: heat transfer in a semi-infinite medium whose surface is submitted to a motion point located heat flux at constant velocity v	138
4.7.2.	Appendix B: heat transfer in a semi-infinite medium whose surface is submitted to a motion disk heat flux at constant velocity v	139
4.7.3.	Appendix C: heat transfer in a semi-infinite medium whose surface is submitted to a heat flux over a motionless disk of radius r_0	141
4.7.4.	Appendix D: heat transfer in a cylindrical coordinate framework.....	147
4.8.	References	151
5.1.	Introduction	153
5.2.	2-point probe in static contact on SiO_2	154
5.3.	Effect of the probe motion on r_0 and R_c	158
5.4.	Radius of the contact area measurement	161
5.4.1.	The step technique.....	161
5.4.2.	Identification of r_0	163
5.5.	Identification of r_0 and R_c under ambient conditions with the probe in motion.....	168
5.6.	SThM experiments in vacuum on samples with known thermal conductivity using the 4-point probe 170	
5.7.	Conclusion.....	177
5.8.	Appendix : the Levenberg-Marquardt (LM) algorithm.....	178

5.9. References	180
6.1. Introduction	181
6.2. Thermal resistance of a In_3SbTe_2 nanowire	181
6.2.1. Context	181
6.2.2. Industrial Applications of Sample	182
6.2.3. Sample Description	182
6.2.4. Experiment	183
6.2.5. Results and analysis	186
6.2.6. Inference	189
6.3. 3D phase change memore Nano Device.....	190
6.3.1. Context	190
6.3.2. Industrial Applications of Sample.....	191
6.3.3. Sample Description	191
6.3.4. Experimental Results.....	193
6.3.5. Simulation	194
6.4. Pyrocarbon Composite	198
6.4.1. Context	198
6.4.2. Industrial Application of the Sample.....	198
6.4.3. Sample Description	198
6.4.4. Thermal Modelling.....	200
6.4.5. Experimental Results.....	204
6.4.6. Analysis.....	205
6.4.7. Conclusion	207
6.5. Global Conclusion.....	208
6.6. Reference.....	209
7.1. Main conclusions.....	212
7.2. Perspectives	217

1. Chapter 1 - INTRODUCTION

Thermal characterization is crucial for the design and development of critical applications in various fields. It finds its use in the detection of defects and hot spots in semiconductor manufacturing, subsurface imaging as well as thermal and charge transport research at sub 100nm lengths. The ability to understand and control the thermal properties of nanostructures at a sub-micron level is essential to obtain desired performance. To accomplish this aim, the Scanning Thermal Microscopy (SThM) is very well suited for mapping thermal conductivity field at the surface of materials and devices at a nanometer scale. SThM enters in the category of “near-field” imaging technique. It is a contact method, the probe being in contact with the surface with a controlled force. SThM utilizes a cantilever structure identical to that of the probes used in an Atomic Force Microscope (AFM). The main difference stands in the fact that a thermal sensor is embedded at the tip of the probe. Moreover, this sensor can be also used as a heater in case of thermoresistive elements as Pt or Pd. Therefore the SThM is the result of an AFM equipped with a thermal probe. This instrument provides a resolution that is sub-micrometer in spatial resolution, i.e., largely more than the resolution of optical techniques in the visible wavelength range. The classical resolution that is achieved nowadays is of the order of less than 100 nanometers whereas that obtained with the first Wollaston probe was about 10 times higher. Additional improvements have been yet achieved so far from other authors and it is now classical to read papers where the spatial resolution of very advanced probe is about 5-10 nm.

Therefore, measuring the temperature and the thermal properties of matter at the microscale are two challenging objectives that monopolized the energy and time of many researchers all over the world for several decades now. These two objectives are not similar. First, measuring a temperature in a domain whose characteristic dimension is lower than the micrometer seems to be less difficult than measuring the thermal conductivity of a material at this scale. Indeed, the Fourier’s law, $\vec{\varphi} = -k\vec{\nabla}T$, informs us that measuring a thermal conductivity k requires not only measuring the temperature at two different locations ($\vec{\nabla}T$) but also the heat flux ($\vec{\varphi}$) by conduction between those two points. On the other hand, it must be reminded that the temperature is a statistic quantity reflecting the change in the average kinetic energy of the heat

carriers (phonons and electrons) within the matter. Therefore, one has to account with the dimension of the domain where the averaging is performed. The notion of heat carriers mean free path (MFP) is fundamental when one wants to access the thermal investigation of matter at the microscale. The MFP of electron and phonon is something difficult to know a priori. It depends, at the first order, on the structuration of the matter and on the temperature itself. Indeed, it has been observed that the MFP varies according to the crystalline state, from amorphous to well-organized structure, and to the quantum effects that inevitably occur at low temperature. Although the MFP analysis does not constitute an objective of the present work, it must remain present at the different stages of our experimental and theoretical developments.

Assuming the conditions for existence of the temperature and temperature gradient are verified at the scale we are working on, i.e. the microscale, the problem of measuring thermal properties remains essentially the same as that at the macroscale. This is an inverse heat conduction problem (IHCP). The resolution of such a problem is now well known. At least, we know that it consists in minimizing the gap between measurements and the simulated outputs of a model that is expected to reproduce the experiment the more faithfully as possible. As usual, the questions that arise when one tries to solve the IHCP are: i/ what are the physical phenomena that need to be accounted within the model?, ii/ what are the parameters that are well known? and iii/ among all the unknown parameters, what are the identifiable ones ? Answering the first point leads to avoid a bias in the model and therefore a bias on the identified parameters by attributing them some physical behavior that are not described within the model. Answering the second point leads to maximize the parsimony and the reliability of the model. Finally, answering the last point is related to the sensitivity analysis of the measured quantity with respect to the unknown parameters using the model. This approach is well established in the community of heat transfer. It has been applied successfully in a very wide range of applications. To our opinion, it has not been applied in its rigorous formulation in the field of scanning thermal microscopy, and this is maybe one of the most original aspects of this thesis.

The basic principle for measuring the thermal properties at the microscale remains essentially identical to that for the macroscale: a thermal disturbance is generated within the investigated medium and the change (absolute or relative) of temperature is measured at one or several locations in the medium. It is therefore not very surprising to find that the methods that have been developed for bulk materials do not change when approaching the lower scale. A schematic

description of the IHCP in relation with the thermal characterization is presented in Figure 1. This figure highlights that now only the unknown thermal properties β_s of the investigated system/material need to be identified. Indeed, the interactions between the disturbance and the system as well as between the measurement and the system involve additional unknown parameters β_d and β_m respectively.

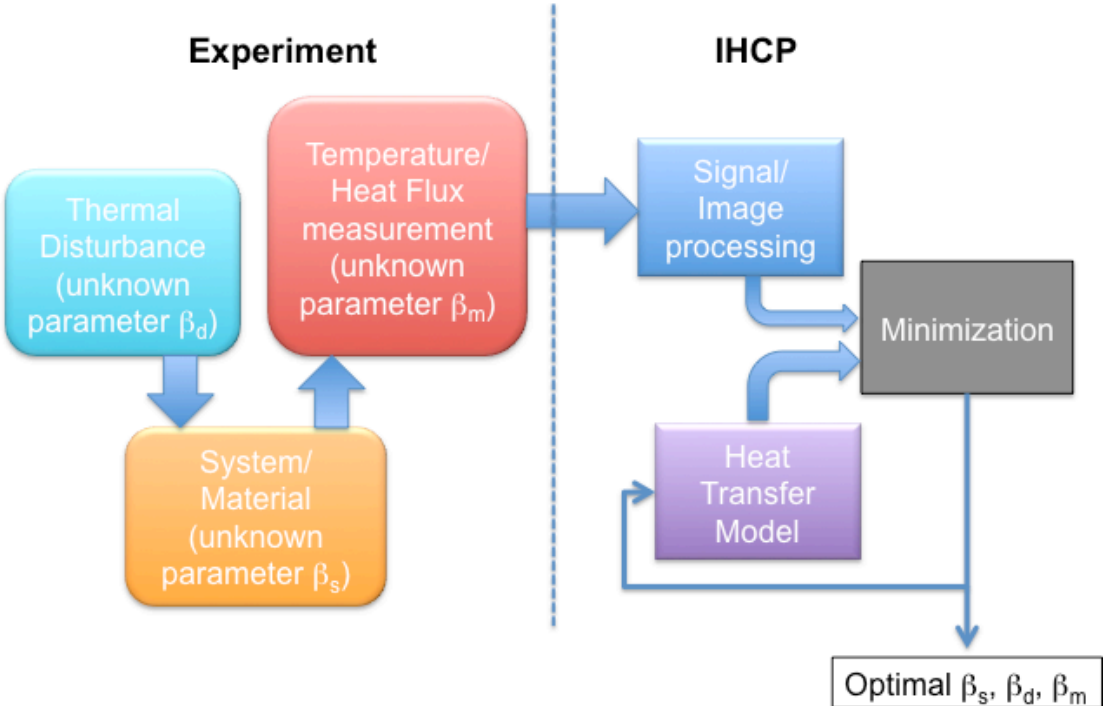


Figure 1. Schematic description of the inverse heat conduction problem in thermal characterization experiment.

In the second chapter, we look into the work that has been published by several authors on scanning thermal microscopy (SThM). We try to see why SThM is more advantageous over other types of microscopic thermal techniques and the progress it has made over a short period of time. We look into the different types of thermal probes (thermoresistive, Wollastone and micro-fabricated) and the different types of experimental modes (AC and DC modes). Through previous literature, we also get to see how researchers have defined the heat transfer between the probe and the material (radiation, water meniscus, heat transfer in air and solid-solid thermal conduction) which finally allowed them to obtain the temperature and/or thermal property measurements.

In the third chapter, we start taking a closer look at the research we have performed for this Ph.D. by trying to explain the experiment setup we have developed (thermal probes, function generator, lock-in amplifier, 3ω measurement and workstation). We look into the working modes that can be done using this type of setup (passive mode and active mode) as well as the calibration of the probe and the sensitive parameters (contact force, probe speed motion, integration and acquisition time) which affect the experimental results and allow us to obtain the effective probe radius and thermal contact resistance.

In the fourth chapter, we developed a heat transfer model using thermal impedances network that rest on the use of integral transforms. We also present the use of the finite element analysis (FEA) taking into account of semi-infinite domains for high frequency. The main original approach, regarding previous work in the topic, is to use the frequency dependant probe temperature as the probe thermal impedance when the probe is out-of-contact. We justify this approach using the FEA and approximate solutions. To conclude the chapter, we also perform a sensitivity analysis of the probe temperature to critical parameter.

In the fifth chapter, we aim to validate our thermal model and the probe calibration knowing the sensitive parameters by analyzing in-depth the effect of probe motion on the effective contact radius and the resistance of contact between the probe and the sample. We try to identify the effective probe radius experimentally as well via. finite element analysis. Then finally, we conclude by performing experiments on sample with known thermal properties to predict the limit of measureable thermal conductivity using modern SThM probes.

In the sixth chapter, we perform different applications using SThM. These application range from nanowire to 3D GST nano-device and complex pyrocarbon composites. We have made use of experimental techniques and the thermal model we have described in the previous chapters along with finite element analysis to understand and investigate the thermal properties of various types of sample. The results of these analyses have been also published in the following scientific journals.

1) Nanowire Device: J.-L. Battaglia, A. Saci, I. De, R. Cecchini, S. Selmo, M. Fanciulli, S. Cecchi, M. Longo, *Thermal resistance measurement of In_3SbTe_2 nanowires*, phys. stat. sol. (a), **DOI:** 10.1002/pssa.201600500 (2016).

2) 3D phase-change memory Device: J.-L. Battaglia, I. De, V. Sousa, *Inverse heat conduction problem in a phase change memory device*, Journal of Physics: Conf. Series **785** (2017) 012002.

3) Pyrocarbon Composite: I. De, J.-L. Battaglia, G. L. Vignoles, *Thermal properties measurements of a silica/pyrocarbon composite at the microscale*, Journal Applied Physics, DOI: 10.1063/1.4967918 (2016).

Finally, in the seventh chapter, we put forth a global conclusion of the work we have performed and try to visualize the bright future of scanning thermal microscopy (SThM).

2. Chapter 2 – BIBLIOGRAPHY

2.1. Introduction

The present chapter is devoted to present the state of the art regarding the field of scanning thermal microscopy. However, in the section 2, we will recall all the used techniques that are now in use to estimate the thermal properties of materials at low scale. This short overview will make us familiar with the two main approaches: the contact and out-of-contact techniques. Each technique will be briefly described and their features and limitations will be outlined. In the section 3, we present the basics of the scanning thermal microscopy technique. When we use an AFM configuration for scanning thermal microscopy, the key feature is the thermal probe and the results obtained vary in resolution and accuracy based on the probe used. We will identify the different type of probes that have been used in the past and are being currently used in the field of scanning thermal microscopy. Moreover, we will also look into the two regimes that can be used for measurements. They are the AC (Alternating Current) mode and the DC (Direct Current) mode that are detailed in the section 4. The results obtained from experimental scanning thermal microscopy not only depend on the type of probe used and/or the experimental approach but also on the different heat transfer phenomena that could occur at the interface between the probe and the investigated surface and the surrounding medium (air, controlled atmosphere, vacuum). The probe and surface contact, the surrounding boundary conditions as well as the heat transfer between the probe and the sample out from the contact have a strong effect on the measured value. These different heat transfer mechanisms are detailed in the section 5. In the section 6, we present some relevant applications of the SThM to measure temperature and thermal properties that have been published already in the literature by different authors.

2.2. Experimental techniques for temperature measurement and thermal characterization at the microscale

One of the easiest and well-known methods is the micro-thermocouple method (Figure 2) where the absolute or differential measure can be obtained at the junction of the probe made of two dissimilar metals due to the intrinsic Seebeck voltage [1]. They are cheap and accurate but they cannot provide imaging and are relatively large with the small commercially available probe diameter being around 13 – 50 μm .

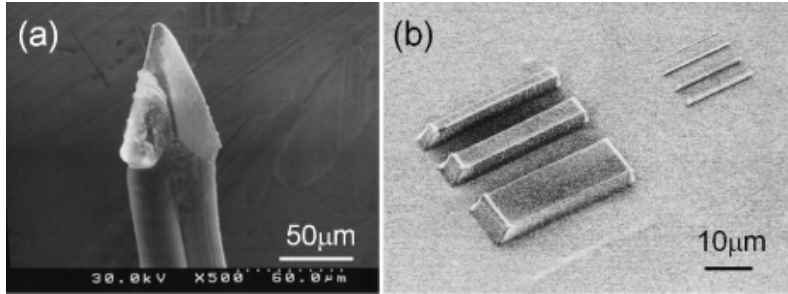


Figure 2. (a) 20 micrometer microthermocouple for direct measuring of (b) resin temperature (Kensuke Tsuchiya, Micro machining technology for micro devices [1]).

Another method in use is the Liquid Crystal Thermography (LCT) method (Figure 3) where a thin layer of liquid crystal is deposited on the surface of the sample under investigation and the color change due to light reflection provides with the temperature [2]. Using a modern technique where the color changes from red to blue over a specified temperature range helps to provide the thermal image. Since this is an optical measurement, theoretical spatial resolution is only limited to the diffraction limit of light in the visible range, about 1 μm . But there are several limitations and question about this process. There is a necessity of knowing the temperature range to determine the proper liquid crystal and a thin and uniform paint on the sample of about 100 μm^2 needs to be placed so knowledge of the thermal conductivity and heat capacity of the coating is necessary. Moreover, questions have been asked regarding its use for vertical specimens. This technique is also used mainly for measuring the relative change of temperature instead of the absolute change due to the difficult calibration stage.

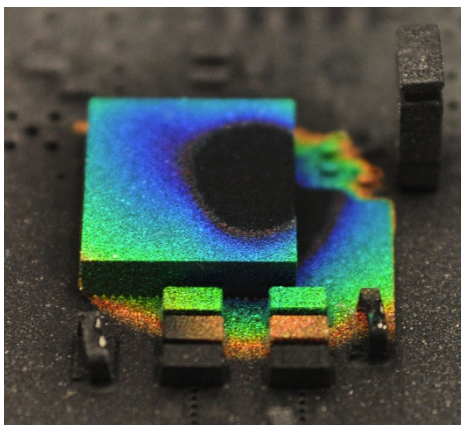


Figure 3. Thermochromic liquid crystals change colour at different temperatures to reveal heat sources on chips and other electronic components. By applying these liquid crystals, engineers can visually find hotspots and temperature fields.

Modern research has seen strides in Infrared (IR) thermography (Figure 4) in tandem with thermorefectance imaging where the former is generally good for low reflectivity materials having high emissivity and the latter is better for high reflectivity materials surface [3]. IR thermography uses infrared sensitive camera to obtain thermal image using Planck’s blackbody law to determine temperature of hot object for minimum wavelengths of 3 μm. Obtaining the radiation intensity at a specific wavelength and considering the surface emissivity, one can measure the absolute change of surface temperature.

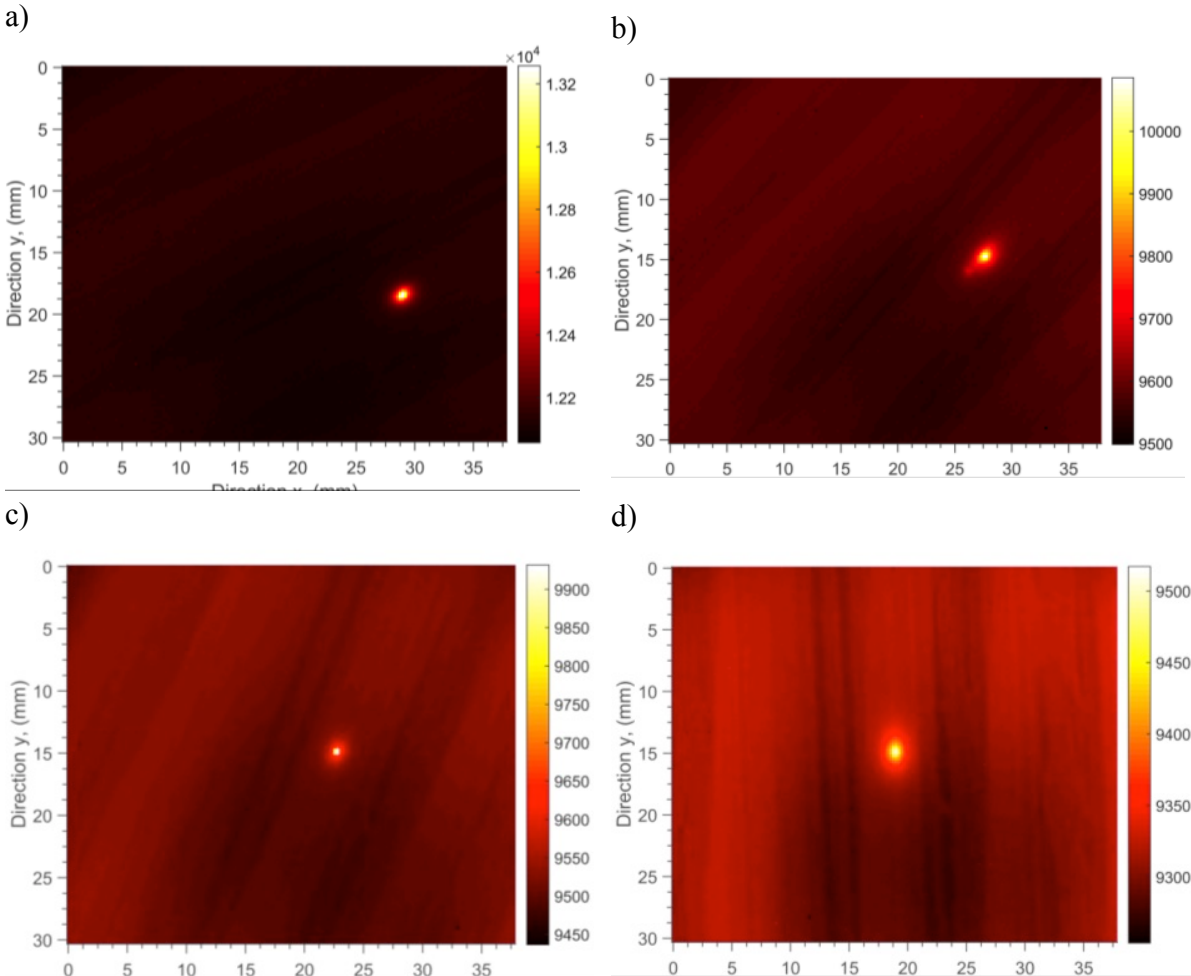


Figure 4. Example of Image obtained with the process of IR Thermography. Those images have been obtained with the laser spot scanning randomly the surface of the medium (flying spot technique, PhD of L. Gaverina [93]).

Thermorefectance method (Figure 5) is well suited for high-speed measurements of thermal transients using a laser beam focused onto a small spot on the sample [4]. Thermorefectance

microscopy uses either p-i-n diode camera or a special high frame rate intensified charge coupled device to capture signals with a good signal-to-noise ratio. It needs an active device that is cycled thermally at a known frequency and a lock-in amplifier. This allows fast single point measurements using a photodetector that can resolve thermal transients with sub microsecond time resolution.

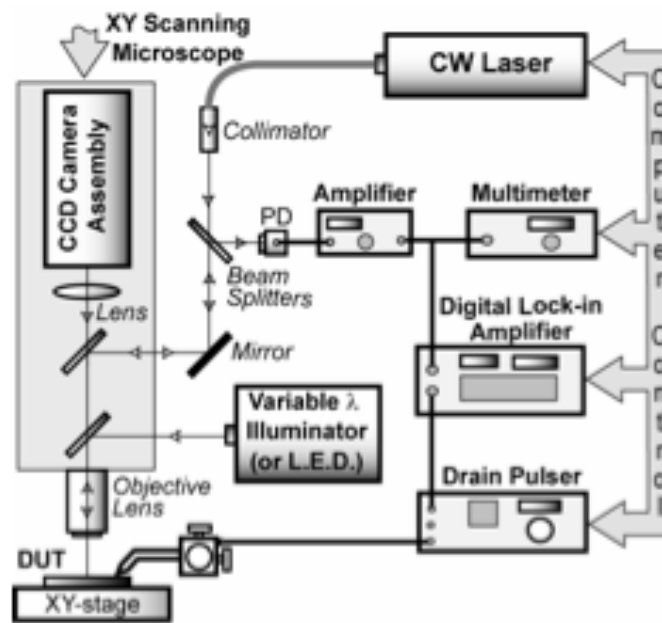


Figure 5. Schematic diagram of the Thermoreflectance Microscopy (Nanoscale Electro-Thermal Sciences Laboratory, Ultrafast laser thermoreflectance microscopy measurement system).

Pump-Probe Picosecond Thermoreflectance (PPPT) is one of the most effective time resolved technique for heat transfer and acoustic studies when it comes to thin films and low dimensional structures (Figure 6). Due to the fact that it is a noncontact and nondestructive optical process providing high temporal and spatial resolutions, PPPT has become very popular in the field of thermal property metrology [5]. Instead of the classical thermoreflectance technique, the heat is generated a modulated or pulsed laser beam, call the pump. Then, a low intensity laser is used to probe the change of reflectivity at the surface sub-sequent to the pump heating. This second laser beam is called the probe. When pulse duration for the pump is close to the pic oar nanosecond then the pump is delayed from the probe using optical delay line or other elaborated techniques.

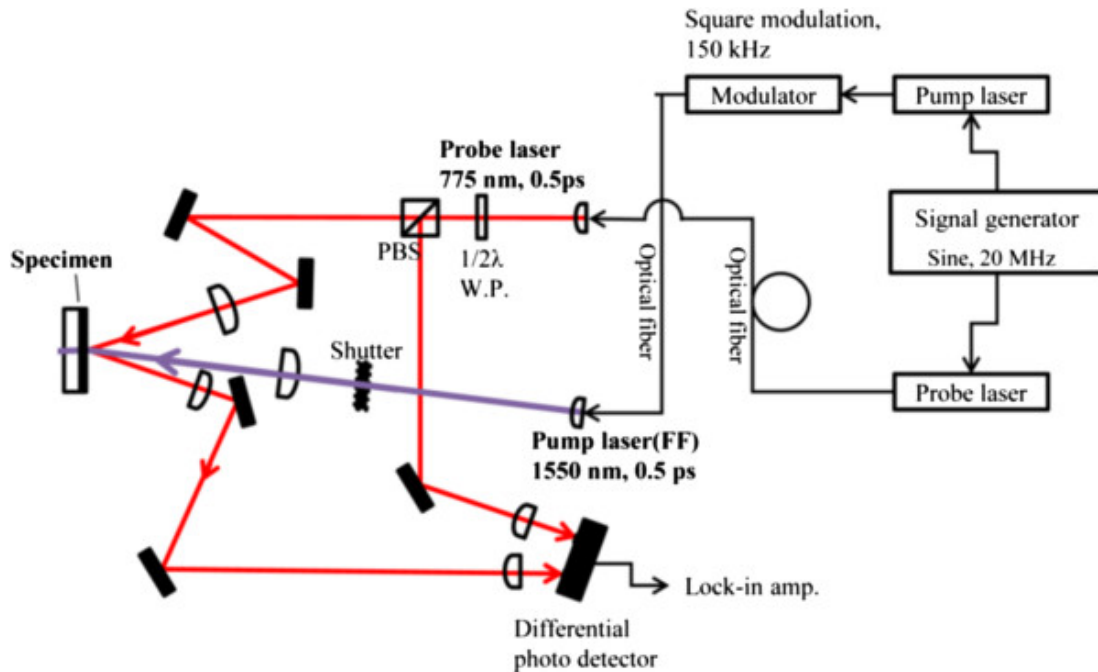


Figure 6. Schematic Diagram of a PPPT Setup from [5].

Another popular form of measurement is the near field scanning optical microscopy (NSOM) that is generally used for topography measurements and for experiments under luminescent and fluorescent conditions [6]. A NSOM probe uses a single mode optical fiber or a specially designed AFM probe approached closely to the surface to collect the near field radiation and therefore to obtain near field imaging through the aperture of about 50 nm (Figure 7). There are several factors that make this method a little complicate. Firstly, there is the construction of the aperture in nanoscale, probe position close enough to the surface of the material under investigation and tip heating resulting in change of geometry that thereby affects the reflected signal. The best thing about NSOM is the spatial resolution it provides, around 50 nm.

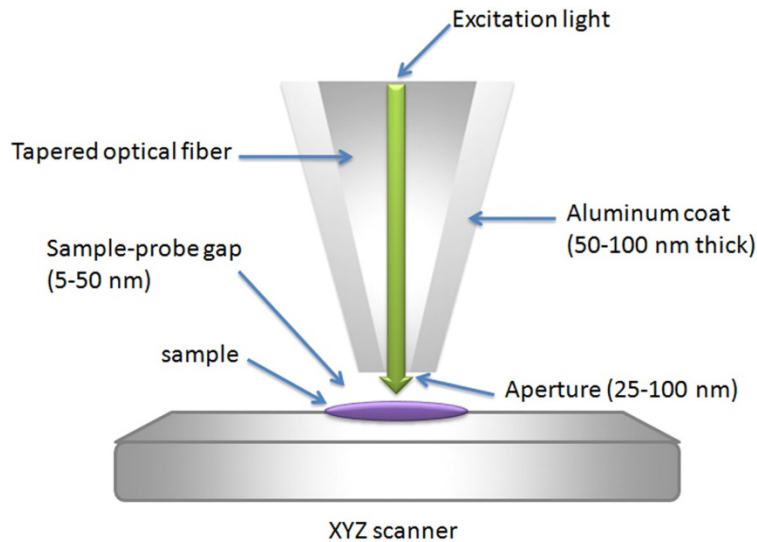


Figure 7. Schematic representation of the aperture of NSOM [6].

Another sort of measurement is achieved using Raman Spectroscopy (Figure 8) that uses short wavelengths from an AR or He-Ne laser providing spatial resolution of less than 1 μm . The scattered photo energy from the sample and the incident photon energy are different as a result of inelastic scatterings and energy exchange with lattice vibrations [7]. Analysis of the amplitude of the downshifted photons (also known as Stokes peaks) and that of the upshifted photons (also called anti-Stokes peaks) is performed. With an increase in temperature, there is an increase in the number of phonons in the excitation mode resulting in the enhancement of the anti-Stokes and Stokes peaks ratio that provides the absolute temperature. Therefore a relationship between the surface temperature and the Raman shift can be observed. However, the calibration of such an experiment is very difficult and even relative changes of the temperature remain challenging.

Another widely used method is to apply built-in temperature sensors directly into the device while fabrication. In this case, the device and sensor geometry becomes very important and the spatial resolution obtained is limited [49].

Now we will compare all the above types of measurement techniques with the basic Scanning Thermal Microscope using the Table 1. As seen from this table, Scanning Thermal Microscopy (SThM) is a contact method that easily provides imaging and high spatial resolution as compared to other techniques. Moreover, the calibration appears less difficult and allows

expecting to measure absolute variation of the surface temperature. We will now enter into the details of this technique.

Table 1 Comparison of various types of Thermal Measurement Techniques at the microscale.

Method	Resolution			Imaging	Notes
	X (μm)	T (K)	t (sec)		
μ thermocouple	50	0.01	0.1 -10	No	Contact Method
IR Thermography	3 -10	0.02 - 1	1 μ	Yes	Emissivity dependent
Lock-in IR Thermography	3 – 10	10 μ	NA	Yes	Need cycling
Liquid Crystal Thermography	2 – 5	0.5	100	Yes	Only near phase transition (ageing issues)
Thermo-reflectance	0.3 – 0.5	0.08	800p – 0.1 μ	Yes	Need Cycling
Optical Interferometry	0.5	100 μ	6n – 0.1 μ	Scan	Indirect measurement (expansion)
Micro Raman	0.5	1	10n	Scan	3D T-distribution
Near Field (NSOM)	0.05	0.1 – 1	0.1 μ	Scan	S/N dependent Tip/sample interaction
Scanning Thermal Microscopy (SThM)	0.05	0.1	10 - 100 μ	Scan	Contact Method Surface morphology

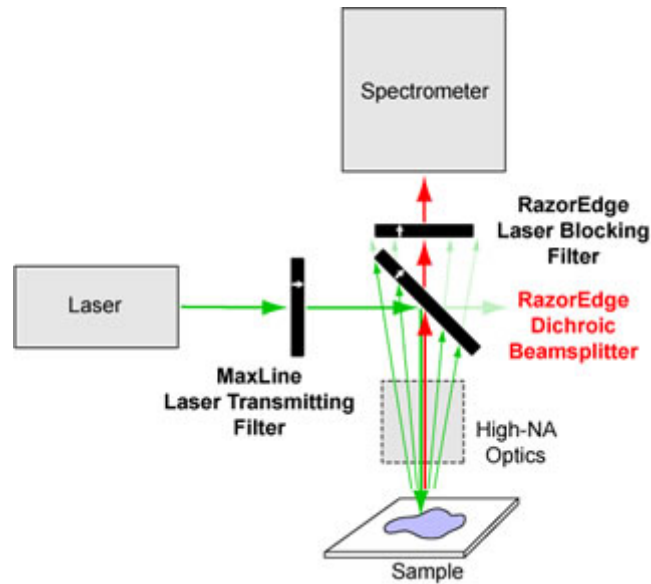


Figure 8. Schematic Diagram of Raman Spectroscopy

2.3.A short overview of progress in SThM, STP and thermocouple probe

In 1986, C. C. Williams and H. K. Wickramasinghe proposed Scanning Thermal Profile (STP) [8] to find a remedy to the shortcoming of Scanning Tunneling Microscope (STM) and the Atomic Force Microscope (AFM). STP was then the new technique for profiling surfaces based on thermal interactions in the near-field between a heated probe tip and the surface (Figure 9). The best features of this new technique was that it could scan all surfaces independent of the material, it didn't need any spacing between the probe tip and the sample as well as could provide image resolutions between 10 and 100 nm as it profiled surfaces over a certain distance in contrast to AFM or STM interactions. The STP was achieved by scanning a small temperature sensor on the end of a heated tip on top of a solid surface. As the heated tip approached the sample, the tip temperature changed due to the thermal coupling between the tip and the sample. The thermal loading between the tip and the sample changes as the tip moves to the sample surface and this provides opportunity for maintaining and controlling the gap between the probe and the sample. Moreover, they also assumed that the temperature of the solid surface remains essentially unchanged. For the practical point of view, the STP was made up of a tiny thermal probe that consisted of a conical thermocouple sensor at the end to provide sensitivity and resolution necessary for high resolution profiling. The thermocouple junction is in contact with two conductors of two different materials separated by an insulator at areas away from the tip

region. The voltage change at the tip is sensed by the other end of the probe and the minimum noticeable change in the tip temperature is less than 0.1 millidegree.

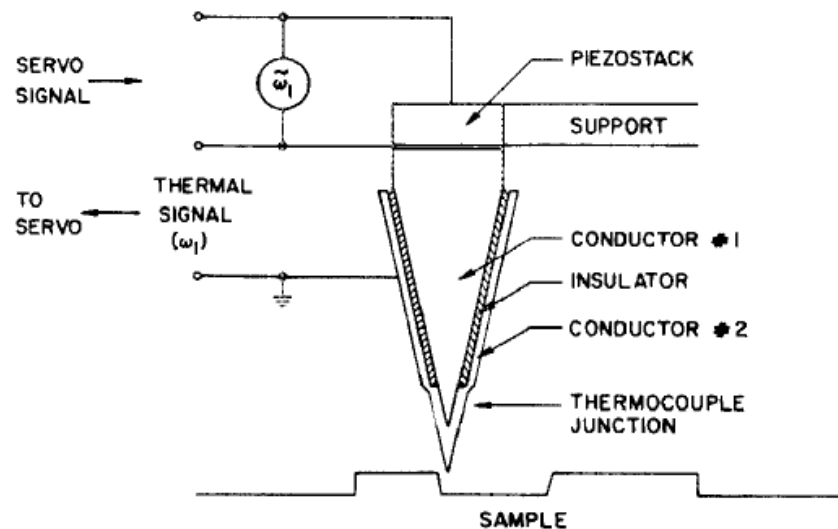


Figure 9. Schematic Diagram of the Scanning Thermal Profiler as described by .C. Williams and H. K. Wickramasinghe in 1986.

STP was based on thermal coupling between the tip and the sample to understand the thermal interactions between solid surfaces of every kind. Moreover, as the conduction takes place through air, it allowed STP to measure surface profiles independent of the material properties because the variation of thermal properties between air and any other forms of solid/liquid is highly different. As the tip moved over the sample of the specimen and over a distance, it was possible to obtain the desired lateral resolution instead of flying the tip over the sample with a certain height. These attractive properties of STP have led to its further development and research to produce our modern age Scanning Thermal Microscopy (SThM).

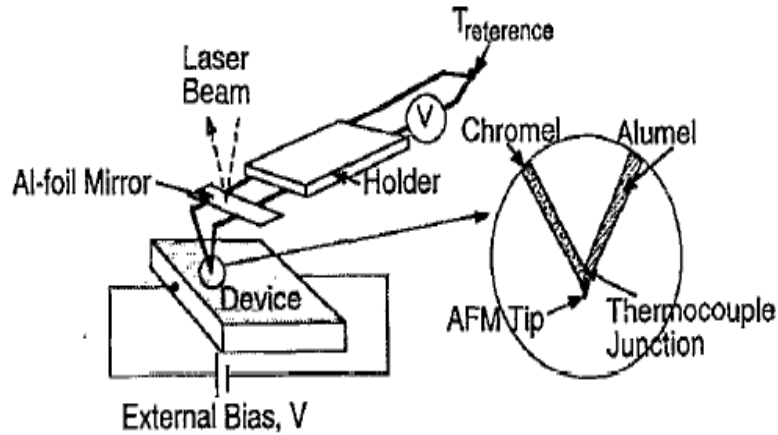


Figure 10. Thermocouple Probe developed by A. Majumdar in 1993 based on a K-type thermocouple [18].

The thermal probe used by C. C. Williams and H. K. Wickramasinghe in 1986 had a few drawbacks with their design. Firstly, due to the fact that the feedback signal was used to maintain a constant probe temperature, it was not possible to obtain thermal surface images. Secondly, the temperature variation across the surface often appeared to be features on the topographical surface image hence making it hard to differentiate between the temperature and the topographical variation. To overcome these problems, in 1993, A. Majumdar, J. P. Carrejo and J. Lai [18] came up with an AFM tip to simultaneously measure the thermal and topographical images of electronic devices. They devised a sharp tip mounted on a cantilever that can be brought in or out-of-contact with the substrate surface using piezoelectric actuators (Figure 10). The thermocouple was made of two wires (K type thermocouple) of which one was chromel and the other was alumel (Figure 11). They used a piece of aluminum foil to act as a reflector for the laser by attaching it to the wires using epoxy. A thermoelectric voltage is generated in the thermocouple junction ($25\mu\text{m}$ in diameter) due to the difference in temperature between the tip and the sample when in contact. The cold junction temperature was held in reference while the variation in the thermoelectric voltage provided thermal image of the sample. Their research demonstrated that this probe could achieve spatial resolution in the range of $0.05\mu\text{m}$. It was also noted that the temperature sensitivity is dependent on various factors including electronic noise, heat transfer through gas conduction, etc. The probe was handmade leading to the problem of reproducibility and the diamond tip often failed to provide high-resolution images.

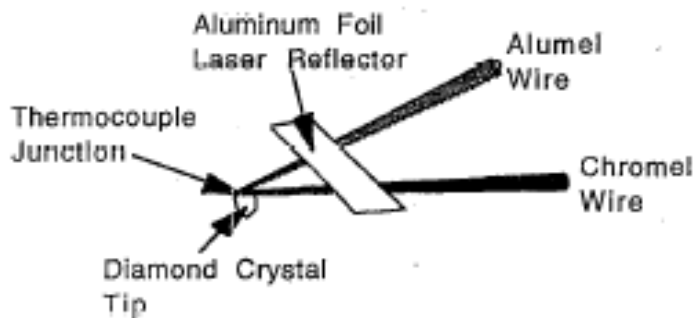


Figure 11. Thin Film Thermocouple Probe devised by A. Majumdar in 1995 [18].

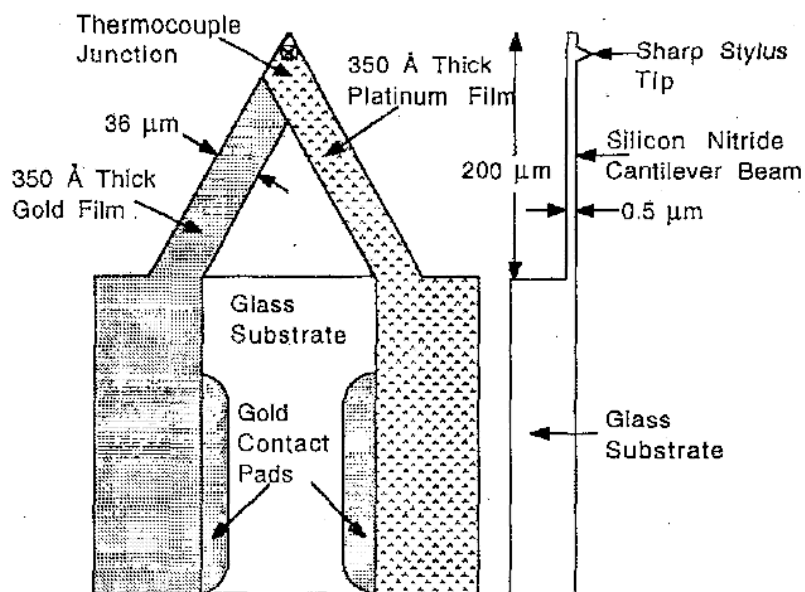


Figure 12. The Diamond tip Thermocouple Probe Introduced by A. Majumdar in 1995 [19].

To account for the problem of reproducibility and image resolution, A. Majumdar proposed a diamond tip thermocouple wire probe that consisted of a small single crystal of diamond attached with the thermocouple wire with the aid of epoxy [19] (Figure 12). Due to the high thermal conductivity of diamond, it reduced the thermal resistance between the tip and the sample and also it was hard enough not to get deformed due to contact forces. However, being handmade, the diamond probe tip was too difficult to refabricate and also didn't improve the spatial resolution. He also proposed a commercially fabricated thin-film thermocouple probe with Au-Pt junction

containing gold contact pads and a glass substrate [19]. The tip was formed by deposited gold and platinum on each arm of a V-shaped cantilever of 35 nm thickness. The tip consisted of a sharp pyramid shaped pointed edge with a tip radius of 10 – 30 nm and a base of 5 μm. Experiments with this probe showed distortion due to thermal images and no marked improvement in spatial resolution. However, there was an increase in the temperature sensitivity from 1 K to 0.1 K.

Since then, a lot of research has been done to produce finer thermocouple probes and thereby try to increase the spatial resolution.

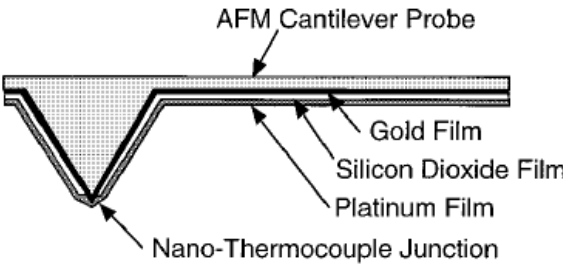


Figure 13. Thermocouple Probe tip demonstrated by K. Luo in 1996 [46].

In 1996, K. Luo used electron beam evaporation technique to deposit a Ti/Au film on a SiN_x cantilever probe [46]. On the Au film, a SiO₂ was deposited followed by a Ti/Pt film. A nano size hole was made on the Pt film at the tip location by a pulsing technique. The AFM cantilever probe tip thus consisted of a Au-Pt thermocouple junction of 200 nm and a sensitivity of 6 μV/K. This probe led to the spatial resolution of the thermal images to 10 nm. However, anomalies in topographical images were a big drawback (Figure 13).

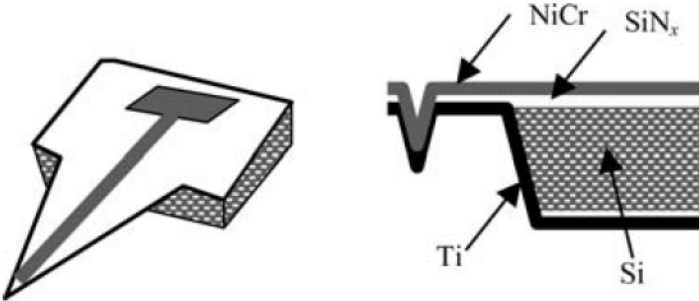


Figure 14. Thermocouple Probe proposed by Y. Suzuki in 1996 [21].

In the same year, Y. Suzuki [21] proposed the use of several techniques such as photolithography, electrochemical etching and low-pressure chemical vapor deposition (LPCVD) to obtain directly integrated thermocouple. The cantilever arm, made of metal film, was attached to the structure, giving rise to a thermocouple junction having a tip apex of 10 nm in radius of curvature and $8 \mu\text{V}/\text{K}$ in sensitivity. This probe lead to good level of performance but still, sadly, didn't manage to obtain proper images (Figure 14).

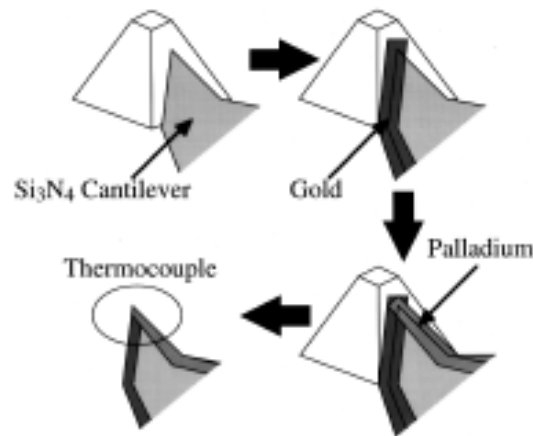


Figure 15. Thermocouple Probe tip as fabricated by G. Mills et al. in 1998 [22].

In 1998, G. Mills [22] and colleagues came up with an Au/Pd thermocouple probe batch fabricated using micromachining of bulk silicon and multiple levels of direct wire electron beam lithography (EBL) (Figure 15). Processes including micromachining, KOH etching, contact lithography and LPCVD allowed them to produce a thermocouple probe using gold and palladium. A silicon structure coated with Si_3N_4 provided structure and shape to the probe tip. The base was then removed giving the final Au/Pd probe having approximately 250 nm junction. The very fine tip obtained as result lead to very high spatial resolution 40 nm for topographic images and 80 nm thermal image resolution. Apart from the fragile nature of the tip, this probe was able to show thermocouple temperature change via image contrast without the signs of artifacts due to the topography on the thermal image.

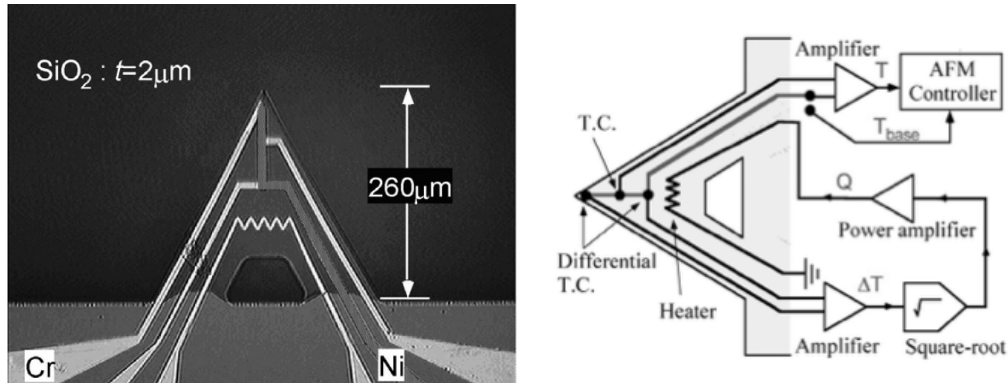


Figure 16. (left) Optical Image of the thermocouple probe devised by O. Nakkabeppu and T. Suzuki [23], (right) working principle.

In 2002, O. Nakkabeppu and T. Suzuki [23] devised a prototype system to report the principle of the active method for real temperature measurement in scanning thermal microscopy with a target to achieve the active method at a temperature accuracy of 1 K, a spatial resolution of 100 nm and a response time of 10 ms. To achieve this, they fabricated and designed a thermal cantilever with a thermal feedback system. The work of a differential thermocouple and an electric heater was done by Nickel and chromium metal lines and there was another thermocouple of about 150 μm region on the SiO₂ cantilever of 260 μm length. First and third junctions lined from the end were used as the differential thermocouple and the second one was used for detecting cantilever temperature. There was a sharp stylus tip, which allowed nanometer interactions with the sample surface (Figure 16). During experiments however, they realized that heat flow detection sensitivity of the thermocouple was insufficient. In more recent times, 2014, K. Kim and her colleagues [24] devised a thermocouple probe containing an Au-Cr nano-thermocouple junction at the end of the tip. This tip allows quantitative temperature measurements, as the thermoelectric voltage generated from the Au-Cr junction is directly proportional to the local temperature of the sample at the contact point. The contact diameter between the tip and the sample has been recorded to be approximately 10 nm (Figure 17). With this advanced probe quantitative temperature profile leading to the knowledge of the thermal resistances of probes and the nano-contact between the probe and the sample as well as give high spatial resolution of approx. 10 nm and a temperature resolution of about 15 mK.

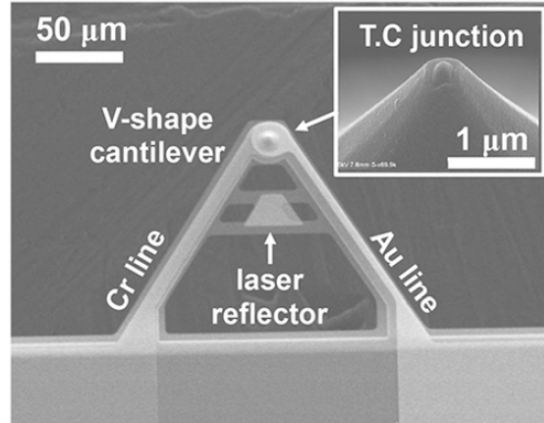


Figure 17. Thermocouple probe demonstrated by K. Kim and colleagues [24].

2.4. The Thermoresistive probes

Thermoresistive probes biggest advantage is that, when used in active mode, it acts as a self-contained device for the supply of heat and temperature measurement. Apart from localized thermal analysis, they can be used, as mentioned above, as AFM and SThM. The sensing element used to this type of near field resistance thermometry has an apex that is very fine and made of V-shaped wire. One of the biggest advantages of using a thermoresistive probe is the absence of any specialized devices necessary for operation [25]. Using simple commercial solutions like simple AC or DC current and Wheatstone bridge are sufficient to provide basic thermal images. Still, there are ways in which the resolution and accuracy of measurement can be improved by changing the connections and/or measurement setup. A SThM probe allows us to monitor the changes in resistance associated with the temperature at the end of the probe. Hence, allowing the system to monitor the relative changes of sample temperature and thermal conductivity. A thermoresistive sensor is integrated at the end of a cantilever and it works as a sensing element as well as heat source with constant power to bias the thermal measurements. The resistor at the tip of the probe as the heater and can measure the temperature simultaneously. Another big advantage of using thermoresistive probes is their small size that provides a high degree of spatial resolution and also protects good thermal isolation to the small thermal mass of probe. It is possible to use thermoresistive probes under constant power or constant temperature to obtain sample temperature and thermal conductivity.

2.4.1. The Wollastone probe

In 1994, R. Pylkki and colleagues came out with a thermoresistive probe that consists of a Wollaston wire made of Pt-Rh alloy and then coated with silver [9] [11]. The probe is then electrochemically etched so that 200 μm of the Pt-Rh wire is exposed outside. This V shaped wire can act both a heater and/or a near-field temperature detector depending on the mode utilized. The main idea is to obtain simultaneously the surface topography as well as qualitative images of thermal conductivity variation using either an active or passive mode depending upon the strength of the current. The basic principle is to measure how the temperature dependence between the tip and the sample affects the electrical resistivity of the probe tip. The thermal probe proposed by Pylkki and colleagues (Figure 18) was designed to investigate properly the physical properties of microstructures such as grains and grain boundaries, thin films and powder particles. It was also able to detect local heating of active samples so as to investigate heat flux transfer and surface temperature fields.

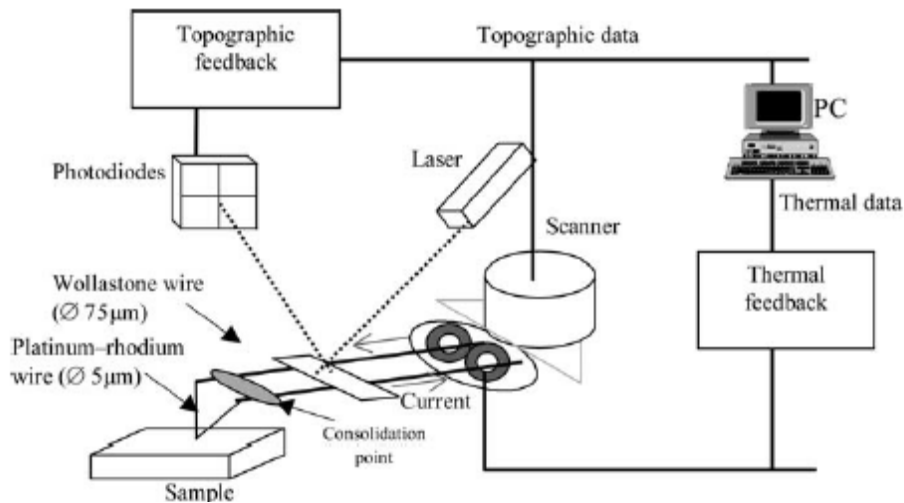


Figure 18. Experimental Setup as proposed by Pylkki and team in 1994 [9].

In 2000, Erwin R. Meinders [10] used scanning thermal microscopy by utilizing an AFM function and a thin platinum wire covered by Wollaston tube as a part of a Wheatstone bridge to analyze the thermal conductivity of thin sputter-deposited film with a thickness range of 10 nm to 10 μm (Figure 19).

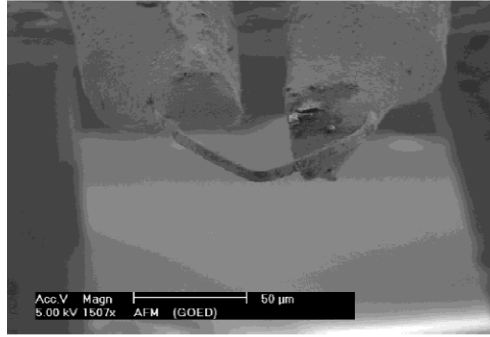


Figure 19. SEM image of the Wollaston Probe proposed by E.R. Meinders in 2000 [10].

One of the most reputed Wollaston probe (Figure 21) was developed by R.B. Dinwiddie where the apex was 5μm diameter Pt/10% rhodium wire. The range of the spring constant varied from 5 – 20 N.m⁻¹ [13]. This type of probe was subsequently used by Balk [14] and Hammiche [11]. These probes could be heated to temperatures around 100°C and were extremely robust – mechanically and electrically.

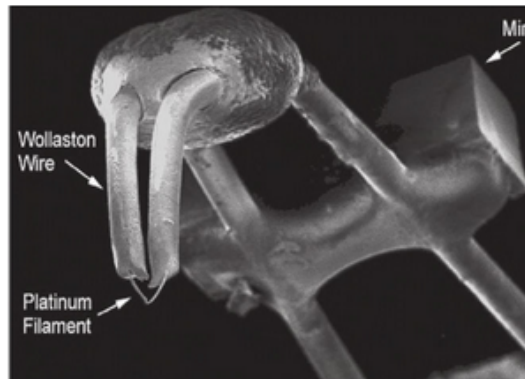


Figure 20. Image of the Wollaston probe developed by R.B. Dinwiddie image from scanning electron microscopy [13]

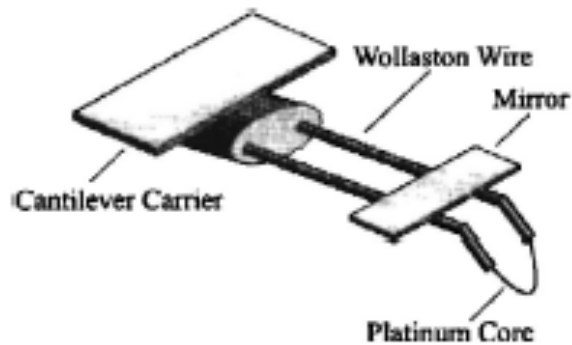


Figure 21. Image showing the principle of the Wollaston probe developed by R.B. Dinwiddie, [13].

In 2002, S. Lefèvre, S. Volz and colleagues [15] used a SThM setup with a Wollaston wire shaped tip with a core of Platinum-Rhodium to understand the spatial resolution in the nanoscale by using the contact method in DC mode. The authors assumed that the current flowing through the probe is controlled, resulting in a controlled wire temperature by the Joule's effect. The current variation was also assumed to be linearly dependent on the heat flux losses. Both Finite Element Analysis and numerical analysis have been performed for the tip-sample system to understand the key features of heat transfer in a conductivity calibration procedure. The authors concluded that scanning thermal microscopy has to be preferably used for low thermal conductivity samples with surface roughness being low.

In 2008, M. Chirtoc and J.F. Henry [16] used a similar probe to measure bulk and localized thermophysical properties using the AC mode. In 2013, J. Pelzl along with M. Chirtoc and R. Meckenstock [17] tried using thermal wave based SThM techniques to obtain thermal images of hot spots in high power and in plane-gate transistors. They went on to perform thermal characterization of nano NiTi memory alloys using the 3ω method. This thermal wave-based SThM technique is used for various purposes including the thermal management, thermal imaging in a submicron scale as well as to study resonance absorption processes.

The thermal probe used by Te-Hua Fang and Win-Jin Chang [20] consisted of a folded Wollaston wire forming a sensitive loop. The variation of the control resistance R_c adjusts the probe temperature, which in turn affects the probe's resistance R_p . The probe is designed with electrically heated resistive element to detect the change in heat flow across the sample surface. Experiments show that the probe's resistance varies linearly with temperature. An increase in the probe temperature causes an increase in the thermal energy along with some dissipated energy.

2.4.2. The micro-fabricated probes

Another popular type of thermoresistive probe is the micro-fabricated probe. Kelvin Nanotechnology, for instance, produces micro-fabricated probes using the monolithic batch fabrication technique where the probe shaves high flexibility and low spring constants. The tip consists of gold pads that are connected to a sensor and heater made of Palladium, located at the

apex of the tip. The cantilever is made of Si_3N_4 (Figure 22). These probes can provide a sub 100 nm topographic and thermal spatial resolution with temperature resolution of 0.1K. [28].

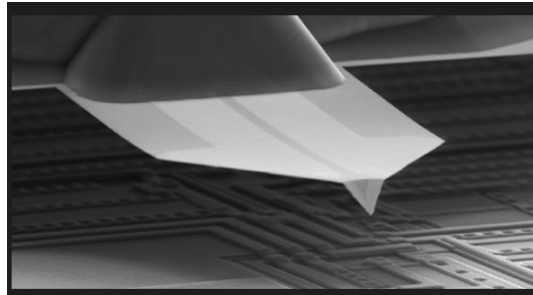


Figure 22. Thermoresistive probe produced by Kelvin Nanotechnology containing a Si_3N_4 cantilever and a Pd heater [28].

The thermoresistive tips used for scanning thermal microscopy are mostly conical in shape with a spherical tip apex for optimal tip thermal conductance and a spring constant of around 0.3 N/m [26]. The tip radius of curvature of modern thermoresistive probes are around 50 nm and they have a very short time response, around few tens of microsecond with the temperature coefficient of the electrical resistance at around 0.0012 /K [27]. The probe tip is around 10 μm . This length allows creating separation necessary between the cantilever and the sample, which thereby, notably in case of hot sample in thermometric measurements, reduces the cantilever heating. A SEM image of the tip of a thermoresistive micro-fabricated probe is given in Figure 23.

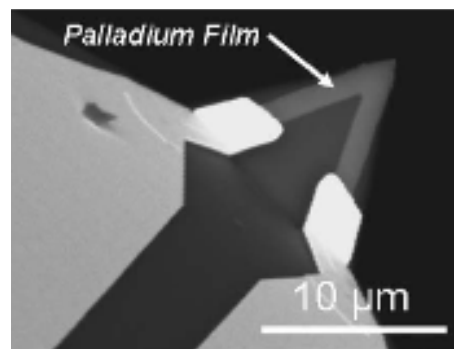


Figure 23. SEM image of a Thermoresistive probe.

Using Carbon NanoTubes (CNT) in order to increase the thermal conductivity can be a great addition to the current SThM to provide higher spatial resolution. This would allow the application of SThM probes on high thermal conducting materials like Si, Cu, Au along with

graphene and carbon nanotube based nanostructures with nanoscale resolution. P. Tovee *et al.* [29] utilize a multiwall CNT at the end of a silicon probe that acts as the point of contact with the specimen. Experiments performed on 50 nm multi-wall nanotubes (MWNT) shows that the CNT tip acts as a distributor of heat. This allows significant cooling of the silicon probe (SP) tip including the Pd resistive heater. It is seen that the SP-CNT tip is much closer to the sample temperature and hence provides better reading than the normal SP tip where only the end of the tip apex is cooled. CNT with thinner diameters of 10-20 nm show good temperature drop along the nanotube whereas thicker multiwall tubes of 50nm are good as thermal probes.

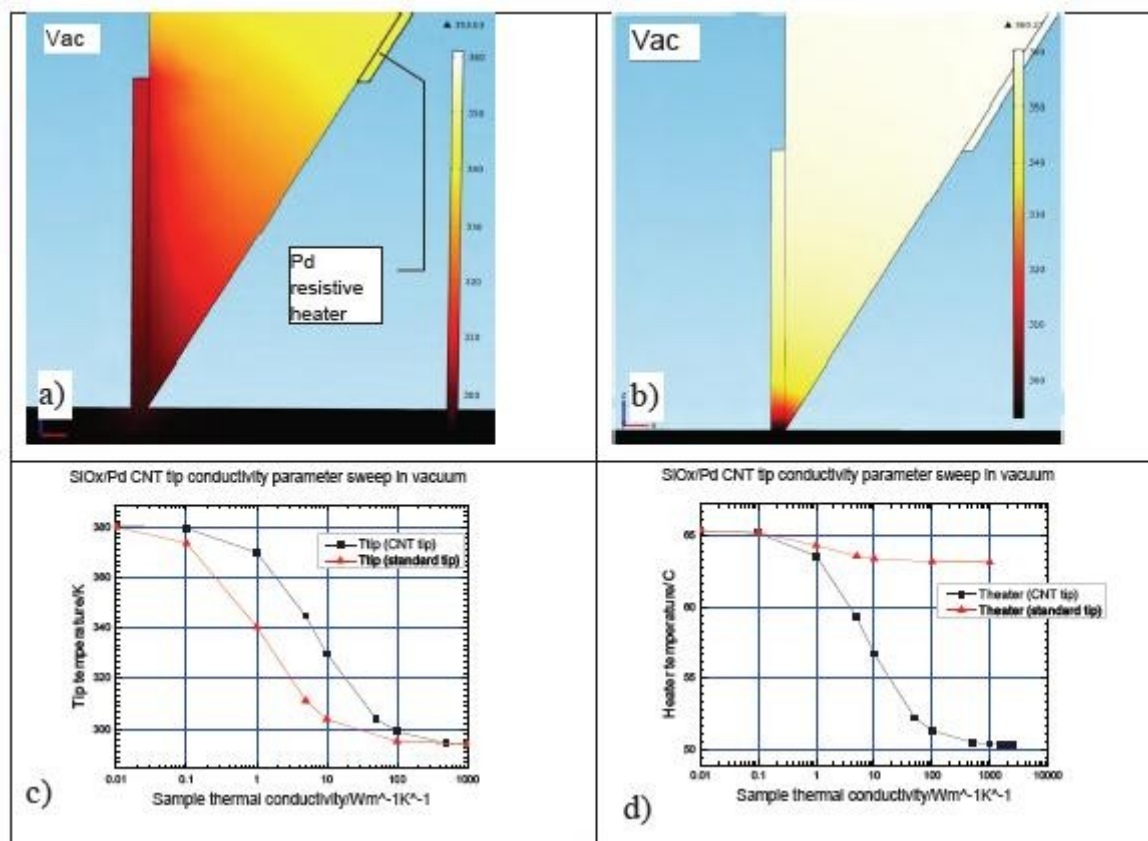


Figure 24. The figure compares the thermal map of a CNT modified SP probe and a standard SiO₂ probe. a) Temperature distribution at the tip of a the CNT modified SP probe providing effective thermal link with the sample, b) Temperature distribution using a standard SiO₂ probe. Both simulations were performed under vacuum condition; c) variation of tip temperature with change of sample thermal conductivity d) sensitivity of CNT and SiO₂ probe [29].

The authors showed that by using CNT there was an increase in the thermal response of the SP SThM probe by an order of magnitude with an increase in the sensitivity exceeding 100 W/m/K (Figure 24). The main mode of heat transfer between the probe and the CNT is heat diffusion due to the high anisotropy of thermal conductivity in the CNT. The authors showed that the new

probe had a thermal response one order of magnitude higher than the existing SThM probes and also had the ability to analyze materials with high thermal conductivity with nanoscale resolution [29].

In 2015, Maria Timofeeva et al. [69] used thermoresistive probes with Au pads as the base of the cantilever and Pd/NiCr heat resistors as well as thermal sensors and apex zone of the probe was in contact with the sample via. an attached nanowire (Figure 25).

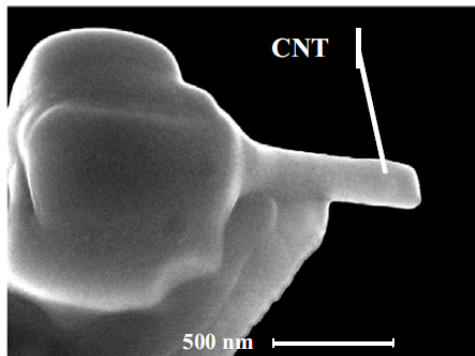


Figure 25. SEM image of SThM cantilever attached with NW [69].

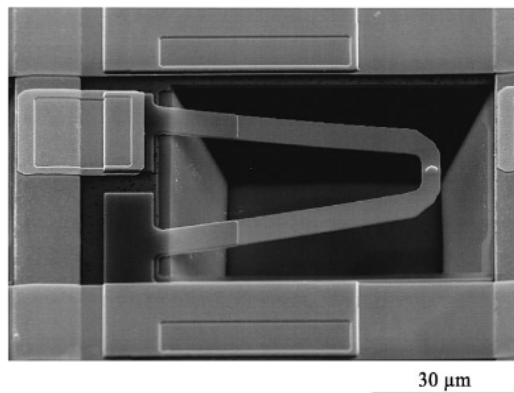


Figure 26. SEM image showing one cantilever of a Doped Si (DS) probe [62].

Another form of thermoresistive probe used notably for data storage systems and lithographic applications is a doped silicon probe (DS) containing a U-shaped cantilever (Figure 26). The tip is extremely fine reaching up to 10 nm. The tip (Figure 27) is shaped like a cone and is placed on a low-doped resistive element platform. This type of probe was first developed by IBM [62].

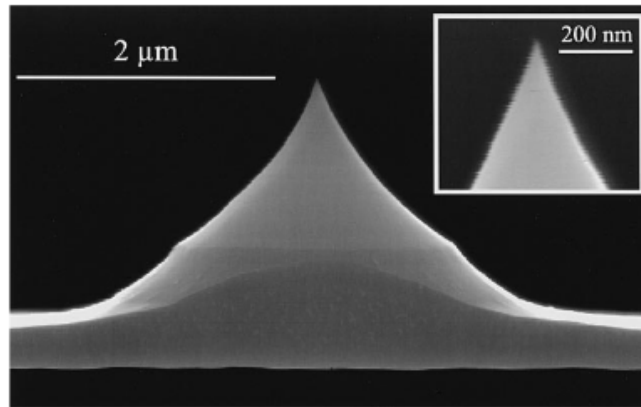


Figure 27. SEM image of the tip of a doped Si probe. The tip is around $1.7\mu\text{m}$ high and has a radius less than 20 nm

The most recent micromachined probes that have been fabricated are also known as the “bow-tie probe” [38]. They are of interest as they provide extremely high resolution. The complete probe including the cantilever, the resistor and the tip are produced in batches using photolithography, etching and lithography. The pyramidal tip (Figure 28) of such probes is generally around 100 nm at their narrowest points. The taper of the tip varies in size with a minimum width of 35 nm. The height of the pyramid is around $20\mu\text{m}$. There is a mirror close to the base of the pyramid, which is surrounded by metals tracks [63].

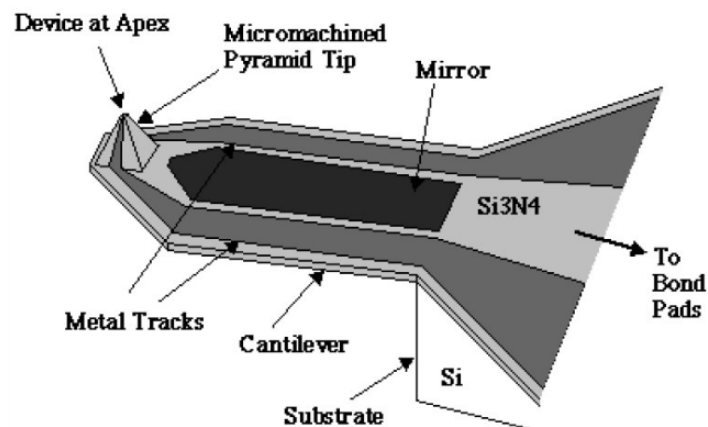


Figure 28. Micromachined probe with its various parts

2.4.3. Dynamic Probes

The main aim of probes using dynamic cantilevers is to take advantage of thermal expansion by measuring the surface temperature contrast with very small resolutions.

In 1995, O. Nakabeppu and colleagues created a composite probe by using commercial Si_3N_4 cantilevers and then depositing a film of gold or aluminum [31]. The metal film of about 50 nm in thickness was deposited using electron beam vaporization technique. This probe takes advantage of the fact that it is composed of two materials and hence can utilize the effect of differential thermal expansion. When the tip comes in contact with the surface, the heat flux in the tip leads to a change in the temperature of the cantilever, which bends due to thermal expansion (Figure 29). Using AC measurement techniques, it is possible to differentiate the deformation due to temperature and topography. Using this technique, the author was able to obtain a spatial resolution of about 400 nm and a temperature sensitivity of 3 mK. The heat conduction in air is a dominant factor in such a technique as the whole cantilever acts as the temperature sensor. The authors concluded by saying that better probe design and a reduction of experimental noise can lead to an increase in the temperature and spatial resolution.

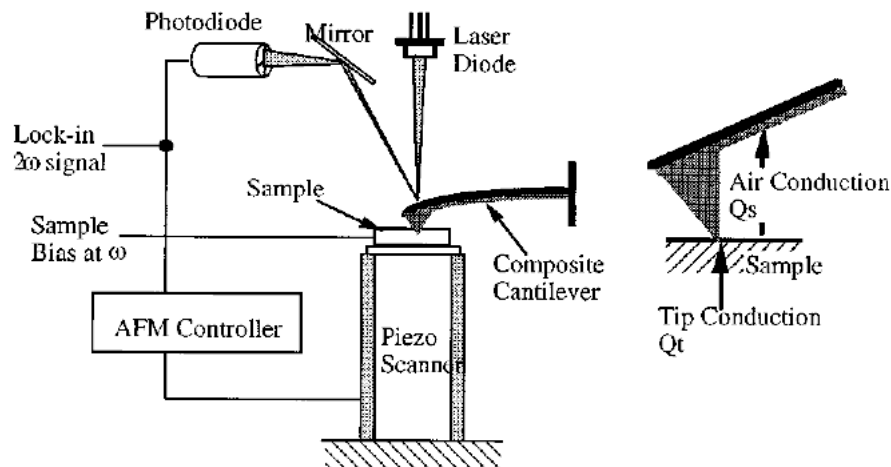


Figure 29. Dynamic Cantilever Probe as suggested by O. Nakabeppu and colleagues in 1995 [31].

In 1998, J. Varesi and A. Majumdar came up with the Scanning Joule Expansion Microscopy (SJEM) [32]. The principle of SJEM is to utilize an electrically conducting sample through which a sinusoidal voltage is passed, thereby causing Joule's heating, a temperature rise and a

thermal expansion of the sample (Figure 30). The AFM photodiode then measures the cantilever deflection due to expansion and sample topography. The authors utilize a AFM cantilever with gold interconnects to show that individual grains of 50 to 100 nm in lateral size can be clearly resolved using this technique with no loss in spatial resolution between topographic and expansion images. The images obtained have a spatial resolution in the order of 10 nm. According to the authors, in the scanning thermal microscopy, it is difficult to achieve an extremely fine (sub micrometer) sensor size due to difficulty in fabrication and even then it is difficult to achieve a spatial resolution of less than 25 nm. This SJEM technique would allow to get rid of the necessity of sensor nanofabrication and also provide very high spatial resolution (1 – 10 nm).

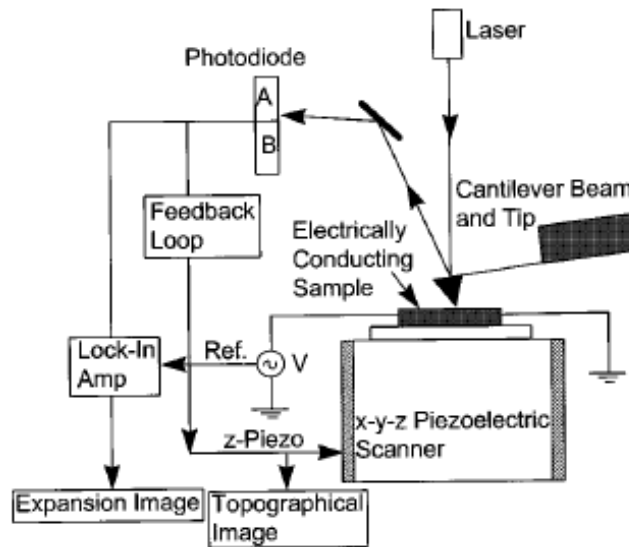


Figure 30. SJEM setup as proposed by J Varesi and A. Majumdar in 1998 (Scanning Joule expansion microscopy at nanometer scales, J Varesi and A. Majumdar)

In 1999, M. Igeta and colleagues tested this Scanning Joules Expansion Microscopy technique by utilizing a standard AFM probe and used its dynamic behavior in contact with an active sample [33]. This resulted in a spatial resolution of around 20 nm. The experiments showed that it's possible to study the generation of heat in a metallic interconnect whose diameter is around 0.5 μm hidden under a passivation layer. SJEM allowed the authors to measure dynamic thermal behaviors under sinusoidal and pulsed current conditions. This process is a little complicated due

to the high level of control necessary to operate the cantilever although it does try to overcome the problem of thermal probe fragility.

Finally in 2008, some researchers in USA utilized the theory of SJEM as described by J. Varesi and A. Majumdar in 1998 to obtain the thermal conductivity in the in-plane direction of thin metallic fins [35]. The thickness of the films was comparable to the electron mean free path. Using the technique of SJEM, they mapped the temperature amplitude gradient close to the constriction between the narrow and wide metallic lines. The thermal conductivity was finally obtained by utilizing a numerical fit to measurements [36].

2.4.4. Other Modern Probes

In 2015, Gwangseok Hwang and Ohmyoung Kwon [68] published a paper where they used null point scanning thermal microscopy (NP SThM) to calculate and analyze the size dependence of the thermal conductivity of graphene. They used such a technique to avoid the three problems faced when using normal SThM – a) to avoid temperature profile distortion when performing tests under atmospheric conditions due to the presence of air gap between the probe and sample, b) difficulty in performing quantitative measurements due to the presence of unknown and variable factors between the tip-sample interface and c) perturbation of the sample temperature due to the heat flux generated by tip-sample contact.

The Figure 31 demonstrates the experimental setup. The function generator applied a high frequency bias to heat the thermocouple. The Wheatstone bridge improved sensitivity of the calculation of dc thermoelectric voltage obtained from the SThM probe's thermocouple junction. This voltage was fed into the signal access module (SAM) while the scanning probe microscope provided the topography signal.

In her PhD. Thesis of 2015, H.J. Kim [67] used a heated cantilever array. The five identical heated cantilevers were made from doped single crystal silicon with the legs acting as electrical leads. Unlike the legs that were heavily doped, the cantilever free end was slightly doped allowing it to act as a resistive heater (Figure 32). The temperature of each cantilever can be controlled and around 90% of the power dissipation occurs near the free end.

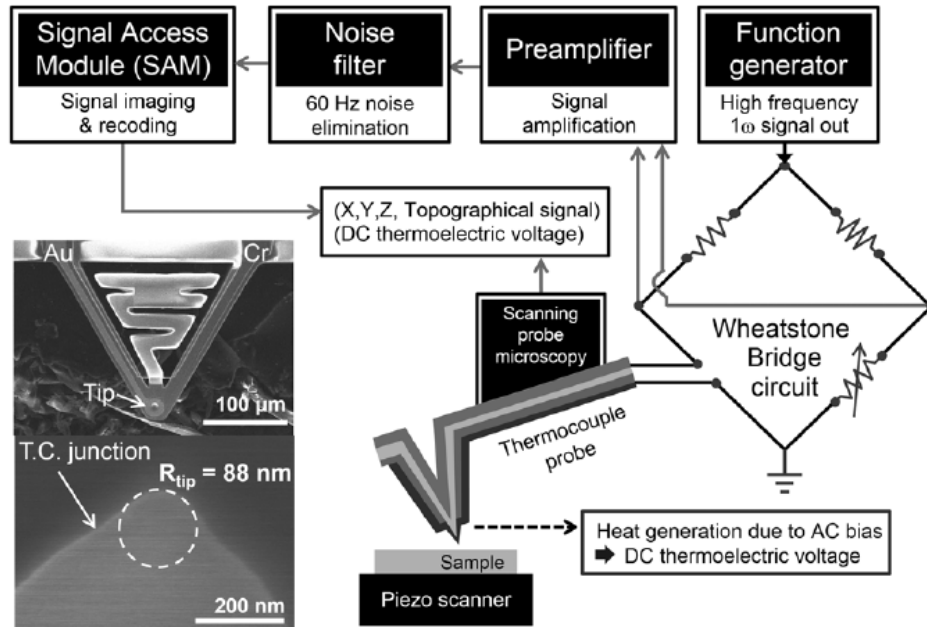


Figure 31. Schematic diagram of the experimental setup for NP SThM and SEM images of thermocouple SThM probes [68].

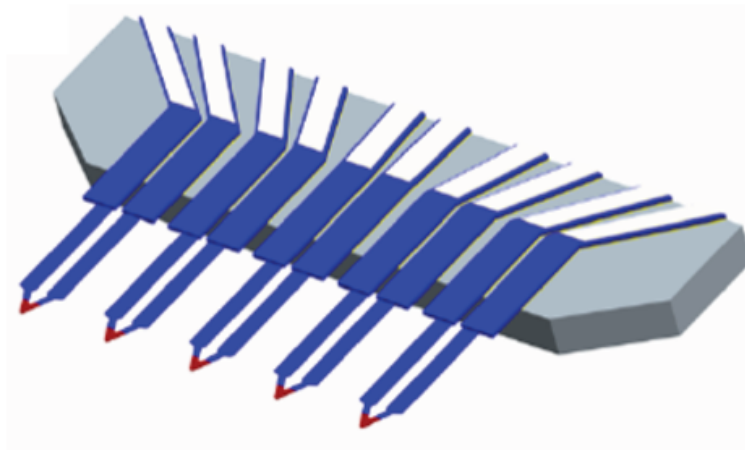


Figure 32. Schematic diagram of a cantilever array [67].

2.4.5. Summarize

The Table 2 gives us an overview of all the different types of probes along with their properties and examples of research work performed with them.

Table 2. Comparison of various types SThM probes including the thermal sensor, temperature change measurement principle, mode of operation, tip size, spatial resolution, durability and examples of published papers [25].

Probe Type	Thermocouple	Thermoresistive	Bimetallic	Fluorescent
Thermal sensor	Chromel-alumel ThC Au-Cr ThC Pt-Cr THc	Pt thermoresistor Pd thermoresistor Si thermoresistor	Al/Si bimetal	Er/Yb co-doped fluoride glass
Temperature change measurement principle	Electrical (Seebeck effect)	Electrical (resistance)	Frequency change	Optical
Mode	Passive	Passive & Active	Passive	Passive
Tip size	Usually < 50 nm	100 nm – 5 μm	<20 nm	200 nm
Spatial resolution	Even below 20 nm	About 100 nm	Unknown	< 1 μm
Durability	Medium	High	Unknown	Unknown

2.5. The Experimental Modes

2.5.1. The DC mode

In 1998, Ruiz et al. devised a relatively simple method for finding thermal conductivity values using a Wollaston wire probe and amorphous ‘diamond-like/quartz-like’ composites as a sample through heat flux measurements [36]. The SThM probe was operated at a temperature of approximately 40°C higher than the test specimen temperature. They used the constant temperature method with the help of a bridge circuit, which maintained the current flow so as to keep the operating temperature between the tip and the sample constant. The variation of power with the tip with and without contact was calculated to hold the temperature constant for each sample. They obtained a calibration curve where the power variation was linearly dependent on the thermal conductivity of the samples. Considering the power variation proportional to the power given by the tip to the sample Q_s , they suggested that Q_s is function of sample thermal conductivity k_s . Therefore, $Q_s = C k_s$ and hence $C = -a \Delta T$ where C is the constant proportional

to the product of tip-sample radius a and the difference of the operating temperature and the ambient temperature given by ΔT .

Hence it can be said that the heat going into the sample (Q_s) can be predicted with the same topography using the same tip and operating conditions. The Figure 33 shows the variation of Q_s as a function of k_s obtained after calibration tests performed by the authors. The solid line seen in the figure denotes the linear least square fit with a slope of 0.153 ± 0.003 cm K.

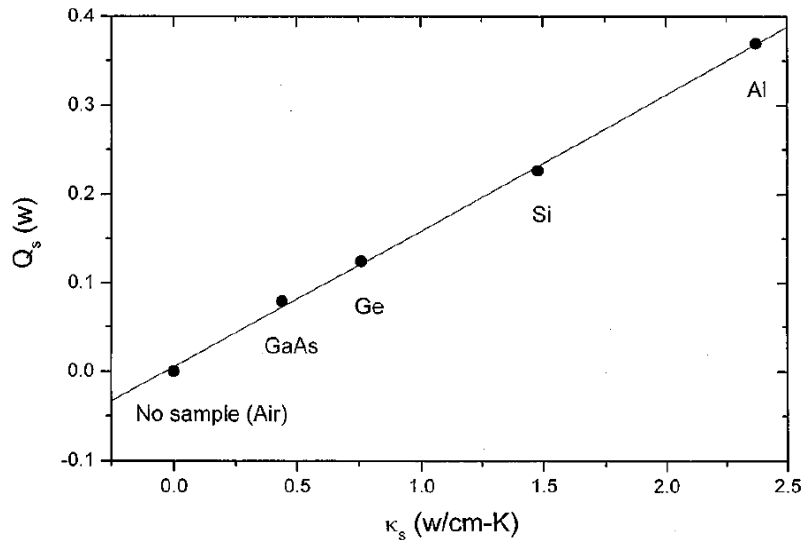


Figure 33. Q_s as a function of k_s for a number of materials as shown by Ruiz in 1998 [36]

In the constant temperature mode, the electrical resistance at the tip is held constant by servo controlling the measured thermal signal at the equilibrium voltage of the Wheatstone bridge. The voltage changes with linear variation with the applied voltage to the thermoresistive sensor and is dependent on the bridge resistance and the wire resistance between the tip and the bridge. The electrical dissipated power in the tip is measured by the heat exchange from the heated tip of the probe to the surrounding which includes the probe supports (Wollastone support), the surrounding gas and water meniscus and the sample during the time of contact. The Wollastone is composed of several high conducting materials, which act as heat sink for the tip. A temperature gradient is caused due to the huge amount of flux transfer along the thermoresistive filaments. Joule's heating allows the local temperature measurements at different points of a heat probe tip to demonstrate the gradient. The rate of heat exchange by convection with the surrounding air can be shown experimentally along with the rate of heat exchange with the sample on which the thermal images depend.

In 2002, Lefèvre performed experiments with sixteen different types of reference samples ranging from 1.48 to 429 W/m/K [37]. The voltage was measured before and after contact and plotted against thermal conductivity values (Figure 34). The results don't comply with Ruiz *et al.* linearity theory. It can be noticed that for specimens with high thermal conductivity, an asymptotic behavior can be observed. This indicates the much-reduced sensitivity of the SThM at high conductivities. Hence it can conclude that the sensitivity of scanning thermal microscopes reduces at high conductivities.

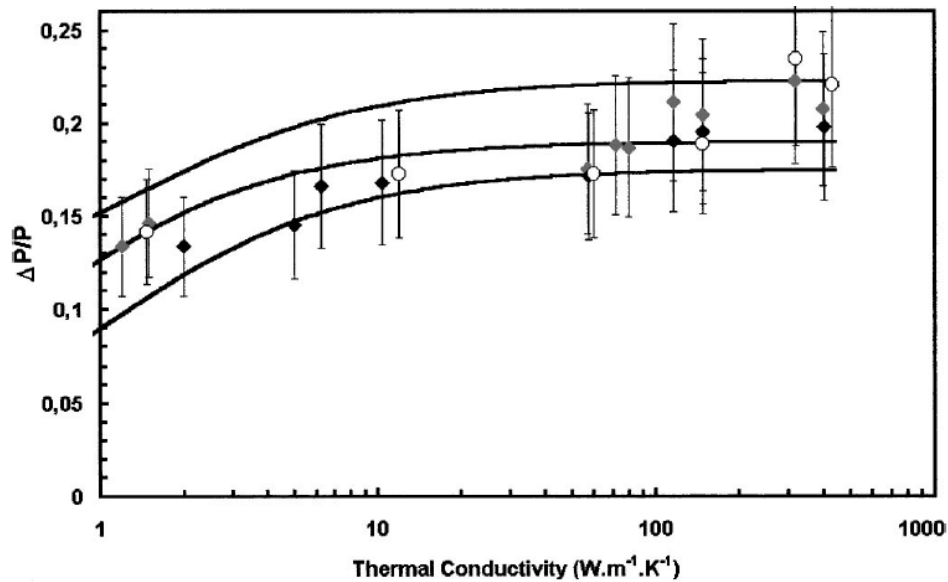


Figure 34. Calibration data obtained with two Wollastone probes with the tips consisting of Au and Pt-Rh (given by diamonds and disks respectively) and different tips (denoted in black and gray) [37].

2.5.2. The AC mode

The major advantage of the AC mode is the fact that the sensitivity of the SThM is highly improved when compared to the results obtained with the DC mode. Moreover, due to the controllability of the modulation frequency of the probe temperature allows easier handling of the volume matter probed. Using AC imaging technique, it is possible to determine quantitatively of sub-surface heat capacity as well as the thermal conductivity [38] for individual regions of a heterogeneous sample. Using the ac technique, three distinct images can be obtained – 1) topographic, 2) amplitude and 3) phase. A properly crafted thermal model will be able to describe the sensitivity of the thermal probe as well detect the spatial variations in thermal

conductivity and diffusivity. In the AC mode, most often the 3ω technique is used as it is considered to be optimal for system measurement in which the heater also acts as the thermometer. Moreover, it allows the proper utilization of the lock-in amplifier for temperature measurement.

In 1990, David G. Cahill used the AC mode to measure the thermal conductivity of dielectrics between 30 and 750K by using a method called the 3ω method as it utilizes radial heat flow from a single element which can be used both as a heater and a thermometer [39]. They utilized a macroscopic yet small sample in which they placed 100 μm heater [64].

In 2000, Moon et al. used a Micro-Thermal Analyzer to characterize phase transition temperatures of small sampling regions by utilizing the principle that thermal penetration depth depends on the frequency and the thermal conductivity and diffusivity profiles can be obtained by modular frequency variation [40]. In addition to the dc current, they utilized ac current on the tip to obtain the desired temperature modulation. The AC voltage was measured by the lock-in amplifier. They measured the amplitude of the ω term in the voltage signal as a function of temperature modulation amplitude, for polypropylene and sapphire.

GBM Fiege et al. in 1998 [41] used the 3ω technique to perform quantitative thermal conductivity measurement of silver and a CVD diamond film with a spatial resolution of approximately 30 nm using gold as reference with a deviation of less than 2%.

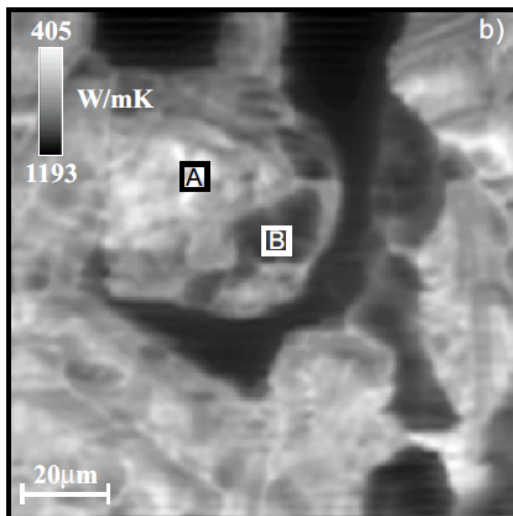


Figure 35. Illustration of the thermal conductivity of the diamond layer

The regions that appear darker in the Figure 35 have higher thermal conductivity due to the fact that the thermal conductivity and the temperature oscillations have inversely proportional logarithmic dependence of amplitude.

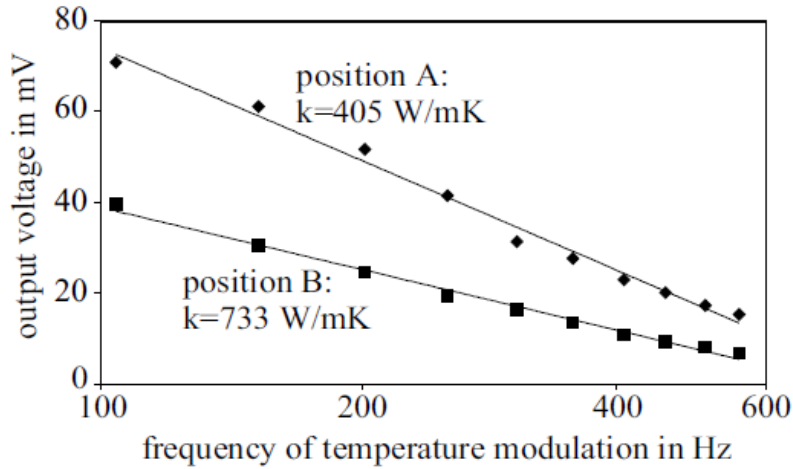


Figure 36. Thermal Conductivity as a function of frequency shown by Fiege in 1998 [41].

The Figure 36 is linear in the logarithm of frequency and the slopes observed are inversely proportional to the material thermal conductivity. The constant values of thermal diffusivity and the distance of the heat source relative to the sample can be determined from reference sample measurements. Hence allowing for the calibration of SThM devices for thermal conductivity measurements under the condition that the roughness and hardness of these reference samples are similar to those of the sample being investigated. With this approach, Fiege et al were able to derive a value for the thermal conductivity of silver with respect to gold, which is within 2% of the correct ratio.

In 1999, A. Majumdar [42] tried to understand thermal image contrast in the AC mode by using Wollastone wire probes. While studying the probe energy balance when it is contact with the sample, he noted that in case of materials with high thermal diffusivity, especially when the samples have lower AC conductance than the probe, the phase will be independent of the material properties for high frequency.

Solving the differential equations that provide the energy balance near the tip can help to better understand the measurements made using AC. [49]

2.5.3. Advantages and drawbacks of DC and AC modes

The use of the 3ω method in the AC mode can allow the elimination of blackbody radiation errors as the effective sample thickness is in the order of $100\ \mu\text{m}$ [39]. Moreover, it has been found that when it comes to precise quantitative measurement of thermal conductivity using DC current in the constant temperature mode, the characterization can only be performed by materials whose thermal conductivity is low (less than a few tens of W/m/K) [65]. Using AC current, one can improve the sensitivity of the microscope as well as reject noise over DC techniques. Furthermore, apart from the amplitude, the AC mode gives us an insight into the phase of the alternating component of the voltage across the tip. The phase has dependence on the subsurface thermophysical properties of the sample material [66]. However, the thermal models involving DC mode are much simpler than that of the AC mode due to the absence of the ω component. The AC regime needs differential equation solution to express the energy balance near the tip.

2.6. Heat Transfer at the probe-material interface

2.6.1. Physical phenomena description

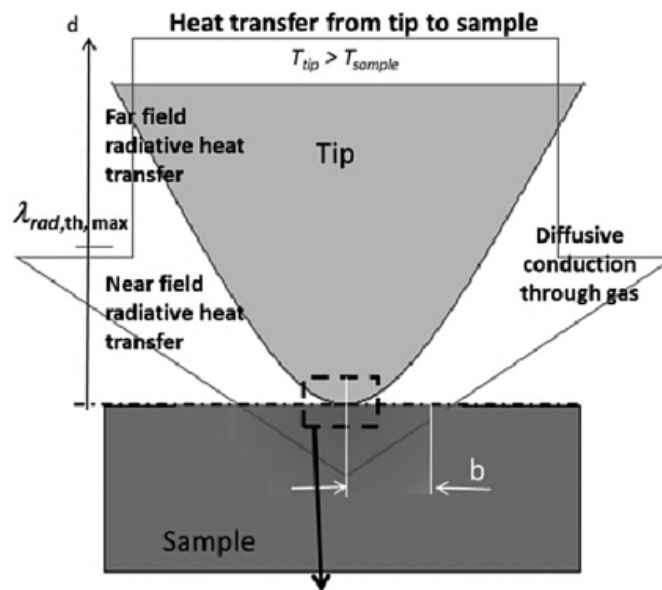


Figure 37. Heat Transfer between the probe tip and the sample in contact mode [43]

Heat transfer between the probe and the sample surface can take place in various forms as seen on Figure 37 [43] [41]. There is the obvious direct heat transfer due to the mechanical contact between the probe tip and the sample but there are other forms of heat transfer around the tip of

the probe. The surrounding environmental conditions have a strong effect on the amount of heat transferred from the probe into the sample. When experiments are performed under ambient conditions, heat conduction can also take place through the microscopic water meniscus or water droplets present on the sample and at the tip-sample contact area. Moreover, there is the effect of heat transfer due to radiation as well as heat transfer through the surrounding air. All these factors lead to an increase in the resistance of heat flow thereby reducing the thermal conductance. In the section below, we will try to look more into these various types of heat transfers that have an effect in the overall thermal property measurement and needs to be taken into account to obtain accurate results.

J. Pelzl et al. [17] used a u-shaped Si cantilever probe with a sharp integrated tip having an apex of 10 nm to demonstrate to perform a quantitative thermal measurement. As the effective contact area between the tip and the sample consists of the geometric area of the probe tip as well as air and water meniscus, the effective radius ' a ' has been considered for calculation. The heat flow across the contact area into the sample is given by $G_s = \pi a k_s$ where G_s is the thermal constriction conductance k_s is the sample thermal conductivity. The other factor that governs the equivalent thermal conductance G_e is the thermal contact conduction G_c between the tip and the sample. Hence the total thermal conduction due to heat diffusion from the tip to the same can be written as $G_e^{-1} = G_s^{-1} + G_c^{-1}$. These parameters vary in every experiment depending upon the contact radius, the roughness of the sample and tip as well as the exerted pressure. For samples of large thermal conductivity, J. Pelzl et al. [17] found that the contact resistance R_c of SThM probe in vacuum provides a value of $R_c = G_c^{-1} = 6 \times 10^6 \text{ K.W}^{-1}$. This result shows that only 3% of the total heat generated by the probe is transferred to the specimen. Using the value of G_c and a Wollaston thermal probe with $a = 100 \text{ nm}$, the derived the equivalent thermal resistance G_e^{-1} for Si (a good thermal conductor) is $1.02 \times 10^6 \text{ K.W}^{-1}$ and for Lucite (bad thermal conductor) $3.3 \times 10^7 \text{ K.W}^{-1}$. For inorganic materials with large thermal conductivity, the influence of the contact resistance between the tip and the sample dominates the heat transfer whereas it is the contrary for organic materials with small thermal conductivity.

2.6.2. Radiation

Under atmospheric condition, the heat lost due to radiation is very difficult to estimate. It is easy to accumulate this form of heat loss with heat loss due to convection, diffusion or even by ballistic heat transfer. As a result of this, most times radiative heat losses are neglect during calculations or it can be included, as done by Lefèvre in his PhD thesis, into another heat transfer mechanism [44]. The classic theory of heat exchange by radiation suggests the validity of Boltzmann law for distance $d > \lambda_{th}$, where λ_{th} is the wavelength of the thermal radiation given by Wien's law where λ_{th} is 10 μm for $T = 27^\circ\text{C}$. Using a Wollaston probe, heat transfer due to thermal radiation acts over a large part of the thermoresistive filament. At room temperature, the classical thermal radiation also referred to as far-field as well as near-field heat transfer due to radiation generated by thermal motion due to tunneling of evanescent surface waves is possible. From this, it can be inferred that there can be an increase in the effective radiative heat in comparison to the far field theory. In 2009, S. Shen and colleagues tried to demonstrate experimentally that surface phonon polaritons dramatically enhance energy transfer between two surfaces at small gaps by measuring radiation heat transfer between a microsphere and a flat surface down to 30 nm separation [45]. The corresponding heat transfer coefficients at nanoscale gaps are 3 orders of magnitude larger than that of the blackbody radiation limit. The high-energy flux can be exploited to develop new radiative cooling and thermo photovoltaic technologies. They used bimetallic probes to which they attached a large sphere thereby increase the area of radiation exchange. In the active mode, the contribution of the heat transfer due to radiation is in the order of 10^{-8} W/K. This value is very less, almost 1/100, in comparison to the other forms of heat exchange mentioned above. The very end of the probe tip which is less than a few micrometers of the Boltzmann distance will be under exposure due to the effective of heat radiation. Hence this sort of heat conduction is generally not considered.

2.6.3. Water Meniscus

The use of thermally designed and fully batch-fabricated cantilever probes for SThM allows the omission of several inaccuracies (the total thermal resistance of cantilever $R_c \ll R_{ts}$ tip - sample thermal resistance) and loss of resolution [46]. Moreover, the low throughput of electron beam lithography prohibits the use of large volume fabrication [47] though they are used for

fabrication of Silicon nitride thermal probes with a thermocouple junction at the tip. This batch-fabricated cantilever probes can be used to obtain thermal images of electrically heated circuits. L. Shi et. al [47] explained that a temperature profile across the surface of a Carbon Nanotube (CN) in the order of 50 nm is produced indicating a superior spatial resolution of the thermal imaging technique which is equal to the tip diameter. The result of this can be explained by the dominance of the tip-to-sample heat conduction through liquid under normal atmospheric condition. This is proved by an experiment using AC current, a lock-in amplifier and the thermal probe cantilever. Prior to the contact between the tip and the sample, the thermal signal was generated due to the conduction through air providing low signals insensitive to the tip and sample distance. When the tip can in contact with the sample, the water meniscus present on the sample surface pulled the cantilever downwards which is indicated by the “jump of contact”. Here a sudden increase in the thermal signal is noted. After this, the sample was moved further towards the tip, which led to the cantilever being bent up due to the increase of contact force. This didn’t cause any change in the signal showing that the solid-solid thermal conduction was not dominant. As the sample was moved down, the tip was being pulled down by the water meniscus until finally it “snapped out of contact”. This led to a sudden drop of the thermal signal. The presence of the liquid bridge between the tip and the sample leads to such hysteresis. The dominance of conduction of heat through the liquid bridge is understood by the thermal hysteresis curve due to the presence of deflection. P. Tovee and Oleg V Kolosov [48] performed an immersion Scanning Thermal Microscopy (iSThM) in- liquid dodecane environment with the same probe as done in-air for comparison. To achieve this, metal- polymer nanostructure in which Al damascene embedded layer is enclosed in benzocyclobutene (BCB) having a low – k dielectric was used. Ultra large scale integration (ULSI) interconnects are represented through the morphology and material of this sample. In-air SThM performed using a constant Joule’s heating power applied to the sensor showed the Al interconnects produce better heat dissipation. The absolute topographical height of around 80 nm has no direct impact on thermal imaging. Moreover, the Al rim looks brighter. This is due to the fact that the nanoscale rough edges created a heat transport barrier, which made the image look “hotter” in the SThM images. In case of iSThM the lateral resolution is much poorer but ones again the absolute topographical height of the Al layer have no relevant effect on the thermal images. The iSThM thermal images

(Figure 38) have darker Al layer with better heat dissipation properties surrounded by a lower conducting BCB layer.

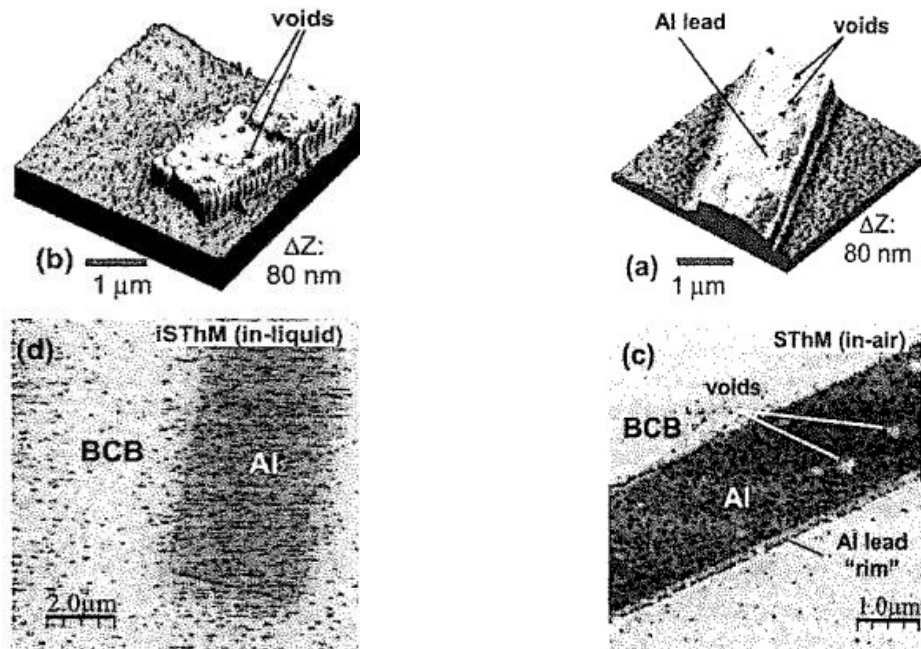


Figure 38. iSThM images performed in liquid and SThM performed in Air for a highly conducting Al layer with voids surrounded by BCB layer

In case of both SThM and iSThM an appreciable amount of signal changed is noticed at the boundary of the Al-BCB boundary at around 50 – 100 nm. Moreover, although the heat dissipation to the cantilever base is common to both modes, it is noticed that the signal-to-noise ratio is much lower for iSThM in comparison with SThM due to the presence of liquid. Hence it can be concluded that iSThM is possible in-liquid for thermal conductivity mapping in nanoscale. It was also observed that iSThM doesn't produce significant thermal response due to the presence of voids in the sample hence providing better thermal contact of the probe and the sample in fully immersed liquid environment. The probe design has a vital effect to the iSThM performance due the fact that changing the heater geometry and probe apex can significantly change the lateral resolution and performance. With a similar probe, the lateral resolution for both in-air and in-liquid are very close down to 30 nm for graphite nano flakes.

In liquid environment using iSThM, the “jump of contact” and “snapped out of contact” phenomena were not noticed. This observation was expected, as there was an absence of

capillary forces. Unlike in-air condition, a steep rise in the heat dissipation was also not noticed in solid-solid contact. Due to this and the above-mentioned factors, a true non-contact nanoscale thermal imaging can be performed using iSThM with the tip hovering at 10 nm above the sample.

Researchers have proved that the conduction through water is not a dominant heat transfer interaction. It has been seen that the value of thermal conductance due to the presence of water meniscus is one order of magnitude lower than the heat transfer through air for a Wollastone probe [92]. The conduction of heat via the water meniscus depends on the size of the meniscus itself and hence there are many factors that come into play to influence the heat path like surface roughness, relative humidity and the nature of the surface of the sample.

2.6.4. Heat transfer in air

Heat is transferred from the hot probe tip to the sample through air when working under atmospheric conditions. A large part of the probe stays in contact with the surrounding air and hence it is possible for the probe to heat up the surrounding air, which in turn heats up the sample under investigation [43]. As the heated tip approaches the sample, there is an increase in the filament power dissipation which holds the temperature constant and this effect is even more pronounced when the sample is thermally conductive [41]. The air heating is complex as it involves a diffusive mode for the sensor surfaces located to a higher altitude than the mean free path of gas molecules of 60 nm in the air but it also involves ballistic and quasi-ballistic regimes (Kundsen regime). Theoretically diffusive heat transfer through air acts only at distances more than 100 times this mean free path. This conductive heat flux is independent of the distance between the probe tip and the sample surface [46]. When the distance between the tip surface and the sample element approach or become lower, the molecules undergo impact on their journey and deposit all their energy on the surface. The transfer becomes much more efficient and becomes independent of distance [44].

Table 3. Effective heat transfer coefficient between the cantilever and surrounding air performed by different researchers

	Effective heat transfer coefficient between the cantilever and the surrounding air (W/m ² K)	Remarks	Type of Process
Chui et al. [83]	3000	0.1 W/mK for two 8 μ m wide legs	Experimental
Hu et al. [87]	2700	Al heater on SiN _x membrane	Experimental
Shen et al. [79]	500	70 nm Au and 450 nm SiN _x bi-material cantilever	Experimental
Serrano et al. [80]	2500 (25°C), 5500 (450°C)	Raman Spectroscopy on Silicon heated cantilever	Experimental
Toda et al. [81]	1670 (20°C), 3900 (143°C)	90 nm Au and 300 nm SiN _x bi-material cantilever	Experimental
Lee et al. [82]	3400 (Air), 44 (1 mbar)	Silicon heated cantilever	Experimental & Simulated
Park et al. [78]	800 (leg), 1000 – 3000 (heater)	Silicon heated cantilever	Experimental & Simulated
Kim et al. [84]	2000 (leg), 7000 (heater)	FEA of silicon heated cantilever	Simulation
Nelson et al. [85]	3100	Silicon heated cantilever used for temperature calibration	Experimental & Simulated
Kwon et al. [86]	850 – 1200 (Al-SiN _x , Au-SiN _x) 500 (Al-Si)	Bi-material cantilever	Experimental & Simulated

During contact measurement, the great impact of this heat transfer can be realized by noticing that the order of conduction through air increase is nearly 2.5×10^{-6} W/K [44]. In 2005, S. Lefèvre concluded that during heat transfer from a Wollaston probe to the sample surface, about 65% of this heat is carried by air under ambient conditions [50]. For micro fabricated probes, the heater can be further from the tip end and in this case, there can be a very high heat transfer due to air between the probe and the sample. The air is heated near the conical tip or directly by the cantilever. At very short distance of a few micrometers or less, heat diffusion is the predominant form of heat transfer through air whereas in large distances heat convection predominates as the heat flux is carried by the movement of the air due to the difference of temperature between the probe and the sample.

The Table 3 lists previous work performed experimentally and numerically to determine the effective heat transfer coefficient between the cantilever and the surrounding air [71]. The effective heat transfer coefficient between the cantilever and surrounding air are 1000 times larger than the natural air convection due to the larger heat capacity of the air surrounding the cantilever relative to the cantilever heat capacity along with the large surface-to-volume ratio of the microcantilever.

2.6.5. Solid-Solid Thermal Conduction

Thermal sensors are not located at the very tip of the probe apex and hence it is essential to know the temperature of the probe apex to derive an expression for the power transferred between the probe and the sample. Hence several researchers have made their model considering several parameters including the dimensional and physical properties of the materials of the probe. The two most important factors that need consideration are the heat loss by the whole probe surface due to the environmental effect (viewed in the previous sections) and the thermal resistance present during the probe sample contact. In this case, the thermal interactions are generally assumed to take place *via* a disc formed by the effective radius of the probe on the sample surface [51]. Due to the presence of imperfections on the sample surface, the mechanical contact radius associated with the real profile of the tip apex is always less than a few nanometers of the contact radius of an ideal profile. To account for such nanoscale contacts, phonon mismatch and mechanical contact geometry are required to be considered to get the contribution of the solid-solid interface measurement. The tip sample interface is never perfect. As said previously, there will be the presence of water meniscus or oxidation layers across the specimen surface. Moreover, due to the surface roughness or weak coupling bonds between the solids' atoms, the contact between the probe and the sample is discontinuous. Researchers tackle this problem by considering the ratio of the average mean free path of heat carriers Λ_c to the radius of the mechanical contact b_c . If $b_c \gg \Lambda_c$ diffusive transport is present. When $b_c < \Lambda_c$ ballistic solutions must be considered and when $b_c \ll \Lambda_c$ the finite contact spots need to be explored in the atomic scale (Figure 39).

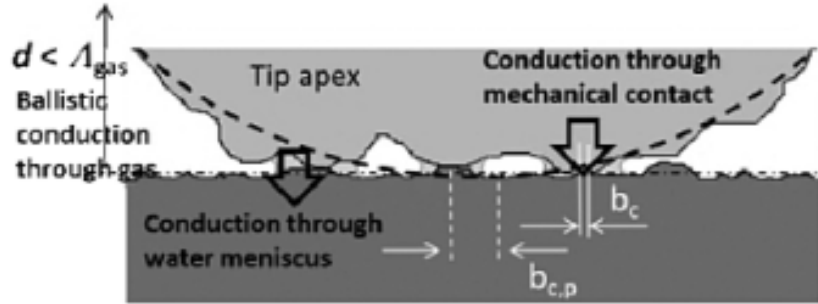


Figure 39. Figure showing the microscopic probe sample contact [43].

The thermal boundary resistance between the probe tip and the sample should be considered at the interface due to the phonon dispersion between the two materials in contact [64]. Considering that R_{th} is the thermal boundary resistance, we can write $R_{th,contact} = R_{th} / \pi b_{c,p}^2$ with $b_{c,p}$ being the mechanical contact radius associated with the real profile of the tip apex as seen in Figure 39. Experiments performed by R. Stoner *et al.* [64] and W. Haeberle *et al.* [70] showed that this value of thermal contact resistance for solid-solid contact not always constant. The tip-sample interface is never perfect due to the presence of oxide layers on the sample surface and/or surface roughness. Therefore, advanced contact methods to determine the transmission probability which is related to the mechanical coupling springs between the two solids need to be modeled.

When a probe tip comes in contact with sample with good thermal conductivity, there is a sudden jump in the exchanged heat flux and then there is a gradual increase in the flux as the tip penetrates into the material. Such phenomenon was noticed when solid – solid contact was made between the probe tip and samples of copper and duralumin and further pressure was applied to the tip at 102°C. There was noticeable variation in the observed thermal signal (Figure 40).

When a tip has a radius of around 30 nm, the diameter of contact is typically about 10 nm when the contact force applied is around 10 nN. The spreading contact conductance as a result of 10 nm contact is 2 nW/K on a polymer sample (Table 4) [71].

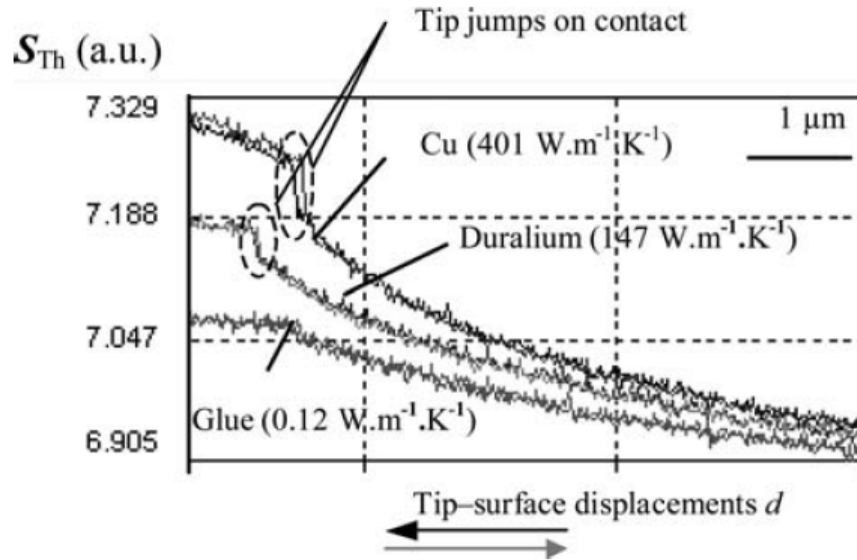


Figure 40. The variation of Sensivity with Displacement obtained in air for Copper, Glue and Duralium in dc mode

Table 4. Demonstration of tip-sample thermal conductance performed using heated cantilever.

Authors	Tip/Sample Thermal Conductance (nW/K)	Remarks
Shi et al. [73]	6 (solid contact) 1.5 (liquid contact)	Measured with SThM thermocouple tip
Park et al. [74]	40	Measured with silicon tip heated cantilever
Nelson et al. [75]	100	Pt-Au nanothermocouple at tip-substrate contact
Lefèvre et al. [50]	1800	Wollastone wire probe with tip radius of 5 – 15 μm
Zhang et al. [76]	9500	Ballistic air conduction between Wollastone wire probe and substrate in separation within 200 nm

2.7. Illustrations of the SThM application

2.7.1. Temperature measurement

Scanning thermal microscopy has been applied in several fields of work and its constant development has been a major factor for advancements in microelectronics and optoelectronics.

A notable accomplishment in the field of SThM application was performed by L. D. P. Lopez and colleagues to perform the thermal characterization of PN thermoelectric couples [53]. The author has applied thermal quadrupole approach to predict the thermal as well as the electrical response of excitation signals at the first harmonic. The reason for utilizing the first harmonic of the AC frequency is to separate the Joule's and Peltier heat sources as well utilize the advantages of a lock-in amplifier, thereby allowing them to obtain the amplitude and phase at the sample surface. The largest heat source is located at the PN junction of the setup due to the fact that the Peltier coefficient is higher there and the junction is made up of materials of low thermal conductivity.

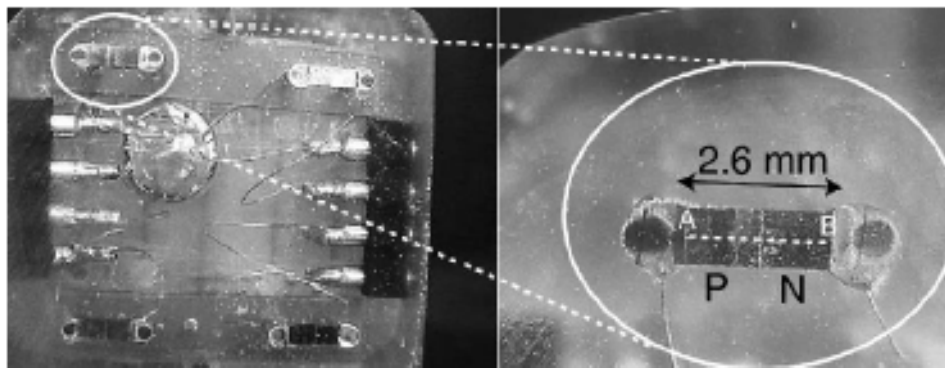


Figure 41. PN thermoelectric couples as used by L.D.P. Lopez and colleagues in 2004 [53].

Moreover, SThM has been used in photothermal setups to obtain materials' surface temperature by A. Hammiche and colleagues in 1996 [11].

Prior to 2002, thermal imaging using SThM was primarily qualitative but in 2003 O. Kwon and colleagues provided basis for SThM for subsurface imaging of buried structures using benchmark experiments where they image the phase lag and amplitude of the thermal waves with sub-micrometric resolution [54]. They found similarity of their results with theoretical measurements and finite element analysis thereby paving the way for 3 dimensional thermal probing of micro and nanostructures.

In the scope of thermometry, SThM has also been used to determine the localization failure and the integrated circuits analysis. In 2007, S. Gomes and colleagues used several ICs and arrays of resistive lines with sub-micrometric sections by using scanning thermal microscopy [55]. The researchers concluded that the size of the thermal probe, the thermal design and the structural composition are detrimental factors in achieving quantitative temperature measurements.

In 1999, Fiege and colleagues [41] and in 2014, F. Menges [56] utilized SThM to show that it is able to detect hot spots. Fiege's paper showed that highly localized energy that is being dissipated can be located by mapping the heated surface using SThM on either the front or rear side of integrated circuits in thinned substrates whereas Menges tried investigate and negate the errors that rise up due to the non-equilibrium of sensor and sample.

In 1995, A. Hammiche and colleagues [11] used scanning thermal microscopy to detect phase change in polymer composites. They used a Wollastone wire consisting of silver wire and a Platinum-rhodium core and a hot pressed polystyrene substrate sprayed with copper particles as the specimen. They qualitatively showed that thermal conductivity variation across heterogeneous samples can be analyzed as well as the depth of the impurities or inclusions under the circumstances that the material properties of all the involved materials are known (Figure 42).

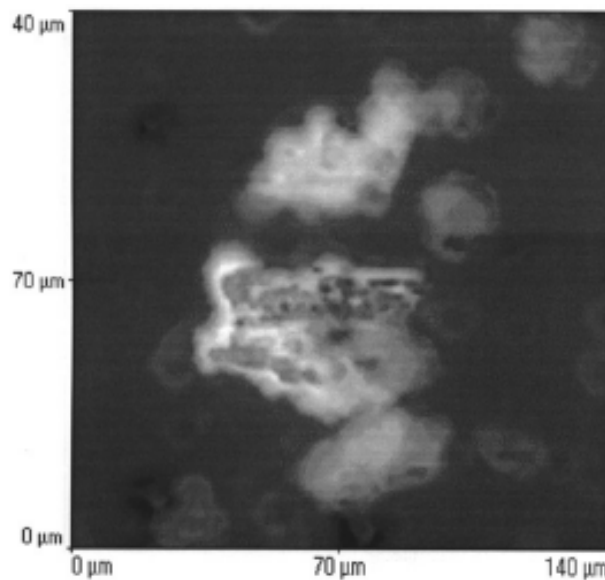


Figure 42. Sub-surface thermal images of copper particles embedded in polystyrene at depth 400 nm as demonstrated by A. Hammiche [11].

2.7.2. Thermal properties measurements

One of the biggest applications for scanning thermal microscopy is its advantage of measuring thermal conductivity. Scanning thermal microscopy has seen a lot of development since its inception in 1986 [8]. Bulk and thin film materials of both porous and mesoporous materials can be successfully analyzed using scanning thermal microscopy. Conventional SThM uses active mode in either AC or DC regimes to analyze thermal properties of micro and nanostructures. The

greatest advancement in thermal properties measurement was seen due to the development of the Wollastone wire probe. Although the probe is sensitive to high thermal conductivity, thermal characterization can be achieved for bulk as well as thin film materials by using a fine layer of insulating material on the surface of the specimen. Through its development, Wollastone probes have achieved to provide thermal images of about few tens of a nanometer. A. Majumdar in 1999 [42] talked about the ability of SThM to measure the temperature distribution of field-effect transistors and A. Buck in 1997 used Wollastone wire probes in the temperature mode to map large voids in metal tracks which were hidden under a polyimide passivation layer [57]. Moreover, scanning thermal microscopy has been used to study and characterize light-emitting diodes as well as study the thermal cure of dielectric polymers. Moreover, in 1997 L. Zhou and colleagues used chemical reaction with a resistive tip. [58] They used SThM and AFM to decompose palladium acetate thin films with palladium metal. This leads to the formation of features on the substrate with proper adhesion by using thinner precursor palladium acetate film. This research has led to the utilization of SThM for device fabrication and writing metallic features in the submicrometer scale by the induction of chemical reaction. We have now advanced and moved beyond the Wollastone wire probes with new and advanced probes being used and developed. In 2011, E. Puyoo used Pd probe under the 3ω ac mode to thermally characterize silicon nanowires embedded within SiO_2 . They obtained a spatial resolution of around 100 nm to produce thermal images under vacuum conditions (Figure 43) [59].

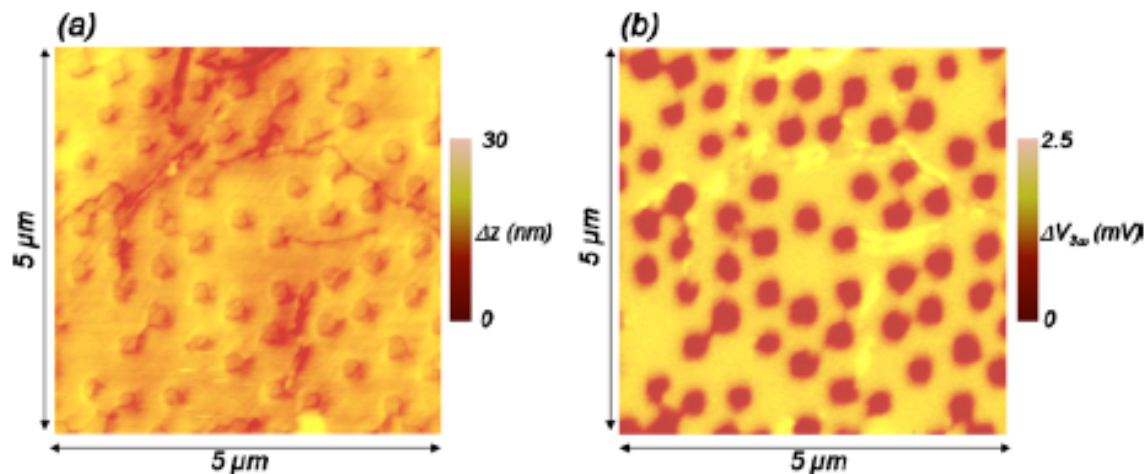


Figure 43. Topographic & Thermal Images of Si Nanowires embedded in silica matrix as demonstrated by E. Puyoo [59].

In 2014, A. Saci thermally characterized Sb_2Te_3 phase change nanowires to under room temperature and using the 3ω method without specific handling of the sample using a Si_3N_4 AFM tip deposited on a palladium wire [52]. Doped Si probes have also been used due to their high spatial resolution and a small radius of curvature of around 10 nm [60] by heating the polymeric samples to study their thermal transitions. In 2008, M. Hinz used such probes to thermally characterize HfO_2 films on a silicon substrate with 25 nm spatial resolution [61].

2.8. Conclusions

In this chapter, we took an in-depth look into the history of scanning thermal microscopy (SThM). Knowing all the previous work that has been performed by scientists is key to moving forward and this knowledge will allow us to further develop the working of SThM. This background is very important for our work as it provides us a basis to carry out our research using various types of nano and micro specimens. We utilize the information we have obtained regarding the probes to gather information regarding the various types of probes available in the market and choose the probes that suit our interests. The knowledge of mode of current allows us to obtain the best possible solution for our desired tests and the different ways of heat transfer help us to develop our model. Having a good knowledge of all the above information is necessary to thermally characterize materials to obtain thermal properties including thermal conductivity. In the next chapter, we will look into all the experimental setups we have utilized to accomplish this thesis.

2.9. References

- [1] J. Christofferson; K. Maize, Y. Ezzahri, J. Shabani, X. Wang, and A. Shakouri, *Microscale and Nanoscale Thermal Characterization Techniques*, J. Electron. Packag 130(4), 041101 (Nov 13, 2008).
- [2] D. G. Oliver, A. H. Sanders, L. Jang, D. Poy, A. Van Heuvelen, *Liquid crystal thermography. A method for monitoring temperature gradients in microtitration plates*, Journal of Immunological Methods **58** (1–2), (1983), 25-29.
- [3] C. Meola and G. M Carlomagno, *Recent advances in the use of infrared thermography*, Measurement Science and Technology, Volume 15, Number 9, (2004).
- [4] A. J. Schmidt, R. Cheaito and M. Chiesa, *A frequency-domain thermoreflectance method for the characterization of thermal properties*, Rev. Sci. Instrum. **80**, 094901 (2009).
- [5] T. Baba, K. Ishikawa, T. Yagi, N. Taketoshi, K. Tamano, T. Ohtsuka, H. Watanabe, Y. Shigesato, *Measurement of thermophysical property of thin films by light pulse heating thermoreflectance method*, Therminic, Nice, Côte d'Azur, France, 27-29 September 2006.

- [6] C. M. Harris, *Shedding Light on NSOM*, Anal. Chem., **75** (9), pp 223–228 (2003).
- [7] E. Smith and G. Dent, *Modern Raman Spectroscopy: A Practical Approach*, John Wiley & Sons, Ltd., 2005.
- [8] C. C. Williams and H. K. Wickramasinghe, *Scanning thermal profiler*, Appl. Phys. Lett. **49**, 1587 (1986).
- [9] Russell J. Pylkki, Patrick J. Moyer and Paul E. West, *Scanning Near-Field Optical Microscopy and Scanning Thermal Microscopy*, Japanese Journal of Applied Physics, Volume 33, Part 1, Number 6B, 1994.
- [10] E. R. Meinders, *Measurement of the thermal conductivity of thin layers using a scanning thermal microscope*, Journal of Materials Research, Vol. 16, Issue 9, 2001.
- [11] A Hammiche, H M Pollock, M Song and D J Hourston, *Sub-surface imaging by scanning thermal microscopy*, Meas. Sci. Technol. **7** (1996) 142–150.
- [12] S. V. Kalinin, A. Gruverman, Scanning Probe Microscopy of Functional Materials, Springer Science+Business Media, LLC 2010
- [13] R. B. Dinwiddie, R. J. Pylkki and P. E. West Thermal Conductivity **22**, ed. T W Tong (Lancaster, PA: Technomics) 1994, p.668.
- [14] L. J. Balk, M. Maywald and R. J. Pylkki, *Nanoscopic Detection of the Thermal Conductivity of Compound Semiconductor Materials by Enhanced Scanning Thermal Microscopy*, 9th Conference on Microscopy of Semiconducting Materials (Inst. Phys. Conf. Ser. 146) ; Cullis, A. G., Staton-Bevan, A. E., Eds., IOP Publishing Ltd.: Bristol, England, 1995; 655–658.
- [15] S. Lefèvre, S. Volz, J.-B. Saulnier, C. Fuentes and N. Trannoy, *Thermal conductivity calibration for hot wire based dc scanning thermal microscopy*, Rev. Sci. Instrum. **74**, 2418, 2013.
- [16] M. Chirtoc, J. F. Henry, *3 ω hot wire method for micro-heat transfer measurements: From anemometry to scanning thermal microscopy (SThM)*, The European Physical Journal Special Topics **153** (1), (2008), p. 343–348.
- [17] J. Pelzl, M. Chirtoc, R. Meckenstock, *Thermal Wave-Based Scanning Probe Microscopy and Its Applications*, International Journal of Thermophysics **34** (8), (2013), p. 1353–1366.
- [18] A. Majumdar, J. P. Carrejo and J. Lai, *Thermal imaging using the atomic force microscope*, Appl. Phys. Lett. **62**, 2501, (1993).
- [19] A. Majumdar, J. Lai, M. Chandrachood, O. Nakabeppu, Y. Wu and Z. Shi, *Thermal imaging by atomic force microscopy using thermocouple cantilever*, Rev. Sci. Instrum. **66**, 3584, (1995).
- [20] T.-H. Fang, W.-J. Chang, *Microthermal machining using scanning thermal microscopy*, Applied Surface Science **240** (1–4), (2005), p. 312–317.
- [21] Y. Suzuki, *Novel Microcantilever for Scanning Thermal Imaging Microscopy*, Japanese Journal of Applied Physics **35**, Part 2, Number 3A, (1996).
- [22] G. Mills, H. Zhou, A. Midha, L. Donaldson and J. M. R. Weaver, *Scanning thermal microscopy using batch fabricated thermocouple probes*, Appl. Phys. Lett. **72**, 2900, (1998).
- [23] O. Nakabeppu T. Suzuki, *Microscale Temperature Measurement by Scanning Thermal Microscopy*, Journal of Thermal Analysis and Calorimetry **69** (3), (2002), p. 727–737.
- [24] K. Kim, W. Jeong, W. Lee, S. Sadat, D. Thompson, E. Meyhofer and P. Reddy, *Quantification of thermal and contact resistances of scanning thermal probes*, Appl. Phys. Lett. **105**, 203107, (2014).

- [25] P. W. Hawkes, *Advances in Imaging and Electron Physics*, Vol 116, Elsevier 2015.
- [26] T. Meier, *Magnetoresistive and Thermoresistive Scanning Probe Microscopy with Applications in Micro- and Nanotechnology*, KIT Scientific Publishing, 2014
- [27] F. Depasse, P. Grossel, N. Trannoy, *Probe temperature and output voltage calculus for the SThM in a.c. mode*, *upperlattices and Microstructures*, 35, 269-82, 2004
- [28] Kelvin Nanotechnology Ltd, *Scanning Thermal Microscopy Probes*
- [29] P. Tovee, M. Pumarol, D. Zeze, Kevin Kjoller, and O. Kolosov, *Nanoscale spatial resolution probes for scanning thermal microscopy of solid state materials*, *Journal of Applied Physics* **112**, 114317 (2012).
- [30] E. Puyoo, S. Grauby, J.-M. Rampnoux, E. Rouvière, and S. Dilhaire, *Rev. Sci. Instrum.* **81** (7), 073701 (2010).
- [31] O. Nakabeppu, M. Chandrachood, Y. Wu, J. Lai and A. Majumdar, *Scanning thermal imaging microscopy using composite cantilever probes*, *Appl. Phys. Lett.* **66**, 694, 1995.
- [32] J. Varesi and A. Majumdar, *Scanning Joule expansion microscopy at nanometer scales*, *Appl. Phys. Lett.* **72**, 37, (1998).
- [33] M. Igeta, K. Banerjee, G. Wu, C. Hu and A. Majumdar, *Thermal Characteristics of Submicron Vias Studied by Scanning Joule Expansion Microscopy*, *EEE Electron Device Letters*, vol. 21, issue 5, pp. 224-226 (2000).
- [34] A. Majumdar and J. Varesi, *Nanoscale Temperature Distributions Measured by Scanning Joule Expansion Microscopy*, *J. Heat Transfer* **120** (2), (1998), p. 297-305.
- [35] S. P. Gurrum, W. P. King, Y. K. Joshi and K. Ramakrishna, *Size Effect on the Thermal Conductivity of Thin Metallic Films Investigated by Scanning Joule Expansion Microscopy*, *J. Heat Transfer* **130** (8), 082403, (2008).
- [36] F. Ruiz, W. D. Sun, F. H. Pollak and C. Venkatraman, *Determination of the thermal conductivity of diamond-like nanocomposite films using a scanning thermal microscope*, *Appl. Phys. Lett.* **73**, 1802, (1998).
- [37] S. Lefèvre, S. Volz, J.-B. Saulnier, C. Fuentes and N. Trannoy, *Thermal conductivity calibration for hot wire based dc scanning thermal microscopy*, *Rev. Sci. Instrum.* **74**, 2418, (2003).
- [38] H. M. Pollock and A. Hammiche, *Micro-thermal analysis: techniques and applications*, *J. Phys. D: Appl. Phys.* **34** R23–R53, (2001).
- [39] D. G. Cahill, *Thermal conductivity measurement from 30 to 750 K: the 3ω method*, *Rev. Sci. Instrum.* **61**, 802, (1990).
- [40] R. Moon, R. Androsch, W. Chen, B. Wunderlich, *The Principles of Micro-Thermal Analysis and its Application to the Study of Macromolecules*, *Journal of Thermal Analysis and Calorimetry* **59** (1), (2000), p. 187–203.
- [41] G. Bernhard, M. Fiege, A. Altes, R. Heiderhoff and L. J. Balk, *Quantitative thermal conductivity measurements with nanometre resolution*, *J. Phys. D: Appl. Phys.* **32** (5), (1999), p. 13-17.
- [42] A. Majumdar, *Scanning Thermal Microscopy*, *Annual Review of Materials Science* **29**, 505-585, (1999).
- [43] S. Gomés, A. Assy, P.-O. Chapuis, *Scanning thermal microscopy: A review*, *Physica Status Solidi (A) Applications and Materials* **212** (3), (2015).
- [44] S. Lefèvre, *Modélisation et élaboration des métrologies de microscopie thermique à sonde locale résistive*, Ph. D. thesis, University of Poitiers, 2004

- [45] S. Shen, A. Narayanaswamy and G. Chen, *Surface Phonon Polaritons Mediated Energy Transfer between Nanoscale Gaps*, Nano Lett. **9** (8), (2009), p. 2909–2913.
- [46] K. Luo, Z. Shi, J. Varesi and A. Majumdar, *Sensor nanofabrication, performance, and conduction mechanisms in scanning thermal microscopy*, J. Vac. Sci. Technol. B **15**, 349, (1997).
- [47] L. Shi, S. Plyasunov, A. Bachtold, P. L. McEuen and A. Majumdar, *Scanning thermal microscopy of carbon nanotubes using batch-fabricated probes*, Appl. Phys. Lett. **77**, 4295, (2000).
- [48] P. D. Tovee & O. Kolosov, *Mapping nanoscale thermal transfer in-liquid environment—immersion scanning thermal microscopy*, Nanotechnology **24** (46), 2013.
- [49] B. Cretin, S. Gomès, N. Trannoy and P. Vairac, *Scanning Thermal Microscopy*, Microscale and Nanoscale Heat Transfer: Volume **107** of the series Topics in Applied Physics pp 181-238, (2006).
- [50] S. Lefèvre, S. Volz and P.-O. Chapuis, *Nanoscale heat transfer at contact between a hot tip and a substrate*, International Journal of Heat and Mass Transfer **49**, (2006), p. 251–258.
- [51] P.-O. Chapuis, E. Rousseau, A. Assy, S. Lefèvre, S. Gomes, and S. Volz, *Heat transfer between a hot AFM tip and a cold sample: impact of the air pressure*, MRS Online Proc. Libr. **1543**, 159–164, (2013).
- [52] A. Saci, J.-L. Battaglia, A. Kusiak, R. Fallica, and M. Longo, *Thermal conductivity measurement of a Sb_2Te_3 phase change nanowire*, Applied Physics Letters **104**, 263103 (2014)
- [53] L. D. Patino Lopez, S. Grauby, S. Dilhaire and M. A. Salhi, *Characterization of the thermal behavior of PN thermoelectric couples by scanning thermal microscope*, Microelectronics Journal **35** (2004), p.797–803.
- [54] O. Kwon, L. Shi and A. Majumdar, *Scanning Thermal Wave Microscopy (STWM)*, J. Heat Transfer **125** (1), (2003), p. 156-163.
- [55] S. Gomès, O. Chapuis, F. Nepveu, N. Trannoy, S. Volz, B. Charlot, G. Tessier, S. Dilhaire, B. Cretin and P. Vairac, *Temperature Study of Sub-Micrometric ICs by Scanning Thermal Microscopy*, IEEE Transactions on Components and Packaging Technologies: Manuscript TCPT-2006-020-R2, 2007.
- [56] F. Menges, P. Mensch, S. Karg, A. Stemmer, H. Riel and B. Gotsmann, *Nanoscale thermometry using scanning thermal microscopy*, Eurotherm **103**: Nanoscale and Microscale Heat Transfer IV, October 15-17, Lyon, France, 2014.
- [57] A. Buck, B. K. Jones and H. M. Pollock, *Temperature and thermal conductivity modes of scanning probe microscopy for electromigration studies*, Microelectronics Reliability **37**, (1997), p. 1495–1498.
- [58] L. Zhou, G. Q. Xu, H. T. Ng and S. F. Y. Li, *Scanning thermal microscope tip-induced chemical reaction on solid organometallic compound thin films*, Journal of Vacuum Science and Technology B **15**, 1871 (1997)
- [59] E. Puyoo, S. Grauby, J.-M. Rampnoux, E. Rouvière and S. Dilhaire, *Scanning thermal microscopy of individual silicon nanowires*, Journal of Applied Physics **109**, 024302, (2011).
- [60] P. Tovee, M. Pumarol, D. Zeze, Kevin Kjoller and O. Kolosov, *Nanoscale special resolution probes for scanning thermal microscopy of solid state materials*, J. Appl. Phys. **112**, 114317 (2012)

- [61] M. Hinz, O. Marti, B. Gotsmann, M. A. Lantz and U. Dürig, *High resolution vacuum scanning thermal microscopy of HfO₂ and SiO₂*, Applied Physics Letters **92**, 043122, (2008).
- [62] M. Despont, J. Brugger, U. Drechsler, U. Durig, W. Haberle, M. Lutwyche, H. Rothuizen, R. Stutz, R. Widmer, G. Binnig, H. Rohrer, P. Vettiger, *VLSI-NEMS chip for parallel AFM data storage*, Sensors and Actuators **80**, 100–107, (1999).
- [63] H. Zhou, A. Midha, G. Mills, S. Thoms, S. K. Murad and J. M. R. Weaver, *Generic scanned-probe microscope sensors by combined micromachining and electron-beam lithography*, J. Vac. Sci. Technol. B **16**, 54, (1998).
- [64] R. Stoner and H. Maris, *Kapitza conductance and heat flow between solids at temperatures from 50 to 300 K*, Phys. Rev. B **48**, 16373, (1993)
- [65] G. Binnig, C. F. Quate, and Ch. Gerber, *Atomic Force Microscope*, Phys. Rev. Lett. **56**, 930, (1986).
- [66] J. Altet, S. Dilhaire, S. Volz, J.-M. Rampnoux, A. Rubio, S. Grauby, L. D. P. Lopez, W. Claeys, J. B. Saulnier, *Four different approaches of IC surface temperature: Application to thermal testing*, Microelectron. J. **33**, 689–696 (2002).
- [67] H. J. Kim, PhD. Thesis, *Advanced Materials Integration and Thermal Operation of Heated Microcantilevers and Cantilever Arrays*, University of Glasgow, 2015
- [68] G. Hwang and O. Kwon, *Measuring the size dependence of thermal conductivity of suspended graphene disks using null-point scanning thermal microscopy*, Nanoscale **8**, 5280, (2016).
- [69] M. Timofeeva, A. Bolshakov, P. D. Tovee, D. A. Zeze, V. G. Dubrovskii, O. V. Kolosov, *Scanning thermal microscopy with heat conductive nanowire probes*, Ultramicroscopy **162** (2016), p. 42–51.
- [70] W. Haeberle, M. Pantea and J. Hoerber, *Nanometer-scale heat-conductivity measurements on biological samples*, Ultramicroscopy **106**, 678–686, (2006).
- [71] W. P. King, B. Bhatia, J. R. Felts, H. J. Kim, B. Kwon, B. Lee, S. Somnath and M. Rosenberger, *Heated Atomic Force Cantilevers and their Applications*, Annual Review of Heat Transfer Vol. 12, 287–326, 2013
- [72] K. Luo, Z. Shi, J. Lai, and A. Majumdar, *Nanofabrication of sensors on cantilever probe tips for scanning multiprobe*, Appl. Phys. Lett. **68**, 325, (1996).
- [73] L. Shi and A. Majumdar, *Thermal transport mechanism at nanoscale point contacts*, ASME J. Heat Trans. **124**, (2002), p. 329–337.
- [74] K. Park, G. L. W. Cross, Z. M. M. Zhang and W.P. King, *Experimental investigation on the heat transfer between a heated microcantilever and a substrate*, ASME J. Heat. Trans. **130**, 102401, (2008)
- [75] B. A. Nelson and A. W. Knoll, *Nanoscale three-dimensional patterning of molecular resists by scanning probes*, Science **328**, (2010), p. 732–735.
- [76] Y. L. Zhang, E. E. Castillo, R. J. Mehta, G. Ramanath and T. Borca-Tasciuc, *A noncontact thermal microprobe for local thermal conductivity measurement*, Rev. Sci. Instrum. **82**, 024902, (2011).
- [77] K. Park, J. Lee, Z. M. M. Zhang, and W. P. King, *Frequency-dependent electrical and thermal response of heated atomic force microscope cantilevers*, J. Microelectromechanical Systems **16**, (2007), p. 213–222.
- [78] K. Park, A. Marchenkov, Z. M. Zhang, and W. P. King, *Low temperature characterization of heated microcantilevers*, J. Appl. Phys. **101**, 094504, (2007).

- [79] S. Shen, A. Narayanaswamy, S. Goh, and G. Chen, *Thermal conductance of bimaterial microcantilevers*, Appl. Phys. Lett. **92**, 063509, (2008).
- [80] R. Serrano, L. M. Phinney, and J. W. Rogers, *Temperature amplification during laser heating of polycrystalline silicon microcantilevers due to temperature-dependent optical properties*, Int. J. Heat Mass Transfer **52**, (2009), p. 2255–2264.
- [81] M. Toda, T. Ono, F. Liu, and I. Voiculescu, *Evaluation of bimaterial cantilever beam for heat sensing at atmospheric pressure*, Rev. Sci. Instrum. **81**, 055104, 2010
- [82] J. Lee, T. L. Wright, M. R. Abel, E. O. Sunden, A. Marchenkov, S. Graham, and W. P. King, *Thermal conduction from microcantilever heaters in partial vacuum*, J. Appl. Phys. **101**, 014906, (2007).
- [83] B. W. Chui, M. Asheghi, Y. S. Ju, K. E. Goodson, T. W. Kenny, and H. J. Mamin, *Intrinsic-carrier thermal runaway in silicon microcantilevers*, Microscale Thermophys. Eng. **3**, (1999), p. 217–228.
- [84] K. J. Kim and W. P. King, *Thermal conduction between a heated microcantilever and a surrounding air environment*, Appl. Therm. Eng. **29**, (2009), p. 1631–1641.
- [85] B. A. Nelson and W. P. King, *Temperature calibration of heated silicon atomic force microscope cantilevers*, Sensor Actuat. A **140**, (2007), p. 51–59.
- [86] B. Kwon, M. Rosenberger, R. Bhargava, D. G. Cahill, and W. P. King, *Dynamic thermo-mechanical response of bimaterial microcantilevers to periodic heating by infrared radiation*, Rev. Sci. Instrum. **83**, 015003, (2012).
- [87] X. J. Hu, A. Jain, and K. E. Goodson, *Investigation of the natural convection boundary condition in microfabricated structures*, Int. J. Therm. Sci. **47**, (2008), p. 820–824.
- [88] Z. T. Dai, E. A. Corbin, and W. P. King, *A microcantilever heater-thermometer with a thermal isolation layer for making thermal nanotopography measurements*, Nanotechnology **21**, 055503, (2010).
- [89] J. H. Bae, T. Ono, and M. Esashi, *Scanning probe with an integrated diamond heater element for nanolithography*, Appl. Phys. Lett. **82**, (2003), p. 814–816.
- [90] U. Drechsler, N. Burer, M. Despont, U. Durig, B. Gotsmann, F. Robin, and P. Vettiger, *Cantilevers with nano-heaters for thermomechanical storage application*, Microelectron. Eng. **67-68**, (2003), p. 397–404.
- [91] H. J. Mamin, *Thermal writing using a heated atomic force microscope tip*, Appl. Phys. Lett. **69**, (1996), p. 433–435.
- [92] Ali Assy, Stéphane Lefèvre, Pierre-Olivier Chapuis and Séverine Gomès, *Analysis of heat transfer in the water meniscus at the tip-sample contact in scanning thermal microscopy*, Journal of Physics D: Applied Physics, Volume 47, Number 44, 2014.
- [93] L. Gaverina, *Mise au point d'un instrument de contrôle non-destructif thermique en milieu industriel*, Ph.D. Thesis, University of Bordeaux 1, 2017

3. Chapter 3 – EXPERIMENTAL SETUP

3.1. Introduction

In this chapter, we are going to take an in-depth look into the different parts of our experimental setup and also at the various factors that affect the final result of the experiments. One of the major components required to perform SThM experiments are the probes. As described in the previous chapter, modern innovation and scientific progress has led to the development of new and advanced probes. In section 2, we describe the experimental setup, detailing the key parts of the setup and the way they work. In section 3, we present the role of surface preparation and its consequences on the measurements. Although we did not find a solution to remove the dust on surface, we observed that it can significantly vary the contact conditions between the probe and the investigated surface. It is also obviously well known that the surface roughness will also play, at a certain level, on the thermal field measured by the probe. We also talk in-depth about the calibration of the probe and the step-by-step approach we have taken to perform the experiments. Moreover, we take a look into the sensitive parameter that can affect the experimental measurement along with the instruments their values are derived from. Sensitive parameters include force contact, probe motion speed, integration time and acquisition time. The knowledge and utilization of these parameters during the experimental phase allows us to obtain the precise effective radius of the probe and the thermal contact resistance, which are then used in our model.

3.2. Experimental setup

3.2.1. *Global presentation*

The Figure 44 provides the global overview of the experimental setup we have used to perform our experiments. Our SThM is based on atomic force microscope (AFM) with a thermal probe. The AFM is described in section 2.2 and the probe will be described in section 2.3. For the purpose of our work, we are only using thermoresistive probes that play the role of the heater and the thermometer. It is therefore possible to use thermoresistive probes to obtain sample temperature and thermal conductivity. One of the biggest advantages of using a thermoresistive

probe is the absence of any specialized devices necessary for operation [1]. Using simple commercial solutions like simple AC or DC current and Wheatstone bridge are sufficient to provide basic thermal images. In our case we have also utilized other industrial devices and a homemade SThM setup to further improve the quality of measurement and accuracy. All the elements of the experimental setup have been connected using GPIB and that have been remotely controlled from a computer using a code developed under Python language. This code allows to make the frequency dependent measurement as well as the probe calibration.

The setup is capable working either with the continuous wave (DC) mode or the 3ω (AC) mode. The two modes are detailed in section 4.1 and 4.2 respectively.

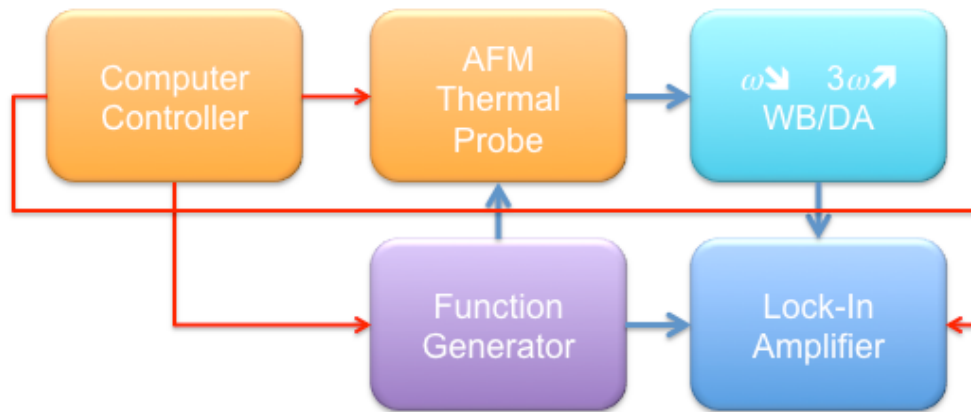


Figure 44. Schematic diagram of the SThM experimental technique.

3.2.2. *The AFM*

The Nanosurf EasyScan 2 is an atomic force microscope that can measure the topography with nanometer resolution along z -axis (Figure 45). It possesses a dual lens observation optics and automatic approach. The Nanosurf EasyScan 2 has two main parts:

1) The controller: the EasyScan 2 controller is a major component of the whole equipment. It allows the user to control the scan head that holds the probe as per his/her requirements (for example in static force or dynamic force modes). Moreover, other modes of operation including Phase Contrast, Force Modulation, Spreading Resistance, Magnetic Force and Electrostatic Force mode can be implemented within this AFM although they have not been involved in the present study.

2) The scan head: the FlexAFM scan head consists of a flexure-based electromagnetic scanner that allows metrology like applications in air or liquid. The scanner is linear, flat, and fast. *XY*-scanner, which forms the basis of the flexure scanner, is mostly flat and rugged. Being electromagnetically actuated, all movements in this plane are highly linear. A piezo-based *Z*-scanner provides fast movements in this direction. Moreover, the magnetic base of the cantilever holder allows easy attachment of the probe. The cantilever holder also allows the user to manually manipulate and adjust the probe and laser alignment. This provides easy positioning and approach of the probe and the sample with good top and side views.

The contact force between the probe and the sample is accurately controlled using a feedback-closed loop on a piezo-element, which ensures the displacement in the *z* direction with precise steps of 1 nm.



Figure 45. AFM Nanosurf Easyscan 2. AFM head and controller.

3.2.3. Thermal Probes

3.2.3.1. Probe Fabrication

The Figure 46 provides a step-by-step demonstration of the processes involved in the fabrication of a SThM probe. (I) A 400 μm thick 3-inch silicon wafer with double-side polish is deposited with 100 nm SiN_x . (II) The position of the cantilever is defined by wet etching of the bottom side. (III) SiN_x mask is used to define the pyramid on the top side. (IV) the mask is then taken off by using a solution of HF and water in a 1:5 ratio. (V) Photolithography and dry etching is used to define the groove on the cantilever. (VI) Using low pressure chemical vapor deposition (LPCVD) technique, 500 nm SiN_x is deposited on both sides. (VII) the top side is used to define

the shape of the cantilever (VIII) Stripping the SiN_x from the bottom side allows the final defining and releasing. (IX) a 40 nm platinum at the end of the tip followed by a 150 nm gold wire is used for the metallization on the cantilever and finally (X) to release the probe, a TMAH wet etching is used [2][3].

After fabrication individual probes can be cleaved from the wafer and used as required with no subsequent processing.

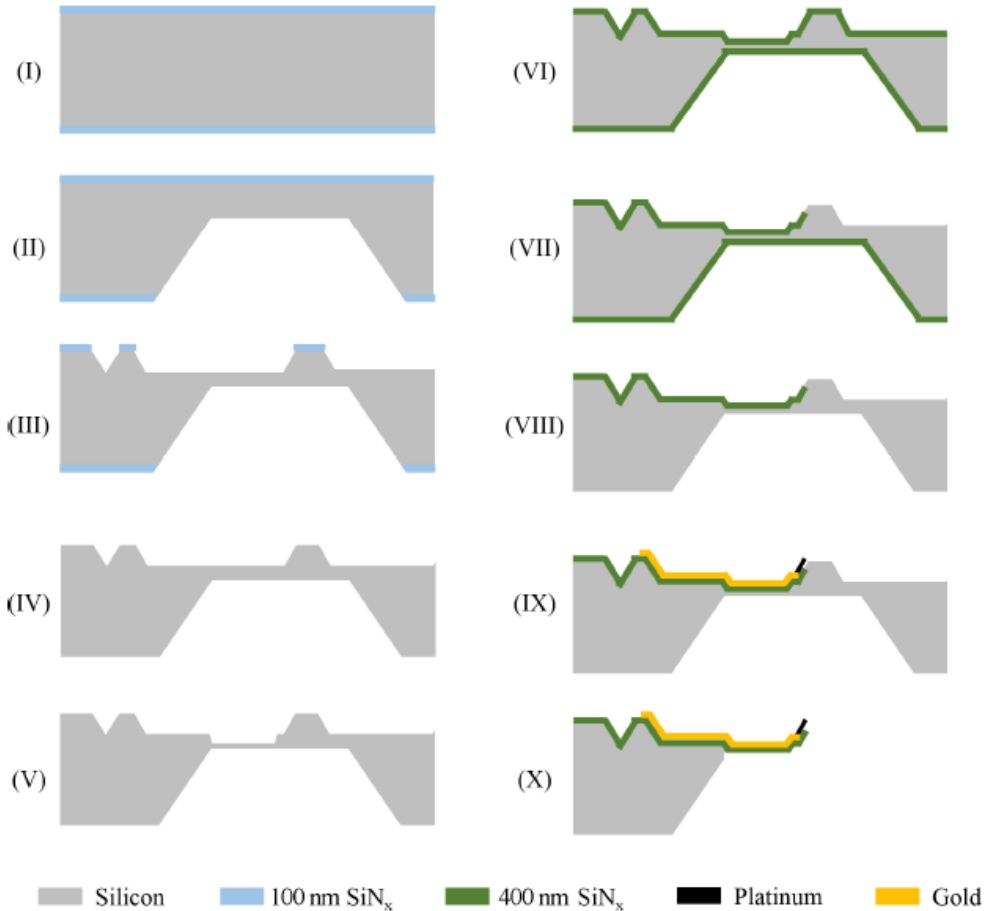


Figure 46. Schematic diagram of the process of fabrication of grooved SThM probe [2][3].

The Figure 47 below provides a general idea of a modern SThM probe.

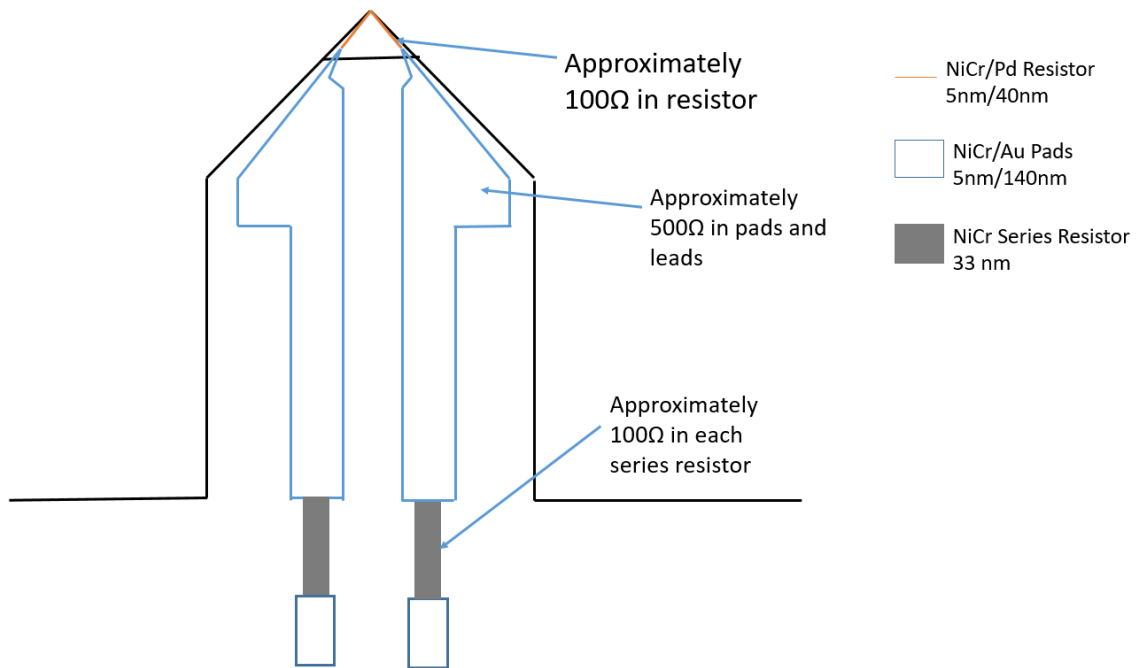


Figure 47. SThM probe setup.

Below, we are going to discuss about the two different types of modern thermoresistive probes that we have used for our work.

3.2.3.2. The 2 point probe

The 2-point probe has only one internal and one external pad. This probe provided by NanoAndMore and Anasys is based on a silicon nitride (Si_3N_4) cantilever on which is deposited a palladium (Pd) strip of 11 m thickness and 101 m length at the tip (Figure 48). This palladium strip plays the role of the heater and the thermometer. We have another type of probe provided by NT-MDT with similar specifications but instead of Si_3N_4 cantilever, it has a SiO_2 one.

Table 5 Thermal properties of thermal SiO_2 and amorphous Si_3N_4 (k : thermal conductivity, ρ : density and C_p : specific heat, Θ_D : Debye temperature, v_T : phonon transverse velocity, v_L : phonon longitudinal velocity) at room temperature.

Material	k ($\text{W.m}^{-1}.\text{K}^{-1}$)	ρ (kg.m^{-3})	C_p ($\text{J.kg}^{-1}.\text{K}^{-1}$)	Θ_D (K)	v_T (m.s^{-1})	v_L (m.s^{-1})
$a\text{-SiO}_2$	1.4	2200	787	380	3125	6070
$a\text{-Si}_3\text{N}_4$	2.1	2900	400	985	6200	10300

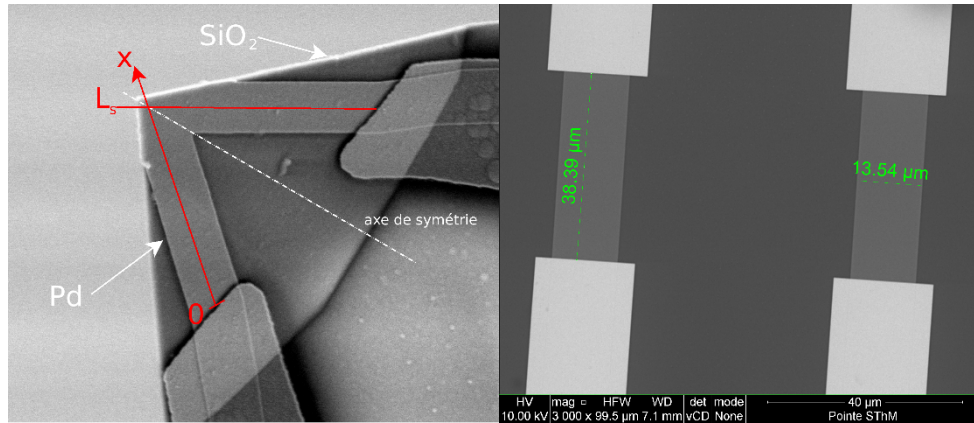


Figure 48. (left) A close up view of the 2-point probe with the Pd strip deposited at the tip. (Right) View of the NiCr Current Limiters that bound the current passing the Pd strip at 1 mA.

Table 6 The different dimensions and parameters of the point probe (in bold the main differences between the two probes).

Provider	Anasys/NanoAndMore	NT-MDT
Cantilever	Si ₃ N ₄	SiO ₂
Resistance metal	5 nm NiCr – 40 nm Pd	5 nm NiCr – 40 nm Pd
	5 nm NiCr – 140 nm Au	5 nm NiCr – 140 nm Au
Length x width	150 x 60 μm	150 x 60 μm
Thickness	0.4 μm	1 μm
Tip Height	10 μm	10 μm
Spring Constant	0.25 N/m	0.45 N/m
Resonant Frequency	50 kHz	48 kHz
Resistance	250-400 Ω (typ. 320 Ω)	300-500 Ω
Sensitivity	Approx. 1 Ω/°C	Approx. 1 Ω/°C
Tip Radius	< 100 nm	< 100 nm
Maximum controllable temperature	160 °C	160 °C

Larger gold strips allow realizing the current flow but with very low Joule dissipation compared to its effect within the Pd strip. Large nickel chromium (NiCr) strips are placed in series, on the gold strip, with the Pd strip and are 38.39 μm in length and 13.54 μm in width (see Figure 48). They have the role of current limiters as they limit the maximum current at 1 mA. The different properties of the probe are given in Table 6 [5]. It must be also said that the NiCr as a thin film (5 nm) is used to improve the adhesion of Au and Pd on the substrate. For information, some useful properties of the thermal SiO_2 and amorphous Si_3N_4 are reported in Table 5. Both materials are very similar with respect to their thermal conductivity and density but they differ significantly for the specific heat, the Debye temperature and the phonon velocity.

3.2.3.3. The 4 Point Probe

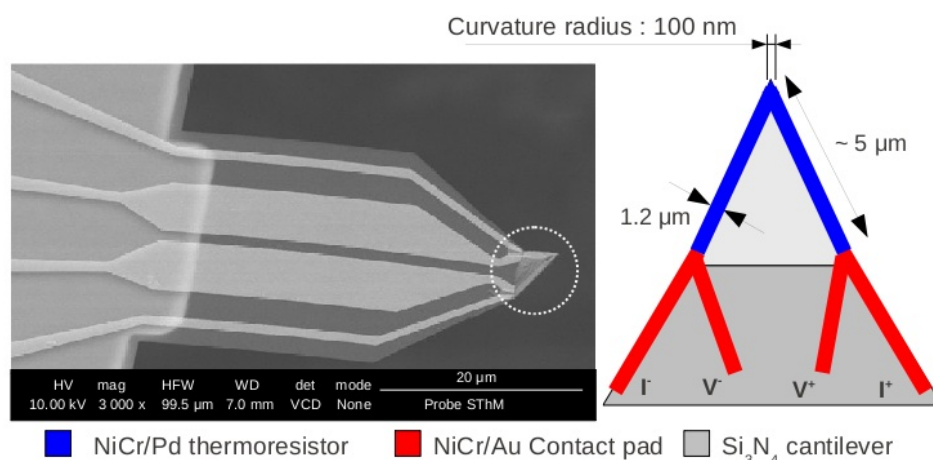


Figure 49. Thermo-resistive 4-point probe and its configuration.

The 4-point probe is very similar to in its functioning and architecture of the 2-point probe but the major difference between the two is the fact that instead of having one external pads for controlling the current and one internal pads for controlling the voltage drop, there are two internal and two external pads which provide more accuracy. As represented on the Figure 49, the two external pad controls the current (I^+ , I^-) while the two internal pads are used for measuring the voltage (V^+ , V^-). Indeed, the 2-point probe accounts not only with the heat generated by Joule effect within the Pd strip but also with that generated within the gold strips although this later is much lower. This is no more the case with the 4-point probe that is only sensitive to the change of electrical of the Pd strip according to its average temperature. The 40-

nm-thick Pd strip is $l_{Pd}=1.2 \mu\text{m}$ in width, and the contact length between the two gold strip is approximately $L_{Pd}=10 \mu\text{m}$. Kelvin Nanotechnology provides the new and advanced 4-point SThM probe with a tip radius of curvature (r_s) less than 100 nm. The figure above shows the image of a probe in a 20 μm scale as well as the different parts of the 4-point configuration [5]. The Table 7 shows the different dimensions and parameters of the various parts of the 4-point probe.

Table 7. The different dimensions and parameters of the various parts of the 4-point probe (from [3]).

Probe base	2 mm x 3 mm
Cantilever (Si_3N_4)	150 μm x 60 μm x 1 μm
Resistor metal	5 nm NiCr – 40 nm Pd
Track and pad metal	5 nm NiCr – 140 nm Au
Resistance	300 – 500 Ohm
Tip Radius	< 100 nm
Maximum Temperature	160 °C
Tip height	10 μm
Si_3N_4 Spring Constant	0.25 N/m
Fo	48 kHz
Sensitivity	app. 1 Ohm/°C

3.2.4. *The function generator*

An Arbitrary Waveform Generator allows us, unlike the Arbitrary Function Generator, to generate user defined waveforms of any size. This electronic test equipment can either be repetitive or

single-shot (one time only) in which case some kind of internal or external triggering source is provided. The Arbitrary Waveform Generator although allows precise generation of waveforms in the arbitrary generation mode, their frequency precision is limited at high frequencies. To achieve our arbitrary waveforms, we have utilized a 33220A Function / Arbitrary Waveform Generator manufactured by KEYSIGHT Technologies.

3.2.5. The lock-in amplifier

Lock-in amplifiers are used to detect and measure very small AC signals all the way down to a few nanovolts. Accurate measurements may be made even when the small signal is obscured by noise sources many thousands of times larger. Lock-in amplifiers use a technique known as phase-sensitive detection to single out the component of the signal at a specific reference frequency and phase. Noise signals, at frequencies other than the reference frequency, are rejected and do not affect the measurement.

Suppose the signal is a 100 nV sine wave at 1 kHz. A good low-noise amplifier will have about 5 nV/ $\sqrt{\text{Hz}}$ of input noise. If the amplifier bandwidth is 100 kHz and the gain is 1000, we can expect our output to be 100 μV of signal ($100 \text{ nV} \times 1000$) and 1.6 mV of broadband noise ($5 \text{ nV}/\sqrt{\text{Hz}} \times \sqrt{100 \text{ kHz}} \times 1000$). Even if we single out the frequency of interest with a band pass filter centered at 1 kHz, the output noise will remain much greater than the signal, and an accurate measurement cannot be made. Further gain will not help the signal-to-noise problem. Now try following the amplifier with a phase-sensitive detector (PSD). The PSD can detect the signal at 1 kHz with a bandwidth as narrow as 0.01 Hz! In this case, the noise in the detection bandwidth will be 0.5 μV ($5 \text{ nV}/\sqrt{\text{Hz}} \times \sqrt{0.01 \text{ Hz}} \times 1000$), while the signal is still 100 μV . The signal-to-noise ratio is now 200, and an accurate measurement of the signal is possible.

The lock-in measurement requires the frequency reference from the sync output of the function generator that fixed the periodic heating of the probe. Let's suppose that the reference signal is a square wave at frequency ω_r . The response might be the signal waveform shown below. Let's state that the measured signal is $S(t)$. The lock-in amplifies the signal and then multiplies it by the lock-in reference using a phase-sensitive detector or multiplier. A lock-in amplifier, because it multiplies the signal with a pure sine wave, measures the single Fourier (sine) component of

the signal at the reference frequency. Let's take a look at an example. Suppose the input signal is a simple square wave at frequency f . The square wave is actually composed of many sine waves at multiples of f with carefully related amplitudes and phases. Fourier's series of a $2 V_{pp}$ square wave is:

$$S(t) = 1.273 \sin(\omega t) + 0.4244 \sin(3\omega t) + 0.2546 \sin(5\omega t) + \dots \quad (3.1)$$

where $\omega = 2\pi f$. The lock-in, locked to f , will single out the first component: $1.273 \sin(\omega t)$ and the displayed magnitude would be $0.90 V_{rms}$ (or $1.273/\sqrt{2}$).

In real measurement, the input consists of signal plus noise. Noise is represented as varying signals at all frequencies. The ideal lock-in only responds to noise at the reference frequency. The low pass filter following the multiplier removes noise at other frequencies. This "bandwidth narrowing" is the primary advantage that a lock-in amplifier provides. Only inputs with frequencies at the reference frequency result in an output.

Let us now consider the signal is $S(t) = V_{sig} \sin(\omega_r t + \theta_{sig})$ where V_{sig} is the signal amplitude and θ_{sig} is the signal's phase. The output of the PSD is simply the product of two sine waves:

$$\begin{aligned} V_{psd} &= V_{sig} \sin(\omega_r t + \theta_{sig}) \times V_L \sin(\omega_L t + \theta_{ref}) \\ &= \frac{1}{2} V_{sig} V_L \cos((\omega_r - \omega_L)t + \theta_{sig} - \theta_{ref}) \\ &\quad - \frac{1}{2} V_{sig} V_L \cos((\omega_r + \omega_L)t + \theta_{sig} + \theta_{ref}) \end{aligned} \quad (3.2)$$

The PSD output is two AC signals, one at the difference frequency $(\omega_r - \omega_L)$ and the other at the sum frequency $(\omega_r + \omega_L)$. If the PSD output is passed through a low pass filter, the AC signals are removed. If $\omega_r = \omega_L$, the difference frequency component will be a DC signal. In this case, the filtered PSD output will be:

$$V_{psd} = \frac{1}{2} V_{sig} V_L \cos(\theta_{sig} - \theta_{ref}) \propto V_{sig} \cos\theta \quad (3.3)$$

θ is the phase difference between the signal and the lock-in reference. By adjusting θ_{ref} we can make θ equal to zero. In which case we can measure V_{sig} . Conversely, if $\theta = 90^\circ$, there will be no output at all. A lock-in with a single PSD is called a single-phase lock-in and its output is $V_{sig} \cos\theta$. This phase dependency can be eliminated by adding a second PSD. If the second PSD multiplies the signal with the reference oscillator shifted by 90° , i.e. $V_L \sin(\omega_L t + \theta_{ref} + 90^\circ)$, its low pass filtered output will be:

$$V_{psd2} = \frac{1}{2} V_{sig} V_L \sin(\theta_{sig} - \theta_{ref}) \propto V_{sig} \sin\theta \quad (3.4)$$

Now we have two outputs: one proportional to $\cos\theta$ and the other proportional to $\sin\theta$. If we call the first output X and the second Y :

$$X = V_{sig} \cos\theta; \quad Y = V_{sig} \sin\theta \quad (3.5)$$

These two quantities represent the signal as a vector relative to the lock-in reference oscillator. X is called the 'in-phase' component and Y the 'quadrature' component. This is because when $\theta = 0$, X measures the signal while Y is zero. The magnitude and phase of the signal vector are computed as:

$$R = (X^2 + Y^2)^{1/2} = V_{sig}; \quad \theta = \tan^{-1}(Y / X) \quad (3.6)$$

The SR830 provided by Standard Research Systems allows measuring simultaneously the signal magnitude and phase [6]. The SR830 uses digital signal processing (DSP) to replace the demodulators, output filters, and amplifiers found in conventional lock-ins. Indeed, in traditional analog lock-ins, the signal and reference are analog voltage signals. The signal and reference are multiplied in an analog multiplier, and the result is filtered with one or more stages of RC filters. In a digital lock-in, such as the SR830, the signal and reference are represented by sequences of numbers. Multiplication and filtering are performed mathematically by a digital signal processing (DSP) chip. It displays and also allows us to control the "Time Constant" (Integration Time), Sensitivity (used for Amplitude calculations) along with "Signal Input", "Reserves" and

“Filters”. Moreover, the “Reference” signal in terms of frequency is also displayed on the system. Figure 50 provides the functional block diagram of the lock-in.

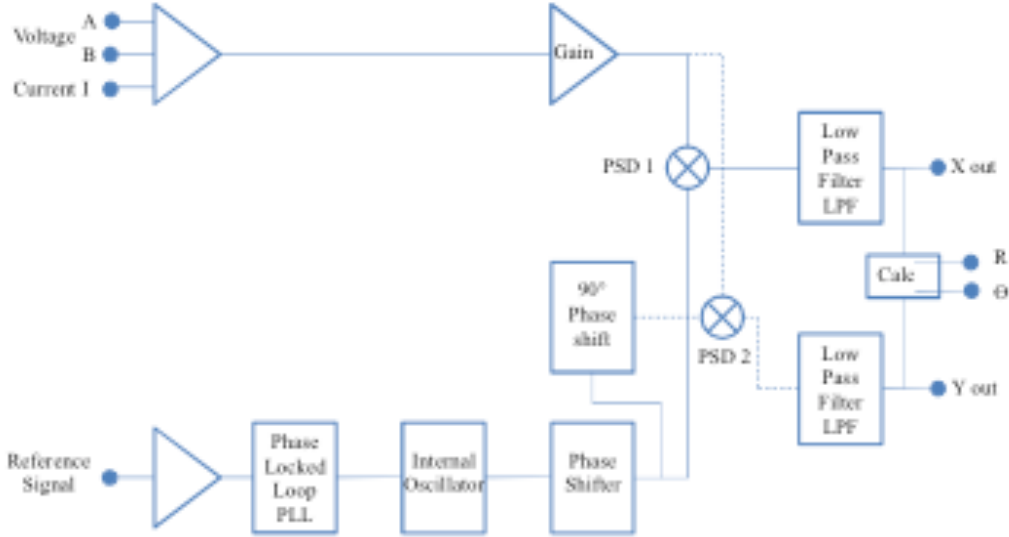


Figure 50. Functional block diagram of the lock-in.

The input noise of the SR830 signal amplifier is about $5 \text{ nV}_{\text{rms}}/\sqrt{\text{Hz}}$. It means that if an amplifier has $5 \text{ nV}_{\text{rms}}/\sqrt{\text{Hz}}$ of input noise and a gain of 1000, then the output will have $5 \text{ } \mu\text{V}_{\text{rms}}/\sqrt{\text{Hz}}$ of noise. Suppose the amplifier output is low-pass filtered with a single RC filter (6 dB/oct rolloff) with a time constant of 100 ms. Suppose the lock-in is set to $5 \text{ } \mu\text{V}$ full scale, with a 100 ms time constant, and 6 dB/oct of filter rolloff. The lock-in will measure the input noise with an equivalent noise bandwidth (ENBW) of 2.5 Hz. This translates to $7.9 \text{ nV}_{\text{rms}}$ at the input. At the output, this represents about 0.16 % of full scale ($7.9 \text{ nV}/5 \text{ } \mu\text{V}$). The peak-to-peak noise will be about 0.8 % of full scale. All of this assumes that the signal input is being driven from a low impedance source. Resistors have Johnson noise equal to $0.13 \times \sqrt{R} \text{ nV}_{\text{rms}}/\sqrt{\text{Hz}}$. Therefore, even a $50 \text{ } \Omega$ resistor has almost $1 \text{ nV}_{\text{rms}}/\sqrt{\text{Hz}}$ of noise! A signal source impedance of $2 \text{ k } \Omega$ will have a Johnson noise greater than the lock-in's input noise. To determine the overall noise of multiple noise sources, one has to take the square root of the sum of the squares of the individual noise figures. For example, if a $2 \text{ k } \Omega$ source impedance is used, the Johnson noise will be $5.8 \text{ nV}_{\text{rms}}/\sqrt{\text{Hz}}$

Hz. The overall noise at the lock-in's input will be $[52 + 5.82]^{1/2}$, or $7.7 \text{ nV}_{\text{rms}}/\sqrt{\text{Hz}}$. Johnson noise and shot noise are intrinsic noise sources and are inherent to all physical processes, meaning they cannot be avoided. Johnson noise is related to the noise voltage generated by a resistor across its terminals due to thermal fluctuations in the electron density within the resistor itself as:

$$V_{\text{noise,Johnson}}(\text{rms}) = (4k_B T R \Delta f)^{1/2} \quad (3.7)$$

where k_B is the Boltzmann's constant ($1.38 \times 10^{-23} \text{ J/K}$), T is the temperature in Kelvin, R is the resistance in ohms, and Δf is the bandwidth of the measurement in Hz. In a lock-in, the ENBW of the low pass filter (time constant) sets the detection bandwidth. In this case, the measured noise of a resistor at the lock-in input, typically the source impedance of the signal, is simply:

$$V_{\text{noise,Johnson}}(\text{rms}) = 0.13 \sqrt{R} \sqrt{ENBW} \text{ nV} \quad (3.8)$$

Shot noise is related to the non-uniformity in the electron flow that generates noise in the current. This can appear as voltage noise when current is passed through a resistor, or as noise in a current measurement. The shot noise, or current noise, is given by:

$$i_{\text{shot noise}}(\text{rms}) = (2q i \Delta f)^{1/2} \quad (3.9)$$

where q is the electron charge ($1.6 \times 10^{-19} \text{ C}$), i is the rms AC current or DC current depending upon the circuit, and Δf is the bandwidth. In a lock-in, the bandwidth is typically so small that shot noise is not important.

3.2.6. The 3ω measurement

The third harmonic measurement can be achieved using either a Wheatstone bridge (WB) or a differential amplifier (DA), both coupled with the lock-in amplifier.

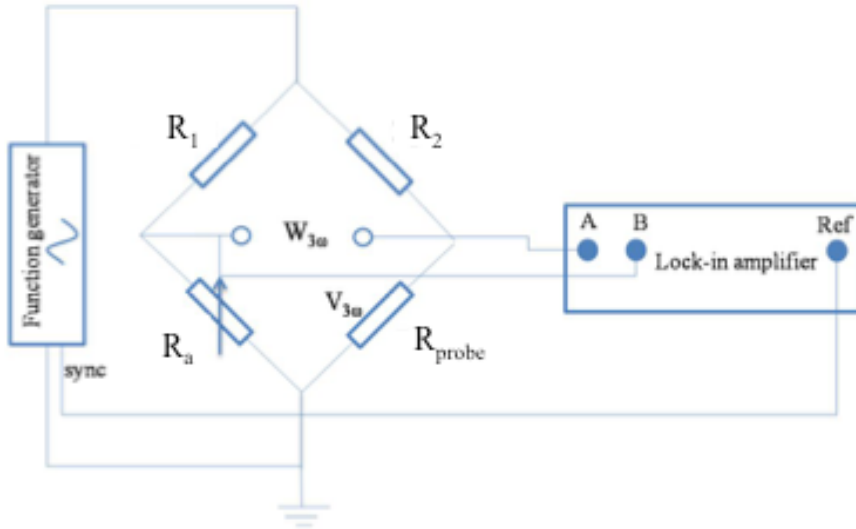


Figure 51. Wheatstone bridge measurement principle.

The Wheatstone bridge (Figure 51) is an electrical circuit with two known resistances R_1 and R_2 , one variable resistance R_a and an unknown one R_{probe} . This is achieved by balancing the bridge where the variable resistance is tuned till reading a zero voltage $V_A - V_B$. Consequently, it leads to:

$$R_{probe} = R_2 \frac{R_a}{R_1} \quad (3.10)$$

Balancing the Wheatstone bridge, the third harmonic voltage $V_{3\omega}$ at the output can be measured through the differential input (A-B) of the lock-in amplifier. The induced third harmonic voltage in the probe is then calculated by considering the Wheatstone bridge as a voltage divider with the input source replaced by the $R_{Gen}=50 \Omega$ resistance of the function generator. Therefore, the third harmonic voltage is:

$$V_{3\omega} = (V_A - V_B) \frac{R_2 + R_{Gen} + R_{probe}}{R_2 + R_{Gen}} \quad (3.11)$$

Obviously, the TCR values for the resistances and potentiometers are the minimum available.

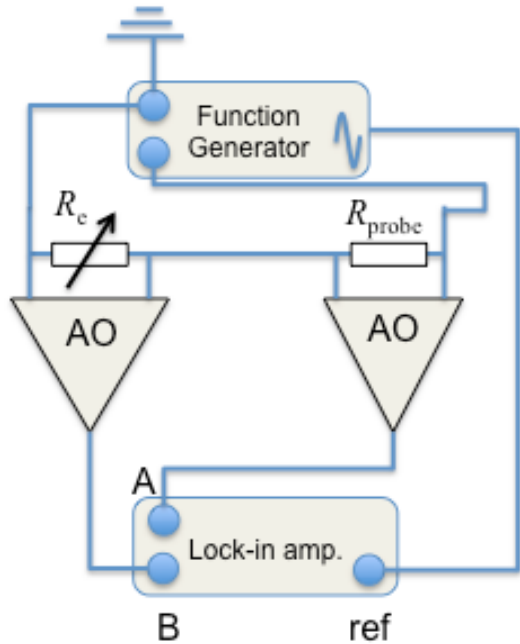


Figure 52. Image showing the process of isolation of the third harmonic using the differential amplifier stage.

As the third harmonic is 10^3 to 10^6 factor less than the fundamental one, the differential amplifier is expected to decrease largely the contribution of the first harmonic in the measured signal before entering the lock-in. The basic principle is presented in Figure 52. Two differential amplifiers of gain=1 are used to isolate the voltages across R_e and R_{probe} line. The outputs of the differential amplifiers are connected to the inputs A and B of the lock-in amplifier and differentiated through (A-B) mode. The variable resistance R_e is tuned till acquiring a zero voltage at frequency ω at the output of the lock-in amplifier. At this moment the variable resistance R_e is equal to the resistance of the probe R_{probe} . Switching the lock-in amplifier harmonic detect number to 3, the third harmonic voltage $V_{3\omega}$ only generated by the probe can be measured.

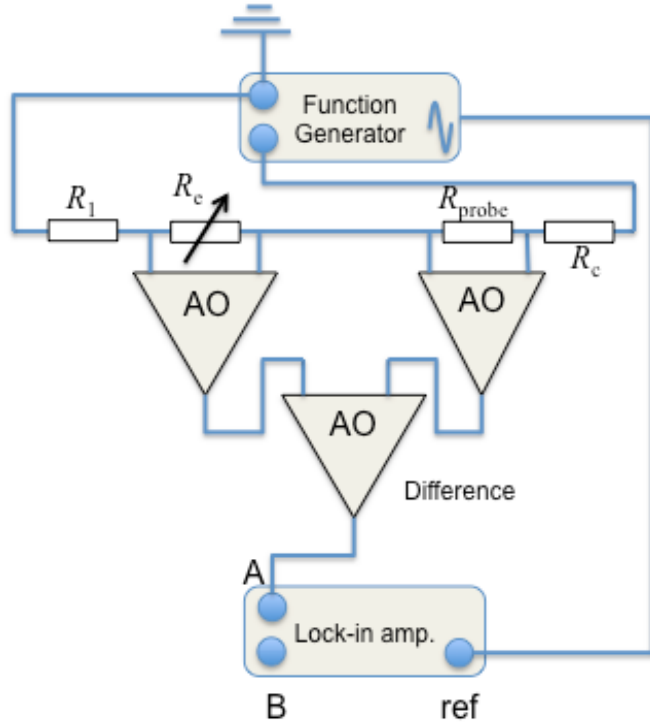


Figure 53. $R_1 = 700\Omega$, $R_c = 1\Omega$.

Resistance R_1 sets the current in the measurement circuit, and resistance R_c allows measuring the current with high accuracy (Figure 53).

Although the Operational Amplifiers (AO) have been chosen to work within a large frequency bandwidth, it is expected that the setup lead to modify the phase slightly at high frequency. Therefore we performed a calibration of the phase by using the function generator output as the input of the differential amplifier instead of the probe. We obtained the variation between the real phase (0 deg) and the output of the setup reported in Figure 54. Therefore the real the measured phase at the lock-in must be corrected as:

$$\phi_{3\omega} = \phi_{\text{lock-in}} + \Delta\phi \quad (3.12)$$

We observed that this correction is very small apart for the highest working frequency at 5123 Hz. We have no argument to explain this abrupt change except that it could be induced by other components as the resistors and capacitors as well as the wires that have been used to connect the devices.

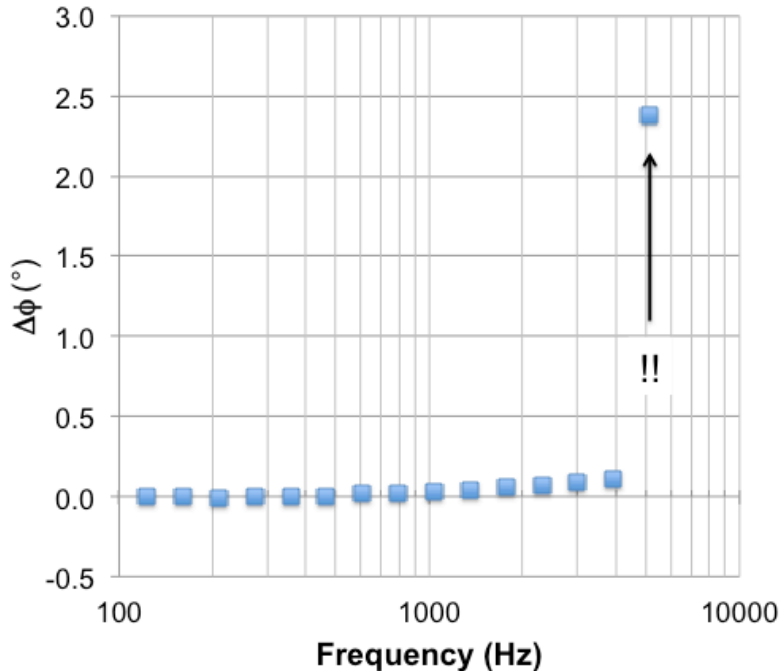


Figure 54. Calibration of the phase by measuring the change induced by the differential amplifier.

3.2.7. *The workstation*

Experiments performed using Scanning Thermal Microscopy is highly sensitive to vibrations. Intense vibrations can not only damage the sample and the probe but also give erroneous results. Hence it is vital to isolate the vibrations. To achieve this, we have utilized Accurion’s active vibration isolation desktop unit halcyonics micro series along with a workstation [7].

The desktop unit consists of low voltage electromagnetic actuators with neodymium magnets and rugged electronics which can provide good isolation especially under dampen building vibrations. The active isolation starts from 0.6 Hz and is active until 200 Hz (and passive above 200 Hz). The Workstation_i4 offers a compact active isolated surface especially for microscopes, surrounded by a conventional non-isolated laboratory desk surface [8]. This surface can be used to place additional equipment, to handle test samples or to simply make notes. The Workstation_i4 is designed for the use with optical microscopes or microscope/SPM combinations and acts as an active isolated surface surrounded by conventional non-isolated laboratory desk surfaces. It provides automatic load adjustment and no low frequency resonance as shown on Figure 55. Moreover, as additional equipment and handling of test samples can be

performed on its surface, we have placed the desktop unit above it and on top of the later is placed the Nanosurf Easyscan 2 AFM setup.

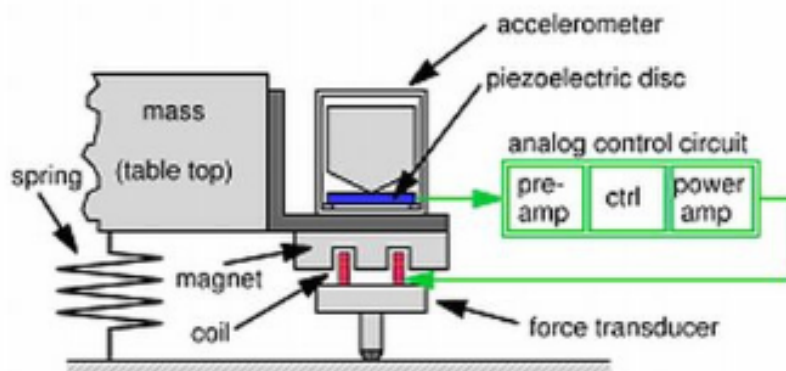


Figure 55. Active Vibration Control using Accurion's workbench (Principles of Halcyonics Active Vibration Isolation Technology, Accurion).

The environment of the setup, e.g., ambient temperature, relative humidity of the air, must be perfectly checked and controlled to guarantee the repeatability of the measurement. To achieve this objective, we place the AFM inside a chamber where primary vacuum was performed and then the volume was filled by Argon. It did not seem that this operation made the measurement more accurate than performing it under atmosphere but it was a way to guaranty exactly the same condition of working. However we have to mention that the *X-Y-Z* actuators provided with the Easyscan AFM are not compatible with working under vacuum. Therefore, the primary vacuum remains very limited and cannot be maintained during the scan. The complete experimental setup at the laboratory is given in the Figure 56.

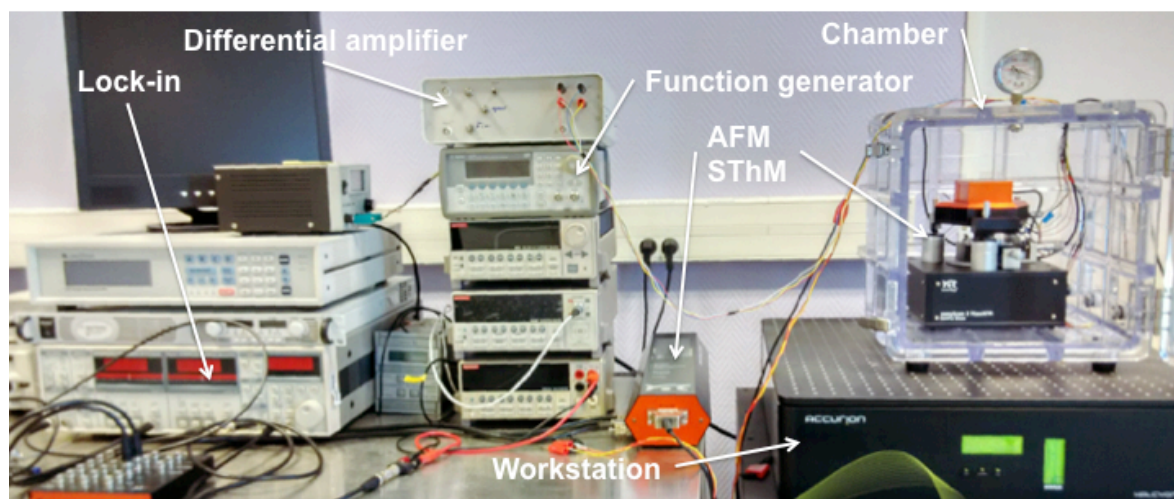


Figure 56. Image showing the experimental setup of SThM in the Laboratory.

3.3. Sample surface preparation

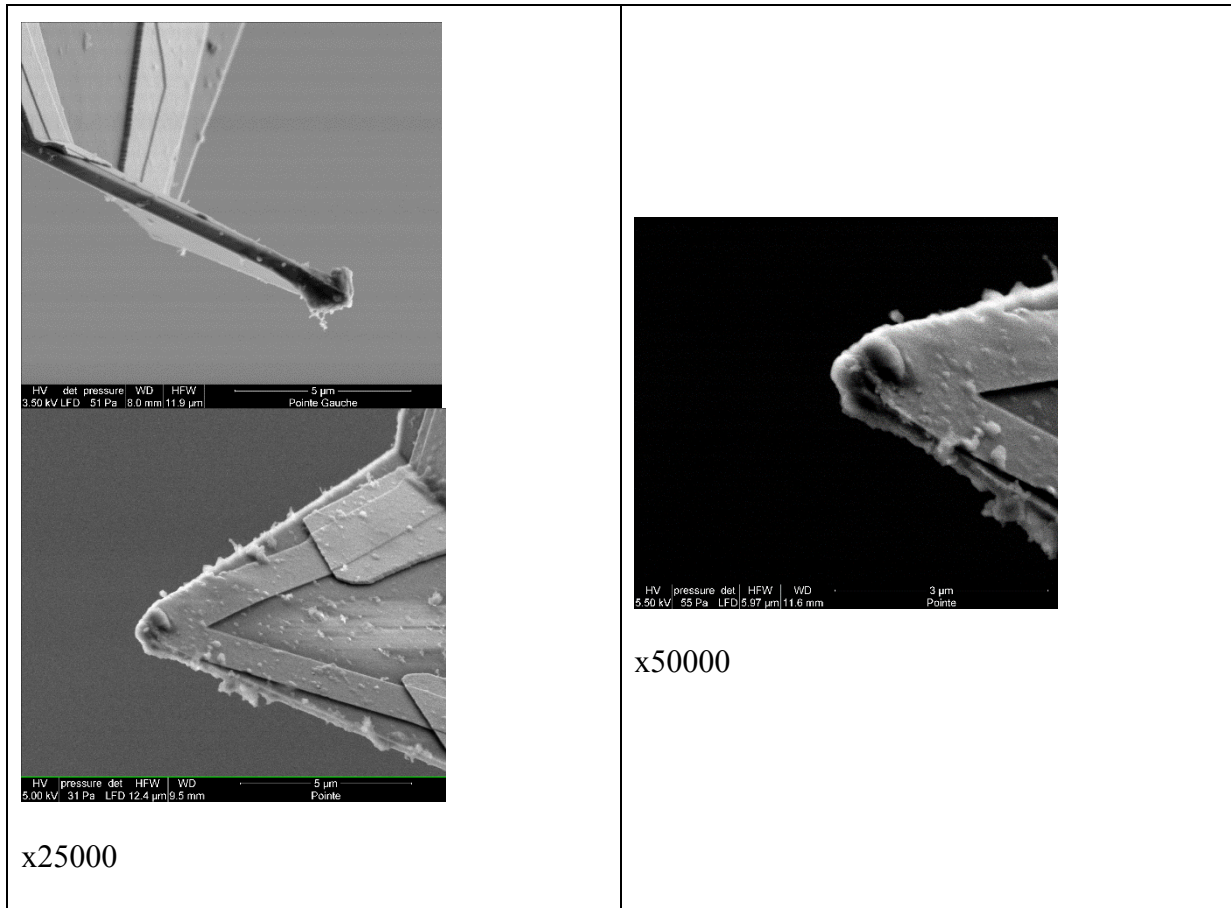


Figure 57. SEM Images showing the adhesion of dust on the probes after several uses.

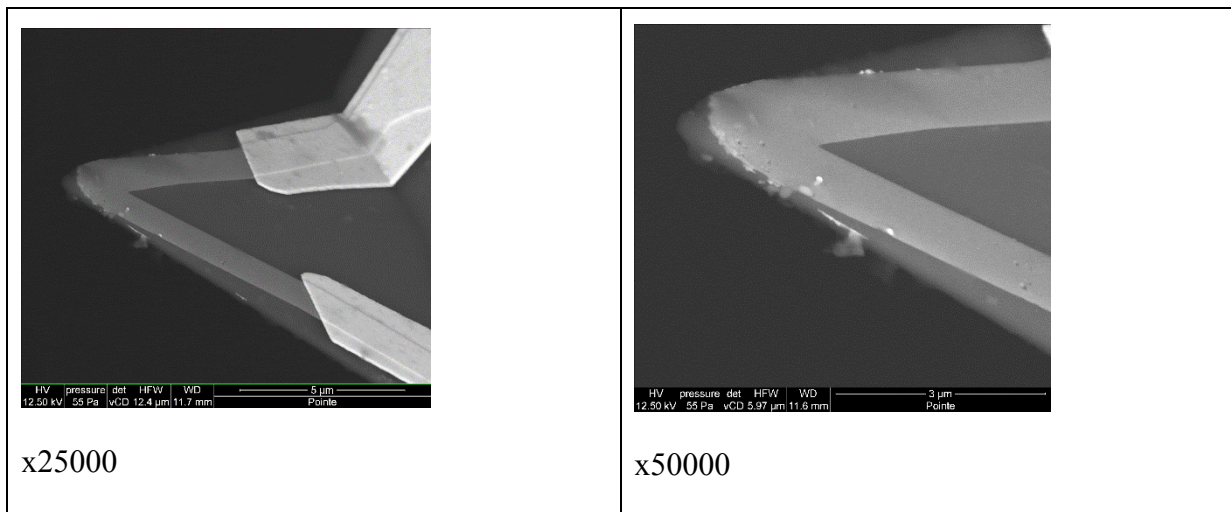


Figure 58. vCD Images showing the state of the tip of the probes after several uses.

The surface preparation of the investigated samples is of first importance regarding the quality and accuracy of the thermal measurements. Indeed, we observed that the quality of the thermal images decreased along their use in time. In order to understand this phenomenon we realized some images of the tip of the used probes using a FEI Quanta FEG 250 microscope.

The Secondary Electron Microscopy mode has been used first on probes that did not make accurate thermal images after several uses. The results are presented on the Figure 57. We observed that dust is stick on the tip of the probe making the contact between the probe and the material not reliable. Although, we took a lot of caution by removing the air in the chamber and filling it with argon, the dust is still present on the surfaces due to electrostatic forces. Therefore, even though we cleaned the surface of the materials before the SThM characterization, the dust can deposit again during the experiment despite of the argon atmosphere. However, as revealed by the vCD images on Figure 58, the integrity of the probe is still preserve, meaning that there is no sign of wear neither than deterioration of the tip. This leads us to conclude that the probes could be used again if we could find a method to clean them. This is a work under progress at this time. Another important effect of the surface preparation is about the effect of the roughness on the measured temperature during the scan. Indeed, we observed that the roughness could interfere with the temperature measurement in case we faced the specific configurations reported in Figure 59. It is assumed that the contact radius is r_0 .

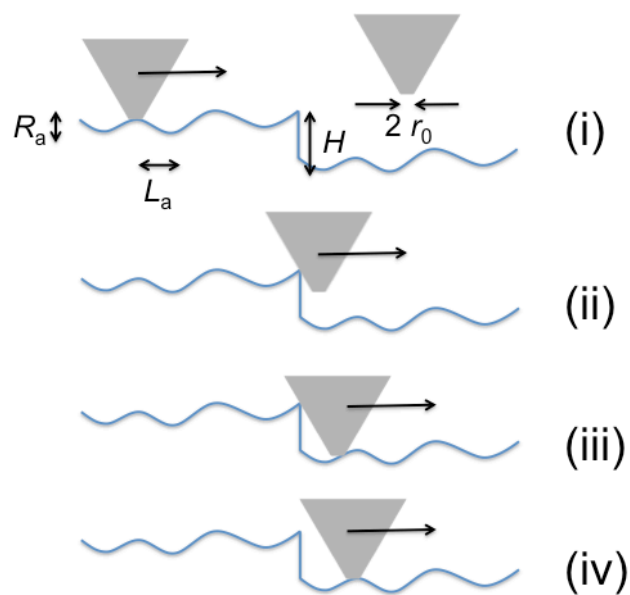


Figure 59. Possible configurations met when according to the surface roughness.

When the surface is such as:

$$\begin{cases} 2r_0 < L_a \\ 2r_0 > R_a \end{cases} \quad (3.13)$$

Then the contact between the surface and the probe is classically described as detailed in the chapter 2 (solid-solid contact, possible water meniscus at the interface). This is the case in the configurations (i) and (iv) of the figure. However, when the surface presents a gap of height H very high behind $2r_0$, the probe lost the contact with the surface at the tip and the contact can appear elsewhere with the probe as represented in (ii), making the heat transfer fully changed between the two parts. In case (iii), the configuration is even more different since the probe contacts the surface at two locations instead of one, making again the heat transfer fully different. This kind of configuration is classically met when the surface is composed from materials with dissimilar hardness. In that case the polishing of the surface leads to different heights of the surface. We will face such case in the chapter 6 regarding the application of SThM on composite material with a pyrocarbon matrix and silicon oxide fibers. Since the heat transfer model is too difficult to derive for the configurations (ii) and (iii), it is better to forget the data collected during this period. Indeed, there is not a simple method to de-correlate the thermal field from the topography unless the material is the same from both sides of the gap and there is no vertical boundary resistance (no crack) at the location of the gap.

On the other hand this configuration is very useful to determine the contact radius r_0 of the contact area between the probe and the surface, as we will show in the chapter 5.

3.4. The working modes

3.4.1. *The passive mode*

The passive mode is used for thermometry, i.e. temperature measurement. In this mode, a very small electrical current is passed through the probe. This results in minimal Joule self-heating and enables the measurement of the electrical resistance. During a scan, heat flows from the hot sample to the probe and changes the electrical resistance R_p of the probe. Indeed at first order:

$$R_p(T) = R_{p0} \left(1 + \alpha_R (T - T_0) \right) = R_{p0} \left(1 + \alpha_R \Delta T \right) \quad (3.14)$$

where $R_p(T)$ is the electrical resistance of the probe thermosensitive element at a reference temperature T , R_{p0} is the electrical resistance of the element at temperature T_0 and The parameter $\alpha_R = (1/R_0)dR/dT$ is the temperature coefficient (TCR) of its electrical resistivity.

Passing a low current i in the probe leads to the voltage drop at the probe to be:

$$\begin{aligned} U &= R_p(T)i = R_{p0}(1 + \alpha_R \Delta T)i \\ &= U_0 + \Delta U \end{aligned} \quad (3.15)$$

with:

$$\Delta T = \frac{\Delta U}{R_{p0} \alpha_R i} \quad (3.16)$$

Since $\Delta U = U$, practical measurement of ΔT is achieved using the Wheatstone bridge principle presented below and represented in DC mode in Figure 60. When $\Delta T=0$ the Wheatstone bridge is balanced in order to have $V=0$, and one has:

$$\frac{R_a}{R_{p0}} = \frac{R_1}{R_2} \quad (3.17)$$

Assuming then that $\Delta T \neq 0$, the bridge is unbalanced and the probe resistance varies as described by (3.14). Then the voltage drop V is:

$$V = E \left(\frac{1}{1 + \frac{R_a}{R_{p0}(1 + \alpha_R \Delta T)}} - \frac{1}{1 + \frac{R_1}{R_2}} \right) = E \left(\frac{1}{1 + \frac{R_1}{R_2(1 + \alpha_R \Delta T)}} - \frac{1}{1 + \frac{R_1}{R_2}} \right) \quad (3.18)$$

Assuming $R_1=R_2$, the temperature change of the probe is therefore:

$$\Delta T = \frac{1}{\alpha_R} \frac{4V}{E - 2V} \quad (3.19)$$

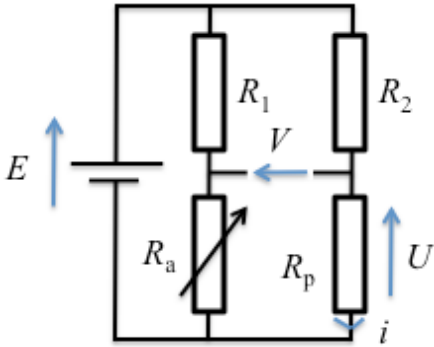


Figure 60. Working in the passive mode

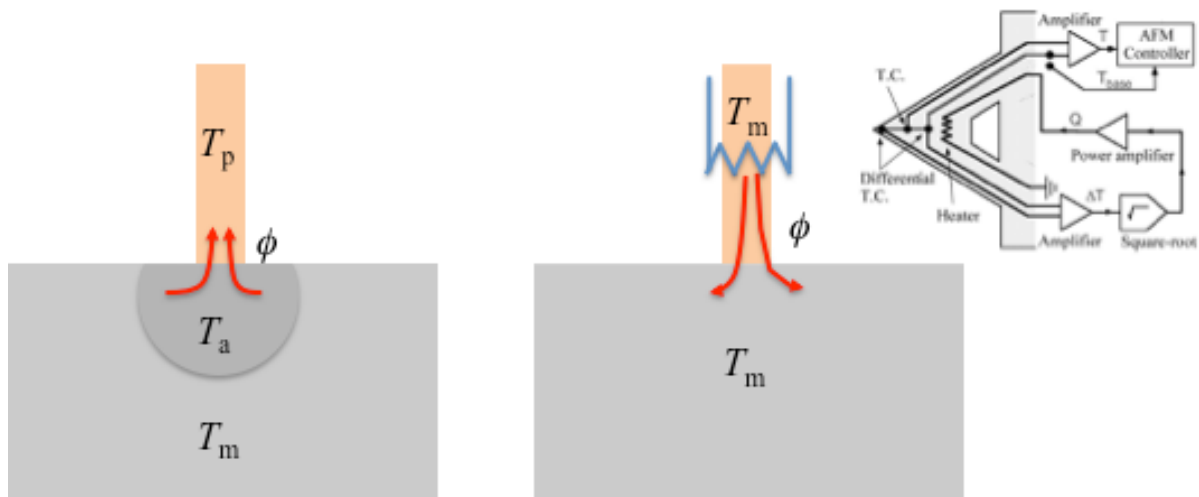


Figure 61. Surface temperature measurement a/ in passive mode (left image), the sensor affects the temperature in the medium (at the surface), b/ in active mode: the sensor is heated in order to balance the probe temperature and the surface temperature. The inset represents the probe developed by O. Nakabeppu and T. Suzuki [10].

However, we have to mention that the presented approach is not satisfying regarding the measurement of the absolute surface temperature. Indeed, making the probe in contact with the investigated surface will lead to a change of the surface temperature itself. The local surface temperature being higher than the probe temperature, a heat flux will flow from the material to the probe, involving a change in the local temperature. Two approaches are envisaged to avoid such a bias. The first one consists in solving the inverse heat conduction problem. However, this method requires knowing perfectly the thermal properties of the material and also the contact conditions [9]. The second approach has been proposed by O. Nakabeppu et al. in 2002 [10]. It

consists in supplying the probe with heat in order to make the heat flux in the probe vanished. This approach is very elegant although it requires a high cost probe to achieve this goal as presented in Figure 61. Using this second approach is considered also as entering into the active SThM mode.

3.4.2. The active mode

The active mode is used to measure thermophysical properties of materials such as thermal conductivity. However, as seen previously, it is also helpful for thermometry purpose. In this case, a larger electrical current is passed through the probe, resulting in a significant Joule heating. Part of the Joule power flows into the sample, depending on its thermal conductivity. Measuring the probe voltage monitors the probe temperature. This temperature is related to the thermal conductivity of the sample.

3.4.2.1. The continuous wave mode (DC)

In the DC mode, the Wheatstone bridge presented in Figure 10 is used to work in the controlled temperature mode. When the probe is out-of-contact from the surface, P_{out} is the Joule power dissipated within the probe. When the probe comes into contact with the sample, a quantity of heat diffuses within the sample and causes a change in the probe temperature and thus a change in the probe electrical resistance. This leads to an imbalance in the Wheatstone bridge used for the DC mode. A feedback loop, as a PID (proportional integral derivative), is thus implemented within the initial setup as presented in Figure 62. It allows the adjustment of the voltage applied to the bridge to regain its balance and thus its initial temperature. This is the constant temperature active mode. In the out-of-contact mode $V_{\text{out}}=V_{\text{shc}}$ denotes the voltage drop at the exit of the controller (applied on the bridge) and in the contact mode the Joule power dissipated by the probe is P_{in} and $V_{\text{out}}=V_{\text{sec}}$ denotes the voltage drop at the exit of the controller.

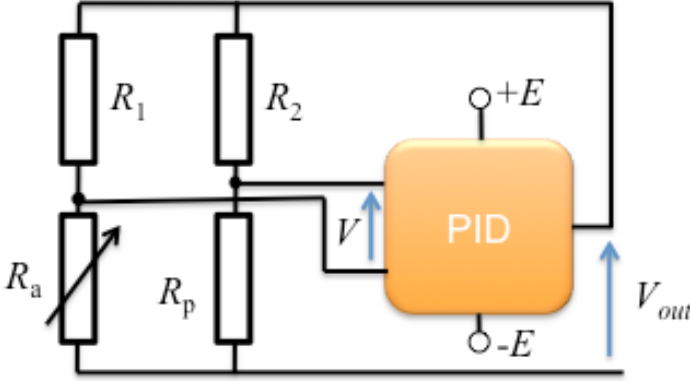


Figure 62. The controlled probe temperature active mode setup.

The relative variation in Joule heating dissipated in the Pd strip of the probe is therefore related to the voltage in both configurations as:

$$\frac{P_{in} - P_{out}}{P_{in}} = \frac{\Delta P}{P_{in}} = \frac{V_{sec}^2 - V_{shc}^2}{V_{sec}^2} = f(k_m) \quad (3.20)$$

where $f(k_m)$ is a function of the thermal conductivity k_m of the material under investigation.

Such a model will be derived in the next chapter.

It must be mentioned here that the PID time constant must be larger than the acquisition time during the scan of the surface by the probe.

3.4.2.2. The 3ω mode (AC)

The Pd strip at the tip of the probe is heated by Joule effect when an AC current generator supplies the current:

$$i = i_0 \cos(\omega t) \quad (3.21)$$

The generated heat power (heat flux) is thus:

$$\begin{aligned} P &= R_p i^2 = R_p i_0^2 \cos^2(\omega t) \\ &= \frac{R_p i_0^2}{2} (1 + \cos(2\omega t)) = P_{2\omega} (1 + \cos(2\omega t)) \end{aligned} \quad (3.22)$$

In this relation, R_p is the electrical resistance of the strip between the two inner pads (V^+ , V^-) whose expression is given by (3.14). The power P is the heat flux generated by the Pd metallic

strip. Assuming the disturbance is small enough to ensure the linear heat transfer in the material, the average temperature rise of the strip is expressed as:

$$\Delta T = \Delta T_0 + \Delta T_{2\omega} \cos(2\omega t + \phi) \quad (3.23)$$

Therefore, the voltage measured between the two pads (V^+ , V^-) is:

$$\begin{aligned} V &= Ri = R_0 (1 + \alpha_R \Delta T) i_0 \cos(\omega t) \\ &= R_0 (1 + \alpha_R (\Delta T_0 + \Delta T_{2\omega} \cos(2\omega t + \phi))) i_0 \cos(\omega t) \\ &= R_0 i_0 \cos(\omega t) (1 + \alpha_R \Delta T_0) + \frac{\alpha_R R_0 i_0}{2} \Delta T_{2\omega} \cos(\omega t + \phi) + \frac{\alpha_R R_0 i_0}{2} \Delta T_{2\omega} \cos(3\omega t + \phi) \\ &= V_0 \cos(\omega t) (1 + \alpha_R \Delta T_0) + V_{1\omega} \cos(\omega t + \phi) + V_{3\omega} \cos(3\omega t + \phi) \end{aligned} \quad (3.24)$$

The first term of the previous equation gives no information on $\Delta T_{2\omega}$. In the second term, $\Delta T_{2\omega}$ appears but it is at the same frequency as in the first term, making the discrimination of $\Delta T_{2\omega}$ impossible from the Lock-in. Only the third harmonic permits to measure the amplitude and the phase of $\Delta T_{2\omega}$ as:

$$\Delta T_{2\omega} = \frac{2}{\alpha_R R_0 i_0} V_{3\omega} = \frac{2}{\alpha_R} \frac{V_{3\omega}}{V_0} = f(k_m) \quad (3.25)$$

As previously, $f(k_m)$ is a function of the thermal conductivity k_m of the material under investigation. Such a model will be derived in the next chapter. The main difficulty to overcome in the method is the measurement of $V_{3\omega}$ that is very low compared to V_0 , which implies the use of the differential stage, presented previously, that allow decreasing the first harmonic before entering a lock-in amplifier seeking the third harmonic of the signal.

We assume in this derivation that the distance between the two measuring points of $U_{3\omega}$ is small enough that it may be considered a uniform temperature between these points for all the investigated frequency.

There is no need to have a control on the probe temperature in the present case although it was proposed such an implementation by [11].

Since we have:

$$\left. \begin{aligned} \Delta T_{2\omega} \propto P = \frac{Ri^2}{2} \\ Ri^2 \propto \frac{V_{3\omega}}{Ri} \end{aligned} \right\} \Rightarrow V_{3\omega} \propto i^3 \quad (3.26)$$

Therefore, we can check in a very simple way that the experimental setup works properly by measuring the third harmonic of the voltage drop as a function of the current for at least two different frequencies. This operation is done obviously when the probe is out-of-contact.

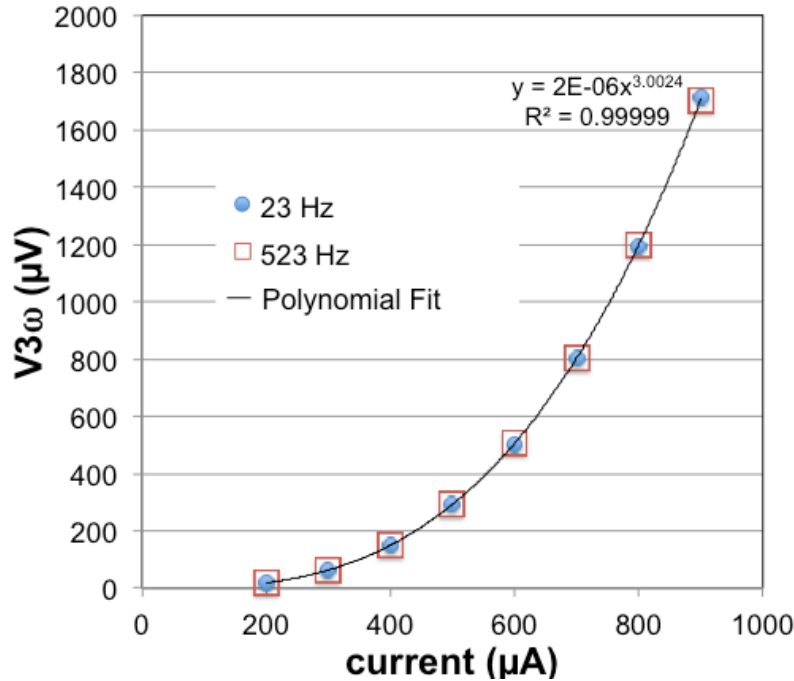


Figure 63. Measured $V_{3\omega}=f(i)$ when the probe is out-of-contact.

Measurements have been reported in the Figure 63. The first observation is that the measurement does not depend, as expected, of the frequency value. Moreover, we identified the polynomial fit and we found that:

$$V_{3\omega} = 2 \times 10^{-6} i^{3.0024} \quad (3.27)$$

This result shows that we retrieve well the theoretical expectation with more than 99% accuracy.

We also check the linearity of the probe by increasing the currents passing through the thermoresistive element and measuring $V_{3\omega}$ and the phase ϕ .

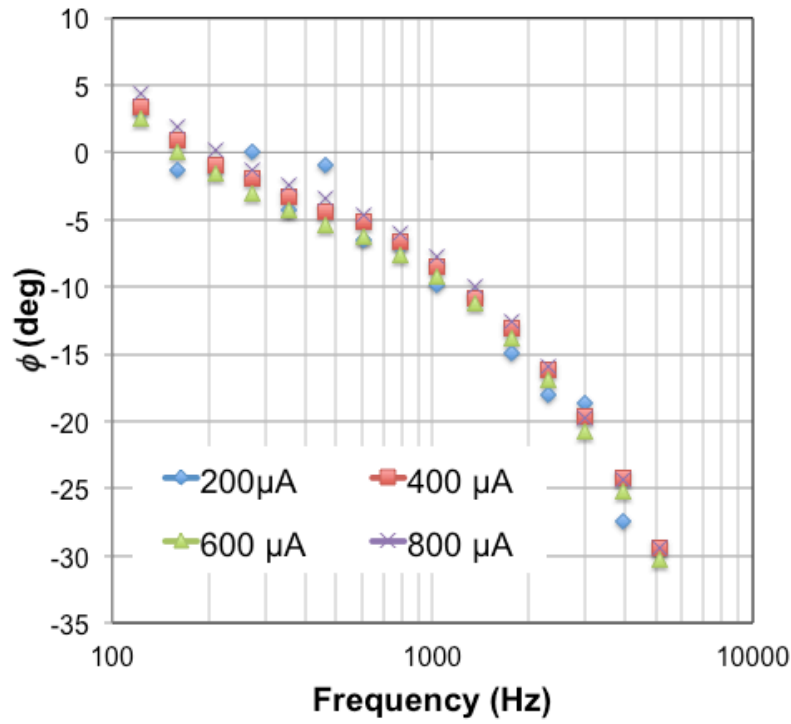
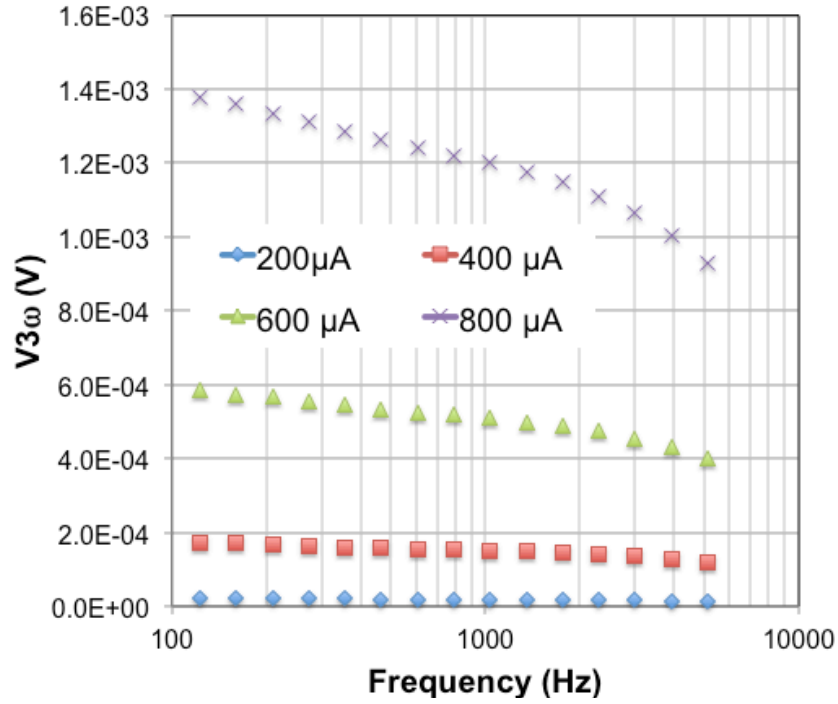


Figure 64. Measured amplitude and phase according to the frequency when the probe is out-of-contact at different values of the current.

We found that $V_{3\omega}(400\mu A)/V_{3\omega}(200\mu A) = 8 \pm 0.3$, $V_{3\omega}(600\mu A)/V_{3\omega}(400\mu A) = 3.37 \pm 0.02$ and $V_{3\omega}(800\mu A)/V_{3\omega}(600\mu A) = 2.35 \pm 0.02$ whatever the frequency value. In addition, it is clear

that the phase does not vary significantly when changing the value of the current. It is noticed however that the values we measured for $i=200 \mu\text{A}$ are very low, the signal being drowned within the noise. It is thus recommended to work with current from $400 \mu\text{A}$ up to $800 \mu\text{A}$. Finally, we can conclude on the linearity of the probe within this range of current.

3.5. Probe coefficient of resistance measurement

3.5.1. Experimental setup for the calibration

In his thesis, E. Puyoo [15] placed the probe in the oven whose temperature was raised to 100°C . Once this temperature was reached, he stopped the heating and allowed chamber to thermalize to room temperature gradually. During this phase, he measured the probe resistance and the temperature within the oven collected at an interval of 5 seconds. Our basic principle in obtaining the coefficient of thermal resistance (α_R) remains very similar. The probe and thermometer are placed very close to each other inside a compact low temperature thermostat (in our case, MGW LAUDA RC 20, *see* Figure 65) connected to electrical resistance and temperature measurement devices respectively. The current is then slowly altered in the thermostat. There is hence a change in the temperature which is recorded by the thermometer and this also changes the temperature of the probe, leading to a change in the resistance of the probe. With the data obtained, a graph can be plotted with the variation of probe resistance due to temperature to achieve the coefficient of resistance.

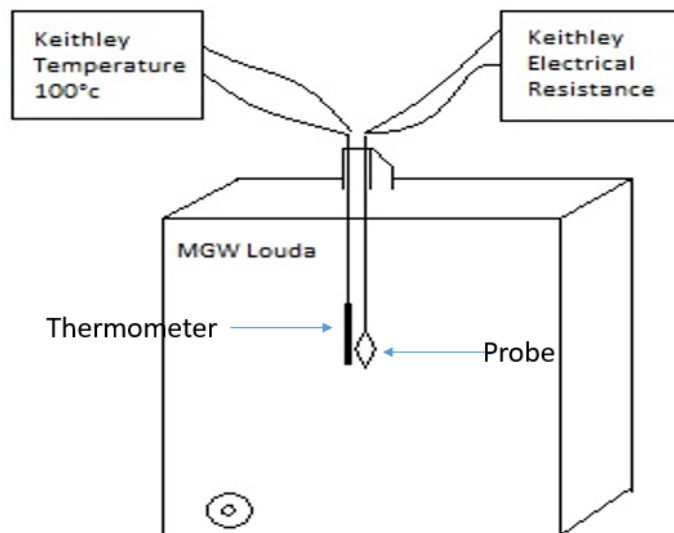


Figure 65. Experimental setup for measuring probe coefficient of resistance.

3.5.2. 2-point probe

Our 2-point probes have been provided by three different companies: NanoAndMore, Anasys and NT-MDT. These different probes have the same geometry but with different physical and geometric nature of the cantilever. The probes provided by NanoAndMore and Anasys have a cantilever made of Silicon Nitride (Si_3N_4) with a thickness of around $0.4\mu\text{m}$ whereas the fabrication done by NT-MDT consists of a Silicon dioxide (SiO_2) cantilever with an approximate thickness of $1\mu\text{m}$. The biggest drawback of using a 2-point probe for calibration is that the probe is prone to mechanical damage and cannot be reused. Even though the probe or cantilever changes, the values obtained from one probe calibration remains very similar to the ones obtained from others and hence, the same data can be reused for different model. We reported the measured values of the resistance in Figure 66 and Figure 67. It is obtained a linear trend that leads to the thermal resistance of the probe at the ambient as well as the TCR from the linear regression.

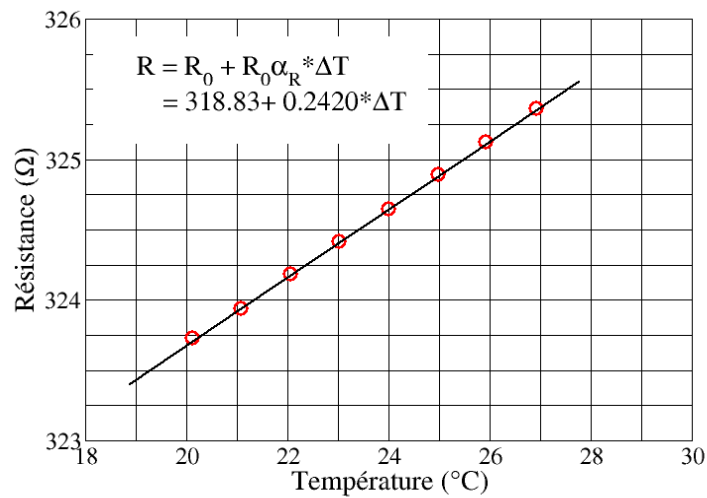


Figure 66. Resistance vs. Temperature for Thermal Probe given by NanoAndMore and Anasys

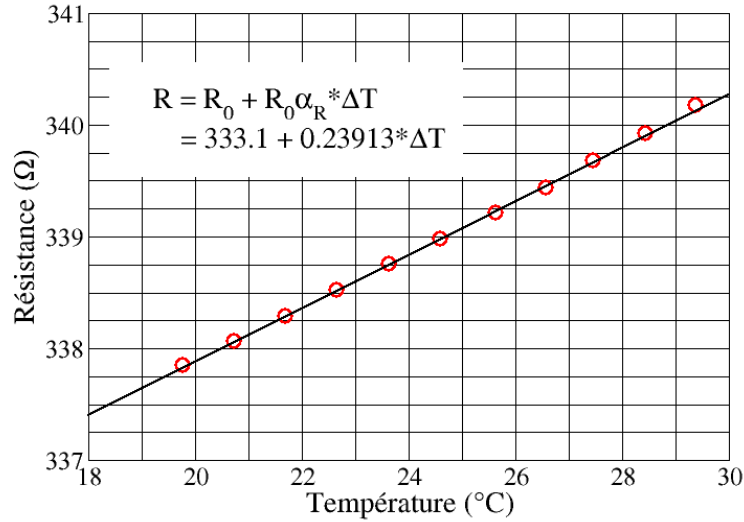


Figure 67. Resistance vs. Temperature for Thermal Probe given by NT-MDT

However, the use of NiCr current limiters doesn't allow us to directly estimate the thermal coefficient of thermo-resistive element (Pd), because these limiters are actually placed in series thereby generating heat and therefore a 3ω signal. To know the contribution of these current limiters, we deliberately short-circuited by using a conductive epoxy at the tip Pd probe (this leads to damage the probe definitively making it not usable anymore). Therefore we can state that the variation of the total electrical resistance of the probe is the sum of the variation of the electrical resistance of the NiCr current limiters and that of the Pd strip as:

$$R_0 + R_0 \alpha_R \Delta T = R_{NiCr} + R_{NiCr} \alpha_{NiCr} \Delta T + R_{Pd} + R_{Pd} \alpha_{Pd} \Delta T \quad (3.28)$$

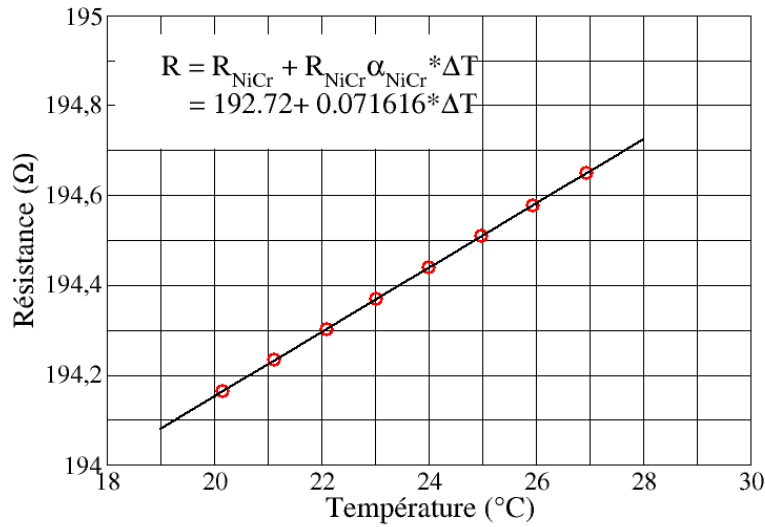


Figure 68. Resistance vs. Temperature using Current Limiters given by NanoAndMore et Anasys

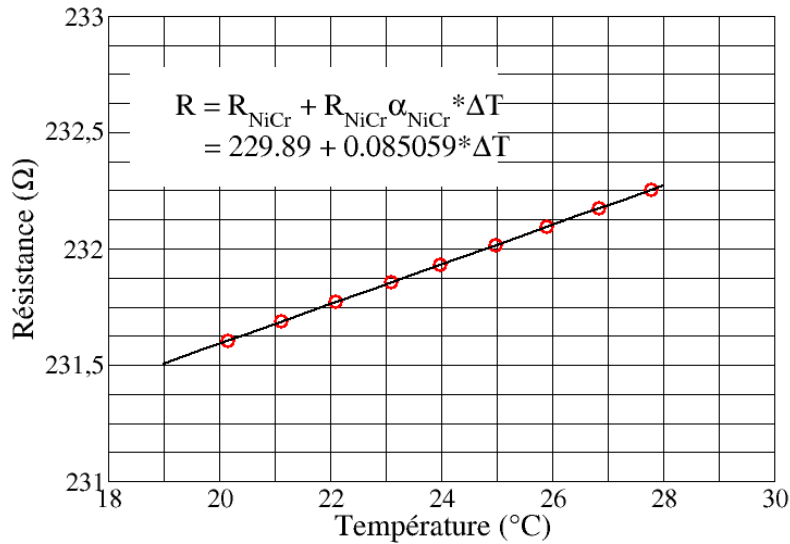


Figure 69. Resistance vs. Temperature using Current Limiters given by NT-MDT

We repeated then the calibration stage in tis new configuration. Figure 68 and Figure 69 give us the variation of the electrical resistance + R for the current limiters as a function of temperature in case of the three probes. At the ambient (20°C), the probes fabricated by NanoAndMore and Anasys have 192 Ω as the resistance for the current limiters (R_{NiCr}) and the Pd resistance (R_{Pd}) of 126 Ω whereas the probes fabricated by NT-MDT have a value of 229 Ω for the current limiters

and 101 Ω for the Palladium. Using the equation (3.28), we can obtain the coefficient of resistance of the Pd as:

$$\alpha_{Pd} = (R_0 \alpha_R - R_{NiCr} \alpha_{NiCr}) / R_{Pd} \quad (3.29)$$

Hence, for the probes fabricated by NanoAndMore and Anasys we found:

$$\alpha_{Pd} = 1.3 \times 10^{-3} \text{ K}^{-1} \quad (3.30)$$

and for the probes fabricated by NT-MDT we have:

$$\alpha_{Pd} = 1.6 \times 10^{-3} \text{ K}^{-1} \quad (3.31)$$

Table 8. Comparison of Palladium Thermal Coefficient of Resistance found in our work with previously published values.

Thermal Coefficient Resistance of Palladium (α_{Pd})	Associated Work	Manufacturer
$(1.3-1.6) \times 10^{-3} \text{ K}^{-1}$	Present work	Anasys Instruments & NanoandMore
$1.2 \times 10^{-3} \text{ K}^{-1}$	Puyoo et al. [12]	Anasys Instruments
$1.37 \times 10^{-3} \text{ K}^{-1}$	A. Assy et al. [13]	Kelvin Nanotechnology

The Table 8 proves that the value of the thermal coefficient resistance (TCR) that we have obtained using the Anasys Instruments probe is similar to the values found in literature. It is to be noted that Kelvin Nanotechnology is the provider of thermal probes for Anasys Instruments and NanoAndMore as well. Therefore we can say that the method of fabrication of the probe and the quality of material used remains more constant.

When we look into the TCR of the probe furnished by NT-MDT, the value is a little lower compared to the other. This can be due to the method of fabrication, the electrical connection and/or the process of deposition.

3.5.3. 4-point probe

The 4-point probe allowed us to obtain the coefficient of resistance without causing damage to the probe and thereby allowing the application of the same probe to perform experiments. This makes sure that the same coefficient of thermal resistance is maintained for each test, when

using the exact same probe, leading to more accurate values for our thermal characterization experiments.

Figure 70 reports the measured variation of the electrical probe resistance as a function of temperature during the calibration experiment.

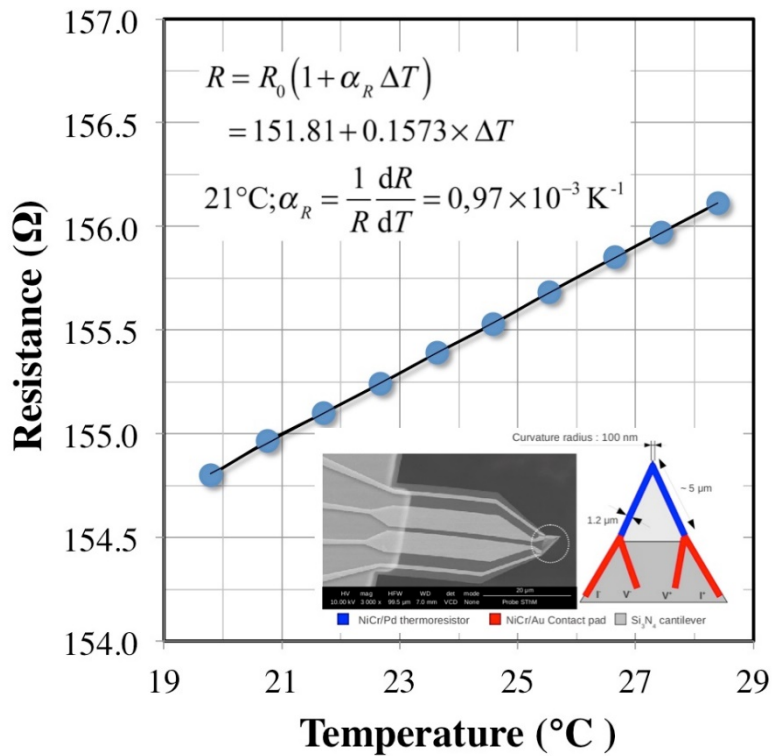


Figure 70 Measurement of the 4-point probe electrical resistance $R(T)$ as a function of temperature. Extraction of the thermal coefficient α_R . Standard deviation is less than 0.5%

We therefore obtained the electrical resistance of the probe at the ambient as 154.5Ω and the TCR obtained in this case is $9.7 \times 10^{-4} \text{ K}^{-1}$. This value is significantly lower than that obtained for the 2-point probes. We can wonder why such a gap occurs between those two different types of probes and even more with the value of the TCR that is reported as $3.8 \times 10^{-3} \text{ K}^{-1}$ for bulk Pd. To our opinion this change comes from the fact that a NiCr thin layer, deposited prior to the Pd layer, participates also in the global TCR. On the other hand, the connections with the Au strips, which make the current flowing the circuit, have also a role in the global TCR. It is found in the literature that $\alpha_R(\text{Au}) = 3.4 \times 10^{-3} \text{ K}^{-1}$ (very close to the value for bulk Pd) and that

$\alpha_R(\text{NiCr}) = 4 \times 10^{-4} \text{ K}^{-1}$. It is therefore very clear that the NiCr is responsible for the decrease of the measured TCR for the probes regarding the value of the Pd bulk.

3.6. Sensitive parameters (force contact, probe motion speed, integration time, acquisition time)

3.6.1. Contact force

The contact force is of immense importance when performing experiments using scanning thermal microscopy. The contact force is the force applied by the probe on the surface of the sample when in contact. This contact force allows the probe to maintain a constant contact with the specimen while it moves across the surface in a raster pattern. There are several vibrations that are present while the experiments are being performed. One of the most important is maybe that related with the frequency current flowing the thermoresistive element (Pd). Indeed, we observed that it was barely impossible to approach the tip to the surface when the current is injected. Obviously higher is the current amplitude; higher are the vibrations of the probe. Those vibrations are clearly related to the thermo-mechanical effects. The Joule heating of the Pd strip at frequency 2ω induces a differential deformation since the thermal expansion coefficient for Pd is strongly different from that of the cantilever (SiO_2 or Si_3N_4). Indeed we found that $\alpha_T(\text{Pd}) = 11.8 \times 10^{-6} \text{ K}^{-1}$, $\alpha_T(\text{SiO}_2) = (0.55 - 0.75) \times 10^{-6} \text{ K}^{-1}$ and $\alpha_T(\text{Si}_3\text{N}_4) = 3.3 \times 10^{-6} \text{ K}^{-1}$. Apart from the internal vibrations generating from the mechanism of the instruments, there are external vibrations that come into picture. Although we utilize vibration isolation units, it is often not sufficient and effective enough to negate the vibrations completely. Hence a constant and uniform contact force becomes essential. The contact force, in principle, should not exceed 15 nN. A higher force might cause damage to the probe itself rendering it useless and/or providing erroneous results. Moreover, applying a very low force (less than 2nN) might cause the probe to get detached from the surface of the sample. Hence utilizing a proper contact force based on the disturbances and vibrations form a key part of successful experimentation using scanning thermal microscopy.

We performed an experiment when the probe is in static contact with a surface of graphite. We increased continuously the acting force on the cantilever, from 5 nN up to 20 nN, and we recorded the amplitude ($V_{3\omega}$) and phase (ϕ) according to the frequency of the current. The results

are reported in Figure 71 for both quantities. We observe that there is no significant difference in that configuration. However, the surface hardness being of first importance in that case, difference can occur, meaning that the contact area between the probe and the surface can increase as the force increases. However this point will be discussed later in more details at chapter 5.

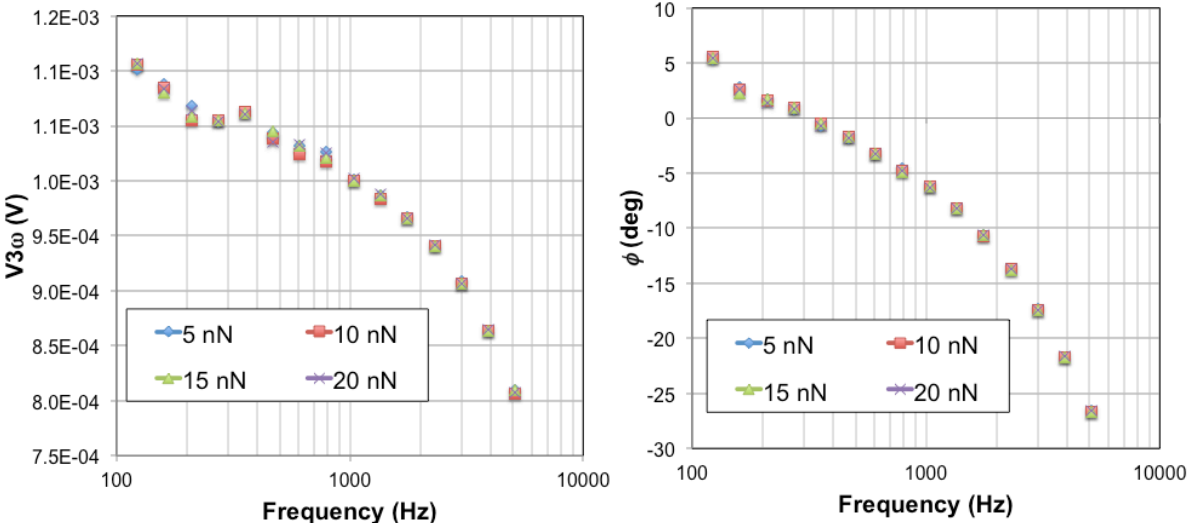


Figure 71. Influence of the force acting on the cantilever when the probe is in static contact with the surface.

3.6.2. Scan velocity, Acquisition Time and Integration Time

The scan velocity of the probe, the acquisition time and the integration time are quantities strongly related. The scanning velocity as well as the acquisition time are parameters linked with the control of the AFM whereas the integration time is linked to the lock-in and is referred as the time constant. In order to better understand the way it works, let’s consider the Figure 72 that is a scheme of the scanning process. The probe scans first one line from left to right (or reverse) and then to pass on the other line.

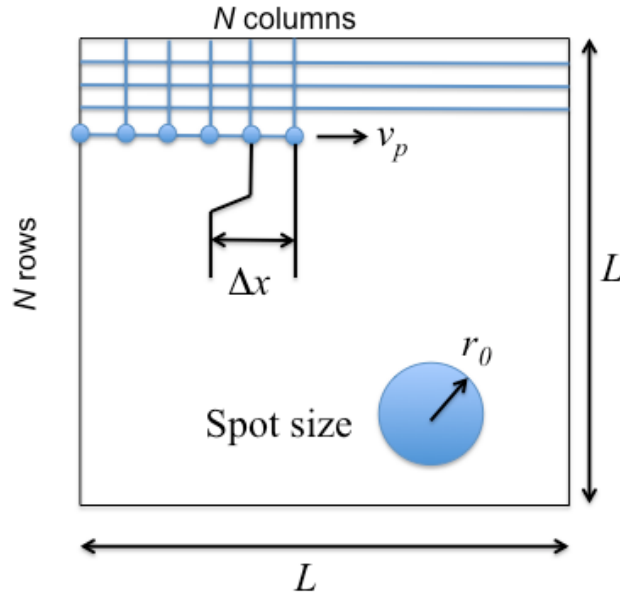


Figure 72. Schematic diagram of the surface scanning process by the probe.

The acquisition time is dependent on the number of experimental points on the surface of the sample. If L is the length of the investigated area (mandatory square), and N is the number of columns/rows that has been chosen, then the sampling interval is:

$$\Delta x = \frac{L}{N} \quad (3.32)$$

The velocity of the probe is defined as the time τ required for the probe to complete one row and it is expressed in sec/line. Since the number of columns is the same that the number of rows, the acquisition time is:

$$\Delta \tau = \frac{\tau}{N} \quad (3.33)$$

The time constant T is the time required for the lock-in to perform the average measurement of the amplitude ($V_{3\omega}$) and phase (ϕ). This value is chosen in order for the probe to reach the stationary behaviour at each location on the surface at the considered frequency of the function generator. It can be chosen according to the frequency f of the function generator as $T = 10/f$. Therefore, in order to have consistent measurement with the model that will be described later on chapter 4, one must respect the condition:

$$\Delta\tau \geq T \quad (3.34)$$

For example, let's consider the following parameters: $L = 50 \mu\text{m}$, $N = 256$ points and $f = 1 \text{ KHz}$. The time constant can be then chosen as $T = 30 \text{ msec}$. Therefore, the minimal value for the acquisition time is $\Delta\tau = 30 \text{ msec}$ and the time required to scan one line is $\tau = N \Delta\tau = 256 \times 0.03 = 7.78 \text{ sec}$ (meaning that the time required to perform the full image scan is about 33 min). The sampling interval is $\Delta x = L/N = 0.19 \mu\text{m} = 190 \text{ nm}$. This value is quite close to the spot area, i.e., the contact area between the probe and the surface, which is $2 r_0$ in diameter. Indeed, as showed in chapter 5 and 6, the value of r_0 can vary from tenths of nanometers up to one hundred nanometers according to the sample and the experimental conditions.

Hence, it is clear that if one decreases the length of the scan area, it is judicious to decrease also the value of N . For example, let's consider the following parameters: $L = 500 \text{ nm}$, $N = 128$ points and $f = 1 \text{ KHz}$. The time constant is still as $T = 30 \text{ msec}$ and therefore, the minimal value for the acquisition time is still $\Delta\tau = 30 \text{ msec}$. The time required to scan one line is $\tau = N \Delta\tau = 128 \times 0.03 = 3.84 \text{ sec}$ (meaning that the time required to perform the full image scan is about 8 min). However, the sampling interval is $\Delta x = L/N = 3.9 \text{ nm}$ that is really low compared to the classical value for $2 r_0$. This will lead, as represented in Figure 73, to a high overlap of the surface at each acquisition time. This will be very interesting with the perspective of the characterization of heterogeneities whose characteristic dimension is lower than the spatial resolution of the probe.

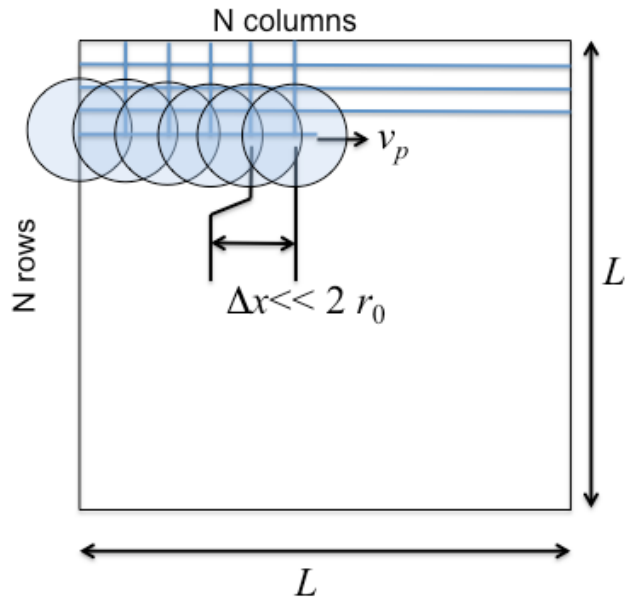


Figure 73. Schematic diagram of the surface scanning process by the probe in the configuration of spot overlapping.

3.7. Influence of the laser

As revealed in some papers, the laser that probes the cantilever deformation during the scan, could also contribute in the heating of the probe, modifying therefore the measured temperature. In order to check this possible influence, we measured the probe temperature as well as the phase with and without the presence of the laser beam on the probe. The results are reported in Figure 74. It can be concluded that the laser does not contribute in both measurement on the frequency range of interest for future applications presented in this work.

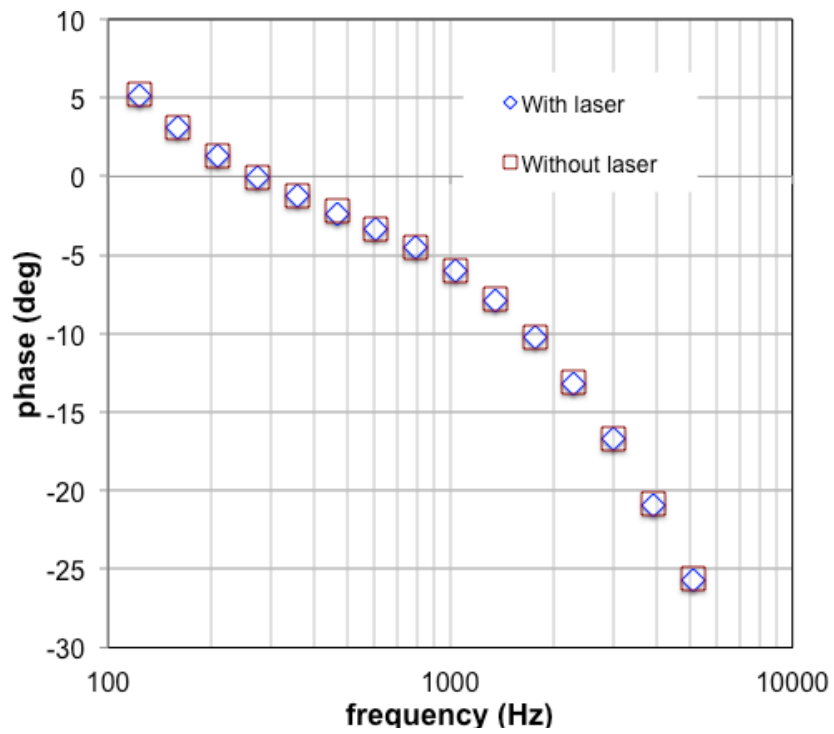
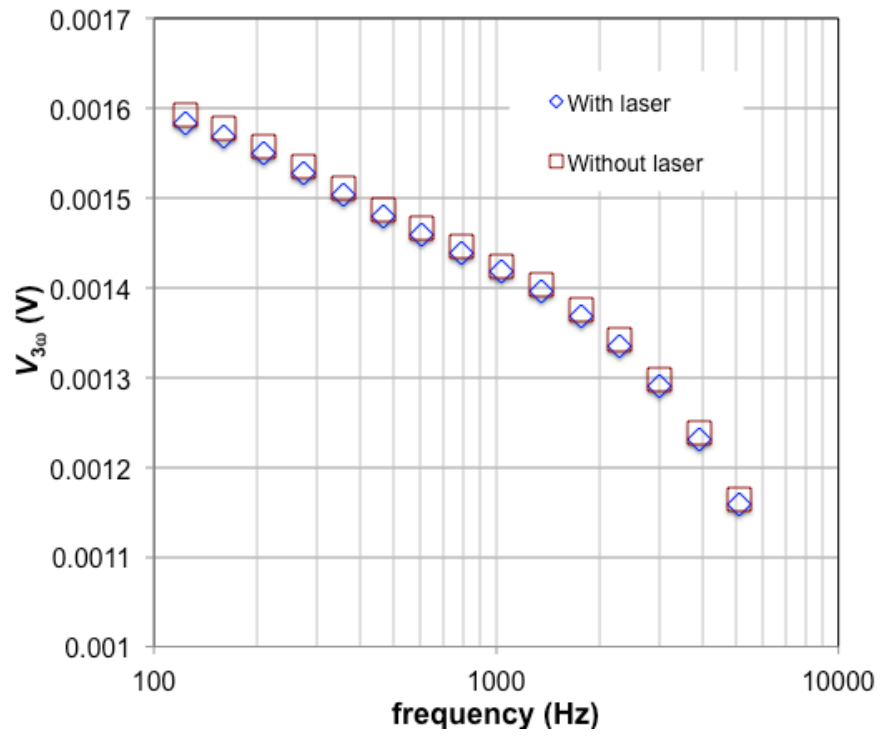


Figure 74. Measured probe temperature and phase with and without the laser beam focused on the probe.

3.8. Conclusion

In this chapter, we have put all our focus on the experimental setup. We have successfully defined the key instruments necessary to accomplish our experiments. These instruments along with the surrounding conditions have an effect on the sensitive parameters related to the experimental results. We have also tried to define these parameters. Moreover, we have also discussed about the types of thermoresistive probes we have utilized and the working modes they have been used in. Having the knowledge of the probe, we have also successfully determined the electrical resistance as well as the coefficient of the probe electrical resistance. It must be said that the two probes (2-contact and 4-contact) behave exactly in the same way with respect to the heat transfer since they have both the same geometry and the same constitutive materials. In addition, the thermoresistive element is exactly the same, regarding the characteristic dimensions and material (Pd). Therefore, the only difference between the two probes stands on the calibration process that is easier with the 4-contact probe than with the 2-contact one since the current limiters did not act anymore with the 4-contact probe. On the other hand, it must be also clearly said here that the 4-contact mask for the 3ω technique with thin film is required to avoid the 3D effects at the two end of the wire. In the present configuration, this has no effect since only the tip of the probe contacts the investigated surface. The force acting on the cantilever did not seem having an impact on the measured amplitude and phase in a reasonable range. The minimum force is chosen to overcome the effects of the probe vibrations that are related to the periodic current passing through the thermoresistive element. On the other hand we have also clearly demonstrated the need to choose accurately the probe velocity according to the spatial resolution and the time constant of the lock-in. It has been also shown the effect of the spot overlapping that leads to increase the spatial resolution of the probe. With the knowledge of all the factors that effect and have an influence on the experimental procedure we can now move onto the modeling phase. In the next chapter, we will discuss about the thermal model that describes the heat transfer within the experimental configuration.

3.9. Reference

- [1] P. W. Hawkes, *Advances in Imaging and Electron Physics*, Elsevier 2015.
- [2] Yunfei Ge, *Quantitative measurement using scanning thermal microscopy*, PhD thesis, 2016

- [3] P. S. Dobson, J. M. R. Weaver and G. Mills, *New Methods for Calibrated Scanning Thermal Microscopy (SThM)*, Sensors, 2007 IEEE, 708-711.
- [4] A. Saci, J.-L. Battaglia, A. Kusiak, R. Fallica, and M. Longo, *Thermal conductivity measurement of a Sb_2Te_3 phase change nanowire*, Applied Physics Letters **104**, 263103 (2014).
- [5] A. Saci, J.-L. Battaglia, and I. De, *Accurate New Methodology in Scanning Thermal Microscopy*, IEEE Transactions on Nanotechnology **14** (6), (2015), p. 1035-1039.
- [6] Standard Research Systems, MODEL SR830: DSP Lock-in Amplifier, 2011.
- [7] Accurion, Principles of Halcyonics Active Vibration Isolation Technology.
- [8] Accurion, Workstation Series.
- [9] S. Gomès, A. Assy and P.-O. Chapuis, *Scanning Thermal Microscopy: A review*, Phys. Status Solidi A **212** (3), (2015), p. 477–494.
- [10] O. Nakabeppu and T. Suzuki, *Microscale Temperature Measurement by Scanning Thermal Microscopy*, Journal of Thermal Analysis and Calorimetry **69** (2002), p. 727–737.
- [11] J. Lee, Y. B. Gianchandani, *A Temperature-Dithering Closed-Loop Interface Circuit for a Scanning Thermal Microscopy System*, J. of Microelectromechanical Systems **14**, (2005), p. 44-53.
- [12] E. Puyoo, S. Grauby, J.-M. Rampnoux, E. Rouvière and S. Dilhaire, *Thermal exchange radius measurement: Application to nanowire thermal imaging*, Review of Scientific Instruments **81**, 073701, (2010).
- [13] A. Assy and S. Gomès, *Heat transfer at nanoscale contacts investigated with scanning thermal microscopy*, Applied Physics Letters **107**, 043105 (2015).
- [14] S. M. Shivaprasad and M. A. Angadi, *Temperature coefficient of resistance of thin palladium films*, J. Phys. D: Appl. Phys. **13**, (1980), L171-2.
- [15] E. Puyoo, *Caractérisation thermique de nanofils de silicium pour des applications à la thermoélectricité*, Ph.D. thesis, University of Bordeaux 1, Nov 2010.

4. Chapter 4 – HEAT TRANSFER MODEL

4.1. Introduction

As we showed in the chapter 2, the heat transfer model within the SThM experiment has been the subject of already intensive work. Our goal in this chapter is to show that a pragmatic and efficient way to model the heat transfer in such a complex experiment can be done by making a parsimonious choice of the main parameters. Indeed, it appears that the most efficient way, with respect to the identification of thermal properties of an investigated material is to:

1. Identify the frequency dependent transfer function of the probe from measurements of the amplitude and the phase when the probe is out-of-contact from the surface;
2. Merge the entire physical phenomena that occur at the interface between the probe and the surface in a single thermal boundary resistance;
3. Use either an analytical or discrete solution for the heat transfer within the investigated material according to its geometry and to the location of the probe on the surface;

This methodology aims to finally identify the entire unknown within such a complex problem.

Point 1 is classically used I system identification theory. It has been used in thermal sciences in very different field of applications. Such approach can be based on experimental measurements only (non parametric methods) or on the use of a specific formulation of the transfer function relating the heat flux generated within the Pd strip of the probe to the average temperature of the Pd strip. Since we used the 3ω method, the transfer function can be obtained by varying the frequency in the working range of the probe. However, we will also propose to identify the probe behaviour from a structure based on non-integer derivatives that account for the semi-infinite behaviour of the probe. As, we will show, the system identification approach is much more accurate and reliable to the use of Finite Elements Analysis or approximate methods since it does not assume any approximation regarding the complex geometry of the probe and it does not require knowing the thermal properties of the constitutive materials of the probe, including the thermal contact resistances between the different parts. The main drawback in the use of such an

approach is that the probe has to be implemented during the surface investigation in the same environmental conditions that those met during the system identification.

In point 2, we assume that the heat transfer between the probe and the surface does not involve any capacitive effect, leading to consider that they can all be merged in a unique thermal resistance. This is indeed true for the heat transfer by conduction and radiation in the air and for that through the water meniscus and the rough surface of the probe and the surface. This allows us to limit the number of unknown parameters in this area.

In the point 3 we will show that both analytical and discrete methods can be used to achieve the identification of the unknown parameters in a SThM experiment. Indeed, we will show that locating the probe in specific area of the investigated surface and varying the frequency of the excitation will lead to identify well the thermal conductivity of the material. In that configuration, an analytical solution can be implemented. On the other hand, the material thermal conductivity and thermal contact resistance at the interface between the probe and the surface can be identified by sweeping the probe on the surface. However, in that case, we will need to implement a discrete method based on the finite element analysis.

In a first step, we propose to use the thermal impedances formalism in order to propose a model for the heat transfer within the SThM experiment. Then, we propose an analytical expression for the thermal impedance of the investigated material, which assumes a semi-infinite behaviour. Since those expressions are well-known they are only recalled in the appendix at the end of this chapter. The use of the finite element method is then presented. This method will be very efficient when application involves a complex 3D geometry that does not permit applying the classical integral transforms. However, the investigated medium behaves as semi-infinite one according to the frequency of the excitation. We will thus present a very efficient tool in FEA that accounts with such behaviour. Finally, we present three different approaches for the heat transfer model within the probe. The first uses the FEA method, the second is based on approximations of the probe geometry and the last one deals with the system identification approach that will be used during the applications. However, the three approaches are closely related since the two first ones explain well the structure of the identified model of the probe.

4.2. General formulation of the heat transfer model

4.2.1. The use of thermal impedances network

Heat transfer in the probe and the investigated material in the contact mode configuration is described in the inset of Figure 76 using the formalism of thermal impedances [1]. The average temperature $T_p(\omega_2)$ of the Pd strip is related to the total heat flux $P(\omega_2)$ generated by the Joule effect as $T_p(\omega_2) = Z_T(\omega_2)P(\omega_2)$, with $1/Z_T(\omega_2) = 1/Z_p(\omega_2) + 1/(R_c + Z_m(\omega_2))$. In this relation, $Z_p(\omega_2)$ denotes the thermal impedance of the probe, $Z_m(\omega_2)$ denotes the thermal impedance of the material, and R_c is the thermal contact resistance at the interface between the probe and the sample. The thermal resistance R_c accounts for several contributions:

- The solid-solid contact resistance including both the heat flux constriction resistance R_{cp} at the probe tip and the resistance R_{ph} related to phonon scattering at the interface between the sample and the probe. Both of them have been described in chapter 2;
- The heat transfer by diffusion and radiation in the air surrounding the contact, also presented in chapter 2, leads to the resistance R_{air} ;
- The heat transfer through the water meniscus that cannot be avoided when working under atmospheric or controlled (argon/nitrogen/primary vacuum) atmosphere that has been presented in chapter 2. This will lead to the thermal resistance R_{wm} ;
- As we will also demonstrate in the following, a change in the isothermal at the probe tip occurs when passing from the out-of-contact to the contact mode. Since we will use the identified model of the probe from out-of-contact mode, the resistance at the interface between the probe and the surface will also account for the isothermal field change using a resistance R_{ct} .

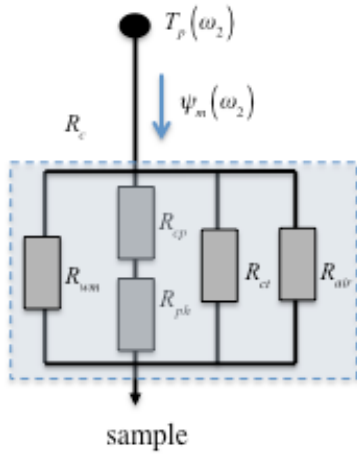


Figure 75: thermal contact resistance at the interface between the probe and the investigated surface.

Therefore, the total contact resistance R_c can be viewed as the arrangement of previous described contributions as represented in Figure 75.

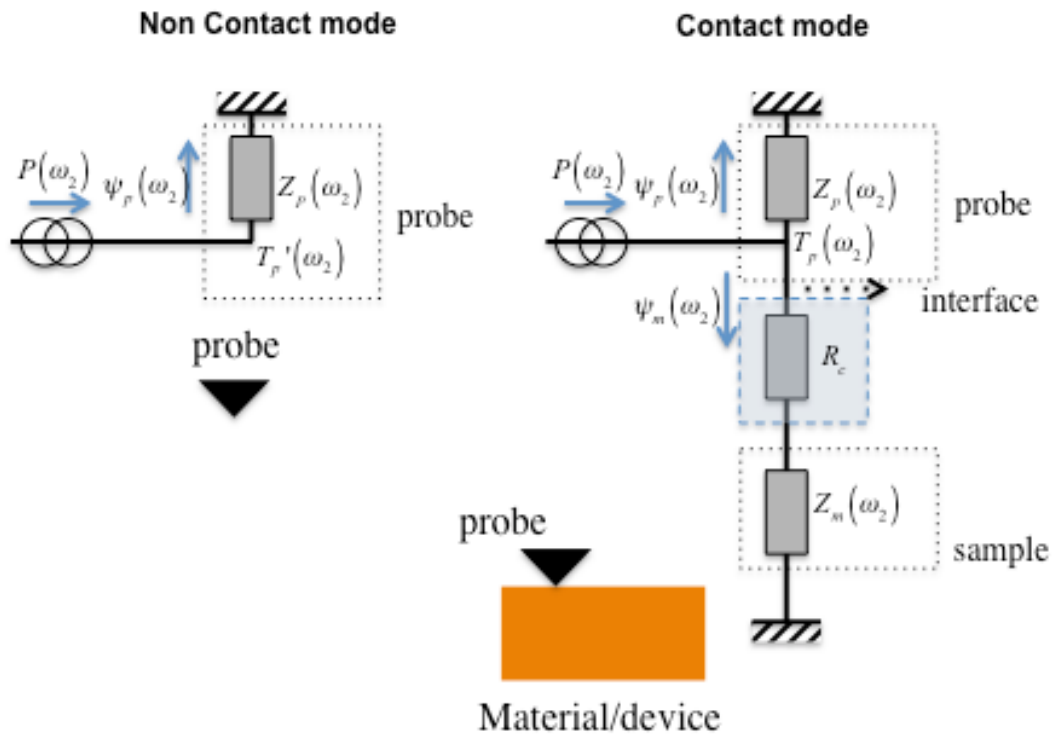


Figure 76: schematic representation of the heat transfer in the probe for the contactless and contact modes.

By referring to Figure 76, one obtains in the out-of-contact mode:

$$Z_p(\omega_2) = \frac{T_p'(\omega)}{\psi_p(\omega)} \Rightarrow \|Z_p(\omega)\| = \frac{\|T_p'(\omega)\|}{P_0} \quad (4.1)$$

With, as demonstrated in chapter 3, $P_0 = R_0 i_0^2 / 2$, where R_0 is the Pd strip electrical resistance at the ambient and i_0 is the *rms* current passing through the Pd strip.

In the contact mode, figure 1 shows that one has:

$$P_0 = \|\psi_p(\omega)\| + \|\psi_m(\omega)\| \quad (4.2)$$

Using this last relation with the expression (4.1) for the out-of-contact mode, this leads to:

$$\|\psi_m(\omega)\| = P_0 - \|\psi_p(\omega)\| = P_0 - \left\| \frac{T_p(\omega)}{Z_p(\omega)} \right\| = P_0 - P_0 \left\| \frac{T_p(\omega)}{T_p'(\omega)} \right\| = \beta(\omega) P_0 \quad (4.3)$$

In this relation, $\beta(\omega) = 1 - \|T_p(\omega)/T_p'(\omega)\|$ denotes the fraction of the heat flux that enters the material. It can be thus determined from experimental data only.

4.2.2. Link with experimental measurements

From previous relations, we obtain the expression for the amplitude $\|T_p(\omega)\|$ and the phase $\delta(\omega)$ for the measured probe temperature in the contact mode as:

$$\|T_p(\omega)\| = \left\| \frac{P_0}{1/Z_p + 1/(R_c + Z_m)} \right\| \quad (4.4)$$

And,

$$\delta(\omega) = \arg\left(\frac{P_0}{1/Z_p + 1/(R_c + Z_m)} \right) \quad (4.5)$$

Those relations will be faced to the measured temperature and phase in order to achieve the seek parameters (that will be clarified within the sensitivity analysis presented after). It must be noted that in DC mode, the phase vanishes, and the thermal impedances Z_p and Z_m in relation (4.4) are replaced by the pure resistances R_p and R_m respectively. In that case, we also find easily that the

relative change in power required keeping the probe temperature constant from the out-of-contact mode and the contact mode is:

$$\frac{\Delta P}{P} = \frac{R_p}{R_c + R_m} \quad (4.6)$$

4.3.-Heat transfer in the investigated medium

4.3.1. Analytical expression based on integral transforms

The contact area between the probe and the sample is considered to be a disk with radius r_0 , and the heat flux on the contact area is assumed to be uniform. Those assumptions are based on experimental observations reported in chapter 2 by other authors.

In addition, we assume here that the sample behaves as a semi-infinite medium for the considered frequency range.

We can first justify the fact that the probe sweep velocity does not play any role in the measured probe temperature within the experimental conditions usually met. Indeed, the impulse response related to the heat transfer in a semi-infinite medium whose surface is submitted to a heat flux located on a moving heat source at constant velocity u along X axis is [2] (see appendix B):

$$h(X, y, z, t) = \frac{1}{2\rho_m C_{pm} \sqrt{\pi} (a_m t)^{3/2}} \int_0^{r_0} r' e^{\left[\frac{-(X+ut)^2 + y^2 + z^2 + r'^2}{4a_m t} \right]} I_0 \left[\frac{\sqrt{(X+ut)^2 + y^2} r'}{2a_m t} \right] dr' \quad (4.7)$$

In this relation, the thermal conductivity, density, specific heat and thermal diffusivity of the material are denoted k_m , ρ_m , C_{pm} and a_m , respectively. $I_0()$ is the modified Bessel function of first kind. Considering a periodic heat flux at frequency $2f$ and radial frequency $\omega_2 = 4\pi f$, with f varying from 10 Hz to 5 KHz, and classical value for the sweep velocity about $u \sim 1-10 \mu\text{m.s}^{-1}$ one has:

$$u^2 / \omega_2 a_m \ll 1 \quad (4.8)$$

Then, the relation (4.7) simplifies as:

$$h(X,y,z,t) = \frac{1}{2\rho_m C_{pm} \sqrt{\pi} (a_m t)^{3/2}} e^{\left[\frac{-z^2}{4a_m t}\right]} \int_0^{r_0} r' e^{\left[\frac{r^2+r'^2}{4a_m t}\right]} I_0\left[\frac{r r'}{2a_m t}\right] dr', r^2 = X^2 + y^2 \quad (4.9)$$

Therefore, the thermal impedance Z_m , relating the average temperature on the heated disk to the heat flux entering the material, is (see appendix C):

$$\bar{\theta}_0(j\omega_2) = \frac{2}{k\pi r_0} \psi_m(j\omega_2) \int_0^\infty \frac{J_1(x)^2}{x \sqrt{x^2 + j\omega_2 r_0^2 / a_m}} dx, j^2 = -1 \quad (4.10)$$

$J_1(\)$ is the Bessel function of the first type of order 1. The integral is numerically computed using the global adaptive quadrature and default error tolerances (routine INTEGRAL or QUAD in Matlab). Taking $\omega \rightarrow 0$ in relation (4.10) leads to the thermal resistance of the sample in DC mode:

$$R_m = \frac{8}{3k\pi^2 r_0} \quad (4.11)$$

Replacing this expression in (4.6) leads to express the power relative change in the probe that allows maintaining the probe temperature at a constant value as:

$$\frac{\Delta P}{P} = \frac{R_p}{R_c + R_m} = \frac{R_p}{R_c + 8 / (3k_m \pi^2 r_0)} \quad (4.12)$$

4.3.2. The use of the finite element Method

The analytical solution found previously is very useful when the associated assumption of semi-infinite medium is satisfied. However, some applications presented in chapter 5 and 6, involved more complex geometries that do not fit the required assumption. In that case, discrete methods, as the finite element analysis one, have to be used. The 3D heat diffusion equation in the periodic regime is:

$$j\omega \rho C_p \theta(M, j\omega) = k \Delta \theta(M, j\omega), M \in \Omega \quad (4.13)$$

Where $\Delta \theta$ denotes the Laplacian of the temperature. This problem is solved using the stationary solver of a finite element code. The $j\omega \rho C_p \theta(M, j\omega)$ complex mathematical term is then

considered as a source term for the equation. The amplitude and phase are calculated from the real and imaginary parts of the solution.

4.3.2.1. 1D case

The 1D case is first considered that leads to tackle two fundamentals aspects that are closely connected with the periodic regime simulation. Let us consider a semi-infinite domain whose surface is subjected to a uniform heat flux. In that configuration, we know that the temperature at the surface is:

$$\theta_{1D}(z=0, j\omega) = \frac{\phi}{\sqrt{k\rho C_p} \sqrt{j\omega}} \quad (4.14)$$

In this relation, k , ρ and C_p are the thermal conductivity, density and specific heat respectively and a denotes the thermal diffusivity. This equation can be also written as:

$$\begin{aligned} \theta_{1D}(z=0, j\omega) &= \frac{\phi}{\sqrt{k\rho C_p} \sqrt{\omega}} j^{-1/2} = \frac{\phi}{\sqrt{k\rho C_p} \sqrt{\omega}} e^{-j\frac{\pi}{4}} \\ &= \frac{\phi}{\sqrt{k\rho C_p} \sqrt{\omega}} \frac{1}{\sqrt{2}} (1-j) \end{aligned} \quad (4.15)$$

Therefore the phase is constant as:

$$\delta = \arctan(-1) = \frac{\pi}{4} \quad (-45^\circ) \quad (4.16)$$

The mesh is thus very critical regarding the expected value of the phase, notably at the high frequency. In order to solve this issue, a distributed mesh must be used with the smallest elements close to the heated surface. The minimal size is then chosen as:

$$\Delta z_{\min} = \frac{1}{5} \sqrt{\frac{a}{\pi 2f}} \quad (4.17)$$

Dealing with the semi-infinite dimension along z is the second issue. Indeed, it will not be judicious having a dimension large enough than will postpone the lower boundary at a distance greater than $\sqrt{a/\pi f_{\min}}$ for the lower frequency. Indeed, this could make the domain very large, thus requiring a heavy mesh and long computation times. Fortunately, the Finite element method offers the opportunity to deal with infinite medium [3][4][5]. An Infinite Element Domain node

applies a rational coordinate scaling to a layer of virtual domains surrounding the physical region of interest. When the dependent variables vary slowly with radial distance from the center of the physical domain, the finite elements can be stretched in the radial direction such that boundary conditions on the outside of the infinite element layer are affectively applied at a very large distance from any region of interest.

Infinite elements apply a semi-infinite coordinate stretching in one, two, or three directions, depending on how the infinite element domain connects to the physical domain. In each direction, the same form of stretching is used, defined as a function of a dimensionless coordinate ξ , which varies linearly from 0 to 1 over the infinite element layer. For an infinite element domain stretched in the direction of unit vector \mathbf{n}_ξ , ξ is defined as:

$$\xi = \frac{\mathbf{n}_\xi \cdot \mathbf{x} - x_0}{\Delta_w} \quad (4.18)$$

where \mathbf{x} is the original, unscaled, coordinate vector, Δ_w is the original thickness of the infinite element domain (as drawn in the geometry), and x_0 is a reference distance defined such that $\xi = 0$ whenever \mathbf{x} lies on the boundary between the infinite element and the physical domain. For a cylindrical or spherical infinite elements, for example, x_0 is its radius.

The corresponding scaled coordinate vector \mathbf{x}' , in which the equations are reformulated inside the infinite element domains, is defined as

$$\mathbf{x}' = \mathbf{x}_0 + \mathbf{n}_\xi f(\xi) \quad (4.19)$$

where $f(\xi)$ is a scalar stretching function, and \mathbf{x}_0 is the projection of the unscaled coordinate vector \mathbf{x} onto the surface $\xi = 0$:

$$\mathbf{x}_0 = \mathbf{x} - \mathbf{n}_\xi (\mathbf{n}_\xi \cdot \mathbf{x}) + x_0 \quad (4.20)$$

The stretching function is defined as:

$$f(\xi) = \frac{\xi}{\gamma - \xi} \Delta_p \quad (4.21)$$

where Δ_p is the, so called, pole distance and γ is a number larger than one, computed as

$$\gamma = \frac{\Delta_s + \Delta_p}{\Delta_s} \quad (4.22)$$

where Δ_s is the scaled thickness of the infinite element domain.

The quantities \mathbf{n}_ξ , x_0 , and Δ_w are computed automatically based on the selected geometry type and an analysis of the actual geometry. The scaled thickness Δ_s and the pole distance Δ_p are user inputs.

The scaled width of the infinite element domain, Δ_s , is by default set to $10^3 \times dGeomChar$, where the constant $dGeomChar$ is a characteristic geometry dimension. The domain is therefore by default scaled to be very much larger than the original geometry, but not quite infinite in order to avoid numerical difficulties. In particular, the finite distance to the far-away boundary allows prescribing standard boundary conditions effectively at infinity.

The coordinate stretching function, equation (4.21), used in the infinite element domain contains a singularity when $\xi = \gamma$. Since $\gamma > 1$, this happens outside the infinite element domain. The pole distance, Δ_p , controls just how far away this singularity is located. If Δ_p is small compared to the scaled width, Δ_s , the coordinate stretching is very nonlinear, progressing from gentle close to the boundary with the physical domain to abrupt toward to quasi-infinite boundary. Conversely, if the pole distance is large compared to the scaled width, the stretching is constant across the domain.

The default pole distance is $dGeomChar$, which is small compared to the physical width. Therefore, the coordinate stretching by default exhibits a nearly $1/r$ behavior, which is suitable for making optimal use of mesh resolution when the dependent variable also behaves as $1/r$ for large r , where r is the distance from any sources or inhomogeneities.

This specific node is coded already within the COMSOL software, leading to largely simplify its implementation. We present an application on the configuration presented in Figure 77 where structured quadrangle elements have been used with regards to the domain geometry. The material is silicon (thermal conductivity is $k=131 \text{ W.m}^{-1}.\text{K}^{-1}$, density is $\rho = 2329 \text{ kg.m}^{-3}$ and specific heat is $C_p = 700 \text{ J.kg}^{-1}.\text{K}^{-1}$). The mesh has been refined close to the surface where the uniform heat flux is applied. Two simulations have been performed. The first one assumes the finite thickness of the layer with a null heat flux on the rear face and the other one assumes the

semi-infinite node for the layer. The direct solver uses the PARDISO algorithm (see appendix E) because of the multithreading capabilities of our computation platform (i7 with four cores).

As reported in Figure 78, the frequency is equal to -90° at the low frequency, meaning that the phase is subjected only to the boundary condition on the rear face, and starts to increase, tending towards -45° , with higher frequency values. Using the semi-infinite node, the frequency is equal to -45° whatever the frequency value.

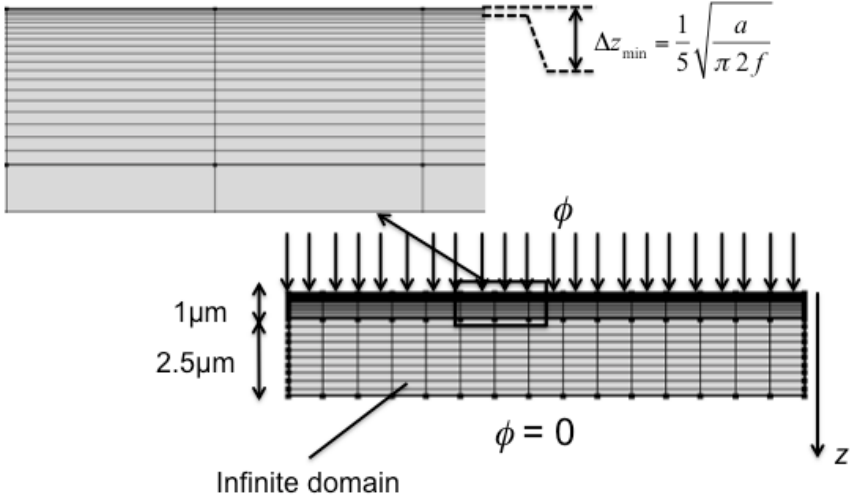


Figure 77: 1D heat transfer in a semi-infinite domain using the infinite domain node.

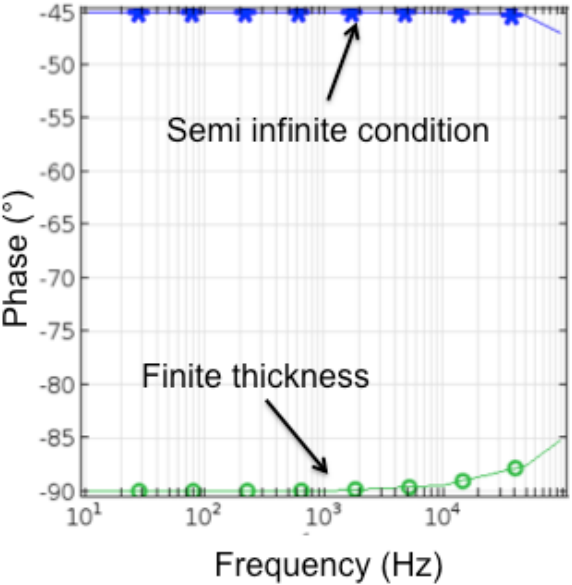


Figure 78: simulation of the phase considering a finite dimension for the layer (green line and circles) and the semi-infinite node for the layer (blue line and crosses).

4.3.2.2. 2D-axi case

In order to approach the real configuration of the SThM, we preformed a FEA simulation considering a 2D axisymmetric configuration represented in Figure 79. The heat flux is applied at the surface of a semi-infinite medium over the disk of radius $r_0=1\mu\text{m}$. Non-structured quadrangles are used for the mesh. This mesh has been refined close to the surface, where the minimal dimension of the element has been chosen according to relation (4.17). The semi-infinite node technique is applied on the medium within the cylindrical coordinates frame. The average amplitude and phase of the temperature over the heated disk are calculated using the integration method with order 4 technique. The same quantities have been calculated using the exact solution given by relation (4.10).

In a first step, the medium is SiO₂ (thermal conductivity is $k=1.45 \text{ W.m}^{-1}.\text{K}^{-1}$, density is $\rho = 2200 \text{ kg.m}^{-3}$ and specific heat is $C_p = 787 \text{ J.kg}^{-1}.\text{K}^{-1}$). The two simulations, performed either the FEA or the exact solutions, fit very well, showing the reliability of the semi-infinite node in the FEA in that configuration.

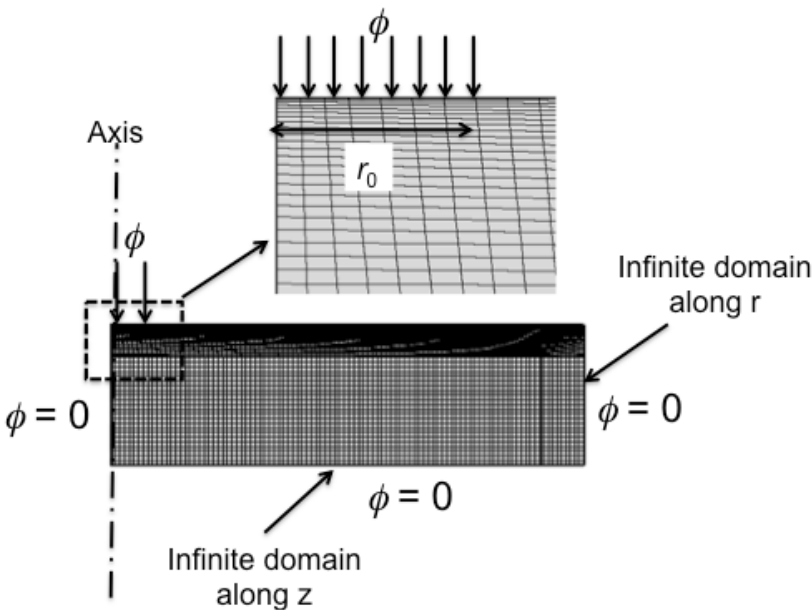


Figure 79: 2D axisymmetric heat transfer in a semi-infinite medium using FEA.

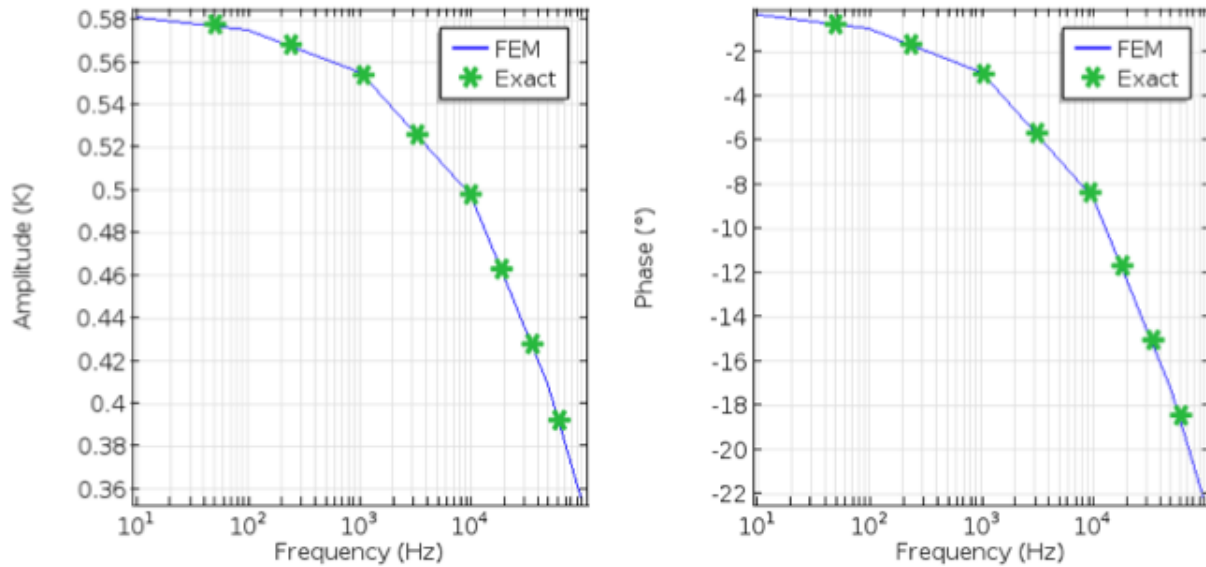


Figure 80: simulation of the amplitude and phase of the frequency dependent average temperature on the heated disk. Comparison between the FEA simulation and exact solution (4.10). Material is SiO_2 .

In order to verify that the technique is not sensitive to the thermal properties of the medium, we repeated the simulations considering a highly more conductive material as silicon. Results, reported in Figure 81, show again a very good agreement between the FEA and the exact solution.

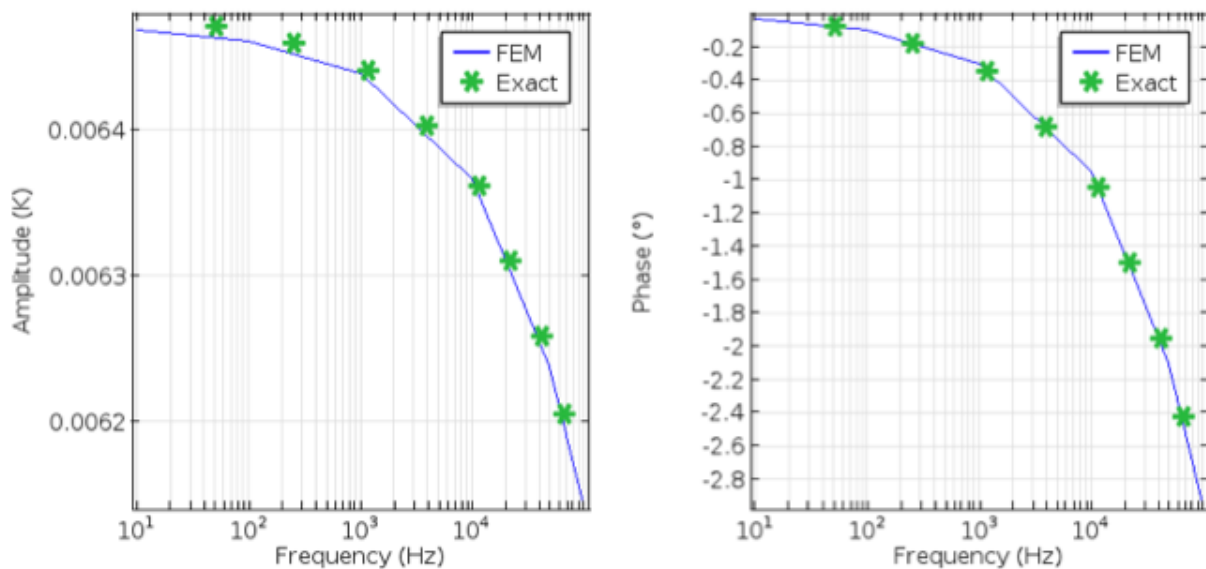


Figure 81: simulation of the amplitude and phase of the frequency dependent average temperature on the heated disk. Comparison between the FEA simulation and exact solution (4.10). Material is Si.

4.4.Heat transfer in the probe

Let us consider first the 2 contact points probe as that represented in Figure 82 whose cantilever is made of Si_3N_4 . A heat transfer model in the probe can be achieved using either an analytical or a discrete approach. The first one will assume assumptions and approximations regarding the real shape of the probe as well as the real boundary conditions. In the second approach, the electro-thermal coupling can be efficiently accounted and no assumption would be stated with respect to the boundary conditions.

4.4.1. Complete model

The required dimensions and thermal properties are reported in Table 9. The geometry of the mesh in the vicinity of the tip are presented in Figure 83. The mesh involves 132284 degrees of freedom. The simulation has been made when the Pd strip is heated at a frequency of 3000 Hz. The total Joule's power dissipated in the Pd strip is $20 \mu\text{W}$. As presented in the Figure 84, the average amplitude and phase over the Pd strip vary strongly if one considers or not the presence of the Au pads. This means that, despite the localized heating that affects the surrounding of the probe tip, the geometry and thermal characteristics of the probe far away from the tip remain critical.

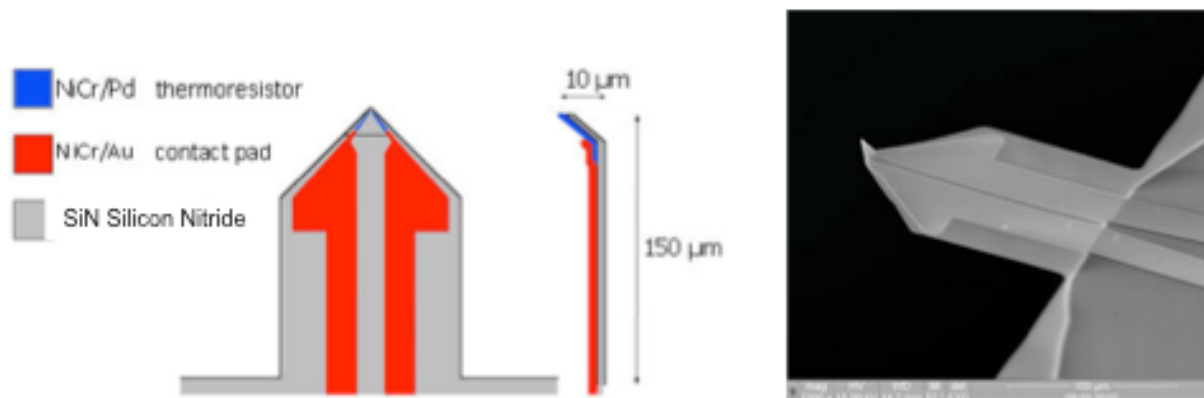


Figure 82: left image: SThM probe scheme; right image: SEM image of the SThM probe provided par Kelvin Tech. company.

Table 9: Some keys properties for the probe.

L_{Au}	150 μm	r_2	70 μm
e_{Au}	140 nm	k_{SiN}	4.9 $\text{W}\cdot\text{m}^{-1}\cdot\text{K}^{-1}$
l_{Au}	10 μm	ρ_{SiN}	2500 $\text{kg}\cdot\text{m}^{-3}$
k_{Au}	128 $\text{W}\cdot\text{m}^{-1}\cdot\text{K}^{-1}$	$C_{p,SiN}$	523 $\text{J}\cdot\text{kg}^{-1}\cdot\text{K}^{-1}$
L_{Pd}, r_1	10 μm	l_{Pd}	1 μm
e_{Pd}	40 nm	e_{SiN}	0.4 μm

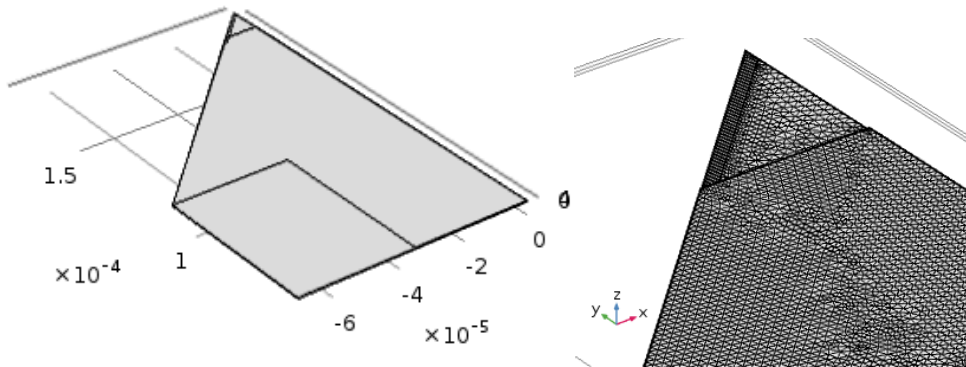


Figure 83: FEA analysis of the heat transfer in the probe using the FEA. Image at the left: probe geometry; Image at the left: mesh of the domain in the vicinity of the tip. The Pd strip has been meshed with a lot of elements.

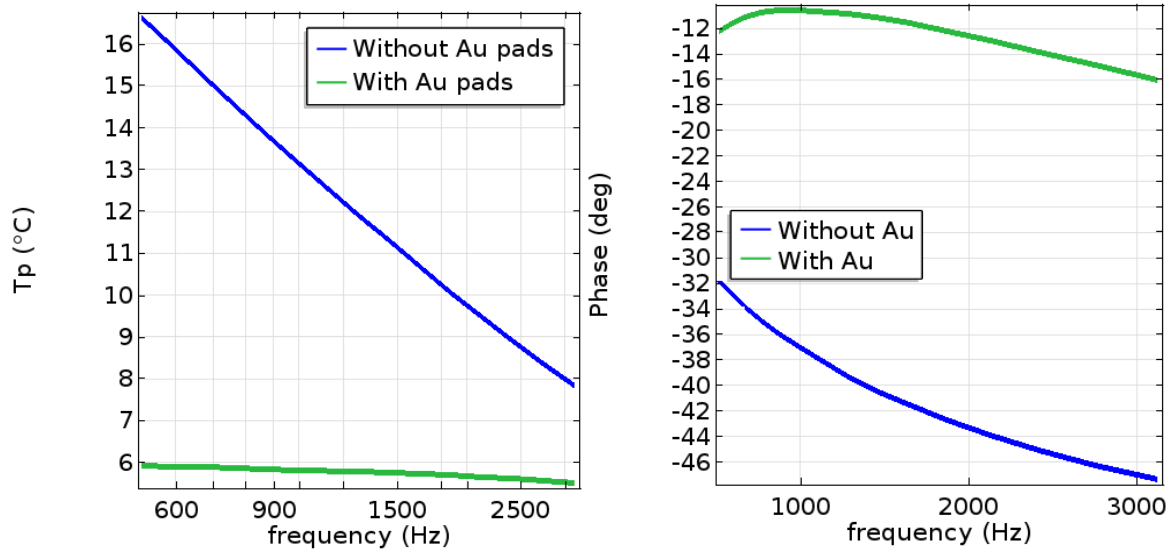


Figure 84: FEA analysis of the SThM probe considering the presence or not of the Au pads

In conclusion, several simulations could be added here, that show that the physical quantities of interest are very sensitive to geometrical and thermal properties of the probe. On the other hand, simulations require significant computation times (1min 38 sec for the simulation at one frequency) that is not suitable for the implementation in an inverse technique approach.

4.4.2. Approximate model

Since the FEA can not be used in an efficient and accurate way to calculate the average temperature and phase of the Pd strip, an approximate model will not do it in a better way obviously. The only interest here is that the approximate model will give some physical insight regarding the system identification procedure that will be implemented finally. An approximate model for the heat transfer in the probe can be expressed assuming cylindrical diffusion. In that case, one assumes that a heat flux is applied on the cylindrical surface in a semi-infinite medium as represented in the figure. The probe can be viewed as a superposition of a Au layer on a SiN substrate. Since the Au layer is very thin (140 nm) and that the Au thermal conductivity ($128 \text{ W}\cdot\text{m}^{-1}\cdot\text{K}^{-1}$) is about 26 times higher than that of SiN ($4.9 \text{ W}\cdot\text{m}^{-1}\cdot\text{K}^{-1}$), the Au layer can be viewed as a fin functioning in the stationary mode.

Therefore, the heat transfer model in this system is constituted from the thermal impedance $Z_{\text{SiN}}(j\omega)$ of the substrate and the thermal resistance of the Au layer in parallel as represented in Figure 85.

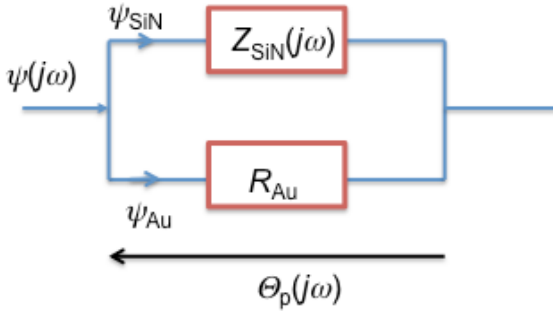


Figure 85 : approximate model of the probe.

The characteristic dimensions required to build the approximate model are reported in Figure 86. The values are reported in Table 9.

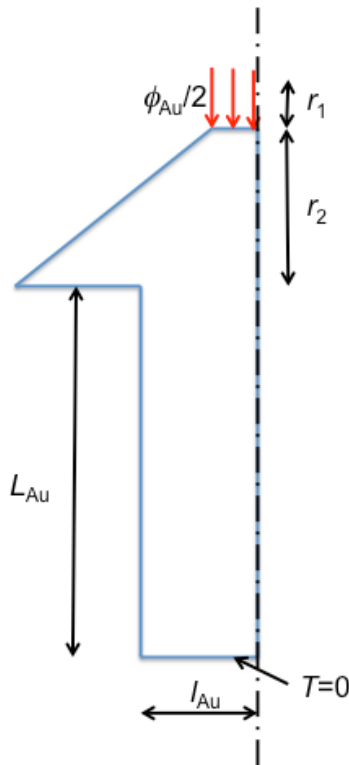


Figure 86: geometry of the probe used to build the approximate model.

In frequency mode, the heat losses at the probe surface have no influence on the temperature in the probe if frequency is high enough (in practice about 100 Hz). Therefore, the thermal resistance of the Au layer can be viewed as the two resistances in series as:

$$R_{Au} = \frac{r_1}{k_{Au} S_1} \ln \frac{r_2}{r_1} + \frac{L_{Au}}{k_{Au} S_2} \quad (4.23)$$

with:

$$S_1 = r_1 \theta e_{Au} \left(\theta = \frac{\pi}{2} \right) \quad \text{and} \quad S_2 = e_{Au} l_{Au} \quad (4.24)$$

That leads to:

$$R_{Au} = \frac{2}{k_{Au} \pi e_{Au}} \ln \frac{r_2}{r_1} + \frac{L_{Au}}{k_{Au} e_{Au} l_{Au}} \quad (4.25)$$

Numerical application gives: $R_{Au} = 6.913 \times 10^4 + 8.37 \times 10^5 = 9.062 \times 10^5 \text{ K.W}^{-1}$

According to the investigated frequency range, the FEA showed that the heat diffusion in the SiN layer is limited to the triangular shape of the probe tip. Therefore, the heat diffusion is that of the cylindrical revolution. As derived in the appendix D, the thermal impedance of the SiN substrate is:

$$Z_{SiN}(j\omega) = \frac{K_0 \left(R \sqrt{\frac{j\omega}{a_{SiN}}} \right)}{S k_{SiN} \sqrt{\frac{j\omega}{a_{SiN}}} K_1 \left(R \sqrt{\frac{j\omega}{a_{SiN}}} \right)} \quad (4.26)$$

Where $K_0(z)$ and $K_1(z)$ are the Bessel functions of second kind, orders 0 and 1 respectively. In this relation R is the equivalent radius where one applies the heat flux and $S = R \theta e_{SiN} (\theta = \pi/2)$ is the cross-section of the heated surface.

Using series of the Bessel functions [15], we showed in Appendix D that:

$$Z_{SiN}(j\omega) \approx \ln \left(\frac{C^2 R^2 j\omega}{4a} \right) \left(\frac{R^2 j\omega}{8a} + \frac{1}{2} \right) - \frac{R^2 j\omega}{4a} \quad (4.27)$$

Where $\gamma = \ln C$ with $C = 0.5772\dots$ is the Euler's constant.

When $0 < \left| R \sqrt{j\omega/a_{SiN}} \right| < 0.3$, we showed that:

$$\frac{K_0(z)}{z K_1(z)} = \frac{1}{a_0 + b_0 (j\omega)^\gamma}; \quad z = R \sqrt{\frac{j\omega}{a_{SiN}}} \quad (4.28)$$

The constants a , b and c depend on the value of R . Using the Levenberg-Marquardt algorithm we obtained: $a_0=0.139$, $b_0=0.0144$, $\gamma=0.2761$. The simulation of the exact expression from relation and its approximation with identified values of a_0 , b_0 and γ is reported in Figure 87.

With the value of S , it comes that:

$$Z_{\text{SiN}}(j\omega) = \frac{2}{\pi e_{\text{SiN}} k_{\text{SiN}} (a_0 + b_0 (j\omega)^\gamma)} \quad (4.29)$$

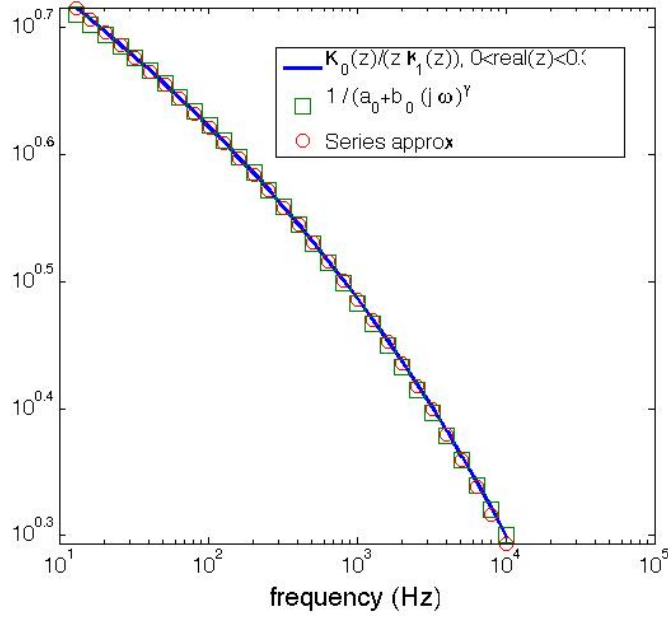


Figure 87: approximation of the absolute value of $z K_1(z)/K_0(z)$ by $1/[a_0+b_0(j\omega)^\gamma]$ when $0 < \text{real}(z) < 0.3$. Use of the series of the Bessel functions.

In DC, it is found the thermal resistance of the SiN layer as:

$$R_{\text{SiN}} = \frac{2}{\pi e_{\text{SiN}} k_{\text{SiN}} c} \quad (4.30)$$

And the thermal impedance of SiN layer can be expressed as:

$$Z_{\text{SiN}}(j\omega) = \frac{R_{\text{SiN}}}{1 + \frac{b_0}{a_0} (j\omega)^\gamma} = \frac{R_{\text{SiN}}}{1 + K_1(j\omega)^\gamma} \quad (4.31)$$

Finally we obtain the value of the thermal impedance for the probe as:

$$Z_p(j\omega) = \frac{1}{\frac{1}{R_{Au}} + \frac{1}{Z_{SiN}(j\omega)}} \quad (4.32)$$

With the thermal resistance of the probe as:

$$R_p = \frac{1}{\frac{1}{R_{Au}} + \frac{1}{R_{SiN}}} \quad (4.33)$$

4.4.3. Identified model

Obviously, the previous analytical expression leads to results even more far from the measured data for the amplitude and the phase than those obtained using the FEA. Several reasons have been viewed that explain such a discrepancy. However, a very small error on the thermal impedance $Z_p(\omega)$ of the probe, will have huge impact on the identification of the seek parameters during a SThM experiment since the major part of the heat power generated within the Pd strip will diffuse within the probe itself. Therefore, we need to approach $Z_p(\omega)$ the more accurately as possible.

In a general way, the thermal impedance $Z_p(\omega)$ of the probe, which relates the heat flux $\phi_p(\omega)$ in the probe to the measured average temperature $T_p(\omega)$ of the Pd strip, can be expressed as $Z_p(\omega) = A_p(\omega)\exp(i\delta_p(\omega))$. Therefore, we propose to identify Z_p from the measurement of the amplitude $A_p(\omega)$ and phase $\delta_p(\omega)$ in the out-of-contact mode. Indeed, we consider that the model bias from this “system identification” approach [6][7] will be much smaller than that obtained either from the FEA or an analytical solution based on a simplified geometry of the probe. In addition, this system identification approach is feasible because the probe can be isolated and characterized independently from the investigated sample during the out-of-contact mode. This system identification approach is classically used in the field of automatics and it has been applied in the field of thermal science considering very different systems. It is very accurate since it does not require knowing the geometry of the system as well as its thermal properties. The exact geometry of the Pd strip as well as its connections with the Au lines is not required

also. This approach does not depend on particular sensor geometry. It can be used whatever the type of probe (Wollaston, micro thermocouple, micro-fabricated probes). The main drawback of this approach is that the “probe calibration” must be realized in the same conditions than those encountered during the use of the probe in the contact mode. This is the most critical point here since we showed that physical phenomena occurred within the contact mode as the heat diffusion/radiation through air and also the heat transfer through the water meniscus that forms at the contact tip. Therefore, those effects have been accounted with the thermal resistance R_{ct} that enters into the total thermal resistance R_c at the interface as reported in the section 2.1.

In order to illustrate the proposed approach we start from measured values of the amplitude and the phase of a two contact Kelvin probe that have been reported in Figure 88 and in Figure 89 respectively. As it is those values are sufficient to express to probe transfer function Z_p . This way of using the data enters into the classical topic of non-parametric methods in system identification. However, a model relating $T_p(\omega)$ and the heat flux $\phi_p(\omega)$ can be identified from those measurements; this is the parametric methods. In a first step, we propose identifying parameters a_0 and b_0 of the following relation:

$$Z_p(\omega) = \frac{a_0}{1 + b_0 \sqrt{j\omega}} \quad (4.34)$$

Measurements of $A_p(\omega)$ when $\omega \rightarrow 0$ leads to the thermal resistance R_p of the probe in DC mode. This means that:

$$\lim_{\omega \rightarrow 0} A_p(\omega) = T_{p,DC} = a_0 P_0 \Rightarrow a_0 = R_p = \frac{T_{p,DC}}{P_0} = 1.868 \times 10^6 \text{ K.W}^{-1} \quad (4.35)$$

Parameter b_0 is identified by minimizing the quadratic gap:

$$J = \sum_{i=1}^N \left(A_p(\omega_i) - \|Z_p(\omega_i) P_0\| \right)^2 \quad (4.36)$$

The minimization is achieved by using the Levenberg-Marquardt algorithm. It is then found:

$$b_0 = (2.7 \pm 0.19) \times 10^{-3} \quad (4.37)$$

As reported on the Figure 88 and Figure 89, this very simplified model fits well the experimental data for the amplitude whereas the fit is less good for the phase. It must be noted that the asymptotic behaviour at the high frequency is $a_0/b_0\sqrt{j\omega}$. This is the behaviour of heat transfer within a semi-infinite domain. The reader can refer to the work based on the non-integer derivatives with fractional order $\frac{1}{2}$ [8]-[14]. In order to improve the fit, we propose to implement the following model:

$$Z_p(\omega) = \frac{a_0}{1 + b_0\sqrt{j\omega} + b_1j\omega} \quad (4.38)$$

Using the same minimization procedure, one found:

$$b_0 = (1.4 \pm 0.16) \times 10^{-3} \quad \text{and} \quad b_1 = (1.32 \pm 0.13) \times 10^{-5} \quad (4.39)$$

As reported in the figure, the fit for the amplitude and the phase are then very satisfactory. This model suggests that the behaviour at the low frequency is a_0 , meaning the probe behaves as a thermal resistance. At high frequency, the asymptotic behaviour is $a_0/b_1j\omega$, meaning the probe behaves as a thermal capacitance. Between those two typical behaviours, a semi-infinite one occurs that is characterized by the $1/\sqrt{j\omega}$ term.

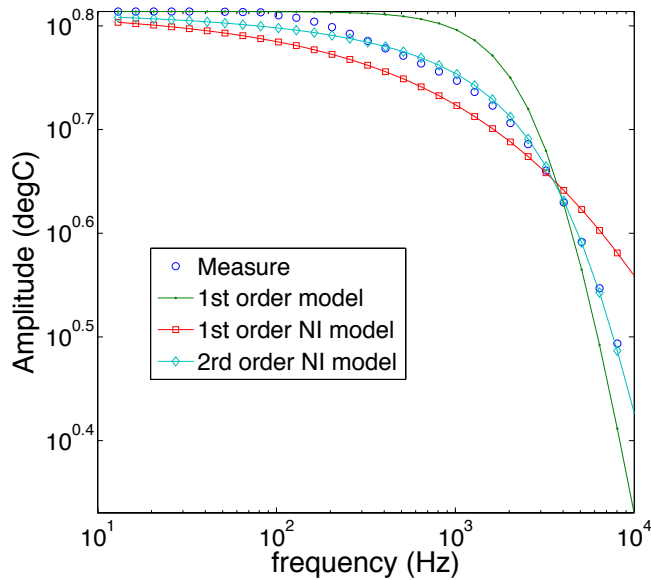


Figure 88: measured amplitude and identified transfer functions for 1st order model $a_0/(1+b_0j\omega)$, 1st order NI model (4.34) and 2rd order NI model (4.38).

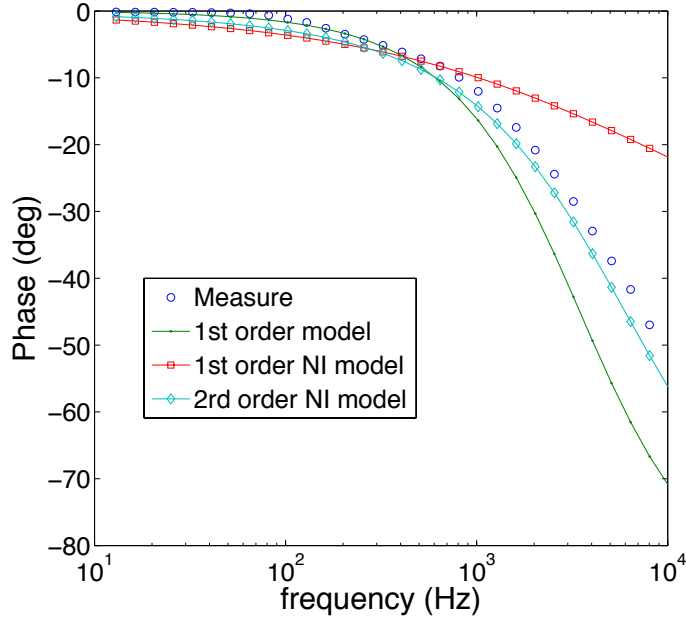


Figure 89: measured amplitude and identified transfer functions for 1st order model $a_0/(1+b_0 j \omega)$, 1st order NI model (4.34) and 2rd order NI model (4.38).

4.5.Sensitivity analysis

The model described by relations (4.4) and (4.5) in the AC mode allows defining the sensitivity functions to several parameters. Starting from this model, the reduced sensitivity $S_A(\theta, \omega_2) = \theta dA(\omega_2)/d\theta$ of the amplitude versus the parameter $\theta = \{k_r, k_z, r_0, R_c\}$, have been calculated and reported in the Figure 90 where k_r is the in-plane thermal conductivity, k_z is the transverse thermal conductivity, r_0 is the radius of the contact area between the probe and the investigated surface and R_c is the thermal contact resistance at this interface. For those simulations we had $k_r = 0.3 \text{ W.m}^{-1}.\text{K}^{-1}$, $k_z = 20 \text{ W.m}^{-1}.\text{K}^{-1}$, $r_0 = 100 \text{ nm}$ and $R_c = 5 \times 10^{-8} \text{ m}^2.\text{K}.\text{W}^{-1}$. From the practical point of view the sensitivity function is calculated using the finite difference formulation as:

$$S_A(\theta, \omega_2) = \theta \frac{dA(\omega_2)}{d\theta} \sim \theta \frac{A(\theta, \omega_2) - A(\theta - \Delta\theta, \omega_2)}{\Delta\theta} \quad (4.40)$$

As showed in the figure, the ratio between sensitivity functions shows that the sensitivity on k_r and k_z being exactly the same, these two parameters cannot be identify separately. Therefore, the measurements achieved when the probe is in contact with the material will only lead to identify its effective thermal conductivity. On the other hand, the ratio of the sensitivity functions to r_0

and R_c is constant; there is thus no chance to identify separately those two parameters simultaneously also from frequency dependent measurements.

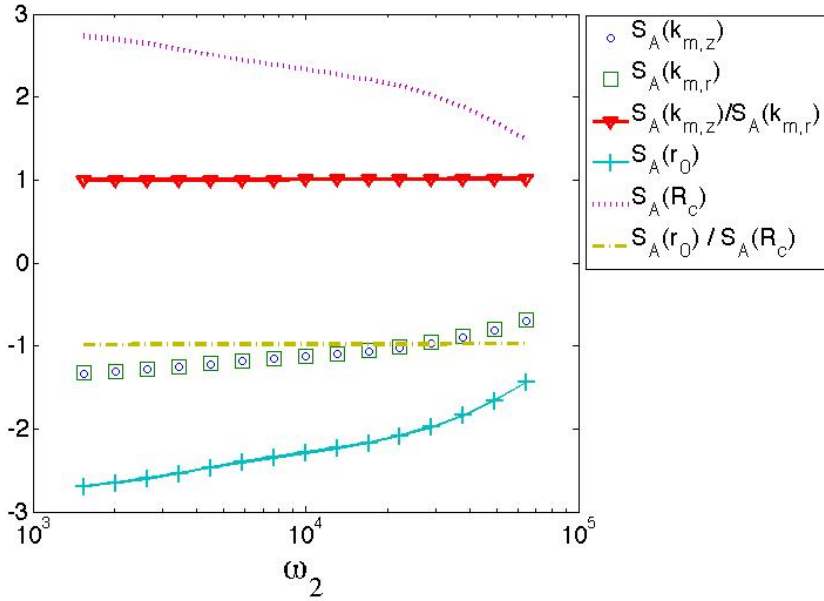


Figure 90. Reduced sensitivities of the amplitude to: the in-plane and out-of-plane thermal conductivity (k_r , k_z), the contact radius r_0 and the thermal contact resistance R_c at the interface between the probe and the investigated surface, as a function of frequency. Ratio between sensitivity functions are also presented.

On the other hand, the functions $S_A(r_0, \omega_2)$ and $S_A(R_c, \omega_2)$, at a given frequency, are represented in Figure 91 when the thermal conductivity k varies in the range $[0.2-40]$ $\text{W}\cdot\text{m}^{-1}\cdot\text{K}^{-1}$. They have been plotted in Figure 91. Plotting the ratio of the two functions on the same figure, it appears that the two functions are clearly linearly independent, thus leading to identification for both r_0 and R_c using a non-linear least-square method (the Levenberg-Marquardt algorithm in this study). This result is also valid in DC mode. Indeed, relation (4.12) shows that $\Delta P/P \rightarrow R_p/R_c$ when $k \rightarrow \infty$ and that $\Delta P/P \rightarrow 3k\pi^2 r_0 R_p/8$ when $k \rightarrow 0$, meaning that r_0 and R_c can be identified from those asymptotic relations.

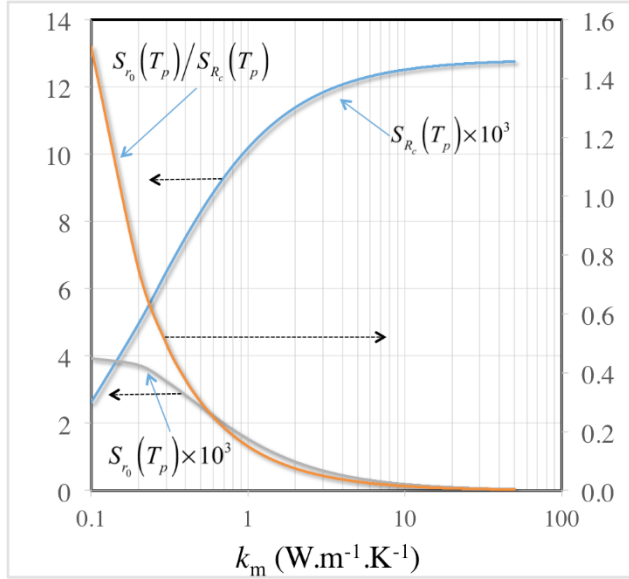


Figure 91: reduced sensitivity functions of the amplitude with respect to R_c and r_0 according to the thermal conductivity of the material.

4.6. Conclusion

In this chapter we have presented a model of the heat transfer within the SThM configuration. The thermal impedances network allows representing in a very synthetic way the heat transfer within the probe and the investigated sample as well as the thermal resistance at the interface between the probe and the surface. The thermal impedance of the sample can be expressed either using an analytical solution or one achieved using a discrete approach. As presented above, the finite element method can be efficiently implemented even considering semi-infinite behaviour of the medium. We showed that the most accurate way to express the thermal impedance of the probe is based on the use of a non-parametric system identification approach that consists to simply measure the amplitude and the phase in the out-of-contact mode. In addition, we identified a parametric model based on the use of the non-integer derivative of fractional order. It was obtained that a model involving only three parameters allowed reproducing the frequency dependent amplitude and phase very accurately. The thermal contact resistance at the interface between the probe and the sample accounts for several contributions as the solid-solid contact, including both the constriction related to roughness and the phonon transmission, the conduction and radiation through air and the heat transfer through the water meniscus that formed at the contact tip. In addition, we also showed that this resistance will include the influence of the contact regarding the change in the isothermals in the area of the probe tip. Obviously, our

objective here is not to quantify each contribution. Finally we used the analytical solution to perform a sensitivity analysis of the amplitude with respect to the main unknown parameters in this experiment, namely: k_r , k_z , r_0 and R_c . It has been showed that the frequency dependent amplitude could only lead to identify only one of these parameters. On the other hand, we showed that two of them could be identified when considering the Amplitude measurement according to the thermal conductivity of the sample.

4.7. Appendix

4.7.1. Appendix A: heat transfer in a semi-infinite medium whose surface is submitted to a motion point located heat flux at constant velocity v .

Considering the impulse response for a motionless point source at the surface of a semi-infinite medium and assuming now a motion of the source at the surface along the x-direction, the impulse response can be at time t_i as:

$$h(x, y, z, t_i) = \frac{1}{4\rho C_p (\pi\alpha)^{3/2}} \frac{1}{t_i^{3/2}} e^{-\left[\frac{(x-ut_i)^2 + y^2 + z^2}{4\alpha t_i}\right]} \quad (4.41)$$

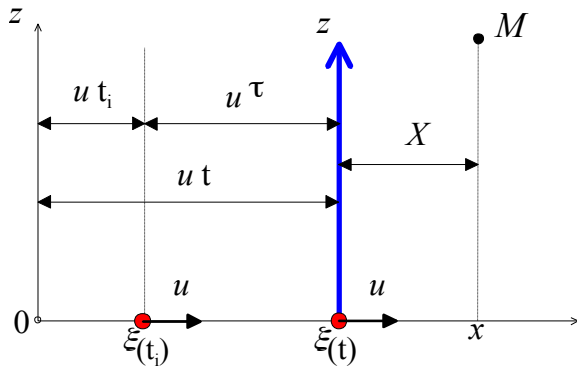


Figure 92: Going from fixed to moving reference frame attached to heat source (representation in the xz plane).

However, what is of interest is the temperature distribution around the heat source, and for this it is more convenient to define a moving reference frame whose origin is fixed to the heat source, as shown in Figure 92. From this figure it can be seen that:

$$x - ut_i = x - u(t - \tau) = x - ut + u\tau = X + u\tau \quad (4.42)$$

X denotes the coordinate of the source at time t in the reference frame fixed to the source. We may now write the temperature rise in the new reference frame:

$$h(X, y, z, t) = \frac{1}{4\rho C_p (\pi\alpha)^{3/2}} \frac{1}{t^{3/2}} e^{\left[-\frac{(X+ut)^2 + y^2 + z^2}{4\alpha t}\right]} = \frac{1}{4\rho C_p (\pi\alpha)^{3/2}} \frac{1}{t^{3/2}} e^{\left[-\frac{ut^2}{4\alpha t}\right]} e^{\left[-\frac{X^2 + y^2 + z^2}{4\alpha t}\right]} \quad (4.43)$$

When $u^2 t / 4\alpha \ll 1$ then (4.43) simplifies as:

$$h(X, y, z, t) = \frac{1}{4\rho C_p (\pi\alpha)^{3/2}} \frac{1}{t^{3/2}} e^{\left[-\frac{X^2 + y^2 + z^2}{4\alpha t}\right]} \quad (4.44)$$

4.7.2. Appendix B: heat transfer in a semi-infinite medium whose surface is submitted to a motion disk heat flux at constant velocity v .

The heat flux is applied on the shape of a disk with radius r_0 with a Gaussian distribution of the heat flux. The linear heat diffusion equation in the semi-infinite domain is:

$$\rho C_p \frac{\partial T(r, z, t)}{\partial t} = k \Delta T(r, z, t), \text{ at } -\infty < r < \infty, 0 < z < \infty \text{ and for } t > 0 \quad (4.45)$$

Obviously, the Laplacian $\Delta T(M, t)$ is expressed according to the adopted coordinate referential.

In that case the Laplacian of relation (4.59) is defined as:

$$\Delta T(r, z, t) = \frac{\partial}{\partial r} \left(r \frac{\partial T(r, z, t)}{\partial r} \right) + \frac{\partial^2 T(r, z, t)}{\partial z^2} \quad (4.46)$$

The boundary conditions are:

$$-k \frac{\partial T(r, z, t)}{\partial n} = \varphi_0(r, t), \text{ at } z = 0 \text{ and for } t > 0 \quad (4.47)$$

$$T(r, z, t) = 0, \text{ when } z \rightarrow \infty \text{ and } r \rightarrow \pm\infty \text{ and for } t > 0 \quad (4.48)$$

Initial condition is:

$$T(r, z, t) = 0, 0 \leq z < \infty, -\infty < r < \infty \text{ and for } t = 0 \quad (4.49)$$

The impulse response for a motionless disk heat source at the surface of a semi-infinite medium is:

$$h(r, z, t) = \frac{1}{2\rho C_p \sqrt{\pi} (\alpha t)^{3/2}} \int_0^{r_0} r' e^{\left[\frac{-r^2 + z^2 + r'^2}{4\alpha t} \right]} I_0 \left[\frac{r r'}{2\alpha t} \right] dr' \quad (4.50)$$

As described in Appendix A, motion of the heat source consists in replacing x by $X + ut$ in relation (4.50) to give:

$$h(X, y, z, t) = \frac{1}{2\rho C_p \sqrt{\pi} (\alpha t)^{3/2}} \int_0^{r_0} r' e^{\left[\frac{(X+ut)^2 + y^2 + z^2 + r'^2}{4\alpha t} \right]} I_0 \left[\frac{\sqrt{(X+ut)^2 + y^2} r'}{2\alpha t} \right] dr' \quad (4.51)$$

That is at the center of the disk ($X=y=z=0$):

$$h_0(t) = \frac{1}{2\rho C_p \sqrt{\pi} (\alpha t)^{3/2}} \int_0^{r_0} r' e^{\left[\frac{(ut)^2 + r'^2}{4\alpha t} \right]} I_0 \left[\frac{u r'}{2\alpha} \right] dr' \quad (4.52)$$

Or:

$$h_0(t) = \frac{1}{2\rho C_p \sqrt{\pi} (\alpha t)^{3/2}} e^{\left[\frac{-u^2 t}{4\alpha} \right]} \int_0^{r_0} r' e^{\left[\frac{-r'^2}{4\alpha t} \right]} I_0 \left[\frac{u r'}{2\alpha} \right] dr' \quad (4.53)$$

When $u^2 t / 4\alpha \ll 1$ and since $u r' / 2\alpha \ll 1$ when $0 \leq r' \leq r_0$, then (4.53) simplifies as:

$$h_0(t) = \frac{1}{2\rho C_p \sqrt{\pi} \alpha t} \left(1 - e^{\left[\frac{-r_0^2}{4\alpha t} \right]} \right) \sim \frac{r_0^2}{8\rho C_p (\alpha t)^{3/2} \sqrt{\pi}} \quad (4.54)$$

The average impulse response over the heated disk is:

$$\overline{h(t)} = \frac{1}{\rho C_p \sqrt{\pi} (\alpha t)^{3/2} r_0^2} \int_0^{r_0} \int_0^{r_0} r' e^{\left[\frac{-R^2 + r'^2}{4\alpha t} \right]} I_0 \left[\frac{R r'}{2\alpha t} \right] dr' R dR \quad (4.55)$$

Considering a periodic heat flux, the average temperature over the disk is obtained using the convolution between the impulse response and the heat flux as:

$$T(X, y, z, t) = \int_0^t \overline{h(t-\tau)} \phi_0 \cos(\omega\tau) d\tau \quad (4.56)$$

4.7.3. Appendix C: heat transfer in a semi-infinite medium whose surface is submitted to a heat flux over a motionless disk of radius r_0 .

Case 1: isotropic medium

In order to work in the frequency domain, a more suitable approach can be found to calculate the amplitude and phase of the average temperature over the heating disk than using equations (4.55) and (4.56). We perform a Laplace transform of the previous equations. Let us note that the Laplace transform is applied to the time variable t of the temperature and the heat flux density respectively as:

$$\theta(M, p) = \mathcal{L}_t [T'(M, t)] = \int_0^\infty T'(M, t) e^{-pt} dt \quad (4.57)$$

$$\psi(M, p) = \mathcal{L}_t [\varphi(M, t)] = \int_0^\infty \varphi(M, t) e^{-pt} dt \quad (4.58)$$

It must be noted that one of the advantages of the Laplace transform is its direct link with the Fourier transform when the initial temperature is zero. This implies that the simple transformation $p = j\omega = j2\pi f$ leads to obtain the expression of the temperature in the frequency domain. By applying this transformation on relations (4.45) to we obtain the new system of partial differential equations as follows:

$$j\omega \rho C_p \theta(r, z, j\omega) = k \Delta \theta(r, z, j\omega), -\infty < r < \infty, 0 < z < \infty \quad (4.59)$$

$$-k \frac{\partial \theta(r, z, j\omega)}{\partial n} = \psi_0(r, z, j\omega), \text{ at } z = 0 \quad (4.60)$$

$$\theta(r, z, j\omega) = 0, \text{ when } z \rightarrow \infty \text{ and } r \rightarrow \pm\infty \quad (4.61)$$

In this relation ρ is the density, (kg.m^{-3}), C_p is the specific heat ($\text{J.kg}^{-1}.\text{K}^{-1}$) and k is the thermal conductivity ($\text{W.m}^{-1}.\text{K}^{-1}$). Let us remind that $a = k/\rho C_p$ is the thermal diffusivity ($\text{m}^2.\text{s}^{-1}$).

We define the Hankel transform of the temperature upon the r coordinate as:

$$\tilde{\theta}(\alpha, z, j\omega) = H\{\theta(r, z, j\omega)\} = \int_0^{\infty} \theta(r, z, j\omega) r J_0(\alpha r) dr \quad (4.62)$$

J_0 is the Bessel transform of the first kind and first order.

Applying this integral transform to relations and (4.59), leads to:

$$\frac{j\omega}{a} \tilde{\theta}(\alpha, z, j\omega) = -\alpha^2 \tilde{\theta}(\alpha, z, j\omega) + \frac{\partial^2 \tilde{\theta}(\alpha, z, j\omega)}{\partial z^2} \quad (4.63)$$

$,-\infty < r < \infty, 0 < z < \infty$

Thus:

$$\frac{\partial^2 \tilde{\theta}(\alpha, z, j\omega)}{\partial z^2} - \underbrace{\left(\alpha^2 + \frac{j\omega}{a}\right)}_{\beta^2} \tilde{\theta}(\alpha, z, j\omega) = 0 \quad (4.64)$$

The solution is:

$$\tilde{\theta}(\alpha, z, j\omega) = A e^{\beta z} + B e^{-\beta z} \quad (4.65)$$

Using the boundary condition (4.61) leads to:

$$\tilde{\theta}(\alpha, z, j\omega) = 0, \text{ when } z \rightarrow \infty \quad (4.66)$$

This implies for relation (4.65) that $A=0$.

Using boundary condition (4.60) leads to:

$$-k \frac{\partial \tilde{\theta}(\alpha, z, j\omega)}{\partial z} = \tilde{\psi}_0(j\omega), \text{ at } z = 0 \quad (4.67)$$

With:

$$\tilde{\psi}_0(j\omega) = \int_0^{\infty} \varphi_0(r, j\omega) r J_0(\alpha r) dr \quad (4.68)$$

Since the heat flux spatial distribution is assumed to be uniform as: $\varphi_0(r, j\omega) = \Pi_{r_0} \varphi_0(j\omega)$

$$\widetilde{\psi}_0(j\omega) = \varphi_0(j\omega) \int_0^\infty \Pi_{r_0} r J_0(\alpha r) dr = \varphi_0(j\omega) \frac{r_0 J_1(\alpha r_0)}{\alpha} \quad (4.69)$$

Replacing $\widetilde{\theta}(\alpha, z, j\omega)$ in (4.65) with its expression in (4.67) leads to:

$$k B \beta e^{-\beta z} = \varphi_0(j\omega) \widetilde{\psi}_0(j\omega) = \varphi_0(j\omega) \frac{r_0 J_1(\alpha r_0)}{\alpha}, \text{ at } z = 0 \quad (4.70)$$

Thus:

$$B = \varphi_0(j\omega) \frac{r_0 J_1(\alpha r_0)}{\alpha k \beta} \quad (4.71)$$

Finally, we obtain:

$$\widetilde{\theta}(\alpha, z, j\omega) = \varphi_0(j\omega) \frac{r_0 J_1(\alpha r_0)}{\alpha k \beta} e^{-\beta z} \quad (4.72)$$

The inverse Hankel transform allows us to retrieve the periodic temperature as:

$$\theta(r, z, j\omega) = \int_0^\infty \widetilde{\theta}(\alpha, z, j\omega) \alpha J_0(\alpha r) d\alpha \quad (4.73)$$

Thus:

$$\theta(r, z, j\omega) = \frac{\varphi_0(j\omega) r_0}{k} \int_0^\infty \frac{J_1(\alpha r_0) J_0(\alpha r)}{\beta} e^{-\beta z} d\alpha \quad (4.74)$$

Or:

$$\theta(r, z, j\omega) = \frac{\phi_0(j\omega)}{k \pi r_0^2} \int_0^\infty \frac{J_1(\alpha r_0) J_0(\alpha r)}{\beta} e^{-\beta z} d\alpha \quad (4.75)$$

When $r_0 \gg \sqrt{a/\omega}$, $\forall \omega$, the solution comes to that of the 1D heat transfer solution in a semi infinite medium as:

$$\theta_{1D}(z, j\omega) = \frac{\phi_0(\omega) \sqrt{a}}{k \pi r_0^2 \sqrt{j\omega}} e^{-\sqrt{j\omega/a} z} \quad (4.76)$$

When $r_0 \ll \sqrt{a/\omega}$, $\forall \omega$, the solution comes to that of the point located heat source at the surface of a semi infinite medium as:

$$\theta_p(r, j\omega) = \frac{\phi_0(\omega)}{8k\pi r} e^{-\sqrt{j\omega/a}r} \quad (4.77)$$

Making $x = \alpha r_0$, leads to:

$$\theta(r, z, j\omega) = \frac{\phi_0(j\omega)}{k\pi r_0^2} \int_0^\infty \frac{J_1(x)J_0(xr/r_0)}{\sqrt{x^2/r_0^2 + j2\omega/a_m}z} e^{-\sqrt{x^2/r_0^2 + j2\omega/a_m}z} dx, \quad j^2 = -1 \quad (4.78)$$

The average temperature on the heated area at $z=0$ is:

$$\bar{\theta}_0(j\omega) = \frac{1}{\pi r_0^2} \int_0^{r_0} \theta_0(r, z, p) r 2\pi dr = \frac{2}{kr_0} \varphi_0(j\omega) \int_0^\infty \frac{J_1(\alpha r_0)}{\beta} \left[\int_0^{r_0} r J_0(\alpha r) dr \right] d\alpha \quad (4.79)$$

Since: $\int_0^{r_0} J_0(\alpha r) r dr = \frac{r_0 J_1(\alpha r_0)}{\alpha}$:

$$\bar{\theta}_0(j\omega) = \frac{2}{kr_0} \varphi_0(j\omega) \int_0^\infty \frac{J_1(\alpha r_0)}{\beta} \frac{r_0 J_1(\alpha r_0)}{\alpha} d\alpha \quad (4.80)$$

And finally:

$$\bar{\theta}_0(j\omega) = \frac{2}{kr_0} \varphi_0(j\omega) \int_0^\infty \frac{J_1(\alpha r_0)^2}{\alpha \beta} d\alpha \quad (4.81)$$

Making $x = \alpha r_0$, leads to:

$$\bar{\theta}_0(j\omega) = \frac{2r_0}{k} \varphi_0(j\omega) \int_0^\infty \frac{J_1(x)^2}{x \sqrt{x^2 + j2\omega r_0^2/a}} dx, \quad j^2 = -1 \quad (4.82)$$

Or:

$$\boxed{\bar{\theta}_0(j\omega) = \frac{2}{k\pi r_0} \phi_0(j\omega) \int_0^\infty \frac{J_1(x)^2}{x \sqrt{x^2 + j2\omega r_0^2/a}} dx, \quad j^2 = -1} \quad (4.83)$$

When $\omega \rightarrow 0$ then $\beta = \alpha$ and the solution in DC mode is:

$$\bar{\theta}_{0DC} = \frac{2\phi_{0DC}}{k\pi r_0^2} \int_0^\infty \frac{J_1(\alpha r_0)^2}{\alpha^2} d\alpha = \frac{8\phi_{0DC}}{3k\pi^2 r_0} \quad (4.84)$$

Case 2: orthotropic conductivity

In that case the thermal conductivity is assumed directionally dependent and we define k_r as the thermal conductivity (W.m⁻¹.K⁻¹) along the radial (r) coordinate and define k_z as the thermal conductivity along the transverse (z) coordinate. Therefore, relations (4.59) to (4.61) become:

$$j\omega\rho C_p\theta(r,z,j\omega) = k_r \frac{\partial}{\partial r} \left(r \frac{\partial\theta(r,z,j\omega)}{\partial r} \right) + k_z \frac{\partial^2\theta(r,z,j\omega)}{\partial z^2}, -\infty < r < \infty, 0 < z < \infty \quad (4.85)$$

$$-k_z \frac{\partial\theta(r,z,j\omega)}{\partial z} = \psi_0(r,z,j\omega), \text{ at } z = 0 \quad (4.86)$$

$$\theta(r,z,j\omega) = 0, \text{ when } z \rightarrow \infty \text{ and } r \rightarrow \pm\infty \quad (4.87)$$

As previously, we define the Hankel transform of the temperature upon the r coordinate as:

$$\tilde{\theta}(\alpha,z,j\omega) = H\{\theta(r,z,j\omega)\} = \int_0^\infty \theta(r,z,j\omega) r J_0(\alpha r) dr \quad (4.88)$$

J_0 is the Bessel transform of the first kind and first order.

Applying this integral transform to relations (4.85) to (4.87), leads to:

$$j\omega\tilde{\theta}(\alpha,z,j\omega) = -a_r\alpha^2\tilde{\theta}(\alpha,z,j\omega) + a_z \frac{\partial^2\tilde{\theta}(\alpha,z,j\omega)}{\partial z^2}, 0 < z < \infty \quad (4.89)$$

Thus:

$$\frac{\partial^2\tilde{\theta}(\alpha,z,j\omega)}{\partial z^2} - \underbrace{\left(\frac{a_r\alpha^2}{a_z} + \frac{j\omega}{a_z} \right)}_{\beta^2} \tilde{\theta}(\alpha,z,j\omega) = 0, 0 < z < \infty \quad (4.90)$$

The solution is:

$$\tilde{\theta}(\alpha,z,j\omega) = A e^{\beta z} + B e^{-\beta z} \quad (4.91)$$

Using the boundary condition (4.87) leads to:

$$\tilde{\theta}(\alpha, z, j\omega) = 0, \text{ when } z \rightarrow \infty \quad (4.92)$$

This implies for relation (4.91) that $A=0$. Using boundary condition (4.86) leads to:

$$-k_z \frac{\partial \tilde{\theta}(\alpha, z, j\omega)}{\partial z} = \tilde{\psi}_0(j\omega), \text{ at } z = 0 \quad (4.93)$$

With:

$$\tilde{\psi}_0(j\omega) = \int_0^{\infty} \varphi_0(r, j\omega) r J_0(\alpha r) dr \quad (4.94)$$

Since the heat flux spatial distribution is assumed to be uniform as: $\varphi_0(r, j\omega) = \Pi_{r_0} \varphi_0(j\omega)$

$$\tilde{\psi}_0(j\omega) = \varphi_0(j\omega) \int_0^{\infty} \Pi_{r_0} r J_0(\alpha r) dr = \varphi_0(j\omega) \frac{r_0 J_1(\alpha r_0)}{\alpha} \quad (4.95)$$

Replacing $\tilde{\theta}(\alpha, z, j\omega)$ in (4.91) with its expression in (4.93) leads to:

$$k_z B \beta e^{-\beta z} = \varphi_0(j\omega) \tilde{\psi}_0(j\omega) = \varphi_0(j\omega) \frac{r_0 J_1(\alpha r_0)}{\alpha}, \text{ at } z = 0 \quad (4.96)$$

Thus:

$$B = \varphi_0(j\omega) \frac{r_0 J_1(\alpha r_0)}{\alpha k_z \beta} \quad (4.97)$$

Finally, we obtain:

$$\tilde{\theta}(\alpha, z, j\omega) = \varphi_0(j\omega) \frac{r_0 J_1(\alpha r_0)}{\alpha k_z \beta} e^{-\beta z} \quad (4.98)$$

The inverse Hankel transform allows us to retrieve the periodic temperature as:

$$\theta(r, z, j\omega) = \int_0^{\infty} \tilde{\theta}(\alpha, z, j\omega) \alpha J_0(\alpha r) d\alpha \quad (4.99)$$

Thus:

$$\theta(r, z, j\omega) = \frac{\varphi_0(j\omega) r_0}{k_z} \int_0^{\infty} \frac{J_1(\alpha r_0) J_0(\alpha r)}{\beta} e^{-\beta z} d\alpha \quad (4.100)$$

The average temperature on the heated area at $z=0$ is:

$$\bar{\theta}_0(j\omega) = \frac{1}{\pi r_0^2} \int_0^{r_0} \theta_0(r, z, p) r 2\pi dr = \frac{2}{k_z r_0} \varphi_0(j\omega) \int_0^\infty \frac{J_1(\alpha r_0)}{\beta} \left[\int_0^{r_0} r J_0(\alpha r) dr \right] d\alpha \quad (4.101)$$

Since: $\int_0^{r_0} J_0(\alpha r) r dr = \frac{r_0 J_1(\alpha r_0)}{\alpha}$:

$$\bar{\theta}_0(j\omega) = \frac{2}{k_z r_0} \varphi_0(j\omega) \int_0^\infty \frac{J_1(\alpha r_0)}{\beta} \frac{r_0 J_1(\alpha r_0)}{\alpha} d\alpha \quad (4.102)$$

And finally:

$$\bar{\theta}_0(j\omega) = \frac{2}{k_z r_0} \varphi_0(j\omega) \int_0^\infty \frac{J_1(\alpha r_0)^2}{\alpha \beta} d\alpha \quad (4.103)$$

Making $x = \alpha r_0$, leads to:

$$\bar{\theta}_0(j\omega) = \frac{2r_0}{k_z} \varphi_0(j\omega) \int_0^\infty \frac{J_1(x)^2}{x \sqrt{\frac{a_r}{a_z} x^2 + \frac{j2\omega r_0^2}{a_z}}} dx, \quad j^2 = -1 \quad (4.104)$$

Or:

$$\boxed{\bar{\theta}_0(j\omega) = \frac{2}{k_z \pi r_0} \varphi_0(j\omega) \int_0^\infty \frac{J_1(x)^2}{x \sqrt{\frac{a_r}{a_z} x^2 + \frac{j2\omega r_0^2}{a_z}}} dx, \quad j^2 = -1} \quad (4.105)$$

When $\omega \rightarrow 0$ then $\beta = \alpha$ and the solution in DC mode is:

$$\bar{\theta}_{0DC} = \frac{2\phi_{0DC}}{k_z \pi r_0^2} \int_0^\infty \frac{J_1(\alpha r_0)^2}{\alpha^2 \sqrt{a_r/a_z}} d\alpha = \frac{8\phi_{0DC}}{3k_z \sqrt{a_r/a_z} \pi^2 r_0} \quad (4.106)$$

4.7.4. Appendix D: heat transfer in a cylindrical coordinate framework

The equations of heat transfer in cylindrical coordinates are:

$$\frac{\partial T(r,t)}{\partial t} = a \left(\frac{\partial^2 T(r,t)}{\partial r^2} + \frac{1}{r} \frac{\partial T(r,t)}{\partial r} \right), \quad R < r < \infty, t > 0 \quad (4.107)$$

$$-kS \frac{\partial T(r,t)}{\partial r} = \phi_R(t), \quad r = R, t > 0 \quad (4.108)$$

$$T(r,t) = 0, \quad r \rightarrow \infty, t > 0 \quad (4.109)$$

$$T(r,t) = 0, \quad 0 \leq r < \infty, t = 0 \quad (4.110)$$

The Laplace transform applied to the time variable gives:

$$\frac{d^2 \theta(r,p)}{dr^2} + \frac{1}{r} \frac{d\theta(r,p)}{dr} - \frac{p}{a} \theta(r,p) = 0, \quad R < r < \infty \quad (4.111)$$

$$-kS \frac{\partial \theta(r,p)}{\partial r} = \psi_R(p), \quad r = R, t > 0 \quad (4.112)$$

$$\theta(r,p) = 0, \quad r \rightarrow \infty \quad (4.113)$$

The solution of the differential equation (4.111) is:

$$\theta(r,p) = AK_0(qr) + BI_0(qr) \quad (4.114)$$

With $q = \sqrt{p/a}$. The boundary condition (4.113) gives $B=0$. Boundary condition (4.112) leads to:

$$\theta(r,p) = \frac{K_0(qr)}{SkqK_1(qR)} \psi_R(p) \quad (4.115)$$

And,

$$\theta(R,p) = \frac{K_0(qR)}{SkqK_1(qR)} \psi_R(p) \quad (4.116)$$

When $p \rightarrow \infty$, the Bessel functions $K_n(z)$ can be replaced by their asymptotic expressions as:

$$K_n(z) \approx \frac{\sqrt{\pi} e^{-z}}{\sqrt{2z}} \left(1 + \frac{\mu-1}{8z} + \frac{(\mu-1)(\mu-9)}{(8z)^2 2!} + \dots \right), \quad \mu = 4n^2 \quad (4.117)$$

We found the useful asymptotic behaviours:

$$\lim_{|z| \rightarrow \infty} \frac{K_0(z)}{K_1(z)} = 1 \quad (4.118)$$

This leads to:

$$\theta(R, p) = \frac{1}{S k \sqrt{\frac{p}{a}}} \psi_R(p) = \frac{1}{S \sqrt{k \rho C_p} \sqrt{p}} \psi_R(p) \quad (4.119)$$

It is thus retrieved that the 1D semi infinite heat conduction at the very high frequency (very small times).

We can also use the equivalent expressions of the $K_n(z)$ Bessel functions as:

$$K_n(z) = \frac{1}{2} \left(\frac{z}{2}\right)^{-n} S_n + (-1)^{n+1} \ln\left(\frac{z}{2}\right) I_n(z) + (-1)^n \frac{1}{2} \left(\frac{z}{2}\right)^n \sum_{k=0}^{N_0} (\psi(k+1) + \psi(n+k+1)) \frac{\left(\frac{z}{2}\right)^{2k}}{k! (n+k)!}, \quad -\infty < z < \infty \quad (4.120)$$

With:

$$S_n = \sum_{k=0}^{n-1} \frac{\left(\frac{z}{2}\right)^{2k}}{k! \Gamma(n+k+1)} \quad (4.121)$$

And:

$$\psi(k) = -\gamma + \sum_{k=1}^{n-1} k^{-1}, \quad \psi(1) = -\gamma = -0,5772157 \quad (4.122)$$

Equivalently, the Bessel functions $I_n(z)$ may be replaced by their series defined as :

$$I_n(z) = \left(\frac{z}{2}\right)^n \sum_{k=0}^{N_0} \frac{\left(\frac{z}{2}\right)^{2k}}{k! (n+k)!}, \quad -\infty < z < \infty \quad (1)$$

This leads to express the following parts of relation (4.116) as:

$$K_0(qR) = \ln\left(\frac{1}{2}CRq\right) + \frac{1}{4}R^2q^2\left(\ln\left(\frac{1}{2}CRq\right) - 1\right) + \dots \quad (4.123)$$

$$qK_1(qR) = 1 + \frac{1}{2}R^2q^2\left(\ln\left(\frac{1}{2}CRq\right) - \frac{1}{2}\right) + \dots \quad (4.124)$$

$$\begin{aligned} \theta(R, p) &= \frac{K_0(qR)}{SkqK_1(qR)}\psi_R(p) \\ &= \frac{\psi_R(p)}{Sk} \left\{ \ln\left(\frac{1}{2}CRq\right) + \frac{1}{4}R^2q^2\left(\ln\left(\frac{1}{2}CRq\right) - 1\right) - \right. \\ &\quad \left. - \frac{1}{2}R^2q^2 \ln\left(\frac{1}{2}CRq\right) \left(\ln\left(\frac{1}{2}CRq\right) + \ln 1 - \frac{1}{2} \right) + \dots \right\} \\ &= \frac{\psi_R(p)}{Sk} \left\{ \frac{1}{2} \ln\left(\frac{C^2R^2p}{4a}\right) + \frac{R^2p}{8a} \ln\left(\frac{C^2R^2p}{4a}\right) - \frac{R^2p}{4a} - \right. \\ &\quad \left. - \frac{R^2p}{8a} \ln\left(\frac{C^2R^2p}{4a}\right) + \frac{R^2p}{8a} \ln\left(\frac{C^2R^2p}{4a}\right) + \dots \right\} \end{aligned} \quad (4.125)$$

Where $\gamma = \ln C$ with $C = 0.5772\dots$ is the Euler's constant. Finally, it comes to:

$$\theta(R, p) = \frac{\psi_R(p)}{Sk} \left\{ \ln\left(\frac{C^2R^2p}{4a}\right) \left(\frac{R^2p}{8a} + \frac{1}{2} \right) - \frac{R^2p}{4a} \right\} \quad (4.126)$$

For low frequency,

Let us assume that the medium is in contact with a wire or radius R that can be view as a perfect conductor. Then, the solution in the Laplace domain is:

$$\theta(r, p) = \frac{RK_0(qr)}{SkqC_w [RqK_0(qR) + \alpha K_1(qR)]} \psi_R(p) \quad (4.127)$$

Where: $\alpha = 2\pi R^2 \rho C_p / C_w$ is twice the ration of the heat capacity of an equivalent volume of the medium to that of the perfect conductor denoted C_w .

Appendix E: The PARDISO solver under Comsol software

The PARDISO solver works on general systems of the form $Ax = b$. In order to improve sequential and parallel sparse numerical factorization performance, the solver algorithms are

based on a Level-3 BLAS update, and they exploit pipelining parallelism with a combination of left-looking and right-looking supernode techniques. PARDISO is multithreaded on platforms that support multithreading. On distributed memory architectures, the solver settings are changed to corresponding MUMPS settings if needed. The code is written in C and Fortran. COMSOL Multiphysics uses the PARDISO version developed by Olaf Schenk and collaborators (www.pardiso-project.org/), which is included with Intel[®] MKL (Intel Math Kernel Libraries).

4.8. References

- [1] D. Maillet, S. André, J.-C. Batsale, A. Degiovanni, C. Moyne, *Thermal Quadrupoles: an efficient method for solving the heat equation through integral Transforms*, J. Wiley and sons, 2000.
- [2] H.S. Carslaw and J.C. Jeager, 1959, *Conduction of heat in solids*, 2nd edition, Oxford University Press, New York.
- [3] Bettess, P., 1977. *Infinite elements*. International Journal for Numerical Methods in Engineering **11**, 53–64.
- [4] Bettess, P., 1992. *Infinite Elements*. Penshaw Press, Sunderland, UK, p. 264.
- [5] COMSOL Multiphysics Modeling Guide, 2005a. *The Convection and Diffusion Application Mode*. COMSOL AB, Palo Alto, CA, p. 348.
- [6] Ljung L., *System identification: theory for the user*, Prentice Hall, 1987.
- [7] Söderstrom T. and Stoïca P., *System identification*, Prentice Hall International, London, 1989.
- [8] Battaglia J.- L., Puigsegur L., Kusiak A., *Représentation non entière de problèmes du transfert de la chaleur par diffusion. Utilité pour la caractérisation et le contrôle non destructif thermique*, Int. J. Therm. Sci. **43**, 69 (2004).
- [9] Miller K. S., Ross B., *An introduction to the fractional calculus and fractional differential equations*, A Wiley-Interscience Publication, 1993.
- [10] Oldham K. B., Spanier J., *The fractional calculus*, Academic Press, New York and London, 1974.
- [11] Samko S. G., Kilbas A. A. and Marichev O. I., *Fractional Integrals and Derivatives. Theory and applications*. Gordon and Breach, Amsterdam, 1993.

- [12] Oldham K. B., Spanier J., *The replacement of Fick's laws by a formulation involving semidifferentiation*, *Electroanalytical Chemistry and Interfacial Electrochemistry* 26 (1970) 331-341.
- [13] Oldham K. B., Spanier J., *A general solution of the diffusive equation for semi infinite geometries*, *Journal of Mathematical Analysis and Applications* 39 (1972) 655-669.
- [14] Oldham K. B., *Diffusive transport to planar, cylindrical and spherical electrodes*, *Electroanalytical Chemistry and Interfacial Electrochemistry* 41 (1973) 351-358.
- [15] Abramowitz M. and Stegun I. E., *Handbook of mathematical functions*, National Bureau of Standards, Applied Mathematics Series 55.

5. Chapter 5 – VALIDATION

5.1. Introduction

In this chapter, we will talk about all the technical factors that come into play while performing experiments using the setup we have mentioned in chapter 3. We started with the 2-point probe in static contact (motionless probe) with a SiO₂ substrate. The thermal properties of the substrate are well known and therefore this experiment leads us to identify the contact resistance at the interface between the probe and the surface assuming a value for the radius contact area. Then, we look into is the effect of the speed of the probe while scanning the SiO₂ surface. Since, as theoretically demonstrated, our numerical model is based on the consideration that the probe is in static condition at each acquisition step, it is easy to check this assumption with the experimentation and to see if the results are in agreement with our model. The next important thing that we look into is the radius of the contact area between the probe and the surface assuming it is the shape of a disk. In this case, we are trying to obtain the effective radius considering the presence of water meniscus. To achieve this objective, we used two different approaches. The first one is based on the “step” method that consists in a SiO₂ thin layer deposited as a step on a GaAs substrate. The edge of the step is expected to have an impact on the measured temperature of the probe and this impact is directly proportional to the contact radius. Therefore the contact radius can be determined ‘graphically’ from the temperature evolution along the scan. On the other hand, we proposed to use those measurements as the input of an inverse heat conduction problem (IHCP) to identify the probe radius. The model is solved using the finite element method using the precautions presented in the chapter 4. Let us remind also that, as we showed in the previous chapter, the contact radius and the thermal contact resistance at the probe-surface interface couldn’t be identified separately. Finally, we performed DC and AC (3ω) measurement on samples whose thermal conductivity is well known and varies from 0.1 to 40 W.m⁻¹.K⁻¹. Those measurements have been performed first in dynamic mode and in ambient conditions. Then the experiments have been repeated in static mode (motionless probe), under vacuum and using the 4-point probe. This kind of experiments is very useful to predict the limit of the measurable thermal conductivity using this probe and to quantify the role

of the experimental conditions on the contact radius and thermal contact resistance at the interface between the probe and the investigated surface.

5.2.2-point probe in static contact on SiO₂.

The 2-point probe from NT-MDT has been used in static mode within argon atmosphere. The experiments were started with 523Hz with gradual increase in the frequency until a frequency of 10123Hz was reached. This wide range of frequency is sufficient to understand the working on the SThM mechanism and obtain workable results. In order to derive the probe thermal impedance $Z_p(2\omega)$, experiments have been performed first with the probe out-of-contact from the surface at a current of amplitude 497.8 μ A through the Pd strip. Then, the probe has been put in contact on a thermal SiO₂ flat substrate with a 5 nN force acting on the cantilever. The properties of the thermal SiO₂ have been reported in Table 10.

The absolute temperature and the phase according to the frequency have been reported in Figure 93. We assumed that $r_0 = 100$ nm, that is the curvature radius of the probe and that is also close to the value that has been reported by other authors. It clearly appears on the figures that the amplitude in out-of-contact and in contact become indiscernible when frequency becomes higher than about 5000 Hz. It comes from the fact, that heat diffuses mainly in the cantilever at high frequency and that a very small amount of heat transfers to the investigated material. Therefore, this experiment allows fixing the useful working frequency range for the probe.

Table 10 Specification of the thermal SiO₂ sample for our experiments. The average roughness has been measured using the AFM mode.

Thermal conductivity	1.38 W.m ⁻¹ .K ⁻¹
Density	2650 kg.m ⁻³
Specific Heat	748 J.kg ⁻¹ .K ⁻¹
Debye Temperature	594 K
Sound Velocity	5700 m.s ⁻¹
Average Roughness	1.827 nm
Approximate phonon mean free path	0.36 nm

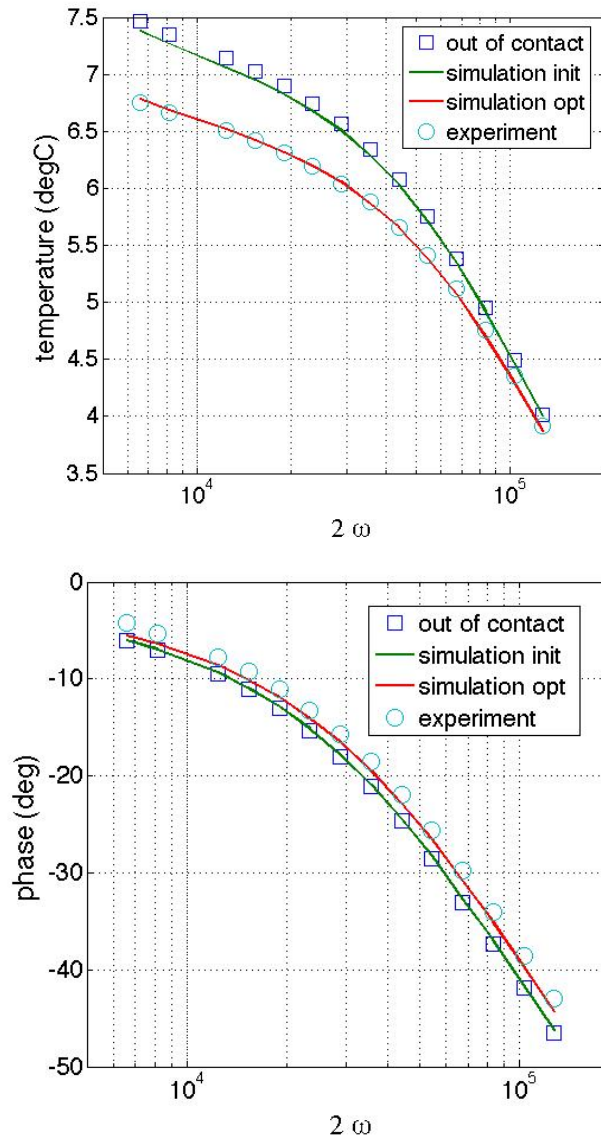


Figure 93. blue square: measured absolute probe temperature and phase in the out-of-contact mode (leading to $Z_p(2\omega)$); cyan circles: measured absolute probe temperature and phase in the contact mode; green line: calculated temperature and phase considering the initial value for R_c ; red line: calculated temperature and phase using the identified value of R_c .

We assume a high initial value as $R_c = 4 \times 10^7 \text{ K.W}^{-1}$. The minimization procedure, based on Levenberg-Marquardt algorithm (see appendix at the end of this chapter) and the model we derived in chapter 4, leads to the optimal value $R_c = (2.83 \pm 0.09) \times 10^6 \text{ K.W}^{-1}$. According to the value of the contact area radius, it means also that: $R_{cs} = R_c \pi r_0^2 = (8.9 \pm 0.29) \times 10^{-8} \text{ K.m}^2.\text{W}^{-1}$. The standard deviation has been calculated from the covariance estimated from the Hessian and

the residuals at the end of the minimization process as presented in chapter 4. Let us notice that this value for R_c is consistent with those also published by other authors using the same probe as reported in Table 11.

Table 11. Contact radius and thermal contact resistance reported in the literature for the used probe.

Authors/probe	Material	r_0 (nm)	R_c (K.m ² .W ⁻¹)
Puyoo et al. [1] 2-point Anasys	Si	100	1.29×10^{-7}
G. Yunfei [2] 2-point KNT	Si ₃ N ₄	50	$10^{-9} - 5 \times 10^{-8}$

Varying the contact radius round its nominal position and at a very higher value (250 nm) leads to the identified values of R_c reported in Figure 94.

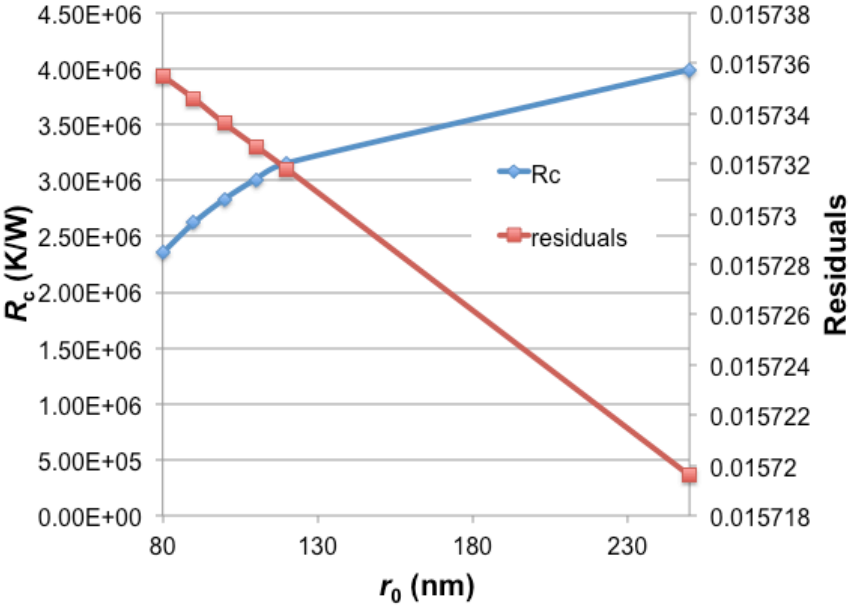


Figure 94. Value of the identified R_c when varying the contact radius r_0 . Residuals at the end of the minimization process are also reported.

It is observed that a relative change of 40% in r_0 leads to a relative change of 28 % in the value of R_c , which is thus very significant. It means, as we expected it from the beginning, that both values need to be identified accurately. On the other hand this simulation leads also to have a clear definition of what is emphasized within the definition of r_0 . Indeed, we presented in chapter

2 all the heat transfer phenomena that take place between the probe and the surface of the investigated material/device. This allows finally to define at least three specific area as represented in Figure 95.

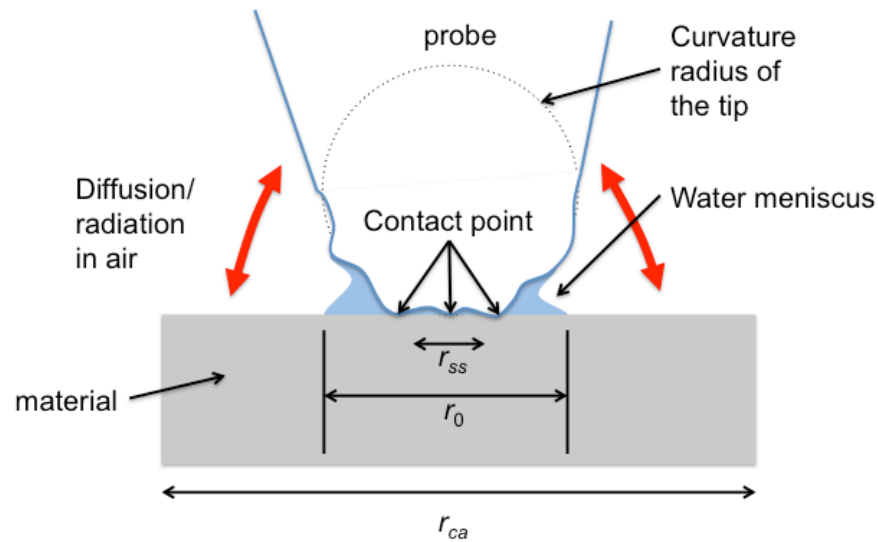


Figure 95. The contact area varies according to the experimental configuration.

Indeed, r_0 denotes in the present work value of the contact area between the probe and the surface in the presence of the meniscus of water. According to simple geometrical tools, it is thus rather normal to find that r_0 is finally very close to the curvature radius r_s of the probe tip. Therefore, measuring the curvature radius of the probe could be systematically the way to define the contact area radius with the least uncertainty when working under atmospheric or controlled atmosphere. Working under vacuum is expected to remove the water meniscus and hence to consider only the solid-solid contact area r_{ss} that is the sum of all the areas at the contact point due to the roughness of both the probe surface and that of the material surface. It is clear that $r_{ss} < r_0$ and maybe $r_{ss} \ll r_0$. In that case, two main drawbacks occur to our opinion. The first one is that the radius r_{ss} of the contact area needs to be identified since any assumption can be made and the value will depend on the roughness value for both surfaces at the low scale, on the curvature radius of the probe and on the force acting on the cantilever. The second drawback is that this smaller contact area will reduce significantly the heat flow from the probe to the material leading to decrease the sensitivity of the measurement for high thermal conductivity of the material. This suggests finally that it would be more judicious to perform SThM

measurements within atmospheric or controlled (Ar, N) atmospheres than under vacuum. The third definition of the contact area is what other authors started to name the “coupling area”. This area is assumed accounting with the conduction and radiation in air between the full probe and the surface. However, we see at least two main drawbacks with such a definition. First, although the diffusion in air can be restricted to a volume surrounding the probe, the radiation is hemispherical and therefore, the coupling area would be of infinite extension, meaning that $r_{ca} \rightarrow \infty$. The second drawback with this definition is that the contact resistance loses its physical sense since there is no more physical contact between the probe and the surface. Indeed, as presented in the Figure 94, very high value for the contact radius will lead to identify very value as well for R_c .

In conclusion, we propose to use systematically $r_0=r_s$, when working under atmospheric or controlled atmosphere and to identify r_0 when working under vacuum or with hydrophobic surfaces. More will be said for the vacuum configuration later in this chapter.

5.3. Effect of the probe motion on r_0 and R_c

We have described already the way the probe scans the surface of the investigated material/device in the chapter 3. We pointed out the fact that the motion of the probe, the acquisition time and the time constant are strongly related and will lead to choose the value of the probe velocity (expressed in sec/line) in the right and consistent way. Also in the chapter 5, we have shown that, for the expected values of the radius of the contact area as well as the probe velocity, the probe can be considered as it was in a static contact at each acquisition time, making the heat transfer model largely simplified.

Hence it becomes necessary to understand the effect of probe speed on the probe temperature measurement and the impact on identified thermal properties. Experiments were devised to understand this effect and also validate our model. Using the same SiO₂ substrate as in the previous section, we performed three scans of the surface with a different probe velocity each time. The Table 11 shows the value for the parameters that have been used to perform those scans. The frequency range has been chose as well large enough to account with possible phenomena that can occur with the frequency.

Table 12 Specifications of First Experiment Performed with Moving Probe

Specimen	SiO ₂
Image Size	1 μm
Points/line	64
Number of Points per scan and per Frequency	4096
Current	497.8 μA
Acting force	5 nN
Lock-in filter	High reserve
Time constant (lock-in)	30 msec

The measurements of the amplitude ($V_3\omega$) and the phase vs. frequency and according to different scan velocity have been reported in Figure 96 and Figure 97 respectively. Moreover, we reported also the amplitude and phase for the probe out-of-contact from the surface and the probe in static contact with the surface. It is then clear that we cannot see any significant difference between the plots when the probe is in motion or when it is motionless. This demonstrates experimentally the conclusion we drawn in the chapter 4 from the theory.

Using those data, we identified the contact thermal resistance R_c (assuming again that $r_0 = 100$ nm). The identified values of R_c are reported in Table 13.

Table 13 Resistance of Contact obtained from different probe speeds under contact condition over a known sample of SiO₂

Speed of Probe	Contact Resistance R_c $\times 10^6 \text{ K.W}^{-1}$	Surface Contact Resistance $R_c \times 10^{-7}$ $\text{K.m}^2.\text{W}^{-1}$
0 μm/sec (static)	(2.83 ± 0.09)	(0.889 ± 0.01)
0.7 μm/sec	(3.5 ± 0.22)	(1.09 ± 0.06)
1.2 μm/sec	(3.42 ± 0.22)	(1.07 ± 0.06)

Although any graphical difference was clearly observable, the identification of R_c indicates that this parameter varies however significantly of about 23% from its value in static contact. This is not a surprising result since several studies at the macroscopic level have shown that the sliding contact resistance is always higher than the static resistance considering the same contact area

and the same force. However, it means that the experiment needs to be as such accurate to observe this difference. Indeed, the average (over the frequency) voltage relative variation between the static contact and the dynamic contact is only 1.14%. It is very low compared to the standard deviation on the measured voltage by the lock-in that is less than 5%.

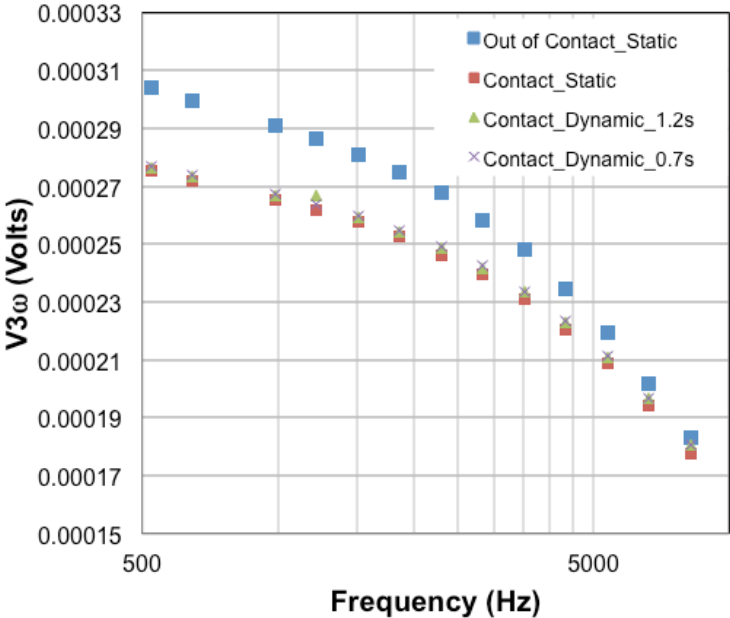


Figure 96 Measured amplitude vs. frequency for contact and non-contact conditions.

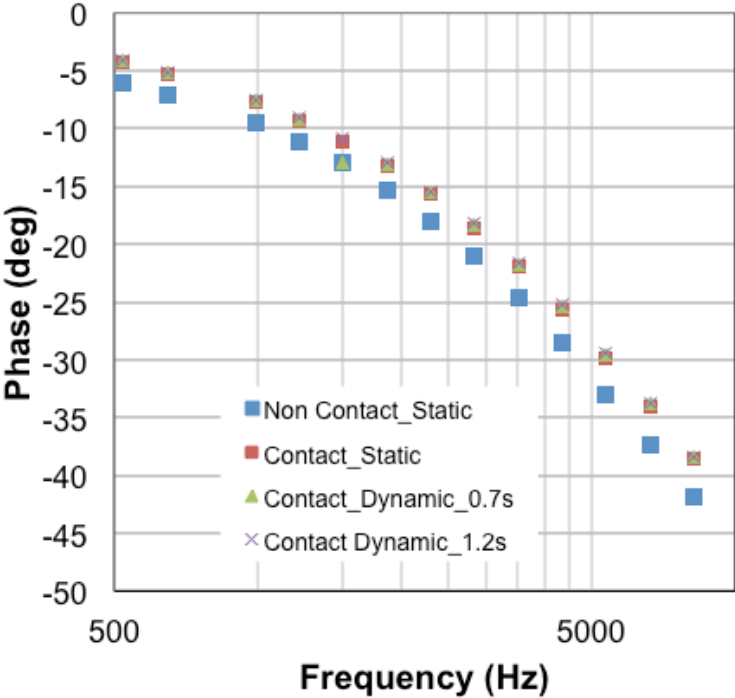


Figure 97 Measured phase vs. frequency for contact and non-contact conditions.

5.4. Radius of the contact area measurement

5.4.1. The step technique

To measure the effective radius of the probe, we have utilized an abrupt step sample utilizing the 3ω technique following the steps of E. Puyoo *et al.* [1] who published a scientific paper on this process in 2010. We have a step sample made of approximately 100 nm thick SiO_2 deposited on a 500 μm thick GaAs substrate. The current in the probe is 800 μA and the force acting on the cantilever is 5 nN. We reported the temperature measured when the probe scanned one line of the image as well as the measured temperature along the line on Figure 99 when $f=3000$ Hz.

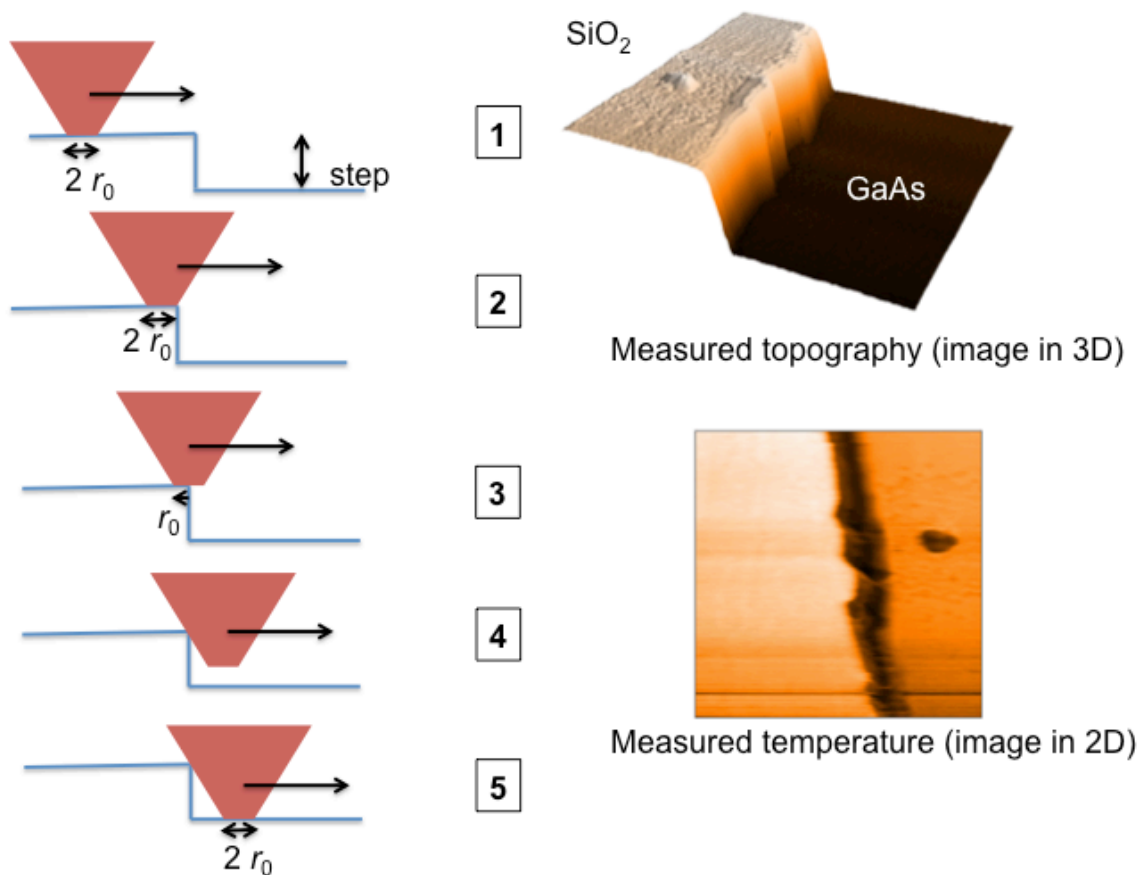


Figure 98. This figure tries to replicate the movement of the probe across one line when the probe scans one line of the surface of the sample. The brown triangles indicate the probe while the blue shapes mark the area of contact. The measured topography and probe temperature are also represented on the right for the image (the shadowed area on the temperature image indicates the temperature increase when the probe approaches the edge of the SiO_2 step).

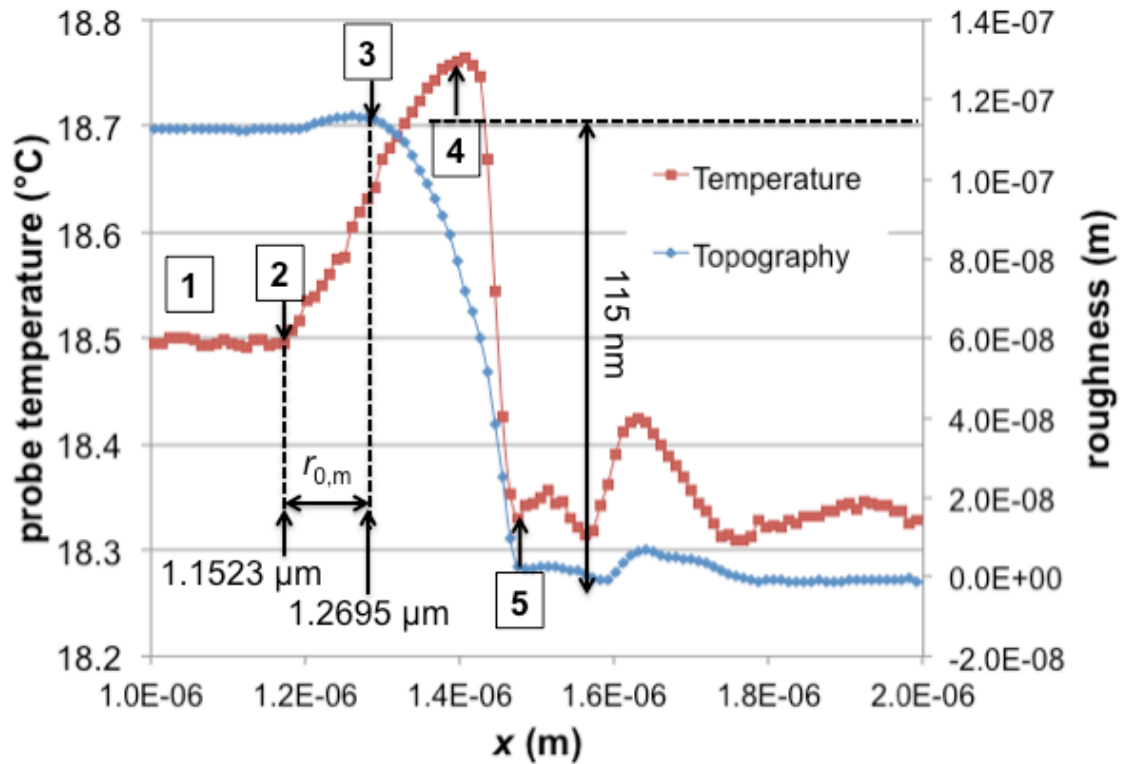


Figure 99. Measure topography and probe temperature when the probe scans one line of the surface of the sample constituted by a SiO₂ (115 nm) layer deposited as a step on a GaAs substrate ($f=3000$ Hz).

In order to analyze the results, 5 strategic locations of the probe have been indicated on the Figure 98 and also reported on the Figure 99. The probe starts moving from the position 1 on the SiO₂ sample. At position 2, as the probe starts getting closer to the edge, the temperature comes to be influenced by the edge and it is observed an increase. The location 2 is arbitrarily defined as when the half-contact area of radius $r_0/2$ is reached between the probe and the surface. This leads to an increase in the probe temperature. Position 3 indicates the edge of the step. When the probes starts to leave the step and comes to “fall” down on the GaAs substrate, there is a time where the probe is in contact only by its side with the step as represented by location 4 on the figure. The reached temperature is more or less equal to that obtained in the out-of-contact mode since the heat flux leaving the probe for the step is very low given to the contact point. Finally, when the probe comes onto contact with the GaAs substrate at location 5, the temperature becomes constant again and lower than that measured when the probe was in contact with the SiO₂.

We thus can estimate the contact radius as the distance between position 2 and 3 on the Figure 99. We found that $r_{0m} = 117$ nm. It is to be remembering that the effective radius takes into consideration the presence of any water meniscus at the edge of the probe tip. This value is rather close to the expected value we found previously (100 nm). However, this technique can only lead to an approximation and a more accurate result could be obtained by using a minimization technique between the measured temperature (from location 1 to 3) and a finite element model. Indeed, we know that the probe temperature is expected to increase as the probe approached closely to the edge. However this influence can be noticed when the probe is far away than $2 r_0$ from the edge of the step since we defined this dimension very arbitrarily.

5.4.2. Identification of r_0

In order to accurately determine the contact radius, we performed a minimization process between the experimental data and the simulated ones. The model is based on a finite element code based on the geometry represented on Figure 100. The SiO₂ layer is 115 nm in thickness, as showed on the Figure 99. The GaAs substrate is considered as a semi-infinite medium with respect to the finite element code (see chapter 4). The mesh is based on tetrahedral elements with a refinement at the location of the contact area between the probe and the surface. The number of DoF (degree of freedom) of the mesh is about 185000. However, this number can change slightly since the geometry is re-meshed considering each location of the probe on the surface during the scan. The average temperature on the contact area is calculated using a 6 order integration technique. The minimization is achieved using the Levenberg-Marquardt algorithm.

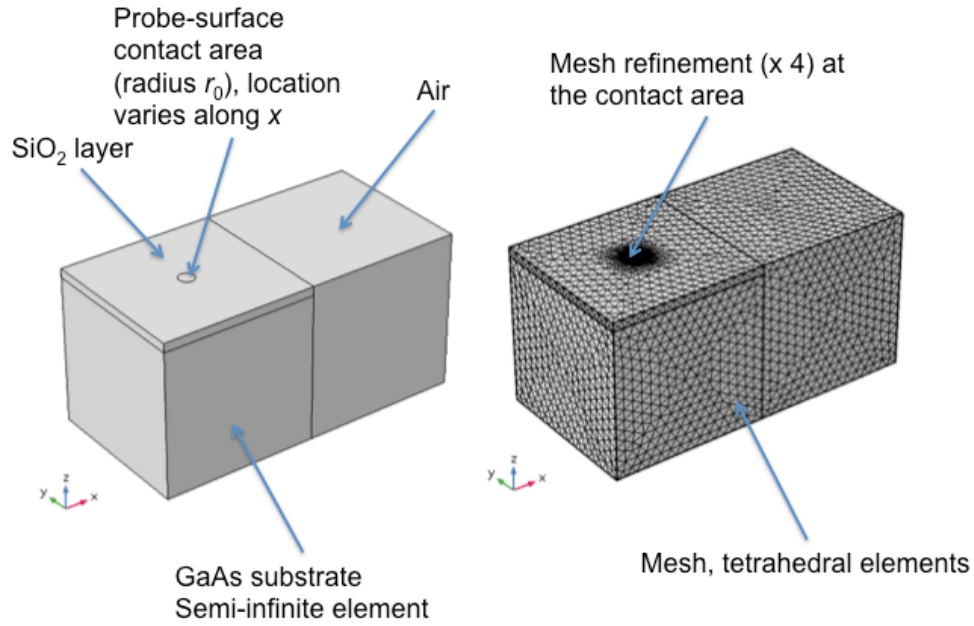


Figure 100. Geometry of the studied configuration represented on the left image. The mesh is represented at the right.

The simulation can be only performed when the probe reaches the edge of the step since we are not able to simulate the configuration 4 of the Figure 98 when the probe leaves the SiO₂ step. Instead, we can simulate the configuration 5 when the probe comes in contact with the GaAs substrate.

The model has been described in chapter 4 and there is no need to remind it here. The thermal properties of the SiO₂ and the GaAs are reminded in Table 14. The thermal impedance of the probe at 3000 Hz is given by the out-of-contact measurement (see Figure 93). The minimization process is quite long since we have to simulate the probe temperature during the scan of the line with time step of 20 nm. For instance the computation time when x varies from $x = -400$ nm to $x = 0$ with 20 nm sampling time interval is 12 min 11 sec.

Table 14. Thermal properties of SiO₂, GaAs and air used for the finite element simulation.

	SiO ₂	GaAs	Air
ρ (kg.m ⁻³)	2200	5320	1
C_p (J.kg ⁻¹ .K ⁻¹)	787	330	1003
k (W.m ⁻¹ .K ⁻¹)	1.4	5.5	0.016

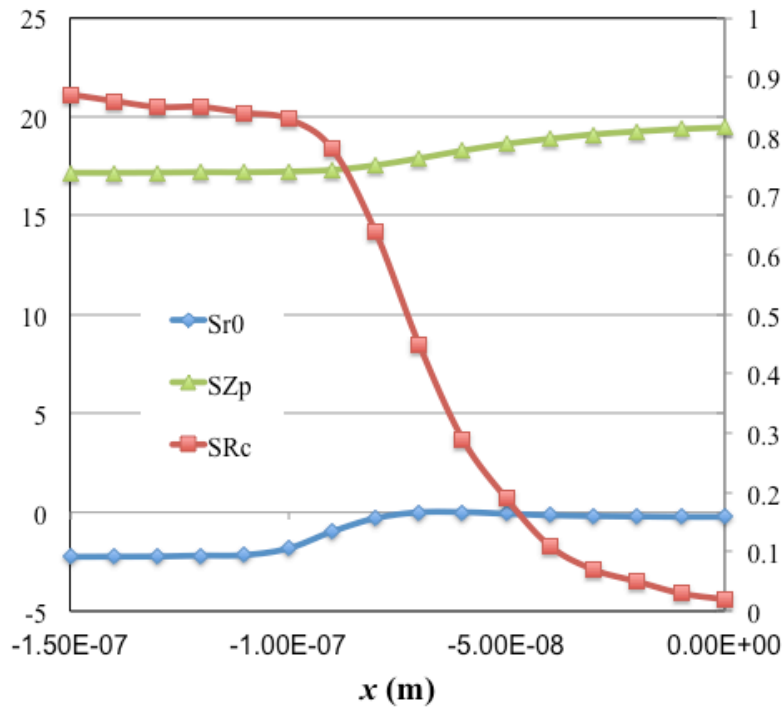


Figure 101. Sensitivity functions of the probe temperature according vs. the contact radius r_0 , the thermal contact resistance R_c and the probe thermal impedance Z_p according to the location x of the probe on the surface.

In a first stage we performed the sensitivity study of the calculated probe temperature according vs. the contact radius r_0 , the thermal contact resistance R_c and the probe thermal impedance Z_p according to the location x of the probe on the surface. The three functions are reported on Figure 101.

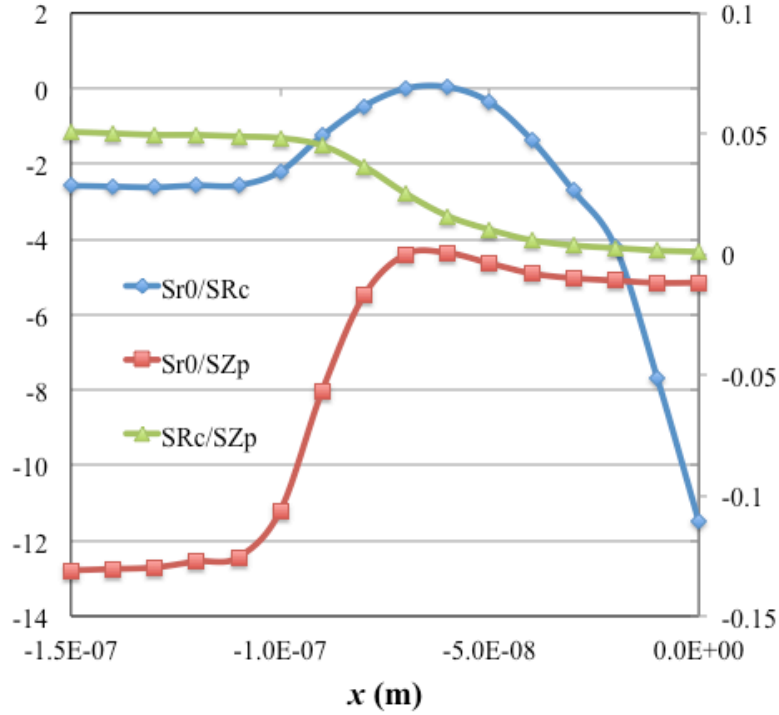


Figure 102. Ratio of the sensitivity functions.

The ratio of the three sensitivity functions have been calculated and plotted on Figure 102. They clearly indicate that the simultaneity estimation of the three parameters is possible since the ratios are not constant on the x range presented on the figure by the x -axis. Obviously it is clear that this range is clearly related to the contact radius r_0 .

The identification of the three parameters leads to: $r_0 = 101 \pm 3 \text{ nm}$, $R_c = 1.39 \times 10^{-7} \text{ K.m}^2.\text{W}^{-1}$ and $Z_p = ((4.58 \pm 0.01) - j(1.83 \pm 0.01)) \times 10^5 \text{ K.W}^{-1}$. The fit with the data is represented on Figure 103 as well as the simulated probe temperature *vs.* x for $r_0 = 50 \text{ nm}$ and $r_0 = 150 \text{ nm}$. It is clear first that the contact radius is very close, almost equal, to the curvature radius of the probe. On the other hand, it appears that the graphical extraction of r_0 as we did in the first approach is not far from the “exact” value, although the minimization approach is much more accurate. We also obtained that the thermal contact resistance R_c is slightly higher than that found previously in the motionless configuration of the probe. It is also very close to the value found by other authors and reported in Table 11. Finally, the value for Z_p at 3000 Hz remains unchanged with respect to the one we measured in the out-of-contact mode (Figure 93). This means that the probe thermal impedance is not sensitive to the contact with the material.

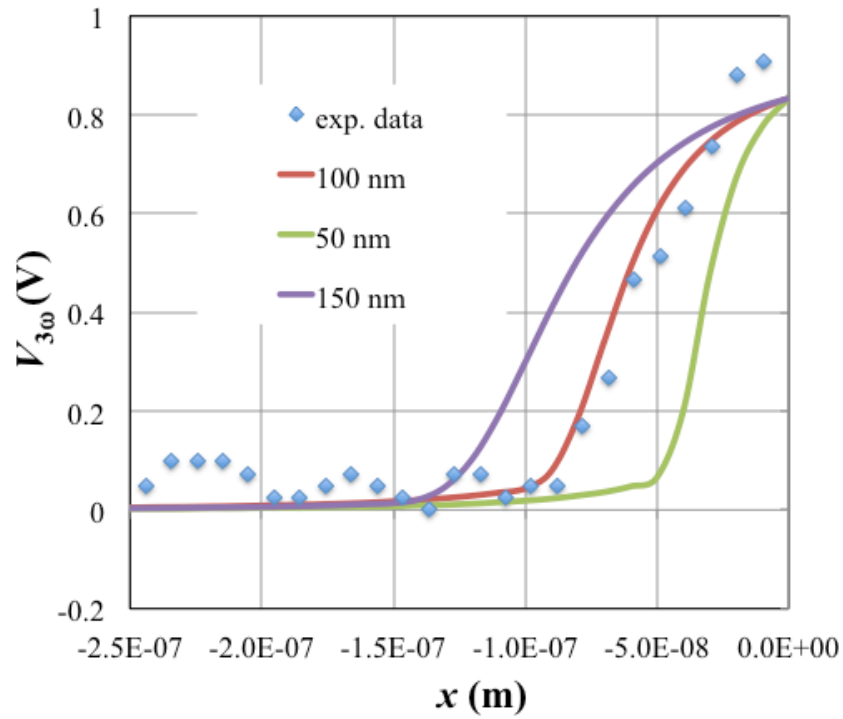


Figure 103. Comparison between the measured data and the calculated one with the identified parameters $r_0 = 101 \pm 3 \text{ nm}$, $R_c = 1.39 \times 10^{-7} \text{ K.m}^2.\text{W}^{-1}$ and $Z_p = ((4.58 \pm 0.01) - j(1.83 \pm 0.01)) \times 10^5 \text{ K.W}^{-1}$. The simulations with two different values for r_0 (50 and 150 nm) are also reported.

It must be also noted that, using the identified parameters we retrieved well the temperature when the probe is in contact with the GaAs substrate after the step as present in Figure 104.

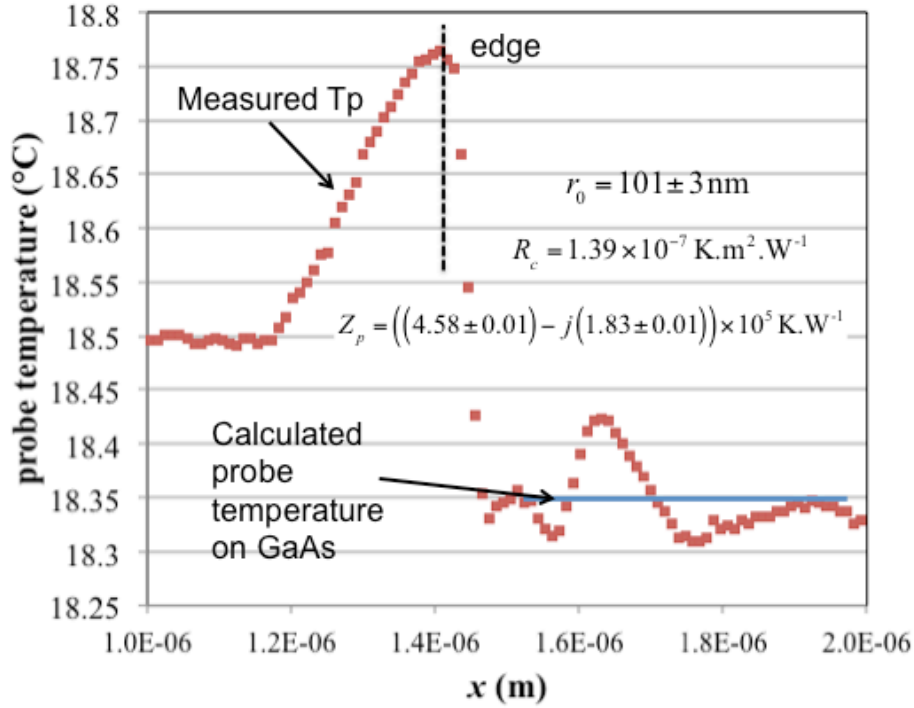


Figure 104. Comparison between the measured data and the calculated one with the identified parameters $r_0 = 101 \pm 3 \text{ nm}$, $R_c = 1.39 \times 10^{-7} \text{ K.m}^2.\text{W}^{-1}$ and $Z_p = ((4.58 \pm 0.01) - j(1.83 \pm 0.01)) \times 10^5 \text{ K.W}^{-1}$ when the probe is in contact with the GaAs substrate (after the edge of the step).

5.5. Identification of r_0 and R_c under ambient conditions with the probe in motion

Six samples, whose thermal conductivity varies from 0.2 to 41 $\text{W.m}^{-1}.\text{K}^{-1}$, have been investigated. The thermal properties of these materials are reported in Table 15. The roughness, measured by AFM, varies from 0.8 nm at the minimum to 1.82 nm at the maximum. The probe is the 2 contact probe from Anasys with a Si_3N_4 cantilever (GLA-1). The force acting on the cantilever is 5 nN, the probe motion is 3 sec/line and the lock-in time constant is 30 msec. The frequency for the 3w method has been chosen as 1123 Hz. A scan has been performed for each sample, considering a frame of 32 lines and 32 columns. The probe temperature has been measured during the scan. An average over all the recorded data for each scan is performed in order to deduce the average probe temperature during the motion. We have reported on Figure 105 the calculated values and the standard deviation calculated from the recorded data on each image. Using those average measured temperature and the analytical model that has been presented in chapter 4, we can identify the values of r_0 and R_c that lead to the minimum quadratic

gap between both values. We applied the Levenberg-Marquardt algorithm detailed in the appendix and we found $r_0 = 101 \pm 4 \text{ nm}$ and $R_c = (1.4 \pm 0.2) \times 10^{-7} \text{ K.m}^2.\text{W}^{-1}$. The simulated probe temperature is reported in the Figure 105 using the identified values.

Table 15. The table above shows the thermal conductivity (k), density (ρ), specific heat (C_p), Debye temperature (Θ), sound velocity (v), roughness (Ra), approximate mean free path (Λ) for Palladium, PMMA, SiO₂, ZnO, TiO₂, Al₂O₃, MgO and Si₃N₄ respectively

	Palladium m Pd (probe)	PMMA	SiO ₂	ZnO	TiO ₂	Al ₂ O ₃	MgO	Si ₃ N ₄ (probe cantilever)
$k \text{ (W.m}^{-1}.\text{K}^{-1}\text{)}$	72	0.19	1.38	2.5	12.6	23.1	40.6	9.6
$\rho \text{ (kg.m}^{-3}\text{)}$	12132	1188	2650	6100	4260	3980	3580	2500
$C_p \text{ (J.kg}^{-1}.\text{K}^{-1}\text{)}$	240	1450	748	495	691	761	837	520
$\Theta_D \text{ (K)}$	275	115	594	416	760	1030	950	1178
$v \text{ (m.s}^{-1}\text{)}$	3070	1700	5700	3868	5594	7929	6870	11000
$Ra \text{ (nm)}$	-	0.752	1.827	0.867	1.265	1.206	0.869	-
$\Lambda = 3k / v\rho C_p$	-	0.19	0.36	0.64	2.29	2.88	5.91	-
Ref.	[9][10]	[12][13]	[10][13]	[10][14]	[10][14][17]	[10][14]	[10][14] [18]	[15][16]

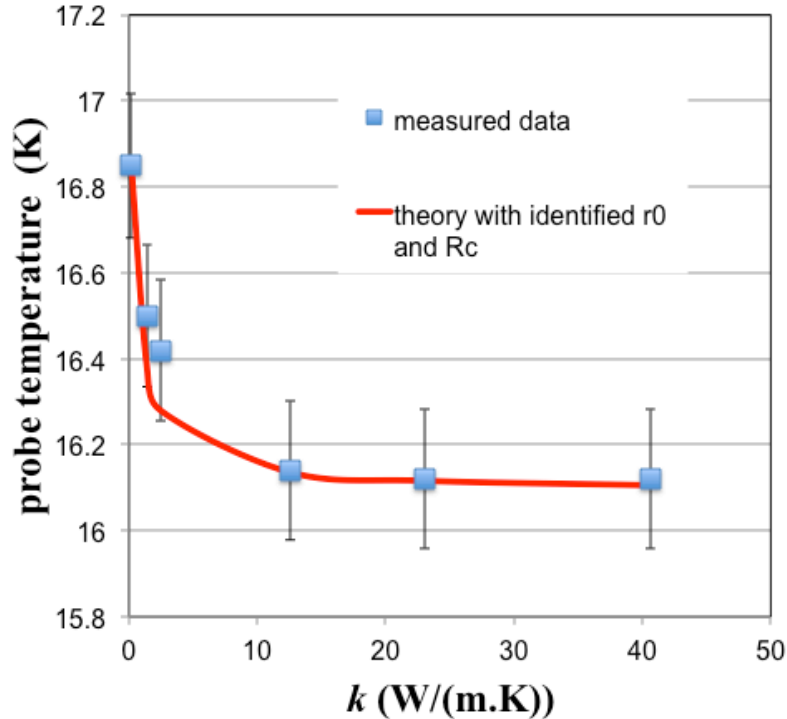


Figure 105. Spatial average probe temperature from (32x32) scan for the 6 samples.

Those results confirm first that considering the same contact radius and thermal contact resistance is valid for a class of materials that includes the dielectrics and the semiconductors. On the other hand, it is also retrieve the value for r_0 and R_c we measured previously.

5.6. SThM experiments in vacuum on samples with known thermal conductivity using the 4-point probe

In order to investigate the SThM measurements under vacuum we realised a specific experimental setup. Indeed, our AFM device being unable to work under vacuum, we needed to realize a homemade setup that is represented in Figure 106. We tested the 4-point probe that has been described in chapter 3. The probe is attached to a 1D piezoelectric device allowing working under secondary vacuum and with 1 nm displacement resolution. The piezo device with the probe are then put inside a vacuum chamber where secondary vacuum is performed thanks to a molecular pump. The most critical point was to approach the probe in safe contact with the surface of the investigated samples without the help of a laser beam reflecting on the cantilever. We therefore used the change in the probe temperature as described. The approach was controlled though a homemade program. It was obviously a longer process than the one on the AFM, and even more difficult because of the transparency of several samples we have

investigated that does not allow us to use the camera to approach manually the probe to the surface the closest. In addition, this setup allowed us to work in static contact only since the scan of the probe was not permitted any longer.

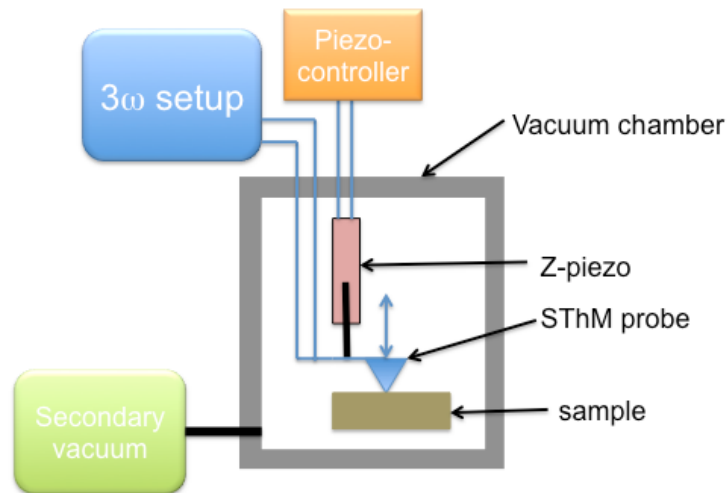


Figure 106. Experimental setup for SThM measurement under vacuum.

The six samples, presented in the previous section, were simultaneously placed in a vacuum chamber at a pressure of 1 mPa. We checked the repeatability of the contact measurement and the absence of hysteresis by successively placing the probe in and out of contact three times at different locations on the surface. The standard deviation on the measurements (amplitude and phase) is less than 5%. The experimental results for the amplitude in the out-of-contact and contact modes are reported in Figure 107. It is not observed significant variation of the measured phase whatever the material in the investigated frequency range.

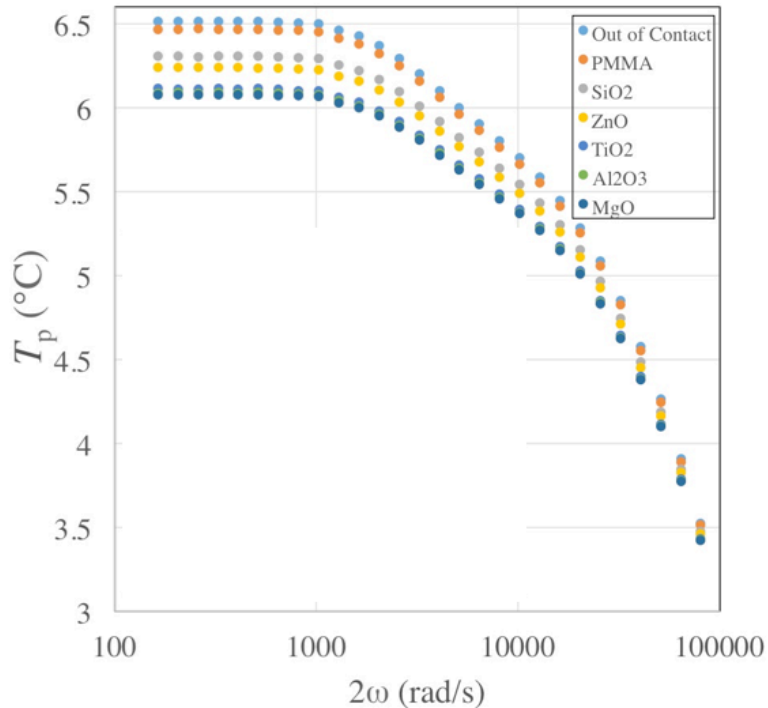


Figure 107 Measured magnitude of the temperature probe according to the frequency for the out of contact and the contact mode with the different materials.

As expected, it is well observed that the measured probe temperature decreases as the sample thermal conductivity increases. However, as the thermal conductivity becomes high, it is quite difficult to discriminate the signals.

As a major assumption, we will consider that the thermal resistance at the interface between the probe and the material as well as the radius of the contact area remain essentially the same for all the investigated samples. From the results of Figure 107, the normalized measured temperature, with respect to the maximum temperature at each frequency, is plotted according to the sample thermal conductivity in Figure 108 for four investigated frequencies. As observed in the previous figure, it is well shown there that the signal becomes quite constant starting from $25 \text{ W}\cdot\text{m}^{-1}\cdot\text{K}^{-1}$ whatever the frequency. However, as observed in the previous representation, we showed it was even more pronounced at high frequency since the generated heat remains confined within the probe. The main reason is of course that decreasing the contact radius in order to improve the spatial resolution, leads also to reduce the amount of flux flowing into the sample. This makes this kind of probe less sensitive to the Wollaston probe that offers much higher contact area with the sample.

In Figure 109, we plotted the quantity $S_{T_p}(R_c)/S_{T_p}(r_0)$ according to k_m , at $f=1219$ Hz, using the model derived in the previous chapter and the difference scheme. Instead of what happen in the frequency range, the identification of both R_c and r_0 is then feasible since the ratio is not constant.

The data of the Figure 108 are used in a Levenberg-Marquardt algorithm to identify R_c and r_0 and their associated standard deviation as $R_c = (6.22 \pm 0.009) \times 10^6 \text{ K.W}^{-1}$ and $r_0 = (25.20 \pm 0.15) \text{ nm}$. This corresponds to a surface thermal contact resistance of $(1.22 \pm 0.014) \times 10^{-8} \text{ K.m}^2.\text{W}^{-1}$. The standard deviation of the identified values has been calculated classically from the covariance matrix of the 2 parameters and from the residuals at the end of the iterative minimization. Therefore, the radius contact area is clear decreased with respect to its value (about 100 nm) when working under atmospheric or controlled atmosphere. This allows us to define the equivalent radius of the solid-solid contact area in vacuum to the about the third of that found under atmosphere. This was therefore not a very surprising result. On the other hand, we found that the thermal resistance at the interface was lower than that we found when performing the experiment on SiO_2 under atmospheric conditions.

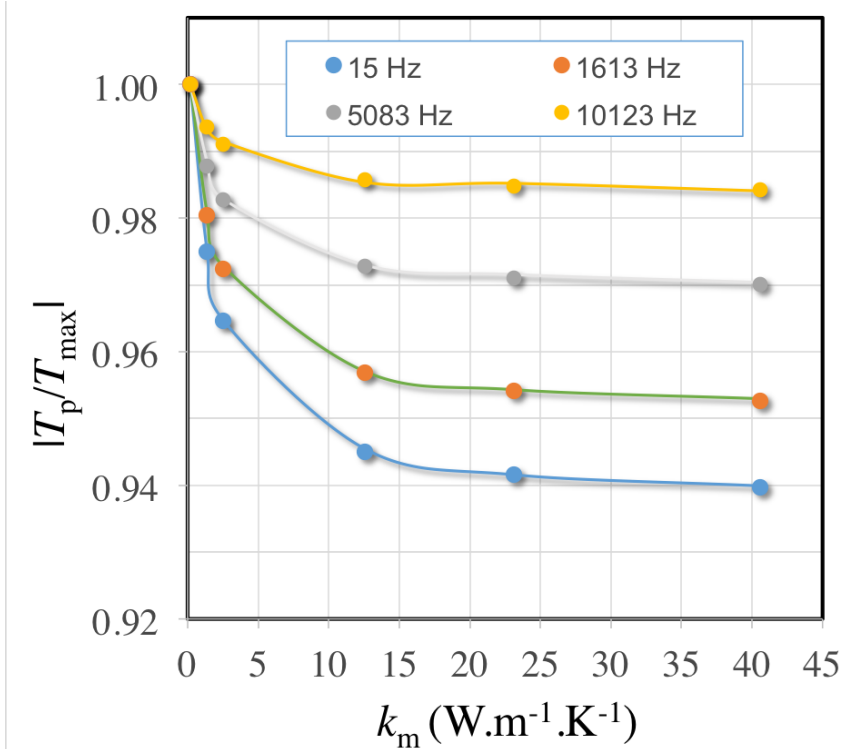


Figure 108. Normalized measured temperature, with respect to the maximum temperature at each frequency, according to the thermal conductivity at four frequencies (filled circles: measurements, plain line: theory from identified values of R_c and r_0).

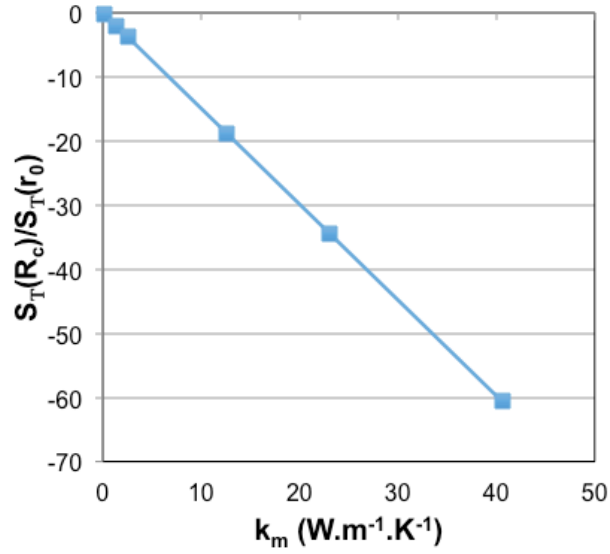


Figure 109. Ratio between the sensitivity function of the probe temperature vs. R_c and that vs. r_0 according to k_m at 1219 Hz (calculation have been made with $r_0=100$ nm and $R_c=4 \times 10^6$ K.W⁻¹).

In order to confirm those results from a different approach, we performed measurements of $\Delta P/P$ in DC mode as it was presented in the chapter 3. The results are reported in Figure 110. Those data show very clearly that approximately 90% – 99% flux generated by the probe diffuses into the probe itself and is not transmitted into the sample.

Using the model, it is clear (as pointed out also in chapter 4) that:

$$\frac{\Delta P}{P} = \frac{R_p}{R_c + R_m} = \frac{R_p}{R_c + 8 / (3k_m \pi^2 r_0)} \quad (5.1)$$

where k_m denotes the thermal conductivity of the sample and R_p is the thermal resistance of the probe. The sensitivity functions of $\Delta P/P$ with respect to R_c and r_0 according to k_m are:

$$S_{\frac{\Delta P}{P}}(R_c) = \frac{-R_p}{(R_c + 8 / (3k_m \pi^2 r_0))^2} \quad (5.2)$$

and

$$S_{\frac{\Delta P}{P}}(r_0) = \frac{-8 R_p / 3 k_m \pi^2 r_0^2}{(R_c + 8 / 3 k_m \pi^2 r_0)^2} \quad (5.3)$$

Therefore,

$$\frac{S_{\frac{\Delta P}{P}}(r_0)}{S_{\frac{\Delta P}{P}}(R_c)} = \frac{8}{3k_m \pi^2 r_0^2} \quad (5.4)$$

That is not constant when km varies, making thus the identification of r_0 and R_c feasible using the data of Figure 110.

By applying the Levenberg-Marquardt minimization algorithm and the model, we obtained $R_c = (6.92 \pm 0.4) \times 10^6 \text{ K.W}^{-1}$ and $r_0 = (28 \pm 5) \text{ nm}$. These values are very close to those identified in AC mode. However, the accuracy in AC mode is a hundred-times higher than that in the DC mode because the number n_f of data points increases with the investigated frequency, thus decreasing the standard deviation by n_f .

Therefore, one obtains the asymptotic behaviours as:

$$\begin{aligned} \frac{\Delta P}{P} &\rightarrow \frac{R_p}{R_c} \text{ when } k_m \rightarrow \infty \\ \frac{\Delta P}{P} &\rightarrow \frac{R_p}{8 / (3k_m \pi^2 r_0^2)} \text{ when } k_m \rightarrow 0 \end{aligned} \quad (5.5)$$

We obtained the thermal resistance R_p of the probe using the frequency dependent experiments (Figure 107) when $\omega = 180 \text{ Hz}$ (since we observed that the signal was constant from this value).

We obtained $R_p = (4.74 \pm 0.12) \times 10^5 \text{ K.W}^{-1}$.

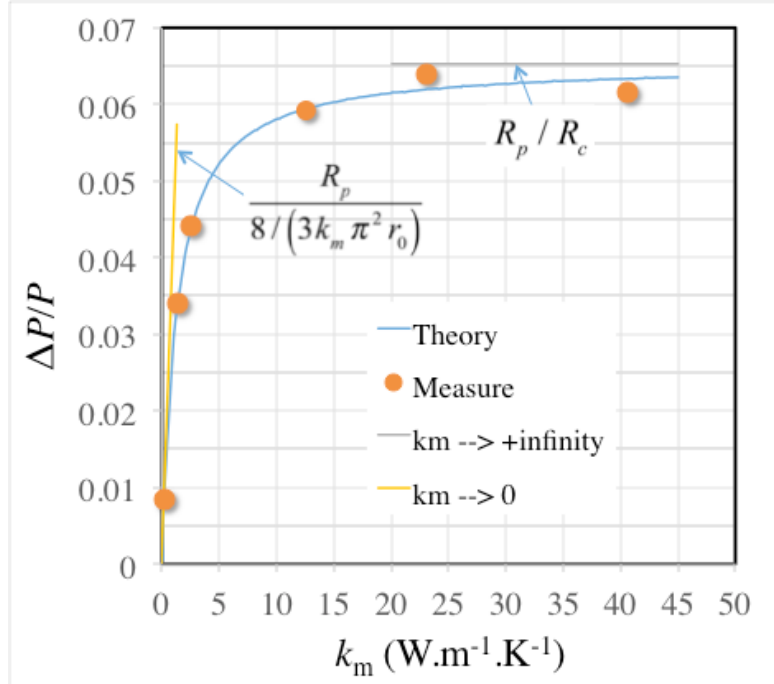


Figure 110. Measured relative variation of power as a function of the thermal conductivity of the samples in the DC mode. The theoretical curve has been calculated from the identified values of R_c and r_0 . The asymptotic behaviors are reported considering both the lowest and highest values for k_m .

Using the asymptotic behaviours in relation (5.5) leads to $R_c = (7.30 \pm 0.4) \times 10^6 \text{ K.W}^{-1}$ and $r_0 = (25.8 \pm 4) \text{ nm}$ using the value of $\Delta P/P$ when $k=0.19 \text{ W.m}^{-1}.\text{K}^{-1}$. Those results are in good agreement with those achieved using the minimization process. However, it is clear that the error comes from the estimation of the asymptotic value of $\Delta P/P$ for large k_m and by the fact that we used only the lowest value of k_m to estimate r_0 .

An estimation of R_{ph} from the Diffuse Mismatch Model can be obtained using the data in Table 15

Since the Debye temperature for all the samples are always smaller than the Palladium in the probe and the working temperature is high, the Diffuse Mismatch Model can be simplified to:

$$R_{ph} = \frac{4}{\tau_{m/Pd} v_m \rho_m C_{p,m}} \quad (5.6)$$

where ρ_m and $C_{p,m}$ are the density and specific heat of the sample and $\tau_{m/Pd} \sim v_m^{-2} / (v_{Pd}^{-2} + v_m^{-2})$ is the phonon transmission coefficient, with v_i denoting the speed of sound in the material i . The results of the calculations are reported in Table 16. It is clear that the calculated values from the DMM are one to two orders of magnitude lower than the measured R_c ($1.527 \times 10^{-8} \text{ K.m}^2.\text{W}^{-1}$).

Moreover, considering that the approximate mean free path Λ is lower than r_0 for all the samples, having a phonon confinement close to the tip leading to an increase in the thermal contact resistance as proposed in [3] is not expected. Therefore, obtaining the same value for R_c for all k_m means that this contact resistance is almost equal to the heat flux constriction resistance in the probe close to the contact area. Indeed, the diffusion in air is not present in vacuum condition. Moreover the absolute temperature change of the probe remains low (below 10 K) and therefore radiation is not expected to act significantly.

Table 16 Calculation of R_{ph} from the approximation of the Diffuse Mismatch Model at high temperature.

	PMMA	SiO ₂	ZnO	TiO ₂	Al ₂ O ₃	MgO
$R_{ph} \times 10^{-9}$ K.m ² .W ⁻¹ (DMM)	5.82	0.89	0.65	0.88	1.31	1.10

5.7. Conclusion

The experiment performed on a SiO₂ substrate leads to consider that the radius of the contact area between the probe and the sample is more or less equal to the curvature radius of the probe.

The probe motion induces a thermal resistance at the interface that is a bit higher than that measured in static contact. This observation is consistent with the results obtained already for a long time regarding the sliding thermal contact resistance at the macroscale.

Measuring the radius r_0 of the contact area between the probe and the investigated surface has been achieved using the graphical ‘step’ response. The result is quite satisfying. However, we have showed that it can be identified more accurately by implementing an inverse approach based on a finite element model and the measurement acquired during the scan of the step. This leads not only to identify r_0 with a higher confidence interval but we have shown that it also allow to identify the thermal contact resistance R_c at the interface between the probe and the surface as well as the value of the probe impedance at the working frequency. We showed that the probe impedance is not changed with respect to the one we measured during the out-of-contact mode. On the other hand we have to insist on the fact that the contact radius as well as

the thermal contact resistance did not vary when the probe scan a heterogeneous surface as that of the step sample. This is a strong assumption since we know that surfaces can behave very differently according to their roughness, hardness and wettability (for the water meniscus shape and size). However, it seems that this assumption is reasonable for a large class of materials, including the dielectrics and semiconductors. It seems maybe difficult to justify this assumption for metallic surfaces since we did not performed such experimental validation so far.

The assumption of unchanged R_c and r_0 has been well validated also for the experiments performed under ambient and vacuum conditions since it allows identifying the change of probe temperature according to the thermal conductivity k_m of the material without a visible bias. However, we are aware that it does not constitute a rigorous demonstration. The radius of the solid-solid contact, when working under vacuum, has been well identified and is approximately the third (approx. 30 nm) of that measured under atmospheric condition (approx. 100 nm). In static condition (motionless probe), the identified R_c under vacuum ($(1.22 \pm 0.014) \times 10^{-8} \text{ K.m}^2.\text{W}^{-1}$) has been found significantly lower than that found under atmospheric condition ($(8.9 \pm 0.29) \times 10^{-8} \text{ K.m}^2.\text{W}^{-1}$). This significant difference could be attributed to both the diffusion in air and to the water meniscus formation that does not occur anymore under vacuum. However, the role of water meniscus is favourable to decrease the value of R_c , considering the same r_0 for vacuum and atmospheric conditions. In a sense, this confrontation would suggest that the diffusion in air is high when working under atmospheric condition and is maybe the most important contribution in R_c . The calculated resistance from the DMM shows that the experimental value is related to other phenomena as the micro constriction resistance linked with the roughness of both surfaces in contact.

5.8. Appendix : the Levenberg-Marquardt (LM) algorithm

The (LM) algorithm consists in minimizing the quadratic gap $J(\theta)$ between experiment data y and simulated ones from a model. With:

$$J(\theta) = \sum_{i=1}^N (y_i - \bar{y}_i)^2 = (\mathbf{y} - \bar{\mathbf{y}})^T (\mathbf{y} - \bar{\mathbf{y}}) \quad (5.7)$$

Using a series expansion it is found:

$$\bar{y}(\theta + \Delta\theta) \approx \bar{y}(\theta) + \frac{d\bar{y}(\theta)}{d\theta} \Delta\theta \quad (5.8)$$

replacing this expression in (5.7), it follows that:

$$J(\theta + \Delta\theta) \approx \mathbf{y}^T \mathbf{y} + \bar{\mathbf{y}}^T \bar{\mathbf{y}} - 2\bar{\mathbf{y}}^T \bar{\mathbf{y}} - 2(\mathbf{y} - \bar{\mathbf{y}})^T \nabla_{\theta} \bar{\mathbf{y}} \Delta\theta + \Delta\theta^T (\nabla_{\theta} \bar{\mathbf{y}})^T (\nabla_{\theta} \bar{\mathbf{y}}) \Delta\theta \quad (5.9)$$

The value $\Delta\theta$ that minimizes J is found from:

$$\frac{d\bar{\mathbf{y}}(\theta + \Delta\theta)}{d\Delta\theta} = 0 \quad (5.10)$$

With relation (5.9), it comes to:

$$\frac{d\bar{\mathbf{y}}(\theta + \Delta\theta)}{d\Delta\theta} \approx -2J(\theta + \Delta\theta) \approx -2(\mathbf{y} - \bar{\mathbf{y}})^T \nabla_{\theta} \bar{\mathbf{y}} + 2\Delta\theta^T (\nabla_{\theta} \bar{\mathbf{y}})^T (\nabla_{\theta} \bar{\mathbf{y}}) \quad (5.11)$$

therefore:

$$\Delta\theta = \left((\nabla_{\theta} \bar{\mathbf{y}})^T (\nabla_{\theta} \bar{\mathbf{y}}) \right)^{-1} (\nabla_{\theta} \bar{\mathbf{y}})^T (\mathbf{y} - \bar{\mathbf{y}}) \quad (5.12)$$

And we procedure is iterative as:

$$\theta^i = \theta^{i-1} + \Delta\theta^{i-1} \quad (5.13)$$

This is the classical Newton-Gauss algorithm. The process stops regarding the relative change of J between two successive iterations. The LM method introduces a parameter λ as:

$$\Delta\theta = \left((\nabla_{\theta} \bar{\mathbf{y}})^T (\nabla_{\theta} \bar{\mathbf{y}}) + \lambda \text{diag} \left[(\nabla_{\theta} \bar{\mathbf{y}})^T (\nabla_{\theta} \bar{\mathbf{y}}) \right] \right)^{-1} (\nabla_{\theta} \bar{\mathbf{y}})^T (\mathbf{y} - \bar{\mathbf{y}}) \quad (5.14)$$

The parameter λ is modified during the iteration process in order to insure the matrix inversion as:

$$\lambda^i = \lambda^{i-1} \text{diag} \left[(\nabla_{\theta} \bar{\mathbf{y}})^T (\nabla_{\theta} \bar{\mathbf{y}}) \right]^{i-1} \quad (5.15)$$

The gradients are the sensitivity functions that are calculated using a difference scheme as:

$$(\nabla_{\theta} \bar{\mathbf{y}}) = \frac{\bar{\mathbf{y}}(\theta + \Delta\theta) - \bar{\mathbf{y}}(\theta)}{\Delta\theta} \quad (5.16)$$

The standard deviation on the identified parameters is calculated as:

$$\sigma_{\theta_{opt}} = \sigma_y \sqrt{\text{diag} \left((\nabla_{\theta_{opt}} \bar{\mathbf{y}})^T (\nabla_{\theta_{opt}} \bar{\mathbf{y}}) \right)} \quad (5.17)$$

With:

$$\sigma_y = \frac{1}{\sqrt{N - M + 1}} J(\theta_{opt}) \quad (5.18)$$

5.9. References

- [1] E. Puyoo, S. Grauby, J.-M. Rampnoux, E. Rouvière and S. Dilhaire, *Scanning thermal microscopy of individual silicon nanowires*, J. Appl. Phys. **109**, 024302, (2011).
- [2] G. Yunfei *Quantitative measurement using scanning thermal microscopy*. PhD thesis, University of Glasgow, 2016.
- [3] R. Prasher, *Predicting the Thermal Resistance of Nanosized Constrictions*, Nano Lett. **5**, (2005), 2155–2159.
- [4] Etienne Puyoo, Stéphane Grauby, Jean-Michel Rampnoux, Emmanuelle Rouvière and Stefan Dilhaire, *Thermal exchange radius measurement: Application to nanowire thermal imaging*, Review of Scientific Instruments **81**, 073701 (2010).
- [5] Abdelhak Saci, Jean-Luc Battaglia, and Indryaush De, *Accurate New Methodology in Scanning Thermal Microscopy*, IEEE Transactions on Nanotechnology, vol. **14**, no. 6, November 2015, pp. 1035-1039.
- [6] M. Chirtoc J. Bodzeta and J. Juszczuk. *Reduced thermal quadrupole heat transport modeling and transient regime scanning thermal microscopy using nanofabricated thermal probes*, Journal of Applied Physics, **116**:054501, 2014.
- [7] D. Maillat, S. André, J.-C. Batsale, A. Degiovanni, and C. Moyne. *Thermal quadrupoles solving the heat equation through integral transforms*, Wiley edition, 2000
- [8] Carslaw H.S. and Jaeger J.C. *Conduction of heat in solids*. Oxford: Clarendon edition, 1959.
- [9] J. S. Brown. *Note on the Debye temperature of palladium*. Phys. Status Solidi, **60**:59–63, November 1973.
- [10] W. Martienssen and H. Warlimont. Springer *Handbook of Condensed Matter and Material Data*. Springer Berlin Heidelberg, New York, 2005.
- [11] E. Kato. *Brillouin scattering in polymethyl methacrylate from 4 to 300 K: Temperature dependence of the Grüneisen constant and thermal properties*. J. Chem. Phys., **73**:1020, August 1980.
- [12] M. J. Assael, K. D. Antoniadis, and Jiangtao Wu. *New Measurements of the Thermal Conductivity of PMMA, BK7, and Pyrex 7740 up to 450K*. Int. J. Thermophys, **29**:1257–1266, (2008).
- [13] D. G. Cahill. *Thermal conductivity measurement from 30 to 750 K: the 3 ω method*. Rev. of Sci. Instr., **61**:802–808, (1990).
- [14] William J. Tropf, Michael E. Thomas, and Terry J. Harris. *Properties of Crystal and Glasses, volume 2*. Handbook of Optics, McGraw-Hill, New York, 1995.
- [15] Costas P. Grigoropoulos Xiang Zhang. *Thermal conductivity and diffusivity of freestanding silicon nitride thin films*. Rev. of Sci. Instr., **66**:1115, (1995).
- [16] K. E. Goodson A. Jain. *Measurement of the thermal conductivity and heat capacity of freestanding shape memory thin films using the 3 ω method*. Journal of Heat Transfer, **130**:102402, 2008.
- [17] E Shojaee and M R Mohammadzadeh. *First-principles elastic and thermal properties of TiO₂: a phonon approach*. J. Phys.: Condens. Mat., **22**, December 2009.
- [18] Thomas S. Duffy and Thomas J. Ahrens. *Compressional sound velocity, equation of state, and constitutive response of shock-compressed magnesium oxide*. Journal of Geophysical Research, **100**, January (1995).

6. Chapter 6 – APPLICATIONS

6.1. Introduction

In this chapter, we will look at the different applications that we have been performed using scanning thermal microscopy. We have utilized the experimental technique and the thermal model we have described in the previous chapters to understand and investigate the thermal properties of various types of sample. We have used a range of samples with varying thermal properties, dimensions and methods of fabrication. We described below the applications of the samples along with the description, an overview of the model based on changes required for each experiment along with the observed results. The samples that have been investigated include nanowires, 3D GST nano-device and complex pyrocarbon composites.

It must be mentioned here that all the applications that have been reported in this chapter have been published in scientific journals.

1) Nanowire Device: J.-L. Battaglia, A. Saci, I. De, R. Cecchini, S. Selmo, M. Fanciulli, S. Cecchi, M. Longo, *Thermal resistance measurement of In_3SbTe_2 nanowires*, phys. stat. sol. (a), DOI: 10.1002/pssa.201600500 (2016).

2) 3D phase-change memory Device: J.-L. Battaglia, I. De, V. Sousa, *Inverse heat conduction problem in a phase change memory device*, Journal of Physics: Conf. Series **785** (2017) 012002.

3) Pyrocarbon Composite: I. De, J.-L. Battaglia, G. L. Vignoles, *Thermal properties measurements of a silica/pyrocarbon composite at the microscale*, Journal Applied Physics, DOI: 10.1063/1.4967918 (2016).

6.2. Thermal resistance of a In_3SbTe_2 nanowire

6.2.1. Context

Thermal resistance of In_3SbTe_2 , which have been obtained by metal organic chemical vapour deposition coupled with vapour-liquid-solid mechanism, have been analyzed using the 3ω method of scanning thermal microscopy. The thermal resistance is measured across the transverse (thickness) direction of the nanowires. One of the most interesting thing about this application is the use of two nanowires of different thickness – 13 nm and 23 nm. Moreover, we

have used two different approaches – 1) using the experimental data and 2) utilizing minimization procedure [1].

6.2.2. Industrial Applications of Sample

Nanowires have wide spread uses as Phase Change Memory devices as they allow a lower volume to be programmed as well as lower electrode/active material contact area, thereby reducing the programming current. It has been observed using chalcogenide $\text{Ge}_2\text{Sb}_2\text{Te}_5$ that a decrease in the nanowire diameter yields lower programming current and therefore less power is required for getting amorphized with an opposite trend noticed when it comes to data retention [2]. This data retention problem can be resolved by chalcogenide alloys that have higher crystallization temperature. The In_3SbTe_2 ternary alloy exhibits a cubic rock salt structure with a crystallization temperature higher than 290°C [3] (two times higher than $\text{Ge}_2\text{Sb}_2\text{Te}_5$) with a metastable temperature less than 420°C [4].

6.2.3. Sample Description

The In_3SbTe_2 nanowires were grown in a MOCVD AIX 200/4 reactor, exploiting the VLS mechanism induced by Au metal-catalyst nano-particles (NPs) with an average size of 10 nm. The substrate of Si (001) were $1 \times 1 \text{ cm}^2$ on which Au nanoparticles were deposited from a colloidal solution from British Bio Cell Company after removal of Si native oxide by immersion on a HF 5% solution. The used metalorganic precursors were electronic grade dimethylaminopropyl-dimethyl-indium ($\text{C}_7\text{H}_{18}\text{InN}$, DADI), antimony trichloride (SbCl_3), and bis(trimethylsilyl) telluride ($\text{Te}(\text{SiMe}_3)_2$, DSMTe), provided by Air Liquide. 4.6×10^{-2} mbar for DADI, 2.2×10^{-2} mbar for SbCl_3 and 3.2×10^{-2} mbar for DSMTe; the reactor temperature was 335°C ; total gas flow was $4.5 \text{ L}\cdot\text{min}^{-1}$; deposition time was 60 min. XRD analysis performed on the sample grown at this optimized temperature shows that the diffracted maxima belongs to the In_3SbTe_2 cubic rock salt Fm3m structure [6]; the inferred lattice parameter is 6.1 Å. For measuring their thermal conductivity, the NWs have been harvested randomly on a SiO_2 (50nm)/Si substrate. Electro-static forces (van der Waals bonds) between the nanowire and the SiO_2 layer are responsible for the adhesion of the NW on the substrate. Indeed, we observed that NWs re-mains motionless during the SThM sweep when the probe is in contact with the NWs. Some thermophysical properties [6][7][8] for the bulk In_3SbTe_2 have been measured and are reported in [Table 17](#).

Table 17. Atomic density (n), density (ρ), specific heat (C_p), Debye temperature (Θ), thermal conductivity (k) & phonon longitudinal (v_L) and transverse (v_T) velocity of bulk In_3SbTe_2

n [m^{-3}]	ρ [kg.m^{-3}]	C_p [$\text{J.kg}^{-1}.\text{K}^{-1}$]	Θ_D [K]	k [$\text{W.m}^{-1}.\text{K}^{-1}$]	v_L [m.s^{-1}]
					v_T [m.s^{-1}]
3.23×10^{28} [9]	6310 [9]	210 [10]	190	21 [10]	3100
					1900

6.2.4. Experiment

The experiments have been performed using a 2-point probe and following the process mentioned in the previous chapter. Experiments have been performed in both contact and out-of-contact mode. It is to be noted that the probe is swept across the sample surface at a constant velocity to produce an image with 320 lines and 320 points on each line. The SThM setup was placed inside a vacuum chamber filled with Argon. It is also necessary to remember that we always assume the contact between the probe and the sample to be a disk of radius r_0 .

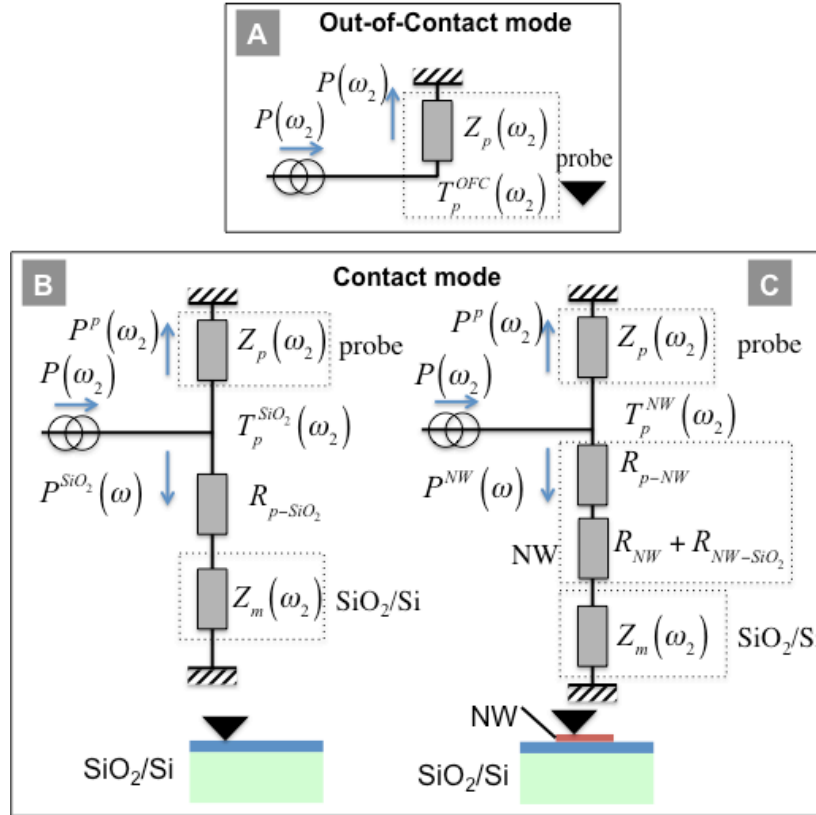


Figure 111 A: Heat transfer model for the out-of-contact operation mode (leading to the identification of Z_p). Heat transfer model for the contact mode when B: the probe is in contact with the SiO₂/Si substrate, C: the probe is in contact with the NW.

As mentioned above, the thickness of the nanowire is very low and hence it can be treated as a pure thermal resistance (R_{NW}) for the investigated frequency, which lies between 523 and 1124 Hz. Since the thickness of the nanowire is much less than the characteristic radius r_0 of the heated area, we can say that the heat flow is unidirectional. Thereby suggesting that the thermal conductivity if the nanowire along its thickness is independent of its length. Figure 111 shows the contactless and contact mode of the experiments mentioning the use of the thermal impedance formalism. We have denoted 2ω as ω_2 , the average temperature $T_p(\omega_2)$ across the surface of the Pd strip which is related to the total heat flux $P(\omega_2)$ generated by the Joule's effect as $T_p(\omega_2) = Z_T(\omega_2)P(\omega_2)$ with $1/Z_T(\omega_2) = 1/(R_c + Z_m(\omega_2)) + 1/Z_p(\omega_2)$. In this relation, as in the chapters 4 and 5, $Z_p(\omega_2)$ signifies the thermal impedance of the probe, $Z_m(\omega_2)$ the thermal impedance of the SiO₂/Si substrate and R_c is the thermal resistance between the probe and the

sample. It is to be noted that R_c is equal to R_{p-SiO_2} when the probe is in contact with the Si/SiO₂ substrate and $R_{p-NW} + R_{NW} + R_{NW-SiO_2}$ when the probe is on the nanowire with R_{NW-SiO_2} denoting the thermal contact resistance between the nanowire and the SiO₂/Si substrate. It is also assumed that the contact resistance at the interface between the probe and the SiO₂ layer remains unchanged when the probe comes in contact with the nanowire i.e. $R_{p-SiO_2} = R_{p-NW}$.

The images obtained from our AFM and SThM measurements are given Figure 112 for the thicker nanowire. The images show the topography (obtained from AFM scan mode) along with the amplitude and phase (obtained by the SThM scan mode) at 523 Hz.

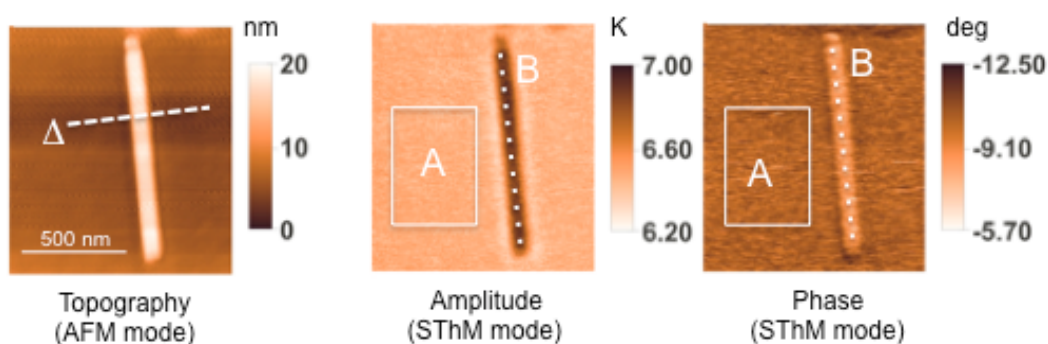


Figure 112. Topography, Amplitude and Phase at 523Hz. The dotted line (Δ) has been used to plot the 23 nm thick nanowire cross-section profile. Areas A and B are used to average the measured temperature with the probe in contact with the SiO₂/Si layer and the NW respectively.

We therefore obtained the cross-section of the two nanowires as represented in Figure 113.

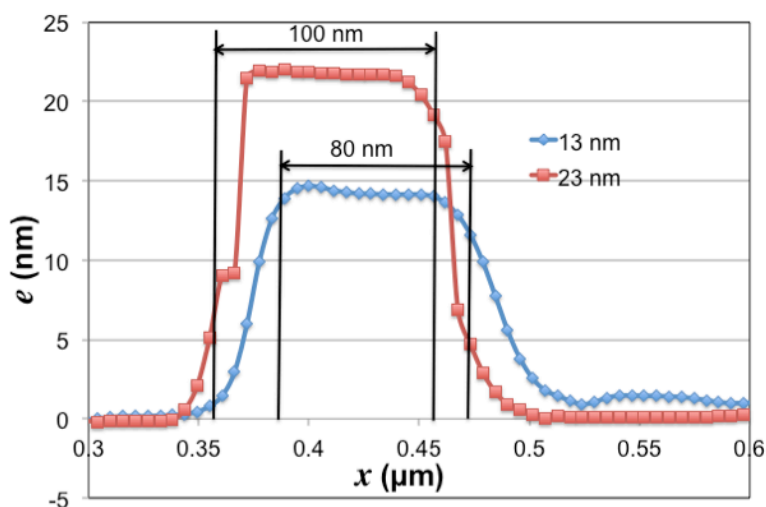


Figure 113 Cross-sectional area measurement of the Nanowire across the Δ line

The cross-section is rectangular and the thickness e_{NW} of the NWs is found to be 13 ± 0.2 nm and 23 ± 0.5 nm respectively. Both NWs have a width l_{NW} of 80 -100 nm.

6.2.5. Results and analysis

From the thermal model presented in Figure 111, one can see the effect of the thermal resistances as the probe passes over the SiO₂ substrate and the nanowire. We can say that,

$$R_t = \left\langle \frac{T^{NW}(\omega_2)}{P^{NW}(\omega_2)} - \frac{T^{SiO_2}(\omega_2)}{P^{SiO_2}(\omega_2)} \right\rangle_{\omega_2} \quad (6.1)$$

Where $R_t = R_{NW} + R_{NW-SiO_2}$ and $\langle \rangle_{\omega_2}$ denotes the average quantity of all the calculated value at each frequency. We now denote notations to the probe temperatures within the sample when the probe is in contact with the Si/SiO₂ substrate and the nanowire as T^{SiO_2} and T^{NW} respectively. Thereby, we can denote similarly the heat flux with in the sample as P^{SiO_2} and P^{NW} . Therefore we can write,

$$P^{NW}(\omega_2) = P_0 \left(1 - \frac{T^{NW}(\omega_2)}{T^{OFC}(\omega_2)} \right); P^{SiO_2}(\omega_2) = P_0 \left(1 - \frac{T^{SiO_2}(\omega_2)}{T^{OFC}(\omega_2)} \right) \quad (6.2)$$

Here we have introduced another new notation to demonstrate the out-of-contact temperature of the probe at ω_2 , $T^{OFC}(\omega_2)$.

Another approach is to consider the identification of the contact resistance R_c by minimizing the quadratic gap [9]:

$$J = \sum_{\omega_2} \left(T_p^{SiO_2, NW}(\omega_2) - T_{meas}^{SiO_2, NW}(\omega_2) \right)^2 \quad (6.3)$$

$T_{meas}^{SiO_2, NW}$ and $T_p^{SiO_2, NW}$ are respectively the measured and calculated temperature (using the expression for Z_p and Z_m) when the probe is in either contact with the SiO₂/Si substrate or the nanowire. The minimization has been performed using the Levenberg-Marquardt algorithm.

Knowing that the thermal impedance of the probe can be expressed as $Z_p(\omega_2) = A_p(\omega_2) \exp(i\delta_p(\omega_2))$, A_p as the amplitude and δ_p as the phase in the out-of-contact [11] mode, we can obtain $T_p^{SiO_2, NW}$.

The analytical solution for the thermal impedance of the heat transfer model with the probe in contact with the SiO₂/Si probe can be written as presented in chapter 4:

$$Z_m(\omega_2) = \frac{e_{\text{SiO}_2}}{k_{\text{SiO}_2}} + \frac{2}{k_{\text{Si}} \pi r_0} \int_0^\infty \frac{[J_1(x)]^2}{x \sqrt{x^2 + j \omega_2 r_0^2 / a_{\text{Si}}}} dx \quad (6.4)$$

$j^2 = -1$

Here, k represents the thermal conductivity and a the thermal diffusivity with $J_1()$ being the first order Bessel function. The integral is numerically calculated using the global adaptive quadrature and default error tolerances. Finally, the theoretical expressions for the temperature and the phase are respectively: $\|T_p(\omega_2)\|$ and $\arg[T_p(\omega_2)]$.

The radius has been calculated by using the method given in the previous chapter using a “step” sample and the radius r_0 is found to be 100 ± 5 nm.

From the experimental results averaged over the areas A and B obtained from the experimental images and our analytical solution we have the results reported in Figure 114 and Figure 115.

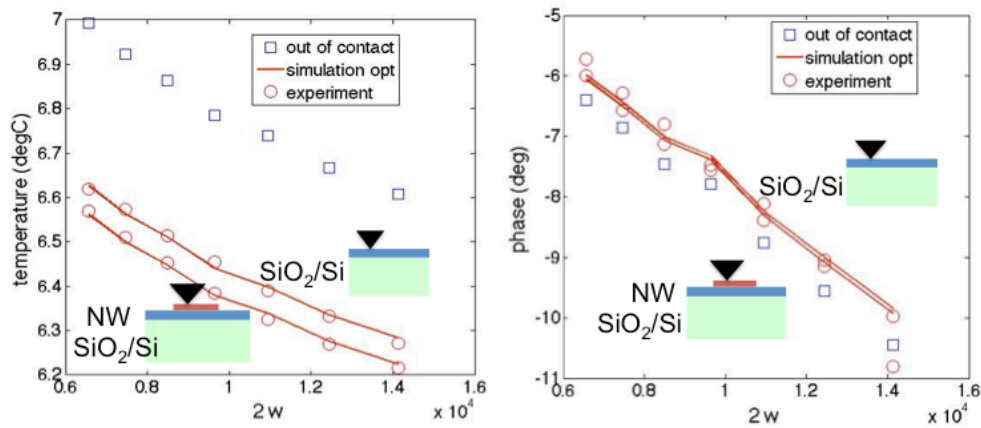


Figure 114. Blue square symbol: temperature and Phase in out-of-contact Measurement; red circle symbol: temperature and phase measurement for the probe in contact either with the SiO₂/Si substrate (averaged over area A, Figure 112) or the nanowire (averaged over area B, Figure 112); the red line is the calculated temperature and phase identified from R_c using the minimization procedure for the 13 nm thickness nanowire.

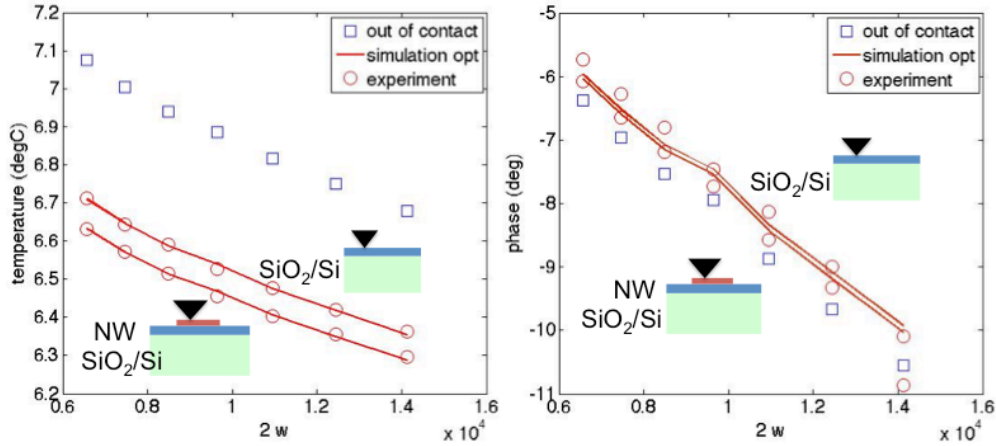


Figure 115. Blue square symbol: temperature and Phase in out-of-contact Measurement; red circle symbol: temperature and phase measurement for the probe in contact either with the SiO₂/Si substrate (averaged over area A, Figure 112) or the nanowire (averaged over area B, Figure 112); the red line is the calculated temperature and phase identified from R_c using the minimization procedure for the 23 nm thickness nanowire.

From the above two graphs it can be clearly noticed that the gap between the measured temperature over the SiO₂/Si substrate (T_{meas}^{sub}) and that over the nanowire (T_{meas}^{NW}) remains constant over our measured frequency range. Moreover, it can also be noticed that the phase doesn't change much, hence we can say that it is insensitive to the contact resistance R_c .

The Table 18 shows the thermal resistances R_t obtained through relation (6.1) or through the minimization process.

Table 18 Calculated thermal resistance R_t from equation (6.1) (line 2) or the minimization procedure [fit] (line 3) in $K \cdot W^{-1}$, calculated R_t in $K \cdot m^2 \cdot W^{-1}$ using the contact area $A_{NW}=2 r_0 l_{NW}$ (line 4), calculated R_{NW} from linear regression (line 5) and value of R_{NW} from the thermal conductivity for bulk In₃SbTe₂ (see Table 17) (line 6).

e_{NW} (nm)	13 ($l_{NW}=80$ nm)	23 ($l_{NW}=100$ nm)
R_t ($K \cdot W^{-1}$) [eq. (6.1)]	3.332×10^5	3.885×10^5
R_t ($K \cdot W^{-1}$) [fit]	$(3.3 \pm 0.2) \times 10^5$	$(3.8 \pm 0.3) \times 10^5$
R_t ($K \cdot m^2 \cdot W^{-1}$)	$(6 \pm 1) \times 10^{-9}$	$(9.5 \pm 1.4) \times 10^{-9}$
R_{NW} ($K \cdot m^2 \cdot W^{-1}$)	$(3.4 \pm 0.7) \times 10^{-9}$	$(6.4 \pm 1.3) \times 10^{-9}$
R_{NW} ($K \cdot m^2 \cdot W^{-1}$) [bulk]	6.19×10^{-10}	1.09×10^{-9}

Although the phase is much less sensitive to the variation of R_t in comparison to the amplitude, the calculated values based on R_t are in good agreement and fit well with the experimental data of both the amplitude and the phase.

Assuming linear thickness dependence between both values of thickness allowed us to obtain the value of thermal contact resistance at the NW-SiO₂ interface and that of the thermal resistance R_{NW} of the nanowires of both thicknesses.

With the help of the thermal model and our measurements, we were able to ascertain the contact resistance at the interface between the probe and either the Si/SiO₂ substrate or the NW surface.

The obtained value is $R_{p-SiO_2} = R_{p-NW} = (6.35 \pm 0.5) \times 10^6 \text{ K.W}^{-1}$.

The minimal theoretical contact resistance at the NW – SiO₂ interface has also been derived using the Diffuse Mismatch Model based on the assumption of full phonon diffusion at the interface as:

$$R_{NW-SiO_2}^{DMM} = \frac{4}{\tau_{SiO_2,NW} \rho_{NW} C_{p,NW} v_{NW}} \quad (6.5)$$

Where,

$$\tau_{SiO_2,NW} = \frac{\sum_{j=1}^3 v_{g,j,SiO_2}^{-2}}{\sum_{j=1}^3 v_{g,j,SiO_2}^{-2} + \sum_{j=1}^3 v_{g,j,NW}^{-2}} \quad (6.6)$$

is the phonon transmission coefficient. Using the data in Table 17 and those for SiO₂ ($v_T=3740 \text{ m.s}^{-1}$, $v_L=5980 \text{ m.s}^{-1}$ [18]), it is found $\tau_{SiO_2,NW} = 0.26$ and $R_{NW-SiO_2}^{DMM} = 5.05 \times 10^{-9} \text{ m}^2.\text{K.W}^{-1}$ or $6.43 \times 10^5 \text{ K.W}^{-1}$ considering the contact area to be $R_{NW} = \pi l_{NW} r_0 / 2$. This theoretical value is obviously lower than the measured one since the adhesion strength between the NW and the substrate is low.

6.2.6. Inference

The thermal resistance of the ultrathin In₃SbTe₂ nanowires was calculated by considering the thermal conductivity of bulk In₃SbTe₂ (see Table 17) as $R_{NW} = e_{NW} / k_{NW}$. As seen from the measured values in Table 18, the thermal resistance of the 13 and 23 nm thick nanowires is 5 times higher than that of the value for the bulk. It can thus be concluded that the expected phonon confinement along the nanowire thickness since we showed that the phonon mean free

path in In_3SbTe_2 is comparable to the NW thickness. It must be emphasized that the increase we found in R_{NW} by a factor 5 is subjected to 20% of uncertainty. In addition, since the identified value for $R_{p-\text{SiO}_2}$ and R_{p-NW} is already in the highest range reported in the literature, the main deviation could be attributed to the estimation of $R_{NW-\text{SiO}_2}$. However, even considering a 100% error in $R_{NW-\text{SiO}_2}$ will not change the conclusion, since the value of R_{NW} would anyway be higher than that calculated by using the thermal conductivity of the IST bulk.

Considering the two identified values for R_{NW} , we could express the effective nanowire thermal conductivity along the transverse direction. However, we must recall here that the thermal conductivity, in the sense of the Fourier law, can be defined only when the characteristic length of the investigated medium is larger than the mean free path of the heat carriers (phonons and electrons).

We can also find out the effective thermal conductivity of the nanowire in the transverse direction from the identified values of R_{NW} . However, we must recall here that the thermal conductivity, in the sense of the Fourier law, can be defined only when the characteristic length of the investigated medium is larger than the mean free path of the heat carriers (phonons and electrons).

Finally, we can conclude that SThM is very good for accurate measurements of temperature and phase associated with a small variation in the thermal resistance of the investigated surface. Moreover, we don't need to handle or prepare the material in any special way to achieve our goals and this procedure is a generalized procedure.

6.3. 3D phase change memore Nano Device

6.3.1. Context

The 3D nano-structure device we have focused our application on is the phase change alloy $\text{Ge}_2\text{Sb}_2\text{Te}_5$ (GST 225) [20]. $\text{Ge}_2\text{Sb}_2\text{Te}_5$ is one of the most used phase change alloy in phase change memory technology due to its rapid and reversible phase switching abilities. Heating the GST above the glass transition temperature of 130°C at the amorphous (α) stage results in a change to the face centered cubic (fcc) metastable stage. Furthermore, when the temperature is raised to around 300°C for the fcc , there is a transition to a hexagonal closed packed (hcp) stable crystalline phase.

6.3.2. Industrial Applications of Sample

One of the major applications of GST is as a phase change memory device in microelectronics. The microelectronics field has tried to utilize the variation of electrical resistance of GST along the crystalline state [21] [22]. In the crystalline phase (SET mode), the specimen displays high electrical conductivity resulting in a low electrical resistance measured between the top electrode contact (TEC) and the bottom electrode contact (BEC) surrounding the phase change memory layer. To convert it into a highly resistive amorphous state, the programming region is first melted and then quickly quenched by applying a large electrical current pulse for a short time period. This amorphous region in series with any crystalline region of the phase change memory provides the effective resistance between the TEC and the BEC. Now, to change the state back into crystalline phase, a medium electrical current pulse is applied to anneal the programming region with a temperature which lies between the crystalline temperature and the melting temperature for a certain time period. To ensure that the crystalline phase has been achieved in the programming region, a small electrical current is passed through the cell to measure the electrical resistance without disturbing the current state of the material. The GST 225 gets amorphised when an electrical pulse is high enough to reach the melting temperature (680°C) and its falling edge is quick enough to quench the molten GST with cooling occurring within a few tens of nanoseconds.

6.3.3. Sample Description

The studied device is given in Figure 116. The sample provided is pretty complex due to the fact that there are juxtapositions of thin films along with the phase change memory placed in the shape of a narrow μ -trench. The figure below shows the different layers of the sample as well as the dimensions.

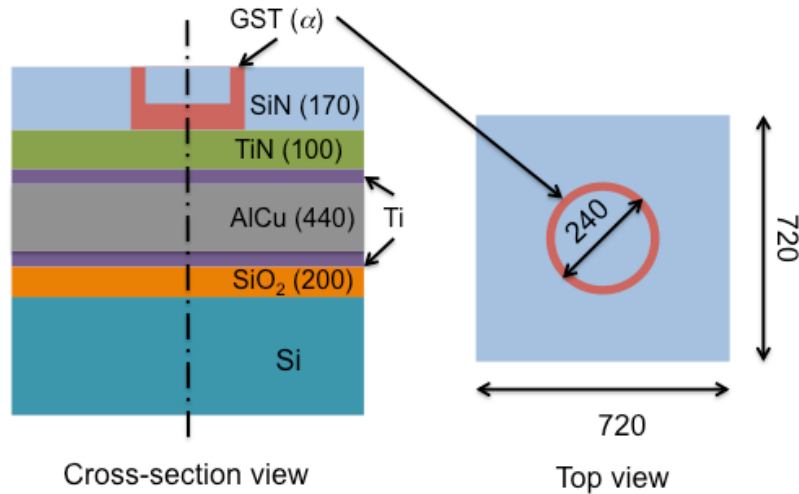


Figure 116 Different Layers and Geometry of the phase change memory cell (cross sectional and top view)

The length of the square sample, as given in the figure above, is 720 nanometer with the diameter of the PCM trench is around 240 nanometer with the thickness of the GST trench being 30 nanometer.

The Table 19 lists all the necessary thermal properties of the different parts of the sample at room temperature obtained from previous analysis.

Material	k ($\text{W}\cdot\text{m}^{-1}\cdot\text{K}^{-1}$)	ρ ($\text{kg}\cdot\text{m}^{-3}$)	C_p ($\text{J}\cdot\text{kg}^{-1}\cdot\text{K}^{-1}$)
Si	131	2329	700
SiO ₂ [48]	1.4	2200	787
AlCu	238	2700	900
Ti [49]	13	4500	540
TiN [49]	33.6	5400	220
GST (α) [46]	0.18	5870	218
Si ₃ N ₄ [47][48]	2.1	2900	300

Table 19 Thermal Properties (Thermal Conductivity (k), Density (ρ) and Specific Heat (C_p)) of the different materials of the microelectronic structure in room temperature

The Titanium (Ti) layer is thin enough to be considered as pure thermal resistance with the thermal boundary resistance (TBR) between the TiN and AlCu interface being around $5 \times 10^{-9} \text{ Km}^2\cdot\text{W}^{-1}$ obtained from literature. The TBR between the TiN layer and the GST (α) layer is around $5.5 \times 10^{-8} \text{ Km}^2\cdot\text{W}^{-1}$ also obtained from previous studies. Hence, our scanning thermal microscopic research will aim to understand the TBR between the vertical interface of GST and

Si₃N₄ layers. The temperature change during the experiment is very small and therefore there is no phase-change of the PCM.

6.3.4. Experimental Results

The first step taken from the experimental point-of-view was to perform an AFM test to determine the surface roughness. It was found that the maximum roughness at the surface never exceeds 2 nm.

The scanning thermal microscopic experiment was then performed on the sample at 3123 Hz to obtain the variation of amplitude and phase as seen in the figure below.

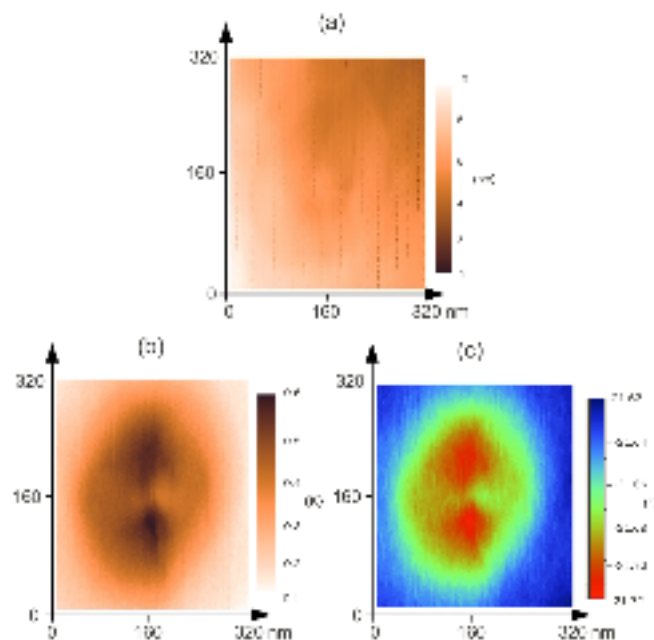


Figure 117 a) Topography (AFM image) b) Amplitude (SThM image) c) Phase (SThM image) at 3123 Hz

From the images above, it can be seen that the maximum temperature is reached at the centre of the cell (shown in dark brown). The amplitude and phase images clearly show the PCM ring even though the trench width (30 nm) is lesser than the radius of the 2 point probe as mentioned in the previous chapter. When an experimental probe sweep is performed in the vicinity of the trench, we can clearly see that the temperature on both sides of the GST trench are influenced by the low thermal conductivity of the amorphous GST as well as the heat confinement when the probe is located inside the cell.

6.3.5. Simulation

We have implemented an inverse approach that leads to exploit better the experimental measurements. First, it leads identifying the sensitive thermal parameters in the model that are the thermal conductivity of the PCM (GST), the TBR at the PCM-Dielectric (SiN) interface and also additional parameters as the probe thermal impedance and the geometrical domain of investigation. Retrieving the thermal impedance of the probe measured using the out-of-contact mode leads also to be confident with the TBR at the interface between the probe and the surface as well as the contact radius area, that have been both measured in a different configuration. On the other hand, such a characterization allows verifying the reliability of the thermal properties that have been measured in different configurations (as thin films) that than met in the device. However, the main drawback in this approach is related to the CPU time required to complete the identification process. Indeed the minimization algorithm appeals to the simulation of the finite element model a lot of time that makes the process very time consuming. In the present study, only very small amounts of data have been exploited whereas the SThM image is composed from (256x256) pixels. Therefore, further work is designed to reduce strongly the computation times [45].

To the complexity of the domain geometry, the thermal impedance $Z_m(\omega_2)$ for the device has been calculated here using the finite element method. As represented on Figure 118 the geometry has been first simplified since we verified that, in the working frequency range [100-5000] Hz, the TiN, AlCu and Ti layers as well as the TBR between those layers can be merged to form the thermal resistance R_i between the SiN and the thermal SiO₂ layer at the top of the Si substrate. This former must be considered as a semi-infinite medium within the finite elements technique (node Infinite Domain with COMSOL Multiphysics code). The mesh of the domain appeals to 458096 degrees of freedom (DoF), the system is solved using an iterative multigrid algorithm based on the generalized minimal residual method. The temperature is integrated over the heated area using a 4-order numerical integration technique. As presented also on Figure 118, a crucial choice has to be made on the value of the characteristic dimension a_{cell} of the cell that is expressed according to the GST tank diameter.

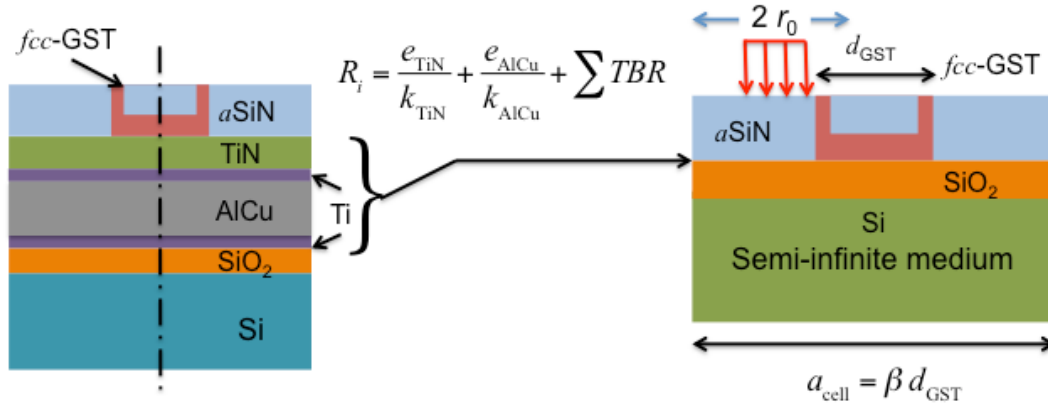


Figure 118 Simplification of the device geometry: the Ti, AlCu and TiN layers are merged to form the thermal resistance R_i , including the TBRs at the interfaces between the layers

As discussed before, we consider the contact area between the probe and the surface as a disk; the radius r_0 of the disk was determined using the step technique presented in the paper of Puyoo *et al.* [17]. It is about 100 ± 10 nm and we assumed this value for our configuration. The probe is assumed passing from the SiN onto the GST trench along the x -direction. The x -dependent reduced sensitivity functions of the probe temperature according to the parameter θ are represented in Figure 119, θ being either the probe thermal impedance Z_p , the geometrical factor β the TBR at the GST-SiN interface and the thermal conductivity k_{GST} of the PCM have been calculated from the classical finite difference:

$$S^*(x, \theta) = \theta \frac{dT_p(x, \theta)}{d\theta} \sim \theta \frac{T_p(x, \theta + \delta\theta) - T_p(x, \theta)}{\delta\theta}$$

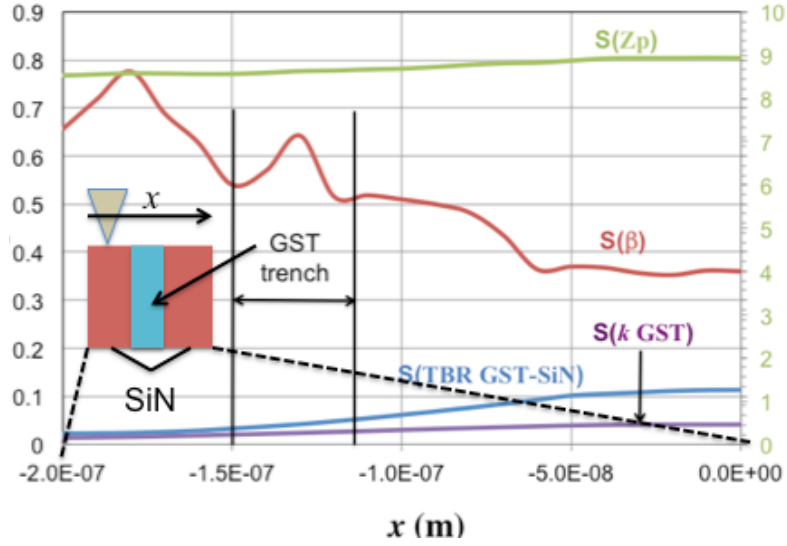


Figure 119. Reduced sensitivity functions of the probe temperature according to the probe thermal impedance Z_p , the geometrical factor β , the TBR at the GST-SiN interface and the thermal conductivity k_{GST} of the PCM.

Obviously we found that the sensitivity on Z_p is huge, meaning that making a small error on this parameter will lead to a very high deviation on the calculated temperature of the probe. Fortunately, we observe that the four sensitivity functions are linearly independent since:

$$\nabla (a_0, a_1, a_2, a_3) \neq 0 \text{ as: } a_0 S^*(Z_p) + a_1 S^*(\beta) + a_2 S^*(k_{GST}) + a_3 S^*(TBR_{SiN-GST}) = 0$$

Therefore, we proposed to identify the four parameters by minimizing the quadratic gap $J = \sum_x (T_p(x) - \widetilde{T}_{p,x})^2$ between the measured temperature, denoted $\widetilde{T}_{p,x}$, and the calculated one using the Levenberg Marquardt algorithm [44].

The four parameters and we found: $Z_p(523 \text{ Hz}) = (11.10 \pm 0.025) / P_0 \text{ K.W}^{-1}$; $TBR_{SiN-GST} = (2.0 \pm 0.2) \times 10^{-8} \text{ K.m}^2.\text{W}^{-1}$; $k_{GST} = 0.46 \pm 0.1 \text{ W.m}^{-1}.\text{K}^{-1}$; $\beta = 3.3 \pm 0.1$. All the known parameters have been reported in the **Erreur ! Source du renvoi introuvable.**

Table 20 Values of Known Parameters

f	523 Hz	$TBR_{AlCu-TiN}$ (DMM)	$3 \times 10^{-9} \text{ m}^2.\text{K.W}^{-1}$
r_0	100 nm	$TBR_{SiO2-AlCu}$ (DMM)	$3 \times 10^{-9} \text{ m}^2.\text{K.W}^{-1}$
R_0	125 Ω	$TBR_{Si-SiO2}$ [26]	$5 \times 10^{-9} \text{ m}^2.\text{K.W}^{-1}$
R_c	$1.2 \times 10^{-8} \text{ m}^2.\text{K.W}^{-1}$	$TBR_{GST-TiN}$ [50][51]	$2 \times 10^{-8} \text{ m}^2.\text{K.W}^{-1}$
i_0	800 μA		

We represented on Figure 120 , the measured and simulated temperature of the probe using the identified parameters. The standard deviations for the parameters have been calculated from the Hessian matrix at the end of the minimization process and the residuals [44]. The value we found for the identified Z_p is exactly the same than that we measured in the out-of-contact mode. As expected we found a value of the TBR at the GST-SiN interface that confirms that the value estimated from the DMM was too low. The GST thermal conductivity is that of the *fcc* state measured when the GST is deposited as a thin film. We observed on Figure 120 that the change in the temperature probe is only 0.2°C. This comes from the fact that the thermal conductivity of both the amorphous SiN and the GST in *fcc* state are not very different although the amorphous SiN is a little bit more conductive. The increase observed after the GST barrier is obviously due to the heat confinement within the GST micro trench. Considering the thermal properties of the amorphous GST instead of the crystalline ones is clearly visible on the simulated probe temperature on Figure 120.

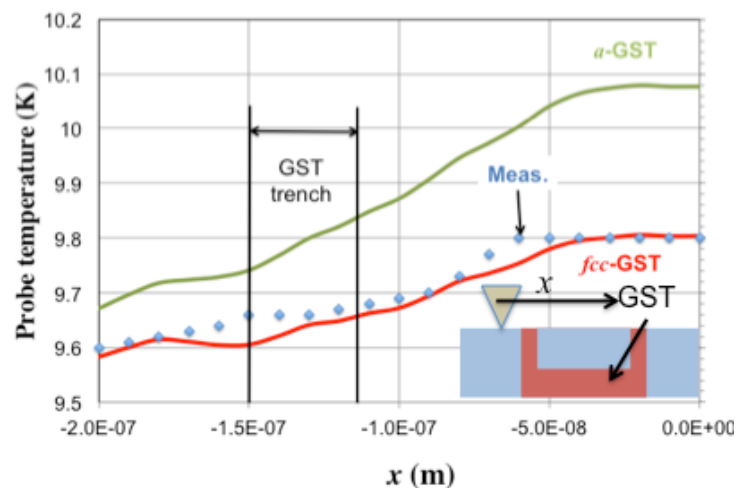


Figure 120. Fit between the experimental data (dots), when the probe follows the direction represented in the inset, and the simulated probe temperature (red line) using the identified values of the four parameters at the end of the minimization process. The simulated probe temperature is calculated from the thermal conductivity of the GST (green line) in order to demonstrate the sensitivity to this parameter for instance.

The only major drawback in this approach is related to the CPU time required to complete the identification process. Indeed the minimization algorithm appeals to the simulation of the finite element model a lot of time that makes the process very time consuming. In the present study, only very small amounts of data have been exploited whereas the SThM image is composed

from (256x256) pixels. Therefore, further work is designed to reduce strongly the computation times.

6.4. Pyrocarbon Composite

6.4.1. Context

Our complex composite structure is made of a silica fibre and a laminar pyrocarbon matrix. Laminar pyrocarbons are used as interphases or matrices of carbon/carbon and ceramic-matrix composites in several high-temperature aerospace applications. Depending on their organization at the nanoscale, they can have a variety of mechanical and thermal properties. Hence, it is important to know, before thermal processing, the properties of these matrices at the micrometer scale in order to improve and control the composite behavior in a macroscopic scale.

6.4.2. Industrial Application of the Sample

Carbon/carbon (C/C) composite materials are choice materials for use in extreme environments, such as space propulsion rocket nozzles, atmospheric re-entry thermal protection systems, aircraft brake discs, and Tokamak plasma-facing components [27]. In addition to carbon fibers, they contain interphases and matrices made of pyrolytic carbon, or pyrocarbon (PyC) [28]. This special type of carbon can be thought of as a heavily faulted graphite. It is prepared via a gas-phase route, called Chemical Vapor Deposition (CVD) or Infiltration (CVI). It is therefore quite unavailable in bulk form. It has, depending on its processing parameters, a very versatile nanostructure [29][30][31] and consequently, broadly varying mechanical and thermal properties, usually anisotropic to a more or less large extent [33]. Posterior heat treatments may further alter their structure and properties [32]. Hence, it is important to know the properties of these matrices at the micrometer scale in order to improve and control the composite behavior in a macroscopic scale.

6.4.3. Sample Description

The composite consists of an as-deposited regenerative laminar (ReL) PyC [34] deposit made on glass fibers as presented on Figure 121. The general orientation of the graphitic sheets is concentric around the fibers, as exhibited in Figure 122 and results in orthotropic thermal properties of the matrix in the cylindrical coordinate frame following the fiber axis. This is due to the fact that the graphitic sheets exhibit strong thermal anisotropy.

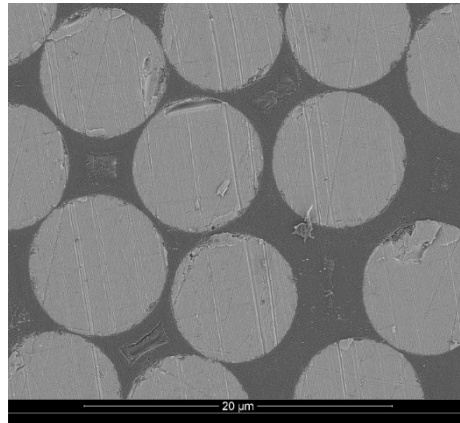


Figure 121. Microscopic Image of the Composite Structure obtained utilizing a Scanning Electron Microscope (SEM).

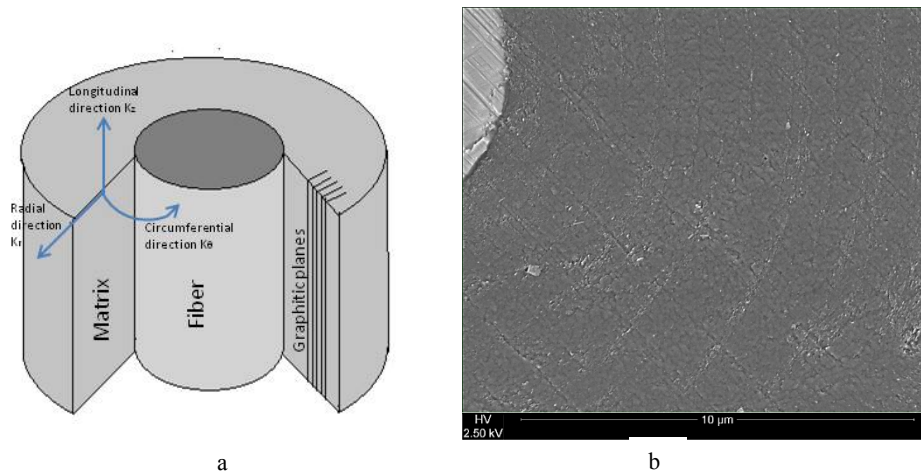


Figure 122. a) Image showing the silica fiber and the pyrocarbon matrix surrounding the fiber in layers; b) Image taken using high resolution SEM confirming the presence of a concentric arrangement of anisotropic graphitic sheets

The thermal behavior of these non-homogeneous composites can be captured through characterization that will provide the thermal properties of the PyC as well as the thermal resistance at the interfaces between the matrix and the fiber. The fiber is made of a single glass structure whose properties are reported in Table 21.

Table 21 Properties of the glass fiber present in the PyC composite sample

Thermal conductivity (k)	$1.1 \text{ W.m}^{-1}.\text{K}^{-1}$
Density (ρ)	2200 Kg.m^{-3}
Specific heat (C_p)	$748 \text{ J.kg}^{-1}.\text{K}^{-1}$

Previous thermorefectance (TR) [35][36][37] experiments have been performed to assess the anisotropic thermal diffusivity of the Smooth Laminar (SL) PyC and of the Rough Laminar (RL) PyC, either pristine or after different heat treatments. It was obtained that the in-plane thermal diffusivity (in orthoradial direction) for the as-prepared SL PyC matrix was $0.14 \text{ cm}^2 \cdot \text{s}^{-1}$ while the ratio of the in-plane and out-of-plane thermal diffusivities was 7; the as-prepared RL exhibits higher figures ($0.42 \text{ cm}^2 \cdot \text{s}^{-1}$ and 20, respectively), denoting a more graphitic and anisotropic structure. ReL PyC had not been investigated: this highly anisotropic form of PyC differs from RL by a larger amount of defects.

The TR method has in the current case some possible drawbacks: first, its spatial resolution is of the same size as the deposit thickness, a fact that could result in inaccuracies; second, this method requires a rather strong temperature increase on the heating area using the TR method in order to increase the signal-to-noise ratio, therefore yielding an effective diffusivity characteristic of some temperature markedly higher than the ambient.

In order (i) to overcome these drawbacks, (ii) to provide new data for ReL PyC, and (iii) to measure as well the thermal boundary resistance at the interface between the PyC and the glass fiber, we have implemented the scanning thermal microscopy (SThM) experiment involving the 3ω mode. The advantage of using SThM is that the spatial resolution achieved is in the sub-micron scale, and that high temperature differences are not involved.

6.4.4. Thermal Modelling

We used the 2-contact point provided by Kelvin Nanotechnology ($R_0=125 \text{ } \Omega$, $\alpha=1.3 \times 10^{-3} \text{ K}^{-1}$ and $I_0=750 \text{ } \mu\text{A}$). Using the thermal impedances formalism, the thermal model within the experimental configuration has been reminded in Figure 123.

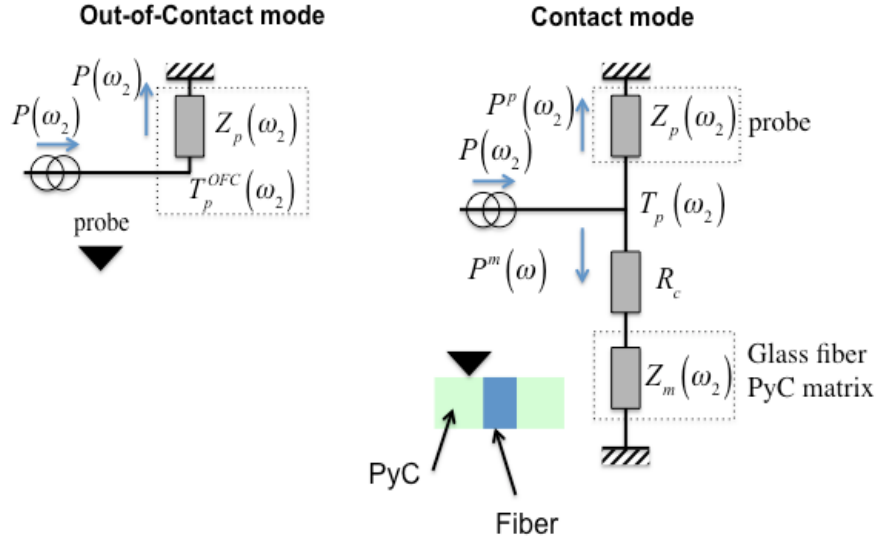


Figure 123. Heat transfer model for the out-of-contact operation mode (leading to the identification of Z_p) and the contact mode, (considering the probe in contact either with the glass fiber or the PyC matrix)

Starting from this model, the reduced sensitivity $S_A(\theta, \omega_2) = \theta d\|T_p(\omega_2)\|/d\theta$ of the amplitude versus the parameter $q = \{k_{r,PyC}, k_{z,PyC}, r_0, R_c\}$, have been calculated and reported on the Figure 124. Sensitivity on $k_{r,PyC}$ and $k_{z,PyC}$ being exactly the same, they cannot be identify separately. Therefore, the measurements achieved when the probe is in contact with the PyC will only lead to identify the effective thermal conductivity. On the other hand, the ratio of the sensitivity functions to r_0 and R_c is constant; it is not possible to identify separately those two parameters. We assume here the motion of the probe is along the radial direction, when the probe passes from the fiber to the matrix, through the interface. The reduced sensitivity functions $S_A(\theta, r) = \theta d\|T_p(r)\|/d\theta$ of the amplitude to the parameters $\theta = \{k_{r,PyC}, k_{z,PyC}, r_0, R_c, TBR\}$ at the frequency 1125 Hz, when r varied from -0.5 to $0.5 \mu\text{m}$, assuming the interface is at $r=0$, are represented in Figure 125 a). The sensitivity functions with respect to r_0 and to R_c , $k_{r,PyC}$, $k_{z,PyC}$ are, as for the frequency behavior, linearly dependent. However, it appears, as revealed on Figure 125 b), that the parameters $k_{r,PyC}$, r_0 , R_c , TBR can be identified since the ratios of the associated sensitivity functions are not constant along r .

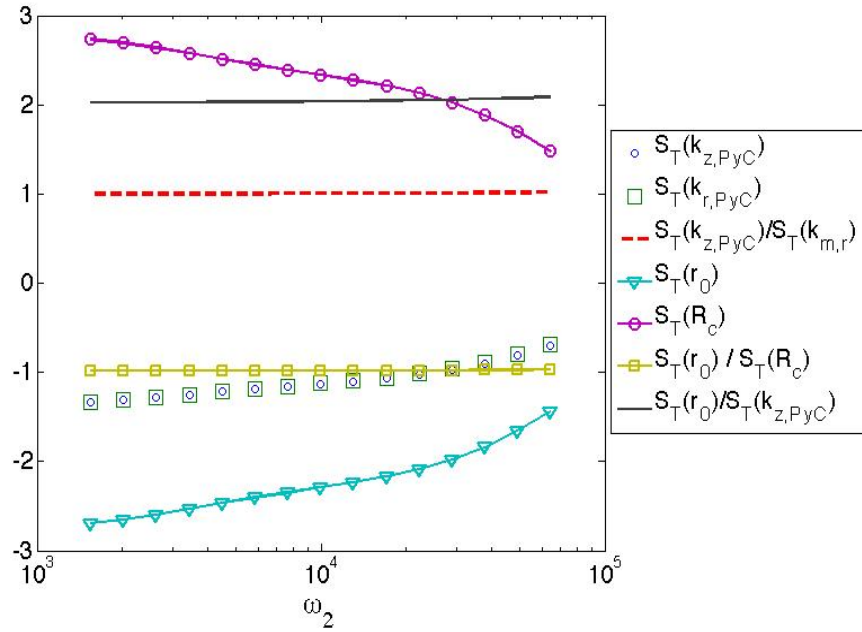


Figure 124. Reduced sensitivities of the amplitude $A(\omega_2) = \|T_p(\omega_2)\|$ to the axial and radial thermal conductivity (k_{r,P_yC} , k_{z,P_yC}) of the material, the contact radius r_0 and the thermal contact resistance R_c at the interface between the probe and the investigated surface, as a function of frequency.

Whatever the experimental configuration for the probe, static or dynamic, the sought properties are identified by minimizing the quadratic gap: $J = \sum_{\omega_2} (A_p(\omega_2) - A_{\text{meas}}(\omega_2))^2$, where A_{meas} and A_p denote respectively the measured and calculated amplitude of the probe temperature. This minimization is achieved using the Levenberg-Marquardt algorithm. The standard deviation for the identified parameter is calculated classically from the covariance matrix and the final value of J at the end of the identification process.

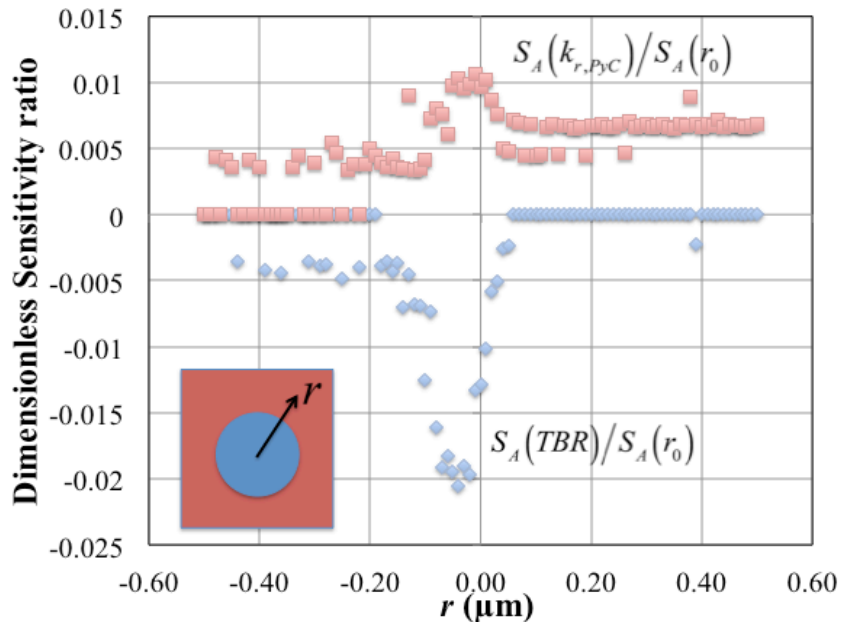
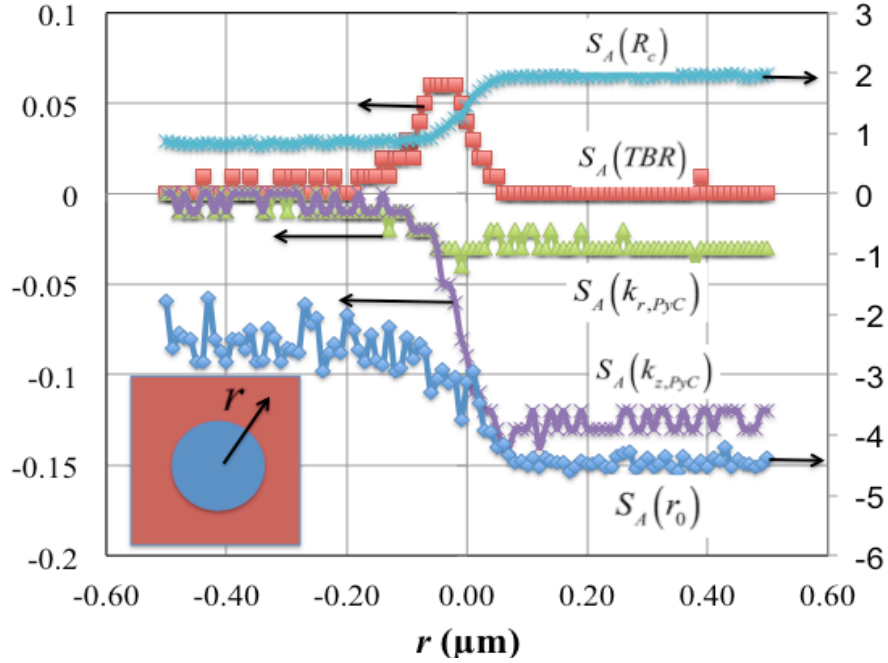


Figure 125. a) Reduced sensitivity of the amplitude $A(r) = \|T_p(r, \omega_2)\|$ with respect to R_c , r_0 , $k_{r,p_{yC}}$, $k_{z,p_{yC}}$ and TBR at 1125 Hz, along a path crossing the fiber/matrix interface b) reduced sensitivity ratios along the same path.

In addition, the same result also clearly appears for the identification of k_r and k_z . Therefore the radius r_0 of the contact area has been experimentally determined using a calibrated “step” sample that consists in a 100 nm thick SiO_2 step deposited on a Si substrate. We found $r_0 = 105 \pm 7$ nm

with a constant force of 10 nN applied on the cantilever. As explained previously, this value is rather high compared to that obtained under vacuum since a small meniscus of water may develop at the probe tip/surface material interface in the present operating conditions and the probe tip is also slightly flattened when it is put in contact with the sample according to the applied force, both contributions leading to enlarge the contact area. It is assumed that the contact radius will remain unchanged on the glass fiber and the PyC with the same force applied on the cantilever. On the other hand, as demonstrated by the sensitivity analysis, the measurements achieved when the probe is in contact with the PyC will only lead to identify the effective thermal conductivity that is here $k_{eff} = \sqrt{k_r^2 + k_z^2}$.

6.4.5. Experimental Results

We performed SThM experiments in contact as well as in out-of-contact mode under argon flow (after a preliminary evacuation to primary vacuum). This has been done to reduce the presence of water meniscus at the interface between the probe and the sample. The probe was carefully placed on different locations of the sample: at the center of the glass fiber and on the PyC matrix far away from the fiber. Figure 126 shows the variation of the amplitude and the phase for the in and out-of-contact modes. The difference in the phase for each condition is very small, meaning that only the amplitude can be used in order to identify the thermal conductivity of the PyC.

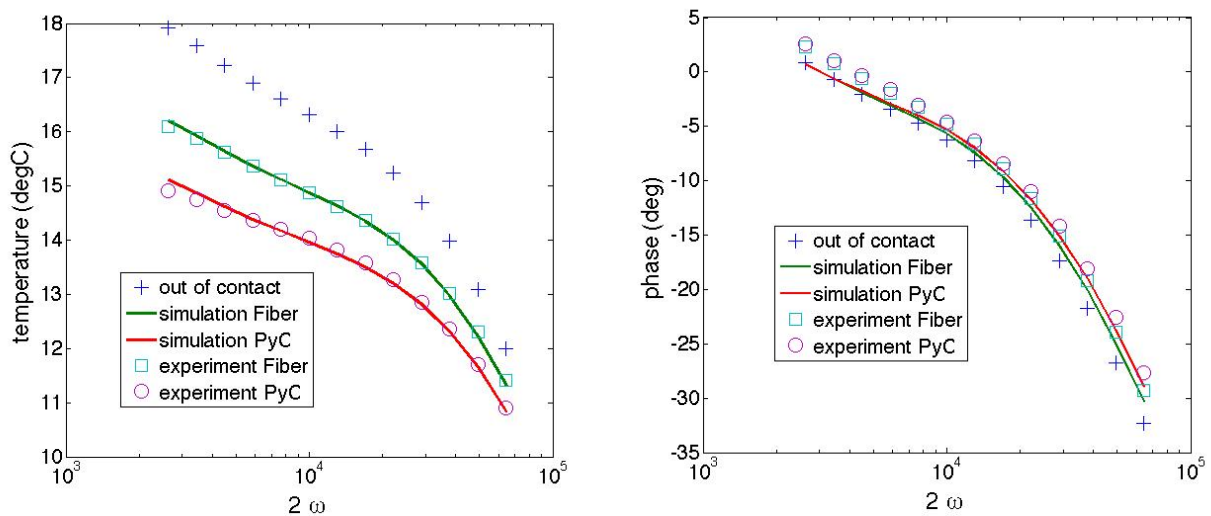


Figure 126. Measured temperature (left) and phase (right) against 2ω . Plain lines are simulations using the identified R_c when the probe is in contact with the silica fiber and the identified k_{eff} of the PyC when the probe is in contact with the PyC.

To measure the thermal boundary resistance between the matrix and the fiber of the sample, we performed a SThM sweep of the specimen at 1125 Hz with a current of 750 μA under atmospheric condition. The experiments have been performed over an image edge size of 50 micrometers with 256 points of measurement per line at a speed of 0.25 lines per second. The topography, amplitude and phase images are represented in Figure 127.

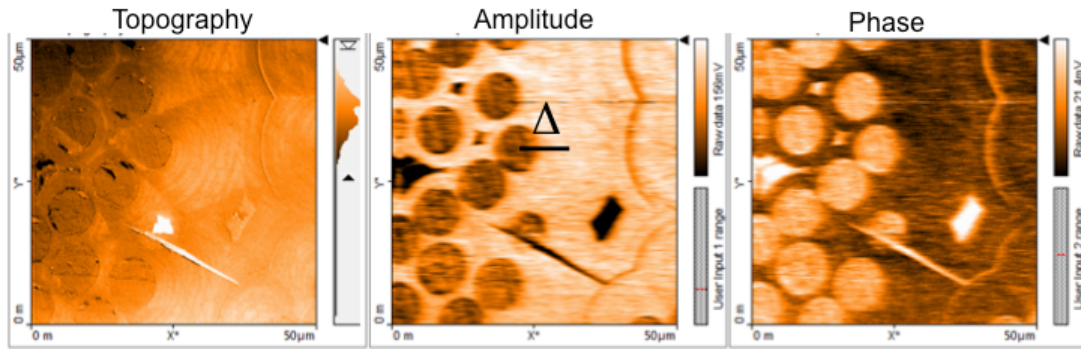


Figure 127. The $50 \times 50 \mu\text{m}^2$ images obtained via experiments under atmospheric conditions using Scanning Thermal Microscopy at 1125 Hz showing the topography, amplitude and phase from left to right respectively.

6.4.6. Analysis

Since the glass fiber thermal properties are known, we used them in order to identify first the thermal contact resistance at the interface between the SThM probe and the material. We found that $R_c = (8.80 \pm 0.3) \times 10^{-8} \text{ K.m}^2.\text{W}^{-1}$. As presented in Figure 126, the fit between experimental data and the theoretical ones is very satisfying, proving the validity of our model. Using this value for R_c , we used the measured amplitude when the probe is in contact with the PyC in order to identify its effective thermal conductivity. Using the values for the density of ReL PyC ($\rho = 2110 \text{ kg.cm}^{-3}$) and the specific heat of carbon ($c_p = 748 \text{ J.K}^{-1}.\text{kg}^{-1}$), we found that $k_{\text{PyC,eff}} = 20.18 \pm 0.12 \text{ W.m}^{-1}.\text{K}^{-1}$. It must be emphasized that the standard deviation on the identified thermal conductivity is high (20% uncertainty) since a small variation in r_0 leads to a very large change in k_{eff} . In addition we have shown in a previous study that this kind of probe does not allow measuring changes in thermal conductivity of material whose value is higher than $25 \text{ W.m}^{-1}.\text{K}^{-1}$. This obviously comes from the very low contact area between the probe and the surface.

The obtained k_{eff} value can be compared to effective values $k_{eff}^{TR} = \sqrt{k_r^2 + k_z^2}$ retrieved from the TR experiments. Using the same heat capacity for all PyCs and densities of 2120 kg.cm^{-3} for RL [36] and 1930 kg.cm^{-3} for SL [37], they are respectively 66.7 and $20.4 \text{ W.K}^{-1}.\text{m}^{-1}$. Actually both RL and ReL have the same degree of textural anisotropy, as measured *e.g.* by polarized light optical microscopy or by selected area electron diffraction in a transmission electron microscope, and only differ by the amount of in-plane defects, as measured by X-ray diffraction, neutron diffraction and by Raman spectroscopy [42], and confirmed by HRTEM image-based atomistic modeling [40]. On the other hand, SL has a lesser anisotropy but a comparable, though lesser, amount of defects as compared to ReL. We conclude here that the room temperature conductivity is more sensitive to structural perfection than to textural arrangement. Indeed, either phonons or electrons, which are responsible for heat transfer in carbons, are scattered by the defects present in the planes.

Finally, it has been possible to investigate the thermal contact resistance between the fiber and the PyC deposit by scanning the material across the interface with the probe. The average value for the amplitude along line Δ (see Figure 127), when the probe moves from the fiber to the PyC, is represented in Figure 128. In order to simulate the probe temperature for each location of the probe, we used the analytical model derived by Lepoutre *et al.* [43] assuming infinite domains on both sides of the interface. This assumption is realistic since the probe is only sensitive to bulk thermal conductivity at distances that do not exceed 5 to 6 times the contact radius r_0 . Varying the thermal contact resistance RTH at the interface between the fiber and the PyC, we obtained different calculated probe temperature profiles as reported in Figure 128. Therefore we can conclude to a value of RTH close to $(5 \pm 1) \times 10^{-8} \text{ K.m}^2.\text{W}^{-1}$.

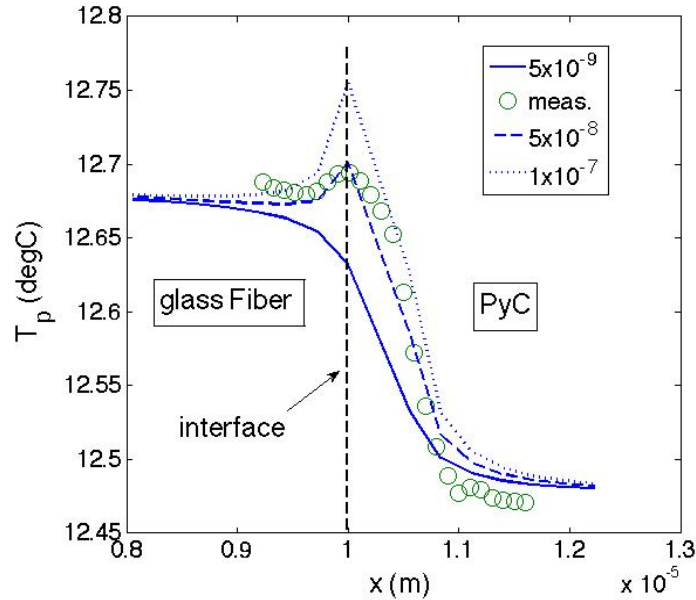


Figure 128 Measured probe temperature along the Δ line (see Figure 127) and simulated probe temperature values considering three different values for RTH (in $\text{K}\cdot\text{m}^2\cdot\text{W}^{-1}$).

This value, of the same order of magnitude as the thermal resistance between the probe and the silica substrate, is rather low. For sake of comparison, in carbon fiber-reinforced epoxy composites, values are in the range $1 - 5 \cdot 10^{-4} \text{ m}^2\cdot\text{K}\cdot\text{W}^{-1}$, *i.e.*, 10^4 times higher [44]. A possible reason for this extremely low value is that the PyC finds itself in a state of compression around the fiber: as a matter of fact, no decohesion has been found between the fibers and the matrices. Another effect is the fact that, on the carbon side, the conductivity is much larger parallel to the interface instead of perpendicularly, therefore providing easy “escape routes” to heat around defects present at the interface.

6.4.7. Conclusion

The SThM method has been applied to a composite made of silica fibers embedded in a regenerative laminar pyrocarbon (RL PyC) matrix. It has allowed obtaining values of the effective conductivity of this type of pyrocarbon, therefore completing the existing database obtained by TR on other types of PyC. The method has proved efficient in yielding effective values of the thermal diffusivity (hence, of the conductivity). Unfortunately, it cannot give the details of the conductivity tensor elements; the uncertainty margin is also rather large. On the other hand, it allows identifying the thermal contact resistance between the carbon matrix and silica fibers.

It is also necessary to mention that the surface of the sample is not fully flat at the interface between the fiber and the PyC. This comes from the different mechanical properties of both materials and their impact on the roughness at the end of the surface polishing. On the other hand, the fiber being an insulator already, the sensitivity of the measured temperature vs. the TBR remains low. Additional measurements of the TBR between a carbon fiber and the PyC matrix need to be performed.

Collecting the values obtained here and previously, it is concluded that the in-plane heat conductivity of pyrocarbons is much more sensitive to the defect density than to the degree of anisotropy. A surprising low value of the thermal contact resistance between matrix and fibers has been found, possibly because of some compressive stress ensuring a strong fiber/matrix adhesion.

Further investigations are desirable in at least two directions. First, the SThM method should be improved in order to reduce its large degree of uncertainty and to obtain direction-dependent data. Second, measurements should be carried out on other pyrocarbons, in order to confirm the tendencies obtained here; measurements at higher temperatures are possible and would be highly interesting, since virtually no actual experimental data is available on these materials at elevated temperatures.

6.5. Global Conclusion

From the applications presented above, it can be seen that even though there are still a few drawback when it comes to using SThM and a lot of advancement is still needed to increase its range of application, SThM is a very good contact method for obtaining the thermal properties of nano and microstructures. We have performed experiments to compare our model and as it can be seen, our thermal model is pretty accurate.

Through these analyses, we not only realize the applications of SThM i.e. obtaining the thermal conductivity and thermal imaging but we also get an insight into the thermal boundary resistances between the different materials of the sample. These applications have made the use of SThM wider in the industry including materials sciences for thermal conductivity measurements, microelectronics industry for thermal imaging to detect hotspots and high temperature applications in aerospace industry to obtain thermal boundary resistances. All this

makes SThM a very vital and important part of the experimental landscape in micro and nano heat studies.

Although the reduction in the size of the probe tip when it comes to modern SThM probes reduces its capacity to analyze materials of higher thermal conductivity, it can be seen from our results that it provides good spatial resolution. When compared to results in vacuum condition, the spatial resolution are even more promising.

Moreover, in our approach, it can be seen that due to the thermal impedance approach, we don't need to go into the details of the probe geometry and we also don't have to handle the specimens in a specific way. Making our experimental approach a very general approach. We have also show with our analyses that the assumption regarding the probe radius and the thermal contact resistance as discussed in Chapter 5 provide good solutions.

6.6. Reference

- [1] J.-L. Battaglia, A. Saci, I. De, R. Cecchini, S. Selmo, M. Fanciulli, S. Cecchi, M. Longo, Thermal resistance measurement of In₃SbTe₂ nanowires, *Phys. Status Solidi A*. doi:10.1002/pssa.201600500
- [2] S.-H. Lee, Y. Jung, and R. Agarwal, *Nature Nanotechnol.* 2(10), 626–630 (2007)
- [3] R. Fallica, C. Wiemer, T. Stoycheva, E. Cianci, M. Longo, H. T. Nguyen, A. Kusiak, and J.-L. Battaglia, *Microelectron. Eng.* 120, 3–8 (2014)
- [4] K. Deneke and A. Rabenau, *Z. f. Anorg. Allg. Chemie* 333 (4–6), 201–208 (1964)
- [5] A. J. O'Reilly, C. Francis, and N. J. Quitoriano, *J. Colloid Interf. Sci.* 370(1), 46–50 (2012)
- [6] S. Selmo, S. Cecchi, R. Cecchini, C. Wiemer, M. Fanciulli, E. Rotunno, L. Lazzarini, and M. Longo, *Phys. Status Solidi A* 213, No. 2, 335–338 (2016).
- [7] J. H. Los, T. D. Kühne, S. Gabardi, M. Bernasconi, *Phys. Rev. B* 88, 174203 (2013)
- [8] T. Schröder, T. Rosenthal, S. Grott, C. Stiewe, J. de Boor, and O. Oeckler, *Z. Anorg. Allg. Chem.* 639, 2536 (2013). The thermal diffusivity a was initially measured between room temperature and 250 °C using a laser-flash apparatus (LFA 427, Netzsch GmbH & Co., Germany). The thermal conductivity k was calculated according to $a = k / \rho C_p$. The heat capacity C_p was measured using a differential scanning calorimeter (DSC 404, Netzsch GmbH & Co., Germany).
- [9] A. Saci, J.-L. Battaglia, A. Kusiak, R. Fallica, M. Longo, *Appl. Phys. Lett.* 104, 263103 (2014)
- [10] J. V. Beck and K. J. Arnold, *Parameter estimation in engineering and science*, Wiley ed. (1977).
- [11] S. Lefèvre and S. Volz, *Rev. Sci. Instrum.* 76, 033701 (2005)
- [12] K. Ahn, K.-W. Park, H.-J. Jung, and S.-G. Yoon, *Nano Lett.* 10(2), 472–477 (2010)
- [13] A. Saci, J.-L. Battaglia and I. De, *IEEE Transactions on Nanotechnology* 14(6), 1-4 (2015)
- [14] S. Gomès, A. Assy, and P.-O. Chapuis, *Phys. Status Solidi A* 212, No. 3, 477–494 (2015)

- [15] A. Assy and S. Gomès, *Applied Physics Letters* 107, 043105 (2015).
- [16] D. Maillet, S. André, J.-C. Batsale, A. Degiovanni, and C. Moyne. *Thermal quadrupoles; solving the heat equation through integral transforms*. Wiley edition, 2000.
- [17] E. Puyoo, S. Grauby, J.-M. Rampoux, E. Rouvière, and S. Dilhaire, *Rev. Sci. Instrum.* 81, 073701 (2010)
- [18] G. Chen, *Phys. Rev. B* 57(23), 14958 (1998)
- [19] D. G. Cahill and R. O. Pohl, *Solid State Commun.* 70, 927 (1989). See also: D. G. Cahill, S. K. Watson and R. O. Pohl, *Phys. Rev. B* 46 (10), 6131 (1992).
- [20] D. Lencer, M. Salinga, B. Grabowski, T. Hickel, J. Neugebauer and M. Wuttig, *A map for phase-change materials*, *Nature Materials* 7, 972-977 (2008).
- [21] R. Fallica, J.-L. Battaglia, S. Cocco, C. Monguzzi, A. Teren, C. Wiemer, E. Varesi, R. Cecchini, A. Gotti and M. Fanciulli, *Thermal and electrical characterization of materials for Phase-Change Memory cell*, *J. Chem. Eng. Data* 54, 1698-1701 (2009).
- [22] J.-L. Battaglia, A. Kusiak, V. Shick, A. Cappella, C. Wiemer, M. Longo, E. Varesi, *Thermal characterization of the SiO₂-Ge₂Sb₂Te₅ interface from the ambient up to 400°C*, *J. Appl. Phys.* 107, 044314 (2010).
- [23] H.-S. Philip Wong, Simone Raoux, SangBum Kim, Jiale Liang, John P. Reifenberg, Bipin Rajendran, Mehdi Asheghi, and Kenneth E. Goodson, *Phase Change Memory*, *Proceedings of the IEEE* Vol. 98, No. 12 (2010).
- [24] J.-L. Battaglia, A. Kusiak, A. Saci, R. Fallica, A. Lamperti, C. Wiemer, *Effect of a thin Ti interfacial layer on the thermal resistance of Ge₂Sb₂Te₅-TiN stack*, *Appl. Phys. Lett.* 105, 121903, September (2015).
- [25] A. J. Griffin, Jr. and F. R. Brotzen, P. J. Loos, *The effective transverse thermal conductivity of amorphous Si₃N₄ thin films*, *J. Appl. Phys.* 76, 7 (1994).
- [26] S.-M. Lee and David G. Cahill, *Heat transport in thin dielectric films*, *J. Appl. Phys.* 81, 6 (1997).
- [27] G. Savage, *Carbon-Carbon composites*, 1st ed., Chapman & Hall, London (1993).
- [28] L. M. Manocha and E. Fitzer, *Carbon reinforcements and C/C composites*, 1st ed., Springer, Berlin (1998)
- [29] A. Oberlin, *Pyrocarbons*, *Carbon* 40(1), 7–24 (2002).
- [30] X. Bourrat, F. Langlais, G. Chollon, G.L. Vignoles, *J. Braz. Chem. Soc.* 117(6), 1090–1095 (2006).
- [31] G. L. Vignoles, R. Pailler, F. Teyssandier, *Ceram. Eng. Sci. Procs.* 33(8), 11–23 (2013).
- [32] A. Oberlin, *Carbonization and graphitization*, *Carbon* 22(6), 521–541 (1984)
- [33] G. L. Vignoles, P. Weisbecker, J.-M. Leyssale, S. Jouannigot, G. Chollon, *Carbones Pyrolytiques ou Pyrocarbones – des Matériaux Multi-Echelles et Multi-Performances*, *Techniques de l'Ingénieur*, ref. NM3150 (2015) (in French)
- [34] X. Bourrat, A. Fillion, R. Naslain, G. Chollon, M. Brendlé, *Carbon* 40(15), 2931–2945 (2002).
- [35] J. Jumel, F. Lepoutre, J-P Roger, D. Fournier, F. Ravel, M. Cataldi, *AIP Conf. Procs.* 557, 1039–1046 (2001).
- [36] J. Jumel, F. Lepoutre, J-P Roger, G. Neuer, M. Cataldi, F. Enguehart, *Rev. Sci. Instrum.* 74(1), 537–539 (2003).
- [37] J. Jumel, J. C. Krapez, F. Lepoutre, F. Enguehart, D. Rochais, G. Neuer, M. Cataldi, *AIP Conf. Procs.* 615, 1439–1446 (2002).

- [38] L. Shi, S. Plyasunov, A. Bachtold, P. L. McEuen, A. Majumdar, *Appl. Phys. Lett.* 77 (26), 4295–4297 (2000).
- [39] A. Assy, S. Gomès, *Appl. Phys. Lett.* 107, 043105 (2015).
- [40] B. Farbos, P. Weisbecker, H. E. Fischer, J.-P. Da Costa, M. Lalanne, G. Chollon, C. Germain, G. L. Vignoles, J.-M. Leyssale, *Carbon* 80(1), 472–489 (2014).
- [41] S. Lefèvre, S. Volz, *Rev. Sci. Instrum.* 76, 033701 (2005).
- [42] J.-M. Vallerot, X. Bourrat, A. Mouchon, G. Chollon, *Carbon* 44 (9), 1833–1844 (2006).
- [43] F. Lepoutre, D. Balageas, Ph. Forge, S. Hirschi, J. L. Joulaud, D. Rochais and F. C. Chen, *J. Appl. Phys.* 78, 2208–2223 (1995).
- [44] J. V. Beck and K. J. Arnold, *Parameter estimation in engineering and science*, Wiley, New York (1977)
- [45] Jean-Luc Battaglia, Indrayush De, Véronique Sousa Inverse heat conduction problem in a phase change memory device, *Journal of Physics: Conf. Series* 785 (2017) 012002
- [46] J.-L. Battaglia, A. Kusiak, V. Shick, A. Cappella, C. Wiemer, M. Longo, E. Varesi, Thermal characterization of the SiO₂-Ge₂Sb₂Te₅ interface from the ambient up to 400°C, *J. Appl. Phys.* 107, 044314 (2010)
- [47] A. J. Griffin, Jr. and F. R. Brotzen, P. J. Loos, The effective transverse thermal conductivity of amorphous Si₃N₄ thin films, *J. Appl. Phys.* 76, 7 (1994)
- [48] S.-M. Lee and David G. Cahill, Heat transport in thin dielectric films, *J. Appl. Phys.* 81, 6 (1997)
- [49] J.-L. Battaglia, A. Kusiak, A. Saci, R. Fallica, A. Lamperti, C. Wiemer, Effect of a thin Ti interfacial layer on the thermal resistance of Ge₂Sb₂Te₅-TiN stack, *Appl. Phys. Lett.* 105, 121903, September (2015).
- [50] Reifenberg J P, Kencke D L and Goodson K E 2008 *IEEE Electron. Device Lett.* 29 1112
- [51] Reifenberg J P, Chang K W, Panzer M A, Kim S, Jeremy A. Rowlette, M. Asheghi, H-S P Wong, and Goodson K E 2010 *IEEE Electron Device Letters* 31 1

7. Chapter 7 – CONCLUSIONS AND PERSPECTIVES

7.1. Main conclusions

The aim of this thesis was to investigate an original approach to perform quantitative thermal characterization on a range of microstructures, including materials and devices, using scanning thermal microscopy (SThM). This approach is based on the main choices:

- The probe are micro-fabricated thermoresistive devices that allow to heat the investigated surface and measure the temperature change of the resistive element with spatial accuracy of 100 nm and lower;
- The probe thermal impedance is derived experimentally from the out-of-contact configuration when the probe is far away from the investigated surface;
- The thermal contact resistance at the interface between the probe and the surface includes all the physical phenomena occurring in this region (solid-solid contact, water meniscus formation, diffusion and radiation through the air in ambient configuration) as well as the influence of the contact on the probe thermal impedance;
- It is assumed a constant contact area and thermal contact resistance when the probe scan heterogeneous surface;
- The unknown parameters are identified from the resolution of the inverse heat conduction problem using the frequency and spatial dependent probe temperature.

Therefore, our efforts have been put in order first to validate those assumptions and second to apply on real configurations.

As can be seen from Chapter 2, we started our investigation by going through the work performed by researchers in the field of nano and micro thermal property measurement. We have compared the solutions obtain from various methods and we showed that SThM provides the best spatial resolution when it comes to thermal property measurement using the contact method. Among all the incredible works that have been performed within this topic, we presented the on-going technological progresses that lead to the micro-fabricated thermoresistive probes with very

high spatial accuracy. Finally, we presented the different experimental configurations that could be adopted allowing choosing between the stationary and 3ω modes for instance.

In Chapter 3, we presented the experimental homemade setup that has been developed in the Lab. It is based on the 3ω technique that consists in varying the frequency of the current through the thermoresistive element and to measure the third harmonic of the voltage drop at both ends of this thermoresistive element. Since the probe temperature increase is linearly related to this voltage, the use of a lock-in amplifier is required to achieve the amplitude and the phase. We presented the two probes we have used for our experiments – 2-contact probe and 4-contact probe. From a specific experimental setup, we have determined the electrical resistance and the coefficient of probe electrical resistance for the two probes. It has been noted that both probes transfer heat in the same way and they possess similar geometry and constitutive materials. The only notable difference is the fact that the 4-contact probe eliminates the use of current limiters. Therefore, the calibration of the 4-point probe is easier than that of the 2-point one. We have also looked into the key sensitive parameters resulting from our experiment and experimental setup as the contact force and the probe motion velocity. We have shown that the velocity of the probe must be chosen according to the characteristic dimension of the investigated area, the number of “pixels” of the scan as well as the integration time of the lock-in. We have demonstrated that an accurate probe speed based on the spatial resolution can also lead to the effect of spot overlapping that allow increasing the spatial accuracy. We have also shown that the contact force between the probe and the sample should be minimum in order to avoid damage to the probe but at the same time high enough to maintain good contact by overcome the vibrational effects due to the frequency heating. It is also shown that the effect of the laser, which is used to monitor the cantilever deformation during the scan, on the probe temperature within the frequency range of interest is negligible. Finally, we have also seen that the surface preparation of the samples should be carefully examined prior to the scan for two main reasons. The first one is that the roughness must be minimized in order to not interfere with the probe temperature measurement. The second is related to the on-going degradation of the probe tip, after performing several experiments, which is due to the dust presents at the surface and in the air.

As seen in the chapter 4, the heat transfer model within the SThM configuration rests on the thermal impedance formalism. This analytical model is based on the integral transforms

technique and involves the probe thermal impedance, that of the investigated material and the thermal contact resistance at the interface between the probe and sample surface. The thermal impedance of the probe is achieved from a non-parametric system identification approach, by measuring the amplitude and the phase in the out-of-contact mode. In addition we have also shown that a transfer function, relating the average probe temperature to the heat flux generated by Joule effect, can be derived that involves non-integer derivative of fractional order. It was observed that a model involving only three parameters allowed us to reproduce the frequency dependent amplitude and phase very accurately. The use of the finite element analysis is required when the geometry does not allow the use of the integral transforms. In that case we demonstrated that the choice of infinite domain and appropriate mesh are mandatory to calculate the thermal impedance of the investigated material/device. Using such models we have performed a sensitivity analysis of the probe temperature with respect to the main unknown parameters that include the in-plane and out-of-plane thermal conductivity (k_r , k_z), the contact radius r_0 and the thermal contact resistance R_c . It was obviously retrieve that those parameters cannot be identified simultaneously using the frequency dependent probe temperature.

The main objective of the chapter 5 was to validate the experimental technique as well as the model on “calibrated” configurations where the thermal properties of the materials are well known. In a first step, we showed that the contact radius can be measured graphically using the “step” configuration that consists in a SiO₂ layer deposited as a step on a GaAS substrate. Although the results are very satisfying, we have also utilized an inverse approach based on finite element analysis and the measurement acquired during “step” experiments to obtain more accurate results. The additional benefit of this approach is that it allows identifying as well the thermal contact resistance at the interface probe/material. This second approach confirmed the result for r_0 obtained using the step configuration. Then, experiments have been performed in ambient condition considering six samples whose thermal conductivity spans in the 0.2-40 W.m⁻¹.K⁻¹. It was found that the contact radius is very close to the curvature radius of the tip. In addition, this experiment showed us first that we could consider the same value for r_0 and R_c for those six samples. This observation suggests that, under comparable experimental conditions and using the same probe, these two parameters can indeed be considered as constant for a class of materials that includes the dielectrics and the semiconductors. As a consequence, we concluded that the contact radius as well as the thermal contact resistance did not vary when the probe scans

a heterogeneous surface. The second conclusion of those results is that it defined the detectivity of the probe, regarding the thermal conductivity about to $20 \text{ W.m}^{-1}.\text{K}^{-1}$. It must be also noticed that the thermal contact resistance is slightly higher when the probe scans the surface that in static (motionless) configuration. This result is not surprising since it has been observed for a long time that the sliding leads to increase this resistance at the macroscale. Although our measurements cannot constitute a definitive conclusion, it seems that it remains true at the microscale. We repeated those experiments when the samples are embedded in a vacuum chamber with the probe in static condition (motionless probe). In that case, we found that the contact radius is the third of the value found under atmospheric condition. The thermal contact resistance is found to be lower than that found in ambient considering the motionless probe. This significant difference could be attributed to both the diffusion in air and to the water meniscus formation that does not occur anymore under vacuum. However, it has been also observed that the detectivity remains comparable of that obtained in ambient configuration with the presence of the water meniscus. All the main results have been reported in Table 22.

Table 22. Main achievements regarding the validation experiments.

Configuration	r_0 (nm)	R_c ($\text{K.m}^2.\text{W}^{-1}$)
Ambient – motionless probe	100 ± 5	$(8.9 \pm 0.29) \times 10^{-8}$
Ambient – moving probe	117 +/- 10 (« step » graphical technique) 101 +/- 3 (IHCP)	$(1.1 - 1.4) \times 10^{-7}$
Vacuum – motionless probe	25.20 ± 0.15	$(1.22 \pm 0.014) \times 10^{-8}$

The chapter 5 is devoted to the use of our experiment and method to reach quantitative values of thermal key parameters for material and devices. Let us note here that those applications have been treated through different collaborations (Synapse EU project, CEA-LETI, LCTS). We have investigated the thermal resistance of an In_3SbTe_2 nanowire across the transverse direction using both experimental and minimization techniques without any specific handling or material

preparation. We also looked into 3D phase change memory nano device based on the $\text{Ge}_2\text{Sb}_2\text{Te}_5$ (GST) phase change alloy. We have utilized both experimental and inverse approach to obtain the thermal boundary resistance between the vertical GST and the surrounding dielectric (Si_3N_4). Our final application concerned a complex composite containing glass fibers and laminar pyrocarbon where we have obtained the effective thermal conductivity to the pyrocarbon and the thermal contact resistance between the carbon matrix and the silica fiber. This investigation allows the completion of the existing database obtained by thermoreflectance on other types of pyrocarbons.

All the results we obtained have been published in international journals [ACL] and have been also presented in international conferences [ACTI]:

- [ACL 1] J.-L. Battaglia, **I. De**, V. Sousa, *Inverse heat conduction problem in a phase change memory device*, Journal of Physics: Conf. Series **785** (2017) 012002.
- [ACL 2] **I. De**, J.-L. Battaglia, G. L. Vignoles, *Thermal properties measurements of a silica/pyrocarbon composite at the microscale*, Journal Applied Physics, DOI: 10.1063/1.4967918 (2016).
- [ACL 3] J.-L. Battaglia, A. Saci, **I. De**, R. Cecchini, S. Selmo, M. Fanciulli, S. Cecchi, M. Longo, *Thermal resistance measurement of In_3SbTe_2 nanowires*, phys. stat. sol. (a) (2016).
- [ACL 4] J.-L. Battaglia, **I. De**, A. Saci, A. Kusiak, V. Sousa, *Thermal investigation of a phase change memory device at the nanoscale*, Journal of Physics: Conference Series 745 (2016) 032098.
- [ACL 5] A. Saci, J.-L. Battaglia and **I. De**, *Accurate new methodology in scanning thermal microscopy*, IEEE Transactions on Nanotechnology **14**(6), 1035-1039 (2015).
- [ACL 6] A. Saci, J.-L. Battaglia, A. Kusiak, **I. De**, R. Fallica, M. Longo, *"Anisotropic Thermal Conductivity of a Sb_2Te_3 Phase Change Nanowire"*, Advances in Science and Technology, Vol. **95**, pp. 120-125, Oct. (2014).
- [ACTI 1] J.-L. Battaglia, **I. De**, A. Saci, A. Kusiak, V. Sousa, *Thermal investigation of a phase change memory device at the nanoscale*, 7th European Thermal-Sciences Conference, 19-23 June 2016, Krakow, Poland.
- [ACTI 2] R. Cecchini, J.-L. Battaglia, A. Saci, **I. De**, S. Selmo, M. Fanciulli, S. Cecchi, M. Longo, *Thermal resistance characterization of $\text{In}_3\text{Sb}_1\text{Te}_2$ nanowires*, Material.it 2016, Catania, Italy, December 12-16 2016.
- [ACTI 3] Jean-Luc Battaglia, **Indrayush De**, Abdelhak Saci, Andrzej Kusiak, Véronique Sousa, *Thermal investigation of a phase change memory device at the nanoscale*, Nanoscale and Microscale Heat Transfer V Eurotherm Seminar No 108, September 26-30, 2016, Santorini, Greece.
- [ACTI 4] A. Saci, J.-L. Battaglia, A. Kusiak, I. De, R. Fallica and M. Longo, *The use of SThM for measuring the thermal conductivity of a Sb_2Te_3 phase change nanowire*, Eurotherm 103, Nanoscale and microscale heat transfer IV, October 15-17 2014, Lyon, France.
- [ACTI 5] A. Saci, J.-L. Battaglia, A. Kusiak, **I. De**, R. Fallica and M. Longo, *Thermal conductivity measurement of a Sb_2Te_3 phase change nanowire*, 20th European Conference Thermophysical Properties (ECTP), Porto, Portugal, August 31st - September 4th 2014.

7.2. Perspectives

One of the main drawbacks of the proposed SThM was that it cannot provide the thermal conductivity tensor. In other words, we have to consider the effective thermal conductivity only. Therefore, a very interesting improvement of the method would be to involve at least two probes on the same cantilever. This perspective requires obviously working together with a provider that is able to fabricate such probes.

A second improvement would be to work systematically under vacuum condition in order to remove the diffusion in air and the water meniscus. Since it has been observed that the detectivity is not higher even in the presence of the water meniscus, it could be expected a higher spatial accuracy in such a configuration. The second advantage of this approach is that the SThM could be embedded within a SEM in order to make direct observations. To our knowledge, this approach has been experienced already very recently in other labs.

With time, we can see advancement in thermal probes and these improvements are guided towards providing higher spatial resolution (less than 30 nm). The contrary effect is the fact that an increase in the spatial resolution leads to a decrease in the probe radius which in-turn reduces the heat transfer and thus the capacity of measuring materials of thermal conductivity higher than 40 W/m/K. Multifunctional probes may be developed and come into practice in the future and this might open a whole new range of application and industry to SThM. Apart from thermal investigation, metrology and patterning may also be added. Multifunctional probes can be a thing of the recent future. For example, the “thermal radiation STM” (TR-STM probe which works on the principle of detection of the heated scattered thermal radiation from a heated sample. The probe tip can also be heated instead of the sample. The scattered radiation can be collected and a Fourier-transform infrared analysis can be performed to obtain the sample’s spectroscopic features. This brings forward the possibility of using the same probe for various purposes at the same time (adding on SThM with other applications like investigation at the nanoscale, electrical and mechanical properties, chemical and magnetic properties, etc.). There has been a lot of development in this field and this will bring further development and advancement in the field of scanning thermal microscopy (SThM).